

**Confidence Bands, Measurement Noise, and
Multiple Input - Multiple Output Measurements
Using the Three-Channel Frequency Response Function Estimator**

by
Richard E. Cobb

Dissertation submitted to the Faculty of the
Virginia Polytechnic Institute and State University
in partial fulfillment of the requirements for the degree of
Doctor of Philosophy
in
Mechanical Engineering

APPROVED:

Larry D. Mitchell, Chairman

Robert H. Fries

Walter R. Pife

Charles F. Reinholtz

Alfred L. Wicks

May, 1988
Blacksburg, Virginia

**Confidence Bands, Measurement Noise, and
Multiple Input - Multiple Output Measurements
Using the Three-Channel Frequency Response Function Estimator**

by

Richard E. Cobb

Larry D. Mitchell, Chairman

Mechanical Engineering

(ABSTRACT)

A three-channel Frequency Response Function (FRF) estimator is discussed and statistical relations developed. Methods for estimating the variance of the FRF magnitude and levels of uncorrelated content in the test signals are developed. FRF magnitude variance estimates allow 'confidence bands' to be placed on FRF magnitude estimates, giving an indication of the variability of the result. Uncorrelated content estimates indicate sources and magnitudes of noise in the measurement system. Both Monte Carlo simulations and experimental work are used to verify the statistical and uncorrelated content estimates. Relations to extend the three-channel FRF estimator to multiple input-multiple output measurements are developed and verified through simulations.

Acknowledgements

*You are never given a wish without also being given
the power to make it true.
You may have to work for it, however.*

Richard Bach - from *Illusions*

There are more people than I can count who have given me help and encouragement on my journey from a virtual high school dropout to a successful Ph.D. candidate, but there are two special people without whom the latter part of the journey may never have occurred. One was my major advisor, . The encouragement, support, help and friendship I have experienced working with can only be described by a long list of superlatives. I could not have worked with a finer person. My other mentor is . Without the encouragement and opportunities I received from I

might never have begun graduate studies. I feel honored to have known and been helped by two such fine people, and a strong responsibility to live up to the opportunities I was given. I hope you both find me worthy of your efforts in the years to come.

I also am indebted to the others on my committee for discussions, help, encouragement, and finally, reading and suggesting improvements in this dissertation. To _____, I have enjoyed our association, and am grateful to you for confirming that the 'killer instinct' isn't necessary for success. _____, your ever present willingness to help were greatly appreciated. And _____, I appreciate both your help and the fact that having an old friend on my committee did not change that.

To my wife, _____ I say thank you for sharing these years of learning. It has been a pleasure to walk our parallel paths together. To my mother and grandmother, _____ thank you for always standing behind me. I am sorry, _____, that you did not live to see this day. And to my grandfather, _____ though you left us long ago, I am sure that the thirst for adventure that lives in me today came from none other than you. I can think of no finer inheritance.

Finally, to _____, my office mate of several years, I have enjoyed the often lengthy discussions between the aging hippie and the young conservative, and for the all the help you provided in the 'nuts and bolts' of cranking out a dissertation.

Table of Contents

Chapter 1 - Introduction	1
Chapter 2 - Statistics for the Three-channel Measurement System	6
2.1 Background Statistics	6
2.2 Development of Some Basic Estimates	9
2.2.1 The Three-channel Measurement Model	9
2.2.2 Some Expectations for the Three-Channel Model	11
2.2.3 Three-Channel-Model Coherences	12
2.2.4 Estimates of Uncorrelated Content	13
2.3 Some Variance Estimates	14
2.4 The Effect of Averaging Raw Samples	17
2.5 Covariance and Correlation	18
2.6 The Three-Channel FRF Estimator	21
Chapter 3 - Bias Errors in Complex Magnitude Estimation	24
3.1 An Example of the Magnitude Bias Error	25
3.2 Magnitude and Variance for a Special Case	30

3.2.1 Application of the Rayleigh Distribution	32
3.2.2 Application of the Taylor Series.	32
3.2.3 Magnitude and Variance by Probability Density Functions	36
3.2.3.1 Probability Density Functions	36
3.2.3.2 PDF's Applied to the Complex Magnitude	37
3.2.3.3 PDF by Transformation of Variables	38
3.2.4 Magnitude Bias and Variance by Numerical Integration	39
3.3 Magnitude and Variance for the General Case	48
Chapter 4 - Variance of the Three-channel FRF Estimator	49
4.1 A Finite Difference Method for Estimating Variance	51
4.1.1 Theoretical Development	51
4.1.2 Problems With the Finite Difference Variance Estimate	52
4.2 A Numerical Method for Estimating Variance	53
4.2.1 Details of the Integrations to Determine FRF Variance	54
4.2.1.1 Cross Spectral Magnitude Variance	54
4.2.1.2 FRF Magnitude Variance	56
4.2.2 Determining an Efficient Integration Region	57
Chapter 5 - Experimental FRF Measurement Simulations	63
5.1 Simulating the FRF Measurement Process	64
5.2 Single Spectral Line Monte Carlo Simulations	65
5.3 Multiple Spectral Line FRF Measurement Simulations	67
Chapter 6 - Results of FRF Measurement Simulations	70
6.1 Comparison of FRF Estimators	70
6.2 Monte Carlo Simulations	72

6.2.1 Auto Spectrum Calculations and Results	81
6.2.2 Cross Spectrum Calculations and Results	83
6.2.3 Coherence Calculations and Results	87
6.2.4 Frequency Response Function Calculations and Results	89
6.2.4.1 Bias and Variance in the FRF Real and Imaginary Components	90
6.2.4.2 Bias and Variance in the FRF Magnitude Estimation	93
6.2.4.3 Estimates of FRF Variance	99
6.2.5 Uncorrelated Content Estimates	104
6.3 Probability Density Function (PDF) Results From the Simulations	106
6.3.1 Cross Spectrum Probability Distributions	107
6.3.2 FRF Probability Distributions	122
6.4 Single Measurement Simulations	132
6.4.1 Variance Estimates	133
6.4.2 Uncorrelated Content Estimates	141
6.4.2.1 Estimates of Shaker and Force Measurement Noise	141
6.4.2.2 Estimates of Response Measurement Noise	148
Chapter 7 - Results of Experimental Measurements	153
7.1 Results of Measurements of the Calibration Mass FRF	156
7.1.1 Variance Estimates for the Calibration Mass	157
7.1.2 Uncorrelated Content Estimates for the Calibration Mass	163
7.2 Results of the Flat-Plate FRF Measurements	168
7.2.1 Flat-Plate FRF Variance Estimates	170
7.2.1.1 Variance Estimates Using Burst Random Excitation	174
7.2.1.2 Variance Estimates Using Continuous Random Excitation	177
7.2.2 Flat-Plate Uncorrelated Content Estimates	181

Chapter 8 - The Three-Channel Estimator in Multiple Input/Output Estimates	191
8.1 Development of the Multiple Input/Output Estimator	193
8.2 Other Multiple Input FRF Estimators	199
8.3 Multiple Input - Multiple Output Measurement Simulations	200
Chapter 9 - Conclusions and Recommendations	202
9.1 Conclusions	202
9.2 Recommendations	203
References	206
Appendix	210
Cross Spectrum Magnitude Covariance Derivation	210
Vita	215

List of Illustrations

Figure 1. Three-Channel Measurement Model	10
Figure 2. Illustration of Rayleigh Distribution	29
Figure 3. Magnitude Variance Referenced to True Magnitude	42
Figure 4. Magnitude Standard Deviation Referenced to True Magnitude	43
Figure 5. Magnitude Standard Deviation Referenced to Magnitude Expectation	44
Figure 6. Magnitude Correction Referenced to Component Standard Deviation	46
Figure 7. Magnitude Correction Based on Magnitude Estimates	47
Figure 8. Comparison of Frequency Response Function Estimators	71
Figure 9. Gaussian Distribution Histogram	108
Figure 10. Histogram - Real Part of Data Set A Cross Spectrum	110
Figure 11. Histogram - Imaginary Part of Data Set A Cross Spectrum	111
Figure 12. Histogram - Magnitude of Data Set A Cross Spectrum	112
Figure 13. Histogram - Real Part of Data Set B Cross Spectrum	114
Figure 14. Histogram - Imaginary Part of Data Set B Cross Spectrum	115
Figure 15. Histogram - Magnitude of Data Set B Cross Spectrum	116
Figure 16. Histogram - Magnitude of Data Set C Cross Spectrum	117
Figure 17. Histogram - Magnitude of Data Set D Cross Spectrum	118
Figure 18. Histogram - Magnitude of Data Set E Cross Spectrum	119
Figure 19. Histogram - Magnitude of Data Set F Cross Spectrum	120

Figure 20. Histogram - Real Part of Data Set A FRF	124
Figure 21. Histogram - Imaginary Part of Data Set A FRF	125
Figure 22. Histogram - Magnitude of Data Set A FRF	126
Figure 23. Histogram - Real Part of Data Set B FRF	127
Figure 24. Histogram - Magnitude of Data Set B FRF	128
Figure 25. Histogram - Magnitude of Data Set C FRF	129
Figure 26. Histogram - Magnitude of Data Set D FRF	130
Figure 27. Histogram - Magnitude of Data Set F FRF	131
Figure 28. Simulated 50-Sample FRF Measurement	136
Figure 29. 95 Percent Confidence Bands - 50 Sample Measurement	137
Figure 30. 95 Percent Confidence Bands - 300 Sample Measurement	138
Figure 31. 68 Percent Confidence Bands - 300 Sample Measurement	139
Figure 32. Estimate of Uncorrelated Content in Shaker System	142
Figure 33. Estimate of Uncorrelated Content in Force Measurement	143
Figure 34. Comparison of Shaker and Measurement Noise Estimates	145
Figure 35. Sum of Shaker and Measurement Noise Estimates	146
Figure 36. Corrected Shaker and Measurement Noise Estimates	147
Figure 37. Response Measurement Noise Estimate	149
Figure 38. Response Measurement Noise Estimate - Increased Scale	151
Figure 39. Response Measurement Noise Estimate - Large Scale	152
Figure 40. Measured Calibration Mass FRF and Average Value	158
Figure 41. Calibration Mass - 95 Percent Confidence Bands	160
Figure 42. Calibration Mass - 99 Percent Confidence Bands	161
Figure 43. Calibration Mass - 68 Percent Confidence Bands	162
Figure 44. Auto Spectra of Force and Shaker Noise - Wire Connector	164
Figure 45. Auto Spectra of Force and Shaker Noise - Ball Joint Connector	165

Figure 46. Response Auto Spectra and Uncorrelated Content Estimate	169
Figure 47. Long Term Variation in FRF Measurements	172
Figure 48. FRF and Two Standard Deviation Bounds for Contiguous Measurements	178
Figure 49. 'Shaker Noise' and Force Auto Spectra - Burst Random Excitation ..	182
Figure 50. 'Force Noise' and Force Auto Spectra - Burst Random Excitation ...	184
Figure 51. 'Shaker Noise' and Force Auto Spectra - Continuous Random Excitation	185
Figure 52. 'Force Noise' and Force Auto Spectra - Continuous Random Excitation	186
Figure 53. 'Response Noise' and Auto Spectra - Burst Random Excitation	188
Figure 54. 'Response Noise' and Auto Spectra - Continuous Random Excitation	189
Figure 55. Multiple Input Measurement Model	192
Figure 56. Simulated Multiple Input-Multiple Output FRF Measurement	201

List of Tables

Table 1. Simulation Data Set A	73
Table 2. Simulation Data Set B	74
Table 3. Simulation Data Set C	75
Table 4. Simulation Data Set D	76
Table 5. Simulation Data Set E	77
Table 6. Simulation Data Set F	78
Table 7. Uncorrelated Content Estimates	103

Chapter 1 - Introduction

Early Frequency Response Function (FRF) measurements of structures were made using swept-sine or stepped-sine techniques. A single frequency sinusoidal force was applied to a structure and the system response (magnitude and phase) was determined from the measured force and response signals. The frequency of the force was swept continuously or incrementally through a range of frequencies to measure frequency dependent behavior. The method resulted in good measurements, but was very slow.

The introduction of the Fast Fourier Transform (FFT) method in the mid 1960's revolutionized FRF measurements. Although other methods of performing 'fast' Fourier transforms have been known since the early 1940's [1], it was the introduction of the Cooley-Tukey algorithm [2] that resulted in the popularity of the FFT method of FRF measurements. The FFT is an efficient method for calculating a Discrete Fourier Transform (DFT). A DFT transforms time signals which have been sampled at discrete intervals into a frequency-domain representation. This allows the use of broad-band excitation to measure frequency-dependent behavior simultaneously over a range of frequency. Most DFT methods require computation times on the order of N^2 (where N

is the number of points in the transformation), while the FFT method reduces the time required to the order of $N \log_2 N$ [1]. This considerable time savings for large N was responsible for the popularity of the method.

Until the early 1980's there was one primary method for calculating FRF estimates using the FFT. This has recently become known as the ${}^1\hat{H}$ estimator, in view of the development of newer estimators. The estimate is found by [3,4]

$${}^1\hat{H}(f) = \frac{\hat{G}_{yx}(f)}{\hat{G}_{xx}(f)} \quad (1.1)$$

where $G_{yx}(f)$ and $G_{xx}(f)$ are the cross and auto spectrum functions, respectively, of the input X (usually a force) and output Y , and the 'hat' (^) is used to denote an estimate. These quantities will be further defined in Chapter 2. The ${}^1\hat{H}(f)$ estimator was based on the assumption of very little 'noise' or uncorrelated (with the response) content in the measured input (force). A test for the presence of uncorrelated content can be made with the 'coherence' function. In terms of estimated quantities this is given by

$$\hat{\gamma}_{yx}^2 = \frac{|\hat{G}_{yx}(f)|^2}{\hat{G}_{xx}(f) \hat{G}_{yy}(f)} \quad (1.2)$$

Non-unity values of coherence indicate the presence of uncorrelated content *somewhere* (in the force and/or response) measurement.

Mitchell [3,4] showed that errors in the estimate of the FRF could be substantial when $\hat{\gamma}_{yx}^2$ was small and proposed two alternative estimators. These are ${}^2\hat{H}(f)$ and ${}^3\hat{H}(f)$, where

$${}^2\hat{H}(f) = \frac{\hat{G}_{yy}(f)}{\hat{G}_{xy}(f)} \quad (1.3)$$

and ${}^3\hat{H}(f)$ is found by an average or other linear combination of ${}^1\hat{H}(f)$ and ${}^2\hat{H}(f)$, and is the basis of the renamed ${}^r\hat{H}(f)$ estimator.

Mitchell's alternate FRF estimators generated a flurry of activity in evaluating the different estimators. Vold [5] compared the FRF estimates obtained, while Elliott and Mitchell [6], Cawley [7], and others [8] evaluated performance of the various estimators in modal 'circle fitting' procedures. Schmidt [9] compared the various estimators in sensitivity to resolution bias errors. Other estimators were also developed. Wicks [10,11,12] used estimates of the 'noise' in the system to optimize the weighting of the ${}^1\hat{H}$ and ${}^2\hat{H}$ estimators at each frequency in the ${}^r\hat{H}(f)$ estimator. All of these estimators are based on two-channel measurements, that is, the applied force (X) and structure response (Y) are measured simultaneously. When there is uncorrelated content present in the system all of the two-channel estimators are dependent on certain assumptions and/or estimates being correct if they are to deliver unbiased estimates of the system FRF.

Goyder proposed a three-channel estimator [13] which would eliminate these problems. This method can only be used in testing situations where a random signal generator produces a signal (S) which is amplified and input to an electrodynamic 'shaker' to produce the force (i.e., this method cannot be applied to, say, hammer impact testing). This third channel is used to form cross spectra with the other two channels. The three-channel estimate is then found by

$${}^c\hat{H}(f) = \frac{\hat{G}_{ys}(f)}{\hat{G}_{xs}(f)} \quad (1.4)$$

The reasoning behind this estimator was that the third signal would provide a reference for force and response measurements that would enable the uncorrelated content to be eliminated in the averaging process. This method has been used to determine an equivalent linear FRF in the presence of large nonlinearities in a heat exchanger [14] and further investigated in respect to nonlinear behavior by Ratcliffe [15]. Further activity in the modal analysis field was generated in comparisons and evaluations of this estimator [16,17] and in new applications. Cobb and Mitchell applied the three-channel FRF estimator to multiple input-multiple output systems [18] and also developed a method for estimating the uncorrelated content present in the measured signals [19].

Most multiple input-multiple output measurement methods have been based on the single input-single output ${}^1\hat{H}$ estimator, a comprehensive discussion of which is given by Allemang [20]. In the development of the three-channel FRF multiple input-multiple output relations the conventional notation method of placing the estimator type as a subscript (i.e., $\hat{H}_1(f)$) was found to be cumbersome and confusing. An alternate notation method was proposed by Cobb and Mitchell [18] to remove ambiguity and confusion. Part of this proposal consisted of placing the estimator type as a 'pre-superscript' (as has been done throughout this dissertation). This removes the possibility of the estimator type being confused with an input or output location (in multi-I/O), or a power (if moved to a 'post-superscript' position).

A wealth of literature exists regarding statistical estimates of data obtained by FFT methods. Of chief interest in this work are estimates of the variance of frequency re-

sponse function estimates. Bendat [21] and Abom [22] have both developed variance estimates for ${}^1\hat{H}$, and Abom [22] discusses some limits of variance for ${}^2\hat{H}$ and ${}^3\hat{H}$. In many fields there are certain texts which are almost universally known. One such text on the statistics of FFT estimates has been written by Bendat and Piersol [23]. This text will be the primary reference in the statistical developments in following chapters.

Chapter 2 - Statistics for the Three-channel Measurement System

This chapter will develop statistics and other relations for the three-channel measurement system. The first section will review some general statistics. For the reader's convenience in locating auxiliary material, this chapter will refer to only one reference text, [23]. Citations will be of the form [23, section 3.1] to help locate the material within the text.

2.1 Background Statistics

Section 2.1 reviews some statistics found in [23, ch.9]. A signal $x(t)$ measured in the time domain may be Fourier transformed to a frequency-domain signal, $X(f)$, where for a record of $x(t)$ measured over some finite period T

$$\begin{aligned}
X(f) &= X_R(f) - jX_I(f) \\
X_R(f) &= \int_0^T x(t) \cos 2\pi f t dt \\
X_I(f) &= \int_0^T x(t) \sin 2\pi f t dt
\end{aligned} \tag{2.1}$$

If $x(t)$ has a Gaussian (Normal) distribution with zero mean, then the real and imaginary terms in Eq. 2.1, $X_R(f)$ and $X_I(f)$, are uncorrelated random variables which are also normally distributed with zero means.

A discrete Fourier transform (DFT) represents real and imaginary parts of $X(f)$ as sets of spectral lines at discrete frequencies, $X_k(f)$. The k^{th} spectral line, $X_k = X_{kR} - jX_{kI}$ is a complex number, where X_{kR} and X_{kI} are zero mean Gaussian variables. At this point the k subscript will be dropped with the understanding that all operations are carried out on every spectral line of a DFT. For a single measurement $x(t)$, a raw (unaveraged) estimate of the auto spectrum at any spectral line is obtained by

$$\tilde{G}_{xx} = \frac{2}{T} [|X(f)|^2] = \frac{2}{T} [X_R^2 + X_I^2] \tag{2.2}$$

where the 'tilde' (-) denotes a raw (single sample) estimate.

Similarly, a raw estimate of the cross spectrum between $x(t)$ and another normally distributed zero mean signal $y(t)$ is given by

$$\begin{aligned}
\tilde{G}_{yx} &= \frac{2}{T} [X(f)^* Y(f)] \\
&= \frac{2}{T} [(X_R + jX_I)(Y_R - jY_I)] = \tilde{C}_{yx} - j\tilde{Q}_{yx} \\
\tilde{C}_{yx} &= \frac{2}{T} [X_R Y_R + X_I Y_I] \quad \tilde{Q}_{yx} = \frac{2}{T} [X_R Y_I - X_I Y_R]
\end{aligned} \tag{2.3}$$

In developments to follow $X(f)$ and $Y(f)$ will generally be quantities that are derived as functions of other random variables. To avoid confusion then, the statistical relations that follow are presented in terms of $S(f)$, $K(f)$, and $M(f)$, which are some of the variables in the target derivations. The quantities that these variables represent will be presented shortly. For the moment it is enough to know that they are mutually uncorrelated random variables with all the discussed properties of $X(f)$, most important of which are the zero mean and Gaussian distribution properties. Since $S(f)$, $K(f)$, and $M(f)$ are uncorrelated, the expected values of any of their products (such as say $S_R K_I$) are zero. From [23,section 9.1] we obtain the expectation of the product and the square of the real and imaginary parts (of say, $S(f)$) as

$$E[S_R S_I] = 0 \quad E[S_R^2] = E[S_I^2] = \frac{T}{4} G_{ss} \quad (2.4)$$

Any zero mean Gaussian random variable raised to an odd power has an expectation of zero. This also applies to products of these variables when the sums of the exponents result in odd powers. That is

$$E[S_R^3] = E[S_R^2 S_I] = E[S_R^3 S_I^2] = 0 \quad (2.5)$$

For the product of 4 Gaussian random variables

$$E[a_1 a_2 a_3 a_4] = E[a_1 a_2] E[a_3 a_4] + E[a_1 a_3] E[a_2 a_4] + E[a_1 a_4] E[a_2 a_3] \quad (2.6)$$

From Eq. 2.4 and Eq. 2.6 it follows that

$$\begin{aligned}
E[S_R^2 S_I^2] &= \left(\frac{T}{4}\right)^2 G_{ss}^2 \\
E[S_R^4] &= 3\left(\frac{T}{4}\right)^2 G_{ss}^2 \\
E[S_R^2 K_R^2] &= \left(\frac{T}{4}\right)^2 G_{ss} G_{kk} \\
E[S_R^2 K_R M_R] &= E[S_R S_I K_R K_I] = 0
\end{aligned} \tag{2.7}$$

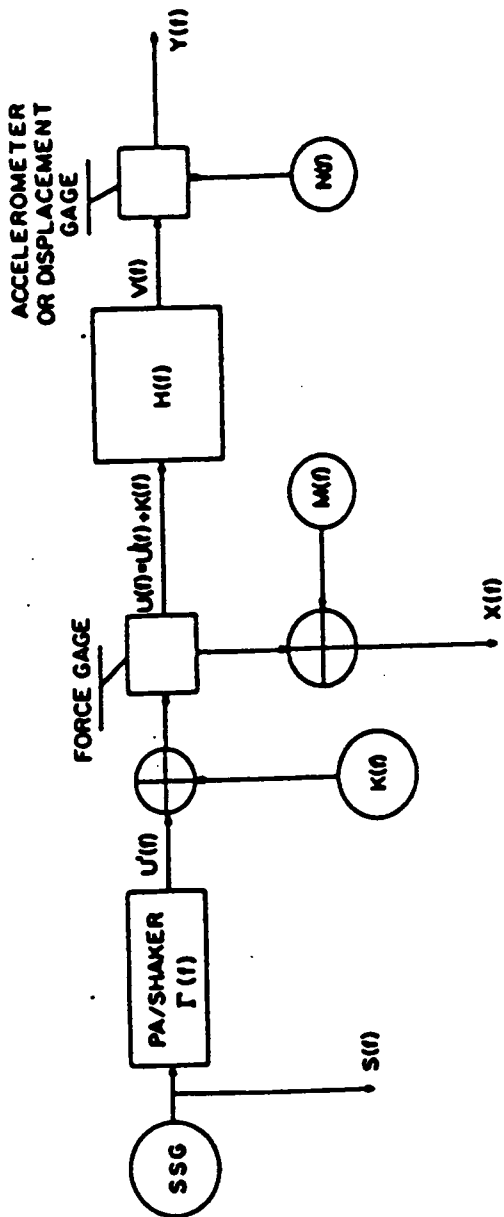
On the other hand, products of 2 correlated variables, say $X(f)$ and $Y(f)$, have non-zero expectations. Specifically,

$$\begin{aligned}
E[X_R Y_R] &= E[X_I Y_I] = \frac{T}{4} C_{yx} \\
E[X_R Y_I] &= -E[X_I Y_R] = \frac{T}{4} Q_{yx}
\end{aligned} \tag{2.8}$$

2.2 Development of Some Basic Estimates

2.2.1 The Three-channel Measurement Model

Figure 1 shows the three-channel measurement model. All terms are described as complex values in the frequency domain. A random signal generator produces the 'source' signal, $S(f)$, which is measured, amplified, and applied to an electro-dynamic shaker. The linear dynamic system responses of the amplifier, shaker, and attachment hardware are combined in a single shaker system gain FRF, $\Gamma(f)$.



- S - Random Signal Generator Output**
- K - Uncorrelated Content - Signal Amplification/Transduction**
- U - True Force Applied to Structure**
- M - Uncorrelated Content in Force Measurement**
- X - Measured Force**
- V - True Structural Response**
- N - Uncorrelated Content in Response Measurement**
- Y - Measured Structural Response**

Figure 1. Three-Channel Measurement Model

Nonlinearities and other uncorrelated content in the source-to-force transduction process appear in the model as $K(f)$. The true force applied to the structure, $U(f)$, acts through the system frequency response function (FRF), $H(f)$, to produce the true system response, $V(f)$. $X(f)$, the attempt to measure the true force $U(f)$, is contaminated by uncorrelated content $M(f)$ in the measurement process. Similarly, $Y(f)$ is an attempt to measure $V(f)$ that has been contaminated by $N(f)$. In equation form these relations are:

$$\begin{aligned} U(f) &= S(f)\Gamma(f) + K(f) & X(f) &= U(f) + M(f) \\ V(f) &= H(f)U(f) & Y(f) &= V(f) + N(f) \end{aligned} \quad (2.9)$$

2.2.2 Some Expectations for the Three-Channel Model

Carrying out the indicated operations for $X(f)$ in Eq. 2.9

$$X(f) = [S_R\Gamma_R - S_I\Gamma_I + K_R + M_R] - j[S_I\Gamma_R + S_R\Gamma_I + K_I + M_I] \quad (2.10)$$

Substituting this expression in Eq. 2.2 and taking the expectation of both sides

$$E[\tilde{G}_{xx}] = \frac{2}{T}E[(S_R\Gamma_R - S_I\Gamma_I + K_R + M_R)^2 + (S_I\Gamma_R + S_R\Gamma_I + K_I + M_I)^2] \quad (2.11)$$

Expanding Eq. 2.11 and taking the expectation with the aid of Eq. 2.4, we get

$$E[\tilde{G}_{xx}] = G_{ss}|\Gamma|^2 + G_{kk} + G_{mm} \quad (2.12)$$

Similarly, carrying out the multiplication and addition operations indicated in Eq. 2.9 while using Eqs. 2.4 and 2.8 the following relations may be developed

$$\begin{aligned}
E[\tilde{G}_{ss}] &= G_{ss} \\
E[\tilde{G}_{yy}] &= |H|^2\{G_{ss}|\Gamma|^2 + G_{kk}\} + G_{nn} \\
E[\tilde{C}_{xs}] &= G_{ss}\Gamma_R \\
E[\tilde{Q}_{xs}] &= G_{ss}\Gamma_I \\
E[\tilde{C}_{ys}] &= G_{ss}\{Re(\Gamma H)\} \\
E[\tilde{Q}_{ys}] &= G_{ss}\{Im(\Gamma H)\} \\
E[\tilde{C}_{yx}] &= H_R\{G_{ss}|\Gamma|^2 + G_{kk}\} \\
E[\tilde{Q}_{yx}] &= H_I\{G_{ss}|\Gamma|^2 + G_{kk}\}
\end{aligned} \tag{2.13}$$

2.2.3 Three-Channel-Model Coherences

The ordinary coherence between X and Y is

$$\gamma_{yx}^2 = \frac{|G_{yx}|^2}{G_{xx}G_{yy}} = \frac{C_{yx}^2 + Q_{yx}^2}{G_{xx}G_{yy}} \tag{2.14}$$

Using Eqs. 2.13 and 2.14 yields

$$\gamma_{xs}^2 = \frac{G_{ss}|\Gamma|^2}{G_{ss}|\Gamma|^2 + G_{kk} + G_{mm}} \tag{2.15a}$$

$$\gamma_{ys}^2 = \frac{G_{ss}|\Gamma H|^2}{G_{ss}|\Gamma H|^2 + G_{kk}|H|^2 + G_{nn}} \tag{2.15b}$$

$$\gamma_{yx}^2 = \frac{\{G_{ss}|\Gamma|^2 + G_{kk}\}^2 |H|^2}{(G_{ss}|\Gamma|^2 + G_{kk} + G_{mm}) (|H|^2\{G_{ss}|\Gamma|^2 + G_{kk}\} + G_{nn})} \tag{2.15c}$$

2.2.4 Estimates of Uncorrelated Content

Solving Eqs. 2.15a and 2.15b for the auto spectra of the uncorrelated content in the measurement of the force and response, we get

$$\begin{aligned} G_{mm} &= \frac{G_{ss} |\Gamma|^2 (1 - \gamma_{xs}^2)}{\gamma_{xs}^2} - G_{kk} \\ G_{nn} &= |H|^2 \left\{ \frac{G_{ss} |\Gamma|^2 (1 - \gamma_{ys}^2)}{\gamma_{ys}^2} - G_{kk} \right\} \end{aligned} \quad (2.16)$$

Substituting Eqs. 2.16 in Eq. 2.15c and solving for G_{kk} yields

$$G_{kk} = G_{ss} |\Gamma|^2 \left\{ \left(\frac{\gamma_{yx}^2}{\gamma_{xs}^2 \gamma_{ys}^2} \right)^{1/2} - 1 \right\} \quad (2.17)$$

Using Eqs 2.14 and 2.17, and the relation

$$\Gamma(f) = \frac{G_{xs}}{G_{ss}} \quad (2.18)$$

we arrive at

$$G_{kk} = |G_{xs}| \left\{ \frac{|G_{yx}|}{|G_{ys}|} - \frac{|G_{xs}|}{G_{ss}} \right\} \quad (2.19)$$

Similarly, by substituting Eq. 2.17 in Eq. 2.16, we arrive at the auto spectra of the other uncorrelated content terms

$$G_{mm} = G_{xx} \left\{ 1 - \left(\frac{\gamma_{yx}^2 \gamma_{xs}^2}{\gamma_{ys}^2} \right)^{1/2} \right\} \quad (2.20)$$

$$G_{nn} = G_{yy} \left\{ 1 - \left(\frac{\gamma_{yx}^2 \gamma_{ys}^2}{\gamma_{xs}^2} \right)^{1/2} \right\} \quad (2.21)$$

Rewriting these in terms of quantities which are computed directly in a state-of-the-art fast Fourier transform (FFT) modal analysis system

$$G_{mm} = G_{xx} - \frac{|G_{yx}| |G_{xs}|}{|G_{ys}|} \quad (2.22)$$

$$G_{nn} = G_{yy} - \frac{|G_{yx}| |G_{ys}|}{|G_{xs}|} \quad (2.23)$$

With these relations it is now possible to estimate the source(s) and magnitudes of uncorrelated content in a measurement system. This has not been possible with 2-channel measurement systems.

2.3 Some Variance Estimates

We may use the Δ notation to describe the variation of a variable about the mean value. For any random sample, \tilde{A} , of a variable whose expected value is A

$$\begin{aligned} \Delta A &= \tilde{A} - A \\ E[\Delta A] &= E[\tilde{A} - A] = 0 \\ E[(\Delta A)^2] &= E[(\tilde{A} - A)^2] = \text{Var}[\tilde{A}] = \sigma_{\tilde{A}}^2 \end{aligned} \quad (2.24)$$

An equivalent expression for the variance of \tilde{A} is also given by

$$\text{Var}[\tilde{A}] = E[\tilde{A}^2] - (E[\tilde{A}])^2 \quad (2.25)$$

Variance estimates of the quantities in Eq. 2.13 will now be developed. From Eqs. 2.3 and 2.9 it can be shown that

$$\tilde{C}_{xs} = \frac{2}{T} [(S_R^2 + S_I^2)\Gamma_R + S_R(K_R + M_R) + S_I(K_I M_I)] \quad (2.26)$$

Squaring Eq. 2.26, taking the expectation, and using Eqs. 2.4, 2.5, and 2.7, it can eventually be shown that

$$E[\tilde{C}_{xs}^2] = 2G_{ss}^2\Gamma_R^2 + \frac{1}{2}G_{ss}(G_{kk} + G_{mm}) \quad (2.27)$$

Using Eq. 2.25 it follows that

$$\text{Var}[\tilde{C}_{xs}] = G_{ss}^2\Gamma_R^2 + \frac{1}{2}G_{ss}(G_{kk} + G_{mm}) \quad (2.28)$$

Compare this to the variance given by [23, section 9.9.1]. This expression is repeated here for convenience.

$$\text{Var}[\tilde{C}_{xs}] = \frac{1}{2}[G_{ss}G_{xx} + C_{xs}^2 - Q_{xs}^2] \quad (2.29)$$

Using Eqs. 2.12 and 2.13 it can be seen that these descriptions of the variance of \tilde{C}_{xs} are equivalent.

In a similar manner the following variances can be developed

$$\begin{aligned}
Var[\tilde{Q}_{xs}] &= G_{ss}^2 \Gamma_I^2 + \frac{1}{2} G_{ss} (G_{kk} + G_{mm}) \\
Var[\tilde{C}_{ys}] &= G_{ss}^2 [Re(\Gamma H)]^2 + \frac{G_{kk} G_{ss}}{2} |H|^2 + \frac{G_{ss} G_{nn}}{2} \\
Var[\tilde{Q}_{ys}] &= G_{ss}^2 [Im(\Gamma H)]^2 + \frac{G_{kk} G_{ss}}{2} |H|^2 + \frac{G_{ss} G_{nn}}{2} \\
Var[\tilde{C}_{yx}] &= H_R^2 (G_{ss} \Gamma^2 + G_{kk})^2 + \frac{1}{2} \{ (H^2 G_{mm} + G_{nn}) (G_{ss} \Gamma^2 + G_{kk}) + G_{mm} G_{nn} \} \\
Var[\tilde{Q}_{yx}] &= H_I^2 (G_{ss} \Gamma^2 + G_{kk})^2 + \frac{1}{2} \{ (H^2 G_{mm} + G_{nn}) (G_{ss} \Gamma^2 + G_{kk}) + G_{mm} G_{nn} \}
\end{aligned} \tag{2.30}$$

These may also be shown to be equivalent to those developed in [23, section 9.1.1]:

$$\begin{aligned}
Var[\tilde{Q}_{xs}] &= \frac{1}{2} [G_{ss} G_{xx} + Q_{xs}^2 - C_{xs}^2] \\
Var[\tilde{C}_{ys}] &= \frac{1}{2} [G_{ss} G_{yy} + C_{ys}^2 - Q_{ys}^2] \\
Var[\tilde{Q}_{ys}] &= \frac{1}{2} [G_{ss} G_{yy} + Q_{ys}^2 - C_{ys}^2] \\
Var[\tilde{C}_{yx}] &= \frac{1}{2} [G_{xx} G_{yy} + C_{yx}^2 - Q_{yx}^2] \\
Var[\tilde{Q}_{yx}] &= \frac{1}{2} [G_{xx} G_{yy} + Q_{yx}^2 - C_{yx}^2]
\end{aligned} \tag{2.31}$$

The equations presented in [23], (Eqs. 2.29 and 2.31) are preferred for calculating numerical values of variance, since they are functions of variables that are directly measured in a fast Fourier transform (FFT) analysis. The value of equations developed in this section (Eqs. 2.28 and 2.30) is that they present insights regarding the contribution of various system elements to the overall variance.

For completeness (and because it will be needed later), the variance of a raw sample of an auto spectrum (say, of X) is given by [23, section 9.1.1] as

$$Var[\tilde{G}_{xx}] = G_{xx}^2 \tag{2.32}$$

2.4 The Effect of Averaging Raw Samples

A typical frequency response function (FRF) estimation is seldom based on a single sample. Estimates are improved and variance reduced by averaging (in the frequency domain) a number of raw samples. Whereas a raw sample of a quantity A is denoted by a 'tilde' (\tilde{A}), an estimate of this quantity based on an average of n_d raw sample records is denoted by a 'hat' (\hat{A}). For the quantities discussed in this chapter averaging does not affect the expectation of the quantity. That is, for an auto spectrum or for the real or imaginary part of a cross spectrum

$$E[\hat{A}] = E[\tilde{A}] = A \quad (2.33)$$

In the next chapter it will be shown that Eq 2.33 does not apply when discussing the *magnitude* of a complex variable, where the expectation of the magnitude will depend on the variance of the real and imaginary components.

The primary reason for averaging multiple samples is that the variance of an estimate is inversely proportional to the number of samples that are averaged. That is

$$Var[\hat{A}] = \frac{Var[\tilde{A}]}{n_d} \quad (2.34)$$

The standard deviation of the quantity \hat{A} , $\sigma_{\hat{A}}$, is given by

$$\sigma_{\hat{A}} = \sqrt{Var[\hat{A}]} = \frac{\sigma_{\tilde{A}}}{\sqrt{n_d}} \quad (2.35)$$

A convenient side benefit of the averaging process is that all averaged estimates of measured quantities *approach* Normality by virtue of the Central Limit Theorem. For example, the auto spectrum of a complex variable (that has been properly normalized) with zero-mean Gaussian real and imaginary parts has a Chi-square distribution with 2 degrees of freedom. But when n_s raw samples are averaged to form estimates of the auto spectrum, those estimates will approach a normal distribution with the variance given by Eqs. 2.32 and 2.34.

2.5 Covariance and Correlation

The covariance of two raw estimates, \tilde{A} and \tilde{B} is given by

$$\begin{aligned} \text{Cov}(\tilde{A}, \tilde{B}) &= E[(\Delta A)(\Delta B)] = E[(\tilde{A} - E[\tilde{A}])(\tilde{B} - E[\tilde{B}])] \\ &= E[\tilde{A}\tilde{B}] - E[\tilde{A}]E[\tilde{B}] \end{aligned} \quad (2.36)$$

This covariance is reduced by averaging, with the covariance of averaged estimates being found by using a relation analogous to Eq. 2.34.

The correlation coefficient of two averaged estimates \hat{A} and \hat{B} , $\rho_{\hat{A}\hat{B}}$, is given by

$$\rho_{\hat{A}\hat{B}} = \frac{\text{Cov}(\hat{A}, \hat{B})}{\sigma_{\hat{A}}\sigma_{\hat{B}}} \quad (2.37)$$

The magnitude of the correlation ranges in value from zero to one. Zero means that there is no correlation between the two variables while $\rho = +/ - 1$ indicates that they are perfectly correlated. The covariance between the real and imaginary parts of a cross

spectrum, say G_{xx} , will be needed later. This relation is developed in [23, section 9.1.2] and repeated here for convenience.

$$\text{Cov}(\tilde{C}_{xs}, \tilde{Q}_{xs}) = C_{xs}Q_{xs} \quad (2.38)$$

From Eqs. 2.29, 2.30, 2.37, and 2.38 we find the correlation coefficient between the real and imaginary parts of G_{xx}

$$\rho_{C_{xs}Q_{xs}} = \frac{2C_{xs}Q_{xs}}{\sqrt{(G_{ss}G_{xx})^2 - (C_{xs}^2 - Q_{xs}^2)^2}} \quad (2.39)$$

Note that this equation applies for both raw samples or averaged estimates. A similar equation may also be found for the correlation between the real and imaginary parts of the G_{yy} cross spectrum.

Another needed set of covariance and correlation terms are those between the G_{xx} and G_{yy} cross spectra. Because this formula is not available we follow the lead of [23] in similar derivations, using the difference operator (Δ) approach for covariance in Eq. 2.36. Applying the difference operator to the cross spectral magnitude, the result [23, section 9.1.2] is

$$\Delta |G_{yx}| \cong \frac{C_{yx}\Delta C_{yx} + Q_{yx}\Delta Q_{yx}}{|G_{yx}|} \quad (2.40)$$

From Eqs. 2.36 and 2.40

$$\begin{aligned} \text{Cov}(|\tilde{G}_{ys}|, |\tilde{G}_{xs}|) &= E[\Delta |G_{ys}| \Delta |G_{xs}|] \\ &\cong E\left[\frac{(C_{ys}(\Delta C_{ys}) + Q_{ys}(\Delta Q_{ys}))(C_{xs}(\Delta C_{xs}) + Q_{xs}(\Delta Q_{xs}))}{|G_{ys}| |G_{xs}|} \right] \end{aligned} \quad (2.41)$$

Quantities such as C_{xx} and $|G_{yy}|$ are considered constants in the expectation operation in Eq. 2.41 and may be factored out when possible. The expectation only applies to variable quantities such as ΔQ_{yy} . Expanding and rewriting Eq 2.41 yields

$$\text{Cov}(|\tilde{G}_{yy}|, |\tilde{G}_{xx}|) \cong \frac{1}{|G_{yy}| |G_{xx}|} [C_{yy}C_{xx}E[\Delta C_{yy}\Delta C_{xx}] + Q_{yy}Q_{xx}E[\Delta Q_{yy}\Delta Q_{xx}] + C_{yy}Q_{xx}E[\Delta C_{yy}\Delta Q_{xx}] + Q_{yy}C_{xx}E[\Delta Q_{yy}\Delta C_{xx}]] \quad (2.42)$$

The task at this point is to find the expectations in Eq. 2.42. This is a lengthy process, and only a few intermediate steps will be presented here. The full derivation is shown in the Appendix. Taking one of the expectation terms in Eq. 2.42

$$\begin{aligned} E[(\Delta C_{yy})(\Delta C_{xx})] &= E[(\tilde{C}_{yy} - C_{yy})(\tilde{C}_{xx} - C_{xx})] \\ &= E[\tilde{C}_{yy}\tilde{C}_{xx}] - E[\tilde{C}_{yy}C_{xx}] - E[C_{yy}\tilde{C}_{xx}] + C_{yy}C_{xx} \\ &= E[\tilde{C}_{yy}\tilde{C}_{xx}] - C_{yy}C_{xx} \end{aligned} \quad (2.43)$$

\tilde{C}_{xx} is given by Eq. 2.26. Suffice it to say that \tilde{C}_{yy} is even longer, with the expanded product of \tilde{C}_{xx} and \tilde{C}_{yy} taking up a considerable amount of space. Using Eqs. 2.4 - 2.8 and 2.13 it can be shown that

$$E[(\Delta C_{yy})(\Delta C_{xx})] = C_{yy}C_{xx} + \frac{1}{2}G_{ss}G_{kk}H_R \quad (2.44)$$

The expectations of the other three terms in Eq 2.42 can be found in a similar manner:

$$\begin{aligned} E[(\Delta C_{yy})(\Delta Q_{xx})] &= C_{yy}Q_{xx} - \frac{1}{2}G_{ss}G_{kk}H_I \\ E[(\Delta Q_{yy})(\Delta Q_{xx})] &= Q_{yy}Q_{xx} + \frac{1}{2}G_{ss}G_{kk}H_R \\ E[(\Delta Q_{yy})(\Delta C_{xx})] &= Q_{yy}C_{xx} + \frac{1}{2}G_{ss}G_{kk}H_I \end{aligned} \quad (2.45)$$

where the one minus sign in Eq. 2.45 is not a mistake. Finally, using the results of Eqs. 2.44 and 2.45 in Eq. 2.42 we can eventually arrive at

$$\text{Cov}[|\tilde{G}_{ys}|, |\tilde{G}_{xs}|] \cong |G_{xs}| \left\{ |G_{ys}| + \frac{\frac{1}{2}G_{ss}G_{kk}|H|^2}{|G_{ys}|} \right\} \quad (2.46)$$

Equation 2.46 can be put in a more computationally convenient form by substituting Eq. 2.19 for G_{kk} which results in

$$\text{Cov}[|\tilde{G}_{ys}|, |\tilde{G}_{xs}|] \cong \frac{1}{2} [|G_{xs}| |G_{ys}| + G_{ss} |G_{yx}|] \quad (2.47)$$

The covariance for an estimate based on n_d raw samples is found by dividing Eq. 2.47 by n_d (as in Eq. 2.34). Using Eq. 2.37 for the correlation coefficient

$$\rho_{|\hat{G}_{ys}|, |\hat{G}_{xs}|} \cong \frac{|G_{xs}| |G_{ys}| + G_{ss} |G_{yx}|}{2n_d(\sigma_{|\hat{G}_{ys}|} \sigma_{|\hat{G}_{xs}|})} \quad (2.48)$$

An important point to be made is that expressions for $\sigma_{|\hat{G}_{ys}|}$ and $\sigma_{|\hat{G}_{xs}|}$ have not yet been developed. As mentioned earlier, the *magnitude* of a complex number (as well as the *variance of that magnitude*) is a topic lengthy enough to deserve a separate chapter!

2.6 The Three-Channel FRF Estimator

Forming the ratio of the expectations of the cross spectra, \tilde{G}_{ys} and \tilde{G}_{xs} , and using the expectations developed in Eqs. 2.13

$$\begin{aligned}\frac{E[\tilde{G}_{ys}]}{E[\tilde{G}_{xs}]} &= \frac{E[\tilde{C}_{ys}] - jE[\tilde{Q}_{ys}]}{E[\tilde{C}_{xs}] - jE[\tilde{Q}_{xs}]} \\ &= \frac{G_{ss}\{Re(\Gamma H)\} - jG_{ss}\{Im(\Gamma H)\}}{G_{ss}\Gamma_R - jG_{ss}\Gamma_I}\end{aligned}\quad (2.49)$$

Canceling the G_{ss} terms, expanding the product $\Gamma(f)H(f)$ and multiplying numerator and denominator by the complex conjugate of $\Gamma(f)$, $\Gamma^*(f)$

$$\frac{E[\tilde{G}_{ys}]}{E[\tilde{G}_{xs}]} = \frac{\{[\Gamma_R H_R - \Gamma_I H_I] - j[\Gamma_R H_I + \Gamma_I H_R]\}[\Gamma_R + j\Gamma_I]}{\Gamma_R^2 + \Gamma_I^2}\quad (2.50)$$

Carrying out the multiplication shown and canceling terms we arrive at

$$\frac{E[\tilde{G}_{ys}]}{E[\tilde{G}_{xs}]} = \frac{G_{ys}}{G_{xs}} = H_R - jH_I = H(f)\quad (2.51)$$

When referring to a variable in complex form (i.e., rather than by say, a magnitude), the expectation of raw or averaged samples are the same, as discussed in section 2.4. Thus, an estimate of a system frequency response function (FRF) may be made with averaged samples by

$$\hat{H} = \frac{\hat{G}_{ys}}{\hat{G}_{xs}}\quad (2.52)$$

While Eq. 2.51 shows that the system FRF is found exactly by a ratio of *expectations*, the estimator \hat{H} is found by using a ratio of *estimates* of these expectations, which is not the same. That is

$$\frac{E[\hat{G}_{ys}]}{E[\hat{G}_{xs}]} \neq E\left[\frac{\hat{G}_{ys}}{\hat{G}_{xs}}\right] \quad (2.53)$$

While Eq. 2.53 indicates a source of bias in the estimate, in practice this bias is small (there will be further discussion on this in the chapter discussing results of simulations), and is reduced as n_d is increased.

Chapter 3 - Bias Errors in Complex Magnitude

Estimation

The magnitude of a complex number Z is a real number

$$|Z| = \sqrt{R^2 + I^2} \quad (3.1)$$

where R and I are the real and imaginary parts of the complex number, $Z = R - jI$. If the real and imaginary parts are random variables then an estimate of the magnitude is given by

$$|\hat{Z}| = \sqrt{\hat{R}^2 + \hat{I}^2} \quad (3.2)$$

where the $\hat{\cdot}$ indicates a random sample (or estimate) of the variable.

The nature of the bias error to be discussed in this chapter is this: given that $E[\hat{R}] = \mu_R$ and $E[\hat{I}] = \mu_I$

$$E[|\hat{Z}|] > |Z| = \sqrt{\mu_R^2 + \mu_I^2} \quad (3.3)$$

While this error is large enough to degrade the value of our magnitude estimate in only a few instances, it is always significant in the effect it has on the *variance* of the magnitude estimator. Before beginning a more detailed discussion, an example will show the nature of the error.

3.1 An Example of the Magnitude Bias Error

Consider an FRF measurement at a spectral line where $H_k(f) = 0$. The cross spectrum G_{yx} will have a 'true' value of zero, and G_{yy} will be identical with G_{nn} . Bendat [23, section 9.1.1] develops the expectation of the magnitude of a raw sample of the cross spectrum squared as

$$E[|\tilde{G}_{yx}|^2] = E[\tilde{C}_{yx}^2] + E[\tilde{Q}_{yx}^2] = G_{xx}G_{yy} + |G_{yx}|^2 \quad (3.4)$$

For our example, with $G_{yy} = G_{nn}$ and $|G_{yx}| = 0$ the expected value of a raw sample of the cross spectrum magnitude squared is simply $G_{xx}G_{nn}$. Bendat [23] then assumes that the expected value of the magnitude of \tilde{G}_{yx} is the same as the 'true' value (in this case zero) and uses Eq. 2.25 to find the variance of the magnitude estimate to be

$$\text{Var}[|\tilde{G}_{yx}|] = G_{xx}G_{nn} \quad (3.5)$$

This result is extended to averaged estimates based on n_d raw samples per Eq. 2.34

$$\text{Var}[|\hat{G}_{yx}|] = \frac{G_{xx}G_{nn}}{n_d} \quad (3.6)$$

Let us look more closely at the magnitude assumption used in this variance calculation. Remember that although the expected values of \tilde{C}_{yx} and \tilde{Q}_{yx} are zero, the probability that any individual sample of these quantities will be exactly zero is zero. Thus, we may expect that samples of \tilde{C}_{yx} and \tilde{Q}_{yx} will always have some finite values. Referring to Eq. 3.2 we see that because these values are squared that the magnitude estimate will always be real and positive.

From Eqs. 2.31 we see that the variances of \tilde{C}_{yx} and \tilde{Q}_{yx} are, in this case, equal and given by

$$\text{Var}[\tilde{C}_{yx}] = \text{Var}[\tilde{Q}_{yx}] = \frac{1}{2}G_{xx}G_{yy} = \frac{1}{2}G_{xx}G_{nn} = \sigma^2 \quad (3.7)$$

with the variances for n_d averaged samples

$$\text{Var}[\hat{C}_{yx}] = \text{Var}[\hat{Q}_{yx}] = \frac{G_{xx}G_{yy}}{2n_d} = \frac{G_{xx}G_{nn}}{2n_d} = \frac{\sigma^2}{n_d} \quad (3.8)$$

From Eq. 2.38 we find that the covariance in our example is zero meaning that \tilde{C}_{yx} and \tilde{Q}_{yx} are, in this instance, uncorrelated (this should not be taken as a general result).

The *Rayleigh* [24] or *Chi* distribution is the square root of a 2-degree-of-freedom Chi-Square distribution. That is, it is the distribution of the function $x = \frac{\sqrt{a_1^2 + a_2^2}}{\sigma_a}$ where a_1 and a_2 are uncorrelated, zero-mean Gaussian variables with equal variances, σ_a^2 , and x is used as a general variable.

The Rayleigh distribution will be the subject of further discussion later in this chapter. For the moment it is enough to know that

$$E[x] = \sigma_a \sqrt{\frac{\pi}{2}} \quad (3.9)$$

Before we can apply the Rayleigh distribution to our example we must justify the Gaussian (Normality) assumption. There is no reason to believe that the raw samples \tilde{C}_{yx} and \tilde{Q}_{yx} are Normally distributed, but the Central Limit Theorem can be used to justify Normality for the averaged estimates \hat{C}_{yx} and \hat{Q}_{yx} . Applying the Rayleigh distribution to the averaged estimates, with the square root of Eq. 3.8 substituted for σ , in Eq. 3.9

$$\begin{aligned} E[|\hat{G}_{yx}|] &= \sqrt{\frac{G_{xx}G_{nn}}{2n_d}} \sqrt{\frac{\pi}{2}} \\ [E[|\hat{G}_{yx}|]]^2 &= \frac{\pi G_{xx}G_{nn}}{4n_d} \end{aligned} \quad (3.10)$$

Before we can complete our example by calculating an improved estimate of the variance using Eq. 2.25 we need $E[|\hat{G}_{yx}|^2]$. Bendat [23,section 9.1.1] only develops $E[|\tilde{G}_{yx}|^2]$. We must develop this term.

The Chi-Square distribution may be thought of as a sum of squared zero-mean, unit-variance Gaussian variables. The number of degrees of freedom is the number of variables in the sum, and the expectation is the number of degrees of freedom. Applying this distribution to our real and imaginary *estimates* and taking the expectation

$$E \left[\left(\frac{\hat{C}_{yx} - C_{yx}}{\frac{\sigma_{\tilde{C}_{yx}}}{\sqrt{n_d}}} \right)^2 + \left(\frac{\hat{Q}_{yx} - Q_{yx}}{\frac{\sigma_{\tilde{Q}_{yx}}}{\sqrt{n_d}}} \right)^2 \right] = 2 \quad (3.11)$$

Recalling that C_{yx} and Q_{yx} are both zero, and that the σ terms in Eq. 3.11 are equal and given by Eq. 3.7 we arrive at

$$E[\hat{C}_{yx}^2 + \hat{Q}_{yx}^2] = E[|\hat{G}_{yx}|^2] = 2\left(\frac{\sigma^2}{n_d}\right) = \frac{G_{xx}G_{nn}}{n_d} \quad (3.12)$$

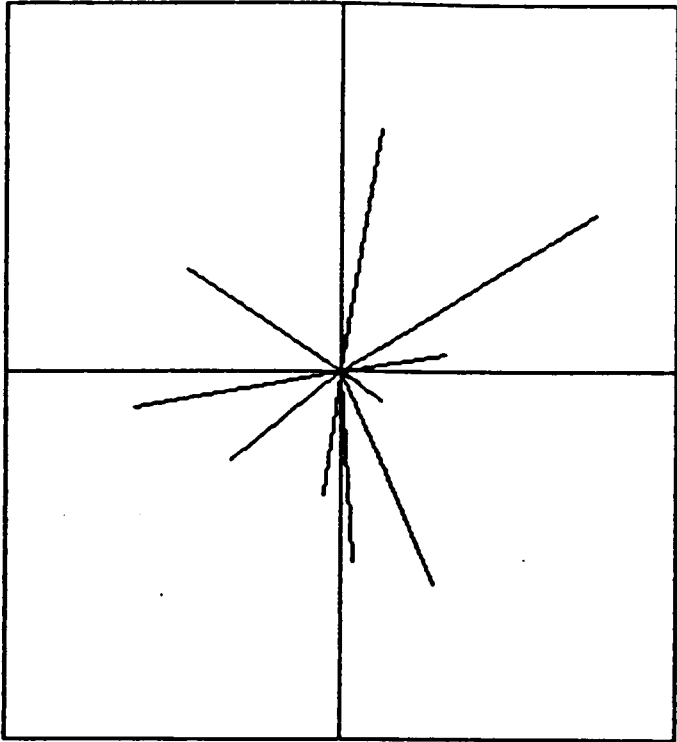
Before continuing with our 'improved' variance estimate, let us compute the variance of $|\hat{G}_{yx}|$ using the assumption (from [23]) of zero expected value for the magnitude of this particular cross spectrum. Equation 2.25 would then lead to the variance being given by the result of Eq. 3.12, which agrees with Eq. 3.6. To compute our 'improved' variance, we use Eqs. 3.10 and 3.12 in Eq. 2.25 to find

$$Var[|\hat{G}_{yx}|] = \frac{G_{xx}G_{nn}}{n_d}\left(1 - \frac{\pi}{4}\right) = 0.2146\frac{G_{xx}G_{nn}}{n_d} \quad (3.13)$$

Thus we find our revised estimate of the variance of the magnitude estimator in this case to be 21% of the estimate in [23]! Note also that, with a zero 'true' value of the cross spectrum magnitude, any finite expected value of the magnitude estimator represents an infinite error in the estimate.

No claim is made that errors of these magnitudes are always the case. Indeed, the example presented is probably a worst case. What is significant, however, is that the errors in magnitude and variance estimates shown here *are always present to some degree* in every estimate of a complex variable magnitude when the real and imaginary parts of that variable are random variables.

Before we leave our example, it would be informative to look at a graphic example of the Rayleigh distribution. Figure 2 shows 11 samples of \hat{Z} where the real and imaginary parts are zero-mean, independent Gaussian random variables with variance σ^2 . From these samples we find an estimate of the standard deviation, $\hat{\sigma}$, to be 3.05. From Eq. 3.9 we find $E[|\hat{Z}|] = 3.8$, which compares well (for a small sampling) to the average



	Real	Imag	Magnitude
	3.389	-6.041	6.926
	-0.627	-0.924	1.117
	0.370	-2.496	2.524
	-0.214	-0.442	0.491
	5.245	-0.966	5.333
	-0.772	4.876	4.937
	-1.913	2.613	3.238
	2.205	3.615	4.234
	-4.113	-0.328	4.128
	-4.645	-2.223	5.149
	-2.650	0.369	2.675
Average	-0.339	-0.177	3.705
Variance	9.294	9.321	3.679
Std Dev	3.049	3.053	1.918

Figure 2. Illustration of Rayleigh Distribution

value in Fig. 2 , 3.7. Thus, although both real and imaginary parts are *zero mean*, the expectation of the magnitude is even larger than the component standard deviation. Furthermore, the *standard deviation of the magnitude is much less than the component standard deviations*.

3.2 Magnitude and Variance for a Special Case

For the most general case of a magnitude estimate we must consider the real and imaginary parts of the complex variable to be at least partially correlated but with differing variances. This is in fact the case for the magnitude of any cross spectrum estimate (other than the special case of a zero 'true' magnitude shown in our example). The mathematics of dealing with the general case become intractable except by numerical solutions, however. The special case we are about to consider defies closed form solution for all but a limited range of values.

The special case we will consider in this section has the properties that the real and imaginary parts of the complex variable are 1.) uncorrelated and 2.) of equal variance. Though no way was found to prove it analytically, the simulations to be discussed in later chapters consistently showed that this special case applies to the estimators of the magnitude of the FRF, $|\hat{H}(f)|$ and $|\hat{H}(f)|$. It also applies to $|\hat{H}(f)|$ when the system $H(f)$ is *not* near an antiresonance region.

While the expected value of the *magnitude* of a complex random variable, $|\hat{Z}|$, is difficult to find, the expectation of $|\hat{Z}|^2$ is not. It can be gotten directly from the Chi-square distribution *for our special case*. If we rewrite Eq. 3.11 in terms of \hat{R} , \hat{I} , μ_R , μ_I , and the denominators are replaced by σ 's, then it follows that

$$E[(\hat{R} - \mu_R)^2 + (\hat{I} - \mu_I)^2] = 2\sigma^2 \quad (3.14)$$

It is important to remember that the Chi-square distribution applies only as long as the real and imaginary parts are *uncorrelated*. Expanding the left side

$$\begin{aligned} E[\hat{R}^2 - 2\hat{R}\mu_R + \mu_R^2 + \hat{I}^2 - 2\hat{I}\mu_I + \mu_I^2] \\ = E[\hat{R}^2 + \hat{I}^2] - 2\mu_R E[\hat{R}] - 2\mu_I E[\hat{I}] + \mu_R^2 + \mu_I^2 \quad (3.15) \\ = E[\hat{R}^2 + \hat{I}^2] - \mu_R^2 - \mu_I^2 \end{aligned}$$

from which we find

$$E[|\hat{Z}|^2] = E[\hat{R}^2 + \hat{I}^2] = \mu_R^2 + \mu_I^2 + 2\sigma^2 = |Z|^2 + 2\sigma^2 \quad (3.16)$$

If we were to *ignore the effect of the magnitude bias* for a moment and calculate the variance using Eq. 2.25 we would find that

$$\text{Var}[|\hat{Z}|] = (|Z|^2 + 2\sigma^2) - (|Z|)^2 = 2\sigma^2 \quad (3.17)$$

In a later section we will prove that this is a *high* estimate of the variance which *exceeds the true variance by a factor of at least 2*.

3.2.1 Application of the Rayleigh Distribution

As mentioned in the previous section, the Rayleigh (or Chi) distribution is the square root of a 2 degree-of-freedom Chi-square distribution, with the expectation given by Eq. 3.9. It would at first seem a simple matter to apply this distribution to our special case in order to obtain the expectation and variance of the magnitude of our complex number. Expanding the distribution in terms of our variables

$$E \left[\sqrt{\left(\frac{\hat{R} - \mu_R}{\sigma_{\hat{R}}} \right)^2 + \left(\frac{\hat{I} - \mu_I}{\sigma_{\hat{I}}} \right)^2} \right] = \sqrt{\frac{\pi}{2}} \quad (3.18)$$

where μ_R and μ_I are the expectations of \hat{R} and \hat{I} . Eq. 3.18 differs slightly from Eq. 3.9 in the form of the expectation because Eq. 3.18 has been written so that the σ_s of Eq. 3.9 is unity. Even given, for our special case, that $\sigma_{\hat{R}} = \sigma_{\hat{I}} = \sigma$, we still cannot directly solve for our desired result

$$E[|\hat{Z}|] = E[\sqrt{\hat{R}^2 + \hat{I}^2}] \quad (3.19)$$

except for the special case derived in the previous section where $\mu_R = \mu_I = 0$

3.2.2 Application of the Taylor Series.

The Taylor Series expansion for a function of two variables, written in terms of our notation for $|\hat{Z}|$ and expanded about $\hat{R} = \mu_R$, $\hat{I} = \mu_I$

$$\begin{aligned}
|\hat{Z}(\mu_R + \Delta R, \mu_I + \Delta I)| &= |\hat{Z}(\mu_R, \mu_I)| + \left(\frac{\partial |\hat{Z}|}{\partial \hat{R}} \Delta R + \frac{\partial |\hat{Z}|}{\partial \hat{I}} \Delta I \right) + \\
&\frac{1}{2} \left(\frac{\partial^2 |\hat{Z}|}{\partial \hat{R}^2} (\Delta R)^2 + 2 \frac{\partial^2 |\hat{Z}|}{\partial \hat{R} \partial \hat{I}} \Delta R \Delta I + \frac{\partial^2 |\hat{Z}|}{\partial \hat{I}^2} (\Delta I)^2 \right) + \dots
\end{aligned} \tag{3.20}$$

where ΔR and ΔI are by definition uncorrelated zero-mean Gaussian variables representing fluctuations of the estimates about their expected values and the derivative terms are evaluated at $\hat{R} = \mu_R$ and $\hat{I} = \mu_I$. If we take the expectation of the expanded expression for $|\hat{Z}|$ in Eq. 3.20 we find that all except the Δ terms are taken as constants in the expectation operation. Thus, similar to Eqs. 2.4 to 2.7 and 2.24 we find certain expectations

$$\begin{aligned}
E[\Delta R] &= E[\Delta I] = 0 \\
E[(\Delta R)^2] &= E[(\Delta I)^2] = \sigma^2 \\
E[(\Delta R)^3] &= E[(\Delta R)(\Delta I)] = E[(\Delta R)(\Delta I)^2] = 0 \\
E[(\Delta R)^2(\Delta I)^2] &= \sigma^4 \quad E[(\Delta R)^4] = E[(\Delta I)^4] = 3\sigma^4
\end{aligned} \tag{3.21}$$

Using Eq. 3.2 for $|\hat{Z}|$ and taking derivatives

$$\begin{aligned}
\frac{\partial |\hat{Z}|}{\partial \hat{R}} &= \frac{\hat{R}}{\sqrt{\hat{R}^2 + \hat{I}^2}} \\
\frac{\partial |\hat{Z}|}{\partial \hat{I}} &= \frac{\hat{I}}{\sqrt{\hat{R}^2 + \hat{I}^2}} \\
\frac{\partial^2 |\hat{Z}|}{\partial \hat{R}^2} &= \frac{\hat{I}^2}{(\hat{R}^2 + \hat{I}^2)^{\frac{3}{2}}} \\
\frac{\partial^2 |\hat{Z}|}{\partial \hat{I}^2} &= \frac{\hat{R}^2}{(\hat{R}^2 + \hat{I}^2)^{\frac{3}{2}}} \\
\frac{\partial^2 |\hat{Z}|}{\partial \hat{R} \partial \hat{I}} &= \frac{-\hat{R}\hat{I}}{(\hat{R}^2 + \hat{I}^2)^{\frac{3}{2}}}
\end{aligned} \tag{3.22}$$

Expanding $|\hat{Z}|$ in a *five* term series (only the first three terms are shown in Eq. 3.20 for brevity), using Eqs. 3.21 and 3.22 along with some higher derivative terms, and evaluating the variables \hat{R} and \hat{I} at μ_R and μ_I , we arrive at

$$E[|\hat{Z}|] = \sqrt{\mu_R^2 + \mu_I^2} + \frac{1}{2} \frac{\sigma^2}{\sqrt{\mu_R^2 + \mu_I^2}} + \frac{1}{8} \frac{\sigma^4}{(\mu_R^2 + \mu_I^2)^{\frac{3}{2}}} + \dots \tag{3.23}$$

Although there were five terms in the series expansion, two of these terms contained only functions of ΔR and ΔI resulting in odd powers (i.e., $(\Delta R)(\Delta I)$) and were, therefore, zero after the expectation operation. These remaining three terms may be rewritten

$$\begin{aligned}
E[|\hat{Z}|] &= |Z| + \frac{1}{2} \frac{\sigma^2}{|Z|} + \frac{1}{8} \frac{\sigma^4}{|Z|^3} + \dots \\
&= |Z| \left[1 + \frac{1}{2} \left(\frac{\sigma}{|Z|} \right)^2 + \frac{1}{8} \left(\frac{\sigma}{|Z|} \right)^4 + \dots \right]
\end{aligned} \tag{3.24}$$

It would seem at first that the problem of finding the expectation of the magnitude has been solved, but this is not so. If we let $|Z| \rightarrow 0$ in Eq. 3.24 we see that $E[|\hat{Z}|] \rightarrow \infty$, while Eq. 3.9 yields a finite value. Equation 3.24 turns out to be valid only over the range of $0 < \frac{\sigma}{|Z|} < 0.5$ above which the series starts diverging rapidly. Although this appears to be a limited range, it actually applies to all cases where the standard deviation is much smaller than the value being measured (a desirable condition for any measurement!). Equation 3.24 also provides valuable qualitative insights. First, we have proved the assertion made in Eq. 3.3 that $E[|\hat{Z}|] > |Z|$ for even small values of σ . Second, this bias error can be described as a function of solely the ratio $\frac{\sigma}{|Z|}$.

Finally, we will use Eqs. 3.16 and 3.24 in the variance equation (2.25) to find

$$\begin{aligned}
 \text{Var}[|\hat{Z}|] &= (|Z|^2 + 2\sigma^2) - |Z|^2 \left[1 + \frac{1}{2} \left(\frac{\sigma}{|Z|} \right)^2 + \frac{1}{8} \left(\frac{\sigma}{|Z|} \right)^4 + \dots \right]^2 \\
 &= |Z|^2 + 2\sigma^2 - |Z|^2 \left[1 + \left(\frac{\sigma}{|Z|} \right)^2 + \frac{1}{2} \left(\frac{\sigma}{|Z|} \right)^4 + \right. \\
 &\quad \left. \frac{1}{8} \left(\frac{\sigma}{|Z|} \right)^6 + \frac{1}{64} \left(\frac{\sigma}{|Z|} \right)^8 + \dots \right] \quad (3.25) \\
 &= \sigma^2 \left[1 - \frac{1}{2} \left(\frac{\sigma}{|Z|} \right)^2 - \frac{1}{8} \left(\frac{\sigma}{|Z|} \right)^4 - \frac{1}{64} \left(\frac{\sigma}{|Z|} \right)^6 - \dots \right]
 \end{aligned}$$

Remembering that this expression is *only valid in the range of $\frac{\sigma}{|Z|}$ from zero to about 0.5*, we may still infer some useful information. Most importantly, note that the *maximum* variance is σ^2 , or *half of that predicted if there were no bias in the magnitude estimate* (see Eq. 3.17). Another interesting observation is that the variance of the magnitude *decreases* as the ratio $\frac{\sigma}{|Z|}$ *increases*.

3.2.3 Magnitude and Variance by Probability Density Functions

Let us review the development so far for our 'special case' of a complex number with uncorrelated but equal-variance real and imaginary Gaussian components. If we parameterize the variance of the magnitude in terms of $\frac{\sigma}{|Z|}$, we have found expressions for the variance in the range of zero to approximately 0.5 (via the Taylor Series), and at $\frac{\sigma}{|Z|} \rightarrow \infty$ (using the Rayleigh distribution with $|Z| = 0$). The range in between is, at present, lost to us via closed-form solution.

3.2.3.1 Probability Density Functions

If a single random variable x assumes a continuous range of values, any one of which is denoted by $x(k)$, then a probability density function may be defined by

$$p(x) = \lim_{\Delta x \rightarrow 0} \left[\frac{\text{Probability}[x < x(k) \leq x + \Delta x]}{\Delta x} \right] \quad (3.26)$$

Some important relations for a probability density function (PDF) are

$$\begin{aligned} \int_{-\infty}^{\infty} p(x) dx &= 1 \\ E[x] &= \mu_x = \int_{-\infty}^{\infty} xp(x) dx \\ E[x^2] &= \psi_x^2 = \int_{-\infty}^{\infty} x^2 p(x) dx \\ \text{Var}[x] &= \psi_x^2 - (\mu_x)^2 \end{aligned} \quad (3.27)$$

where ψ_x^2 indicates the mean square of x . Expectations for a *single valued* function of x , $g(x)$ may be found by

$$\begin{aligned} E[g(x)] &= \int_{-\infty}^{\infty} g(x)p(x)dx \\ E[(g(x))^2] &= \int_{-\infty}^{\infty} (g(x))^2 p(x)dx \end{aligned} \quad (3.28)$$

A second-order probability density function may also be defined for the probability distribution for two variables, and may be written $p(x, y)$. For a function of two variables then

$$\begin{aligned} E[g(x, y)] &= \int_{-\infty}^{\infty} \int_{-\infty}^{\infty} g(x, y)p(x, y)dx dy \\ E[(g(x, y))^2] &= \int_{-\infty}^{\infty} \int_{-\infty}^{\infty} (g(x, y))^2 p(x, y)dx dy \end{aligned} \quad (3.29)$$

3.2.3.2 PDF's Applied to the Complex Magnitude

The joint probability density function for a general case of two Gaussian (Normal) variables is given by

$$p(x, y) = \frac{1}{2\pi\sigma_x\sigma_y\sqrt{(1-\rho_{xy}^2)}} \exp^{-\frac{1}{2(1-\rho_{xy}^2)} \left\{ \frac{(x-\mu_x)^2}{\sigma_x^2} + \frac{(y-\mu_y)^2}{\sigma_y^2} - \frac{2\rho_{xy}(x-\mu_x)(y-\mu_y)}{\sigma_x\sigma_y} \right\}} \quad (3.30)$$

We may use Eqs. 3.29 and 3.30 to write expressions for $E[|\hat{Z}|]$ and $E[|\hat{Z}|^2]$ where the variables \hat{R} and \hat{I} are used in place of x and y , and $g(\hat{R}, \hat{I}) = |\hat{Z}| = \sqrt{\hat{R}^2 + \hat{I}^2}$. For

our special case, $\rho_{R,I} = 0$, and because the special case real and imaginary part standard deviations are equal, we use $\sigma_x = \sigma_y = \sigma_{R,I}$. Unfortunately, these expressions defy integration for even our simplified special case.

3.2.3.3 PDF by Transformation of Variables

Our function of uncorrelated real and imaginary components may be transformed to a polar form in terms of a magnitude and angle by

$$|\hat{Z}| = \sqrt{\hat{R}^2 + \hat{I}^2} \quad \hat{\theta} = \tan^{-1}\left(\frac{\hat{I}}{\hat{R}}\right) \quad (3.31)$$

where the reverse transformation is given by

$$\hat{R} = |\hat{Z}| \cos(\hat{\theta}) \quad \hat{I} = |\hat{Z}| \sin(\hat{\theta}) \quad (3.32)$$

Transformation of the PDF is made by [25]

$$p(|\hat{Z}|, \hat{\theta}) = p(\hat{R}, \hat{I}) |J| \quad (3.33)$$

where $|J|$ is the determinant of the Jacobian Transformation matrix. The transformation matrix for our complex magnitude is defined by

$$\frac{1}{J} = \begin{vmatrix} \frac{\partial |\hat{Z}|}{\partial \hat{R}} & \frac{\partial |\hat{Z}|}{\partial \hat{I}} \\ \frac{\partial \hat{\theta}}{\partial \hat{R}} & \frac{\partial \hat{\theta}}{\partial \hat{I}} \end{vmatrix} \quad (3.34)$$

Combining Eqs. 3.30 - 3.34 we arrive at the transformed probability density function (for equal variance, uncorrelated real and imaginary parts)

$$p(|\hat{Z}|, \hat{\theta}) = \frac{|\hat{Z}|}{2\pi\sigma^2} \exp^{-\frac{1}{2\sigma^2}((|\hat{Z}| \cos \hat{\theta} - \mu_R)^2 + (|\hat{Z}| \sin \hat{\theta} - \mu_I)^2)} \quad (3.35)$$

The PDF of $|\hat{Z}|$ is given by

$$p(|\hat{Z}|) = \int_0^{2\pi} p(|\hat{Z}|, \hat{\theta}) d\hat{\theta} \quad (3.36)$$

which is unfortunately no easier to integrate than the previous result. But before we leave this approach, let us apply Eqs. 3.35 and 3.36 to the example at the beginning of this chapter, where $\mu_R = \mu_I = |Z| = 0$. With that substitution Eq. 3.35 is greatly simplified and we arrive at

$$p(|\hat{Z}|) = \frac{|\hat{Z}|}{\sigma^2} \exp^{-\frac{|\hat{Z}|^2}{2\sigma^2}} \quad (3.37)$$

Equation 3.37 turns out to be the Rayleigh probability density function [24] in terms of the variable $|\hat{Z}|$. This proves the assertion in Section 3.1 that $|\hat{Z}|$ has a Rayleigh distribution when $|Z| = 0$.

3.2.4 Magnitude Bias and Variance by Numerical Integration

As a result of the above investigations, only one method has been found that is capable of determining the magnitude bias and variance at all values of $\frac{\sigma}{|Z|}$: numerical inte-

gration. While it may be considered a 'brute force' method in that any one result is valid only for one value of $\frac{\sigma}{|Z|}$, it has the advantage that it will work as well for the general case (i.e., correlated real and imaginary parts of differing variance) as for our 'special case' (uncorrelated and equal variance).

For our special case, the probability density function of Eq. 3.30 is greatly simplified by virtue of the fact that the correlation coefficient ρ_{xy} is zero. Under this condition, it can be shown that

$$p(x, y) = p(x)p(y) \quad (3.38)$$

where $p(x)$ and $p(y)$ are single variable Gaussian probability density functions. For equal variances Eq. 3.38 can be written in terms of \hat{R} and \hat{I} as

$$p(\hat{R}, \hat{I}) = \frac{1}{2\pi\sigma^2} \exp -\frac{1}{2\sigma^2}((\hat{R} - \mu_R)^2 + (\hat{I} - \mu_I)^2) \quad (3.39)$$

Then the first of Eqs. 3.29 can be written as

$$E[|\hat{Z}|] = \mu_{|\hat{Z}|} = E[\sqrt{\hat{R}^2 + \hat{I}^2}] = \int_{-\infty}^{\infty} \int_{-\infty}^{\infty} \sqrt{\hat{R}^2 + \hat{I}^2} p(\hat{R}, \hat{I}) d\hat{R} d\hat{I} \quad (3.40)$$

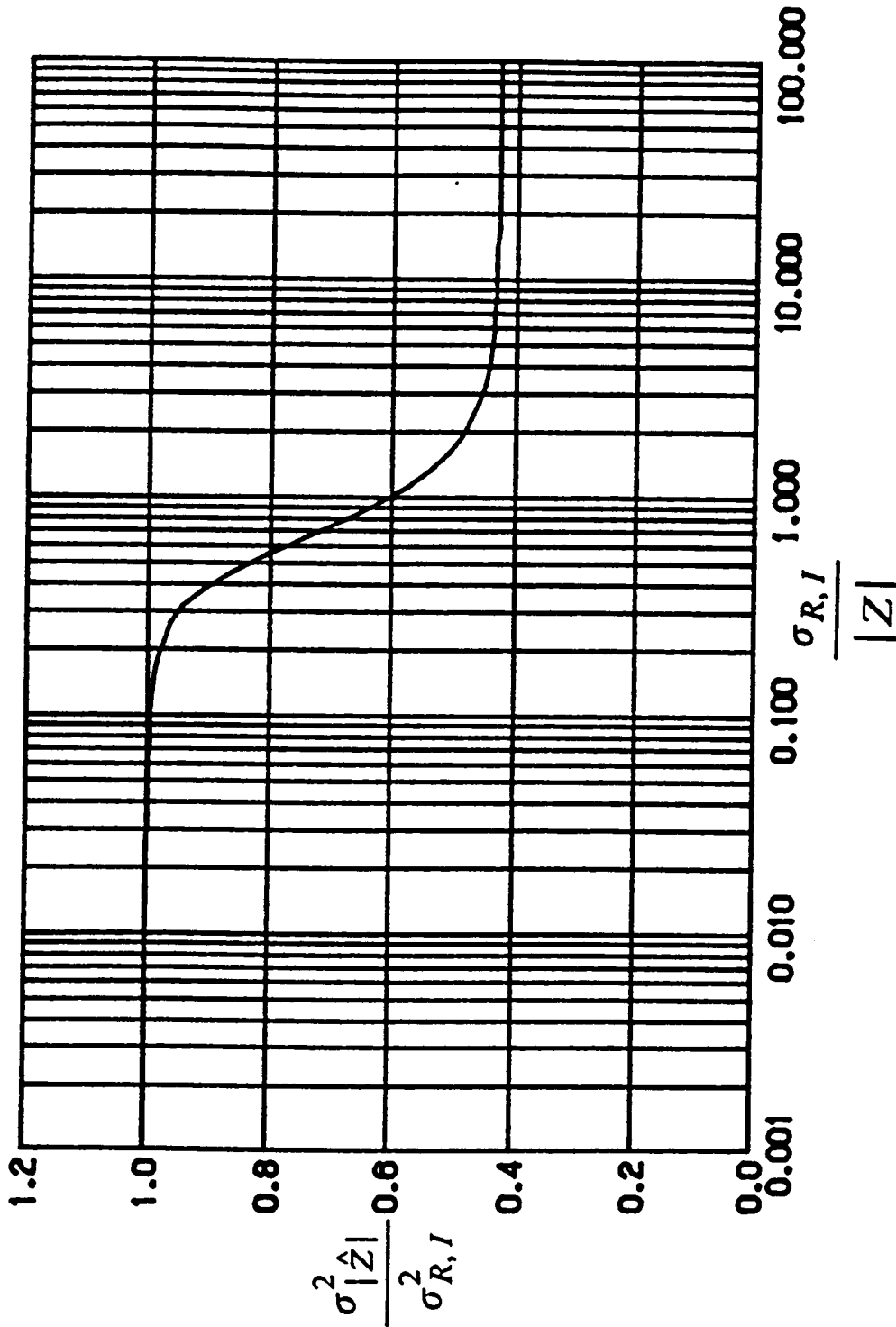
The integration limits at plus and minus infinity in two directions can more pragmatically be replaced by a square region about 10σ square and centered on (μ_R, μ_I) . A 60 x 60 integration grid was used to generate the figures in this section, although acceptable results were obtained with 30 x 30 and coarser grids. The second of Eqs. 3.29 (for $E[|\hat{Z}|^2]$) need not be evaluated numerically (though the result is the same), since Eq. 3.16 provides a simpler calculation. The variance then follows from Eq. 2.25.

Numerous numerical integrations over a range of values confirmed what was discovered in the Taylor Series development: that the standard deviation of the components (σ) and the 'true' magnitude ($|Z|$, as shown in Eq. 3.3) were the only parameters needed to describe the magnitude and variance of $|\hat{Z}|$. That is, the results for a given value of $|Z|$ apply to any combination of μ_R and μ_I producing that value.

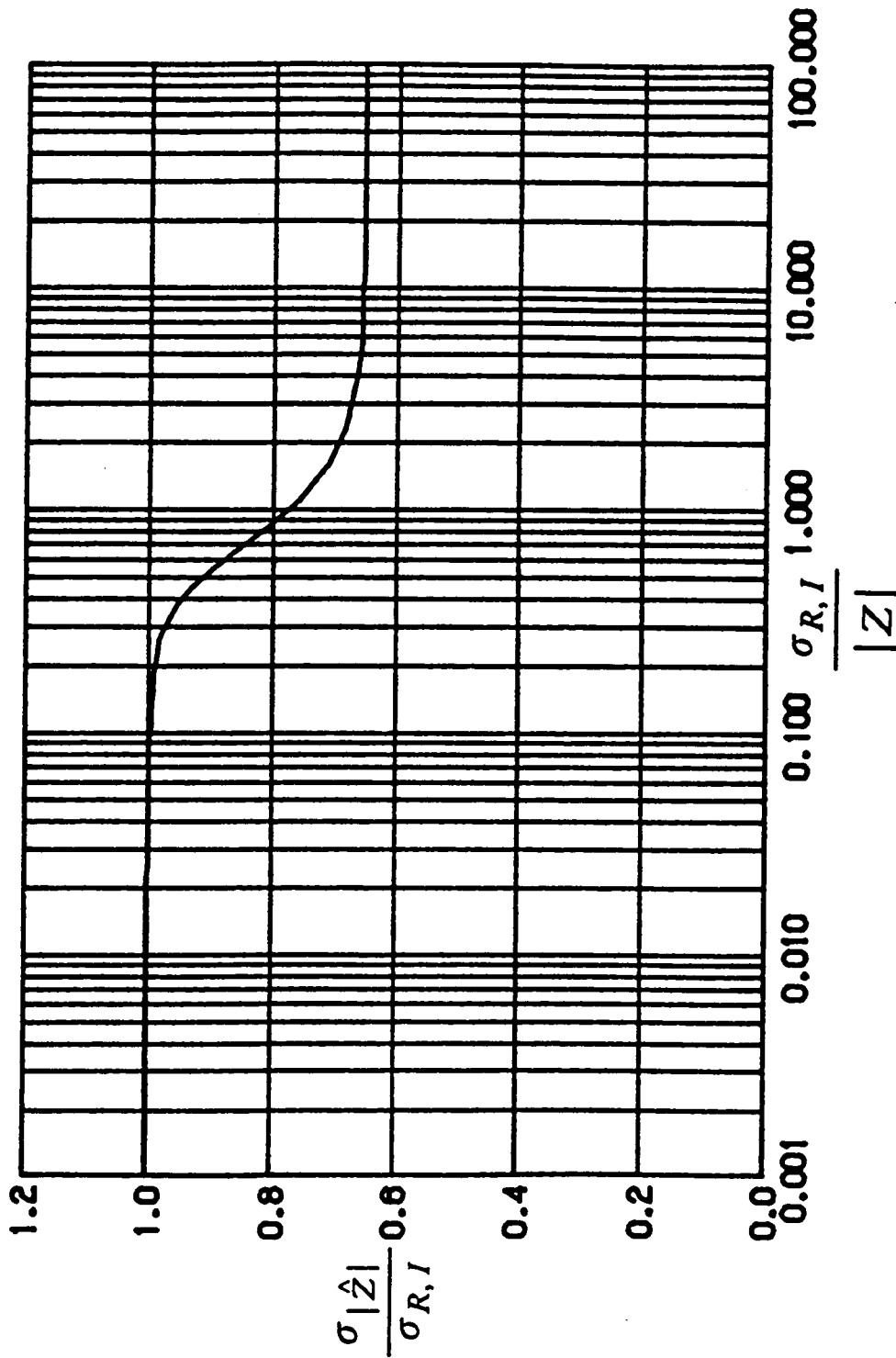
Figure 3 shows normalized variance, where the ratio of $\frac{\sigma^2_{|\hat{Z}|}}{\sigma^2}$ is plotted as a function of $\frac{\sigma}{|Z|}$. As shown in the figure, values of $\frac{\sigma}{|Z|} < 0.10$ result in values of the variance of $|\hat{Z}|$ being within one percent of the variance of the real and imaginary components. *Increasing σ (or decreasing $|Z|$) actually decreases the variance ratio towards a lower bound asymptote.* This limiting value of the variance ratio, 0.4292, (occurring for $|Z| = 0$) can also be verified by the Raleigh distribution. Figure 4 presents the same information as Fig. 3, except the ordinate is the ratio of standard deviations rather than the ratio of variances.

Figure 5 presents a more useful form, plotting a normalized standard deviation ratio as a function of $\frac{\sigma}{\mu_{|\hat{Z}|}}$. In a real-life measurement situation, the 'true' magnitude $|Z|$ would likely be unknown, and only $|\hat{Z}|$ would be available. Taking $|\hat{Z}|$ as an estimate of $\mu_{|\hat{Z}|}$ would then provide a means for obtaining an estimate of the variance of $|\hat{Z}|$ (providing of course that one had at least an estimate of σ). The limiting value of the abscissa, 0.798, is found from Eq. 3.9 ($\sqrt{\frac{2}{\pi}}$) for the Rayleigh distribution, which is the limiting case.

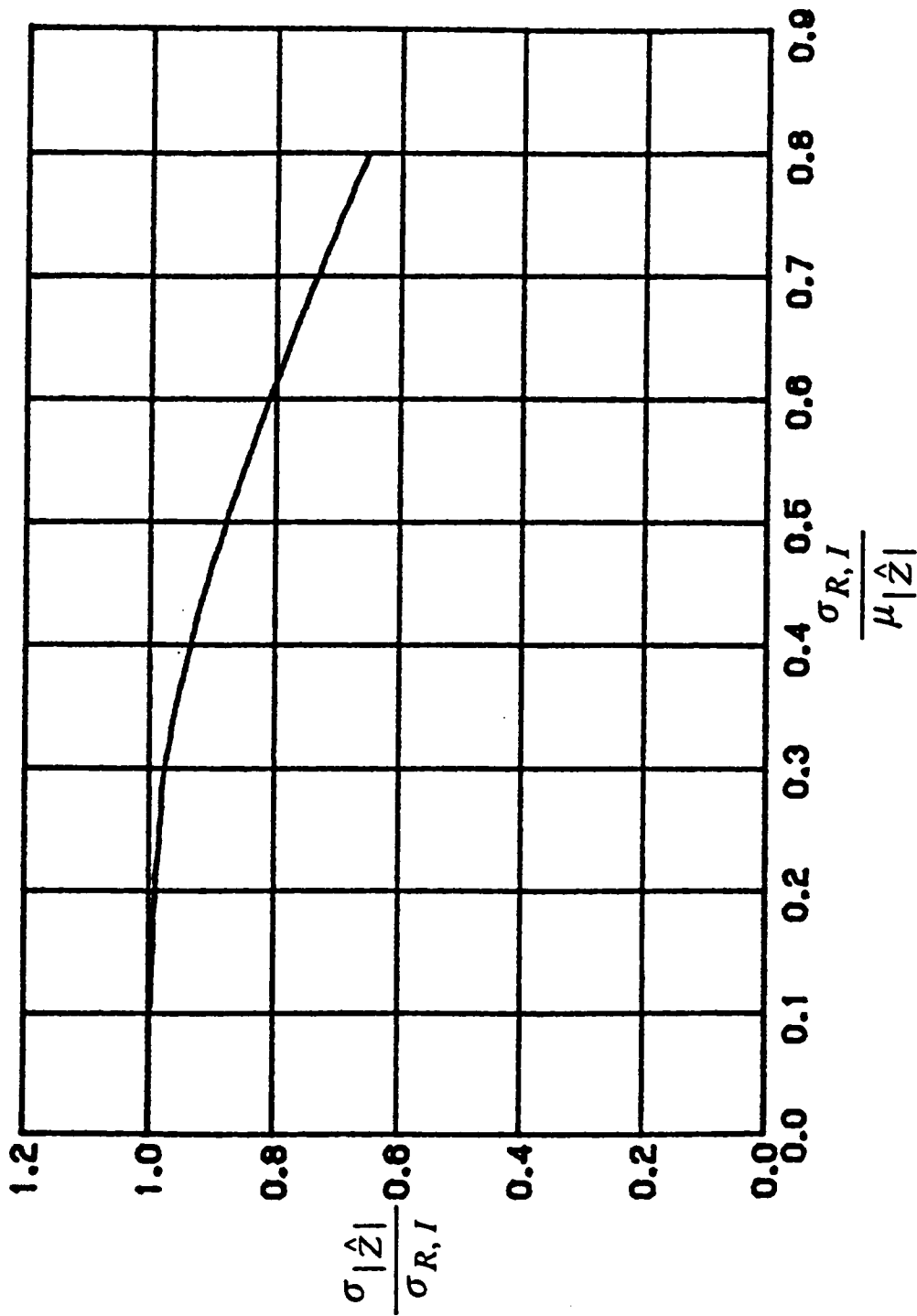
Figure 6 is useful for correcting magnitude bias errors (providing once again that an estimate of σ is available). Here we have the ratio $\frac{|Z|}{\mu_{|\hat{Z}|}}$ plotted as a function of the ratio $\frac{\sigma}{\mu_{|\hat{Z}|}}$. Note the the limiting value of $\frac{\sigma}{\mu_{|\hat{Z}|}}$ is about 0.798, which occurs for $|Z| = 0$.



Ratio of Magnitude Variance to Component Variance
(Based on Component Standard Deviation and True Magnitude)
Figure 3. Magnitude Variance Referenced to True Magnitude



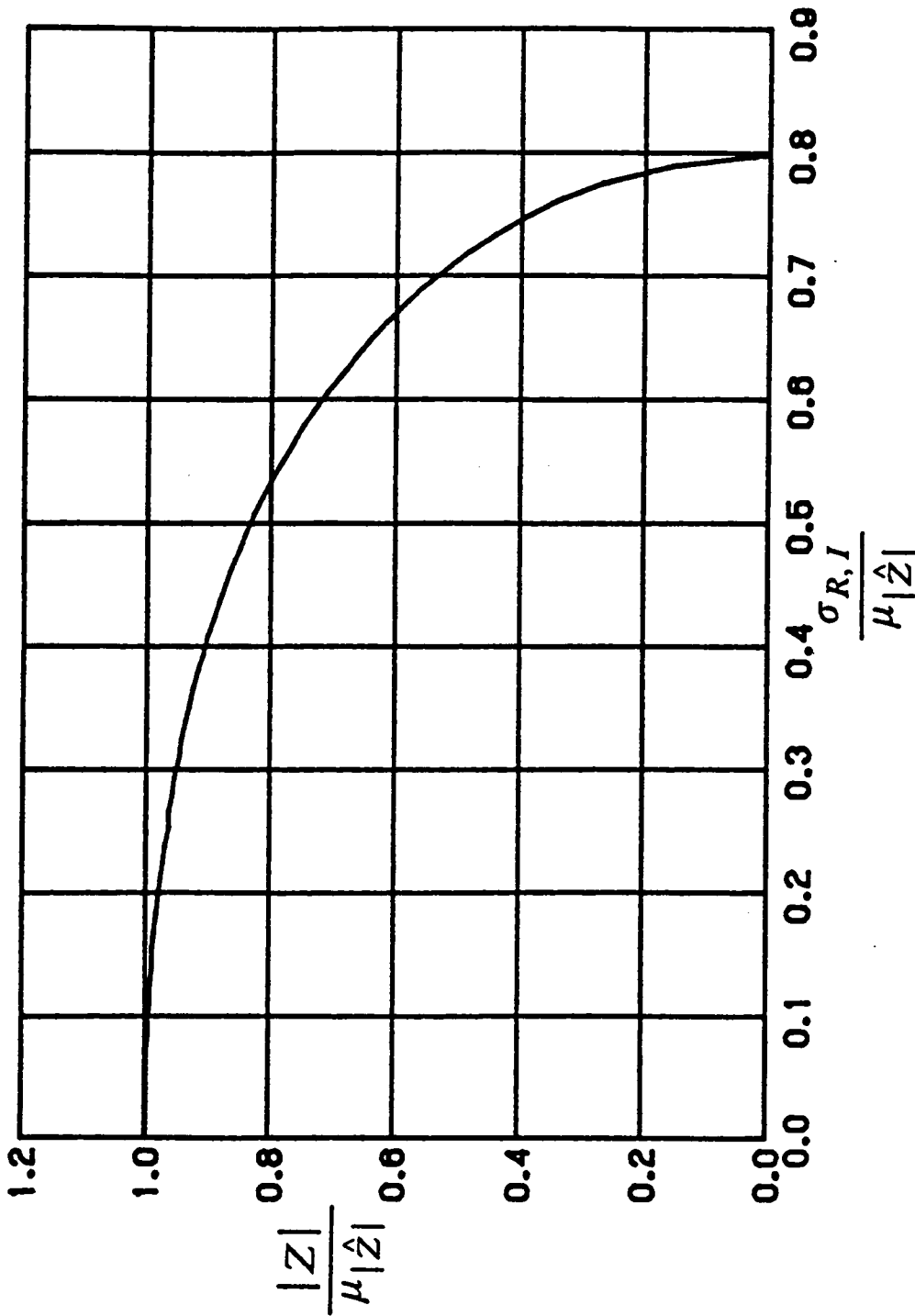
**Ratio of Magnitude Standard Deviation to Component Standard Deviation
 (Based on Component Standard Deviation and True Magnitude)
 Figure 4. Magnitude Standard Deviation Referenced to True Magnitude**



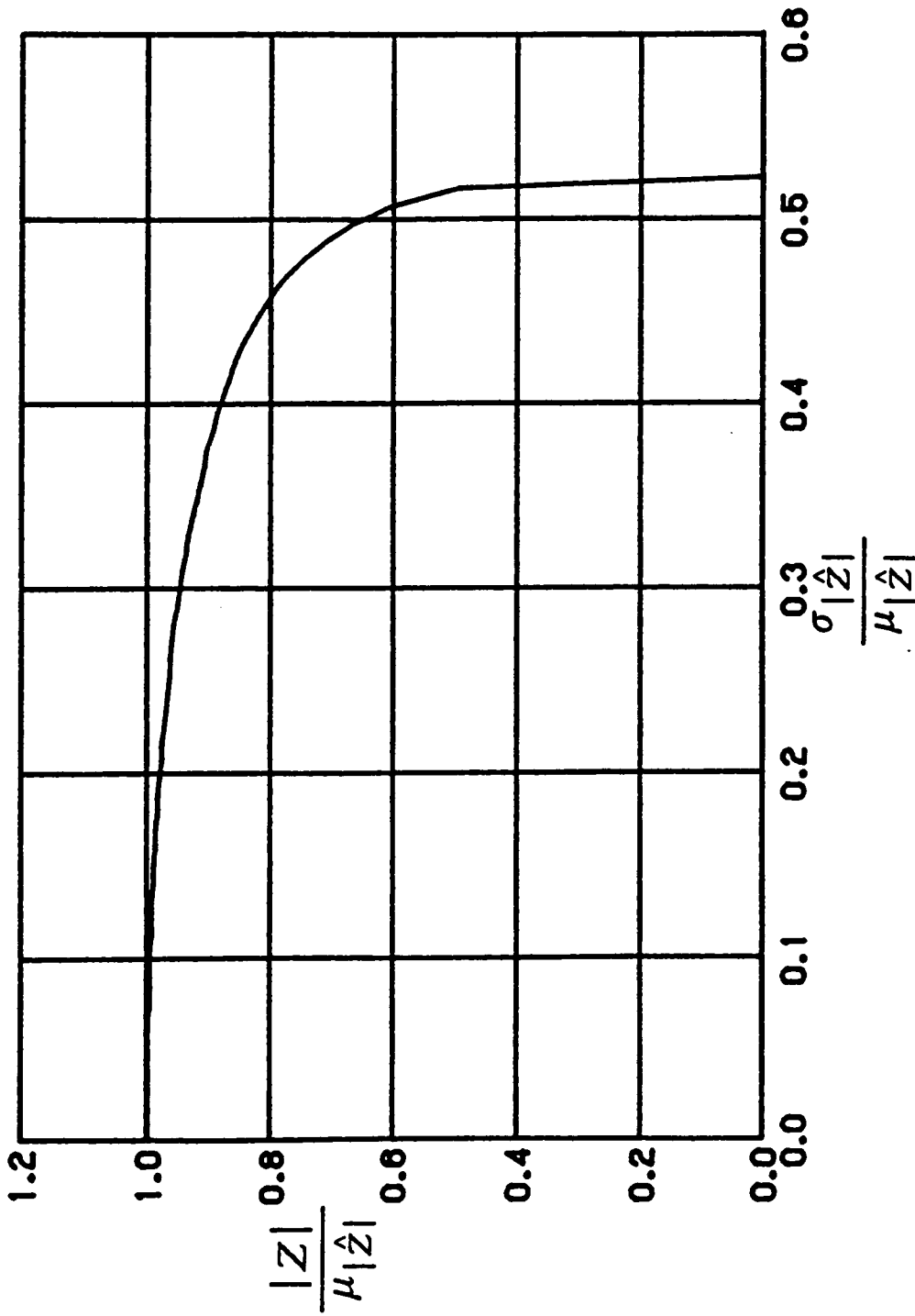
**Ratio of Magnitude Standard Deviation to Component Standard Deviation
(Based on Component Standard Deviation and Magnitude Expectation)**
 Figure 5. Magnitude Standard Deviation Referenced to Magnitude Expectation

When estimates are used in place of σ and $\mu_{|\hat{Z}|}$ it is quite possible that this limiting value may be exceeded. This only indicates that $|Z|$ has a value very close to zero.

In the next chapter, a method is developed for finding the variance of the magnitude of the FRF estimator directly (i.e., $\sigma_{|\hat{Z}|}^2$ is found without knowledge of σ^2). In a later chapter on the results of the simulations, it was found that the FRF estimator $|\hat{H}|$ has the same properties that $|\hat{Z}|$ has in our special case example (real and imaginary parts which are uncorrelated and of equal variance). In order to correct our estimate of the magnitude for bias error, it would be useful to have a magnitude bias correction factor which is a function of estimated quantities. Figure 7 presents the data of the previous figures in this form. The ratio $\frac{|Z|}{\mu_{|\hat{Z}|}}$ is plotted as a function of $\frac{\sigma_{|\hat{Z}|}}{\mu_{|\hat{Z}|}}$, where $|\hat{Z}|$ may be used as an estimate of $\mu_{|\hat{Z}|}$. For convenience we denote the ratio $\frac{|Z|}{\mu_{|\hat{Z}|}}$ (ordinate of Fig. 7) as c . Then our magnitude estimate may be corrected for magnitude bias by $|\hat{Z}|_{cor} = |\hat{Z}|c$. The variance of the corrected estimate is found by $\sigma_{|\hat{Z}|_{cor}}^2 = c^2\sigma_{|\hat{Z}|}^2$. From this figure we can note several things. One is that the magnitude bias error is very small when $\frac{\sigma_{|\hat{Z}|}}{\mu_{|\hat{Z}|}} < 0.1$. Another is that the curve becomes nearly vertical around $\frac{\sigma_{|\hat{Z}|}}{\mu_{|\hat{Z}|}} = 0.5$. Recalling that in an actual measurement situation only *estimates* of $\sigma_{|\hat{Z}|}$ and $\mu_{|\hat{Z}|}$ are available to us, we can see that a meaningful bias correction in this region is doubtful. But consider the significance of such measurements. The standard deviation of the measurement is near half of the measured value. For a Normal (Gaussian) distribution, approximately 95 percent of values fall with a plus/minus two standard deviation range. In the simulations discussed in Chapter 6 it was found for values of $\frac{\sigma_{|\hat{Z}|}}{\mu_{|\hat{Z}|}} \cong 0.5$ that the distribution of $|\hat{Z}|$ is only approximately Normal, with the actual distribution skewed towards lower values. Even with a Normal distribution, the near vertical region of Fig. 7 represents data that has zero within the 95 percent confidence range. The true distribution would indicate a higher probability of a zero true magnitude



Ratio of True Magnitude to the Magnitude Expectation
 (Based on Component Standard Deviation and Magnitude Expectation)
Figure 6. Magnitude Correction Referenced to Component Standard Deviation



**Ratio of True Magnitude to the Magnitude Expectation
 (Based on the Magnitude Standard Deviation and Magnitude Expectation)**
Figure 7. Magnitude Correction Based on Magnitude Estimates

value than the Normal distribution. We conclude the discussion of Fig. 7 by observing that estimates of $\sigma_{|\hat{z}|}$ and $\mu_{|\hat{z}|}$ resulting in ratios of $\frac{\sigma_{|\hat{z}|}}{\mu_{|\hat{z}|}}$ in the vicinity of 0.5 have a very high probability that the 'true' value of the magnitude ($|Z|$) is very close to zero.

3.3 Magnitude and Variance for the General Case

For the 'general case' of a complex number with correlated real and imaginary parts with differing variances, the only recourse is numerical integration for each set of values of $\sigma_R^{\wedge}, \sigma_I^{\wedge}, \mu_R, \mu_I$, and ρ_{RI}^{\wedge} . No simplification for the expected value of the magnitude squared via the Chi-square distribution is possible if there is a non-zero correlation or differing variances. Equation 3.30, rewritten in terms of R and I instead of x and y , must be substituted in both of Eqs. 3.29 and numerically integrated.

This task is made even more difficult because there is no longer an easily defined integration region as there was with our 'special case'. The size and shape of the region depend on $\sigma_R^{\wedge}, \sigma_I^{\wedge}$, and ρ_{RI}^{\wedge} . The correlation coefficient is particularly troublesome. One problem is that $\rho = 1$ causes a zero in the denominator of Eq. 3.30. Another is that while our 'special case' integration region was square and parallel with the real and imaginary axes, any non-zero values of the correlation coefficient result in an integration region that is neither square nor parallel to the complex axes. The general integration region becomes a tilted rectangle, with one dimension of this rectangle approaching zero as the correlation coefficient approaches one. A method for dealing with this variable integration region will be discussed in Chapter 4.

Chapter 4 - Variance of the Three-channel FRF

Estimator

This chapter will present two methods for estimating variance of the three-channel FRF estimator, \hat{H} . Knowing the variance of a measured FRF gives the experimenter a quantitative measure of its variability. Traditional evaluations of the accuracy of results have been based on values of the ordinary coherence, γ_{xx}^2 . Estimates of an FRF associated with values of the coherence near unity were considered 'good', while estimates with coherences near zero were considered doubtful. 'Good' is a qualitative measure and does not provide any information about what might be an expected range of values. Does 'good' mean we might expect a five percent variation in the magnitude estimate, or might it be a fraction of a percent? On the other hand, it is well known that the variance of an estimate decreases with the number of sample records averaged to obtain that estimate. But with large amounts of uncorrelated content in the measurements, no amount of averaging will increase the coherence. Indeed, the only effect of averaging on coherence is to improve the estimate of it. Coherence estimates are generally high for a small number of samples, and decrease towards the 'true' value as the number of

samples averaged increases. If the low coherence results only from uncorrelated content in the measured signal and not from, say, FFT leakage, then even with a low coherence estimate we would, at some number of averaged samples expect to finally achieve a result with an acceptable degree of variability. Whether or not this result is 'good' in terms of being accurate is another question. Depending on the estimator type and source(s) of uncorrelated content, large biases may still be possible. The three-channel estimator is chosen because its estimates are unbiased in the presence of uncorrelated content. An accurate estimate of the variance at each spectral line allows 'confidence bands' to be plotted about an estimate. The experimenter then has a determination of the range of possible values of the estimate for a given probability of error, as well as a determination of how many sample records are required to reduce variability to a desired degree.

An approximate method for the variance of the ${}^1\hat{H}$ FRF estimator has been developed by Bendat [23, section 9.2.4]. While this variance estimate was found to be reasonably accurate (in the simulations to be discussed) it is associated with a possibly biased result. Only the ${}^c\hat{H}$ method consistently converges to an unbiased result, so further work in this chapter will concentrate on developing variance estimates for this estimator.

The first method presented is an analytical one, following a similar development to that of the ${}^1\hat{H}$ estimator presented by Bendat [23]. Unfortunately, while this method produced a stable variance calculation for the ${}^1\hat{H}$ estimator, the resulting three-channel variance calculation proves to be undesirable because of computational stability problems. Large fluctuations in the variance estimate result from small changes in the experimentally measured quantities. The second method might be considered a 'brute force' approach, with the variance being calculated numerically at each spectral line. It does have the advantage however, of producing accurate and stable results.

4.1 A Finite Difference Method for Estimating Variance

4.1.1 Theoretical Development

We begin by rewriting Eq. 2.52 in the form

$$|\hat{G}_{ys}| = |{}^c\hat{H}| |\hat{G}_{xs}| \quad (4.1)$$

Again using the difference (Δ) operator

$$\Delta |\hat{G}_{ys}| \cong |{}^c\hat{H}| (\Delta |\hat{G}_{xs}|) + |\hat{G}_{xs}| (\Delta |{}^c\hat{H}|) \quad (4.2)$$

Squaring this result yields

$$(\Delta |\hat{G}_{ys}|)^2 \cong |{}^c\hat{H}|^2 (\Delta |\hat{G}_{xs}|)^2 + 2 |{}^c\hat{H}| |\hat{G}_{xs}| (\Delta |\hat{G}_{xs}|) (\Delta |{}^c\hat{H}|) + |\hat{G}_{xs}|^2 (\Delta |{}^c\hat{H}|)^2 \quad (4.3)$$

Before rewriting Eq. 4.3 and taking the expectation to find the variance, we must develop an alternate expression for the product $(\Delta |\hat{G}_{xs}|) (\Delta |{}^c\hat{H}|)$ appearing on the right side of Eq. 4.3. We start with

$$\Delta |{}^c\hat{H}| = \Delta \left| \frac{|\hat{G}_{ys}|}{|\hat{G}_{xs}|} \right| \cong \frac{\Delta |\hat{G}_{ys}|}{|\hat{G}_{xs}|} - \frac{|\hat{G}_{ys}| (\Delta |\hat{G}_{xs}|)}{|\hat{G}_{xs}|^2} \quad (4.4)$$

from which we find

$$(\Delta |{}^c\hat{H}|) (\Delta |\hat{G}_{xs}|) \cong \frac{|\hat{G}_{xs}| (\Delta |\hat{G}_{ys}|) (\Delta |\hat{G}_{xs}|) - |\hat{G}_{ys}| (\Delta |\hat{G}_{xs}|)^2}{|\hat{G}_{xs}|^2} \quad (4.5)$$

Substituting Eq 4.5 in Eq 4.3 and solving for $(\Delta|\hat{c}\hat{H}|)^2$

$$(\Delta|\hat{c}\hat{H}|)^2 \cong \frac{[|\Delta\hat{G}_{ys}|^2 + |\hat{c}\hat{H}|^2(\Delta\hat{G}_{xs})^2 - 2|\hat{c}\hat{H}|(\Delta\hat{G}_{ys})(\Delta\hat{G}_{xs})]}{|\hat{G}_{xs}|^2} \quad (4.6)$$

where Eq. 2.52 was used in the simplification process. Taking the expectation of Eq 4.6 with the aid of Eqs. 2.24 and 2.36, we find

$$Var(|\hat{c}\hat{H}|) \cong \frac{Var(|\hat{G}_{ys}|) + |\hat{c}\hat{H}|^2 Var(|\hat{G}_{xs}|) - 2|\hat{c}\hat{H}| Cov(|\hat{G}_{ys}|, |\hat{G}_{xs}|)}{|\hat{G}_{xs}|^2} \quad (4.7)$$

where the covariance may be found from Eqs. 2.46 or 2.47 by the relation

$$Cov(|\hat{G}_{ys}|, |\hat{G}_{xs}|) = \frac{Cov(|\tilde{G}_{ys}|, |\tilde{G}_{xs}|)}{n_d} \quad (4.8)$$

4.1.2 Problems With the Finite Difference Variance Estimate

The first problem with Eq. 4.7 is that estimates of the variance of $|\hat{G}_{ys}|$ and $|\hat{G}_{xs}|$ are in themselves difficult to find, because of the magnitude bias effect discussed in Chapter 3. Note that the cross spectral magnitude estimate does not have any simplifying properties: the real and imaginary parts are correlated and of differing variances. That leaves only numerical integration for finding accurate estimates of these variances.

The second problem is that the variance of $|\hat{c}\hat{H}|$ is a small number compared to the values on the right side of Eq. 4.7. That is, the term containing the covariance in Eq.

4.7 approaches the sum of the other two terms. Therefore, even small percentage errors in the variances and covariance of $|\hat{G}_x|$ and $|\hat{G}_y|$ can result in large errors for the estimate of $|\hat{H}|$ variance. With one set of data that was investigated in the simulations, a five percent change in the covariance estimate caused the $|\hat{H}|$ variance estimate to range from a fraction to several times the true variance.

4.2 A Numerical Method for Estimating Variance

The only method that has been found to accurately compute magnitude expectation and variance is numerical integration of Eqs. 3.29 and 3.30. To estimate the variance of $|\hat{H}|$ three sets of integrations must be performed for each spectral line. The first two are to determine the variance of $|\hat{G}_x|$ and $|\hat{G}_y|$, while the third integration set determines the variance of the ratio of these cross spectra (and therefore that of $|\hat{H}|$). These integrations use only values that are measured experimentally in a three-channel FRF system: n_s , \hat{C}_{xx} , \hat{Q}_{xx} , \hat{C}_{yy} , and \hat{Q}_{yy} . This section will present this topic in two parts. The first part will deal with the integration method, while the second part will show a method for determining an efficient two-dimensional integration region.

4.2.1 Details of the Integrations to Determine FRF Variance

4.2.1.1 Cross Spectral Magnitude Variance

Before the variance of the FRF estimator can be determined we must first have accurate estimates of the variances of $|\hat{G}_x|$ and $|\hat{G}_y|$ at each spectral line. The integration method is exactly the same for both $|\hat{G}_x|$ and $|\hat{G}_y|$, so in the following discussion we will drop the subscript notation. We will only refer to the quantities \hat{C} , \hat{Q} , and $|\hat{G}|$.

We have previously justified normality of \hat{C} and \hat{Q} by application of the Central Limit Theorem (section 3.1). The standard deviations of \hat{C} and \hat{Q} may be found by use of Eqs. 2.29, 2.31, 2.34, and 2.35 while the correlation coefficient between \hat{C} and \hat{Q} may be found by Eq. 2.39. These values are substituted in Eq. 3.30 as follows: σ_x , σ_y , and ρ_{xy} are replaced with $\sigma_{\hat{C}}$, $\sigma_{\hat{Q}}$ and $\rho_{\hat{C}\hat{Q}}$. The variables x and y are replaced by the variables \hat{C} and \hat{Q} , while μ_x and μ_y are replaced by the *measured estimates* of $\mu_{\hat{C}}$ and $\mu_{\hat{Q}}$, (which are the values obtained from the experimental measurement, $\hat{Q}_{measured}$ and $\hat{C}_{measured}$). With these substitutions Eq. 3.30 becomes the probability density function of \hat{C} and \hat{Q} .

We now need to set up the integration of Eqs. 3.29. For the cross spectral variance estimation, we define $g(x, y) = \sqrt{\hat{C}^2 + \hat{Q}^2}$ and $(g(x, y))^2 = \hat{C}^2 + \hat{Q}^2$. The bi-variate probability density function (PDF) of Eq. 3.30 may be thought of as a circular or elliptical 'mound' on the complex plane. If we pass a plane which is parallel to the complex plane through the mound we will find the intersection to be a circular or elliptical area. The closer the intersection plane is to the complex plane, the larger the intersection area will be. If we can accurately define the region of the plane where this mound has significant height, we need only integrate over this small region, instead of over the entire plane

extending to $+/ - \infty$ in two directions. The next section will discuss the details of determining the actual boundaries of this region, so for the moment we will only present a general discussion. If the parallel intersection plane is some small distance ϵ from the base plane, we need only integrate over this finite intersection region to obtain an approximate value of the integration carried out with limits at $+/ -$ infinity. For ease of computation, the actual integration region will be square or rectangular and just large enough to contain the circular or elliptical intersection region. That is, the circle or ellipse inscribed in the square or rectangle.

The only instance in which we would find a *circular* integration region is when the real and imaginary parts have equal variance and are uncorrelated. Since the cross spectrum components are, in general, correlated and of unequal variance, we will refer only to elliptical intersection and rectangular integration regions henceforth. The next step is to divide the rectangle into a grid of smaller rectangles, using *an equal number of divisions in both directions*. Let us say we are integrating over a region that is L units long and W units wide. Then we divide both dimensions into m equal increments, where $\Delta L = \frac{L}{m}$ and $\Delta W = \frac{W}{m}$. Our region becomes a grid of small rectangular elements, each of area $\Delta L \Delta W$. We will approximate the volume above each element by the area of the element multiplied by the value of $p(\hat{C}, \hat{Q})$ evaluated at a point in the center of the element.

Using this discrete approximation we may replace the integrations of Eq. 3.29 by double summations. If we let i and j be the summation indexes in the L and W directions, then $(\hat{C}_{ij}, \hat{Q}_{ij})$ are the coordinates of the center of element ij . Using this notation, we can rewrite Eqs. 3.29 as

$$\begin{aligned}
E[|\hat{G}|] &\cong \sum_{i=1}^m \sum_{j=1}^m \sqrt{\hat{C}_{ij}^2 + \hat{Q}_{ij}^2} p(\hat{C}_{ij}, \hat{Q}_{ij}) \Delta L \Delta W \\
E[|\hat{G}|^2] &\cong \sum_{i=1}^m \sum_{j=1}^m (\hat{C}_{ij}^2 + \hat{Q}_{ij}^2) p(\hat{C}_{ij}, \hat{Q}_{ij}) \Delta L \Delta W
\end{aligned} \tag{4.9}$$

Note that computations may be reduced if these integrations are done simultaneously, since the value of $p(\hat{C}_{ij}, \hat{Q}_{ij})$ is the same at each point for both summations. Using the results of Eq. 4.9 in Eq. 2.25 we find an estimate of the variance of \hat{G} .

4.2.1.2 FRF Magnitude Variance

We need to integrate once more to arrive at a variance estimate for $|\hat{H}|$. In our previous integrations we arrived at the variances of $|\hat{G}_x|$ and $|\hat{G}_y|$. We will now use these variances with the experimentally measured magnitudes of these quantities (i.e., no bias corrections). Using Eq. 2.48 we can find the correlation coefficient $\rho_{|\hat{G}_y|, |\hat{G}_x|}$. The PDF of Eq. 3.30 is now written as $p(|\hat{G}_x|, |\hat{G}_y|)$, while in Eq. 3.29 $g(x, y)$ becomes $g(|\hat{G}_y|, |\hat{G}_x|) = \frac{|\hat{G}_y|}{|\hat{G}_x|} = |\hat{H}|$. A summation similar to that of Eq. 4.9 is used to find the expectations of the mean and mean square which then give the variance from Eq. 2.25.

Note that in this third integration we assumed that the PDF's of both $|\hat{G}_x|$ and $|\hat{G}_y|$ are Gaussian (Normal). We may use the Central Limit Theorem (CLT) to justify *approximate* Normality for \hat{C} and \hat{Q} . The magnitudes $|\hat{G}_x|$ and $|\hat{G}_y|$ however are *functions* of (approximately) Normal variables, so the CLT does not apply. A function of Normal variables is not necessarily Normal. While there is a basis for assuming

Normality of a function of Normal variables *in the limit* [26], further verification was desired. The primary basis for the assumption of Normality for this integration are the Monte Carlo simulations discussed in Chapter 6. As we shall see there, in most instances the magnitude of a cross spectrum estimate closely follows a Normal distribution.

This third and final integration is fairly insensitive to small variations in the input quantities, with one exception: the correlation coefficient ρ . If our measured data has little uncorrelated content (i.e., $\gamma_{yx}^2 \rightarrow 1$), the correlation coefficient approaches unity. Near unity, small changes in ρ can have a large effect on variance. It can also be seen in Eq. 3.30 that $\rho = 1$ can cause numerical problems with a zero in the denominator. In practice, this can be prevented by placing an upper limit on ρ . When the integration routine was implemented using IEEE double precision format, a value of $\rho_{\max} = 0.999999$ was found to give quite satisfactory results when high correlation coefficients were encountered.

4.2.2 Determining an Efficient Integration Region

To find an efficient integration region, we must first understand what changes can occur in the shape of the bi-variate PDF of Eq. 3.30. Let us use a general case for discussion where σ_x and σ_y are unequal, and we pass a plane through the 'mound' a distance ε from the $x - y$ plane. If the correlation coefficient is zero, we would find that the intersection is elliptical in shape, with the major axes parallel with the coordinate axes. If we hold all else constant and if we increase the correlation coefficient towards unity, we would see the shape of the ellipse narrow and rotate. As $\rho \rightarrow 1$ the intersection region ap-

proaches a zero width line segment tilted at some limiting angle which we will find in a moment. The sides of the mound towards the narrowing dimension become steeper as ρ becomes larger, until at the limiting case of $\rho = 1$ we would find that the mound has reached an infinite height, but only over the infinitesimal area of a line segment in the integration plane (remember that the total volume is always unity, representing a probability of 1). As mentioned previously this is computationally intractable, so an upper limit on ρ must be set.

Our task is to find the smallest rectangular region that will just contain the intersection region discussed above. Reference to Eq. 3.30 will show that a constant height (or constant probability) is defined by a constant argument in the exponential term. That is

$$\left\{ \frac{(x - \mu_x)^2}{\sigma_x^2} + \frac{(y - \mu_y)^2}{\sigma_y^2} - \frac{2\rho_{xy}(x - \mu_x)(y - \mu_y)}{\sigma_x\sigma_y} \right\} = \text{constant} \quad (4.10)$$

This is the equation for an ellipse that has its center at at (μ_x, μ_y) , and is rotated through some angle θ . Since the translation and rotation are independent operations, we will translate the ellipse back to the origin in order to simplify the angle calculation. Using $x' = x - \mu_x$ and $y' = y - \mu_y$, we can rewrite Eq. 4.10 as

$$\frac{x'^2}{\sigma_x^2} - \frac{2\rho x'y'}{\sigma_x\sigma_y} + \frac{y'^2}{\sigma_y^2} = \text{constant} \quad (4.11)$$

From analytic geometry we may find the equations for a rotated and translated ellipse as

$$Ax^2 + Bxy + Cy^2 + Dx + Ey + F = 0$$

$$\tan(2\theta) = \frac{B}{A - C} \quad (4.12)$$

Comparison of Eqs. 4.11 and 4.12 allows us to find

$$\tan(2\theta) = \frac{\frac{-2\rho}{\sigma_x\sigma_y}}{\frac{1}{\sigma_x^2} - \frac{1}{\sigma_y^2}} \quad (4.13)$$

$$= \rho \left(\frac{\frac{2}{\sigma_x\sigma_y}}{\frac{1}{\sigma_y^2} - \frac{1}{\sigma_x^2}} \right) = \rho \left(\frac{2\frac{\sigma_y}{\sigma_x}}{1 - \left(\frac{\sigma_y}{\sigma_x}\right)^2} \right)$$

Using the trigonometric identities

$$\tan(\phi - \psi) = \frac{\tan(\phi) - \tan(\psi)}{1 + \tan(\phi)\tan(\psi)} \quad (4.14)$$

$$\tan(-\psi) = -\tan(\psi)$$

with the substitutions $\tan(\phi) = \frac{\sigma_y}{\sigma_x}$ and $\psi = -\phi$ we find that

$$\tan(2\theta) = \rho \left(\frac{2 \tan(\phi)}{1 - \tan^2(\phi)} \right) \quad (4.15)$$

$$= \rho \left(\frac{\tan(\phi) - \tan(-\phi)}{1 + \tan(\phi)\tan(-\phi)} \right)$$

$$= \rho \tan(\phi - (-\phi)) = \rho \tan(2\phi)$$

Thus, we see that as $|\rho|$ increases $0 \rightarrow 1$, then θ ranges $0 \rightarrow \phi$.

At this point we know the center of the ellipse is at (μ_x, μ_y) , and the major axes are rotated an angle θ . The next step is to find the dimensions L and H . This is done numerically, using a set range of ε between ε_{\min} and ε_{\max} . An incremental step method is used, starting at the center of the ellipse and moving outward along the (tilted) major axis until $p(x, y) < \varepsilon_{\min}$. Then the technique switches to a bisection method until $\varepsilon_{\min} < p(x, y) < \varepsilon_{\max}$ for some coordinate (x, y) that lies along the major axis of the ellipse. The distance between (μ_x, μ_y) and (x, y) is the dimension $\frac{L}{2}$. This process is repeated along the minor axis until the dimension $\frac{H}{2}$ has been found. Once L and H have been found, the region must be divided into elements and the summations of Eq. 4.9 carried out.

We have discussed the method without reference to the actual numbers used. Good results were obtained with the following values:

$$\begin{aligned}
 \varepsilon_{\min} &= 1.0 E - 10 \\
 \varepsilon_{\max} &= 2.0 E - 10 \\
 m &= 15 \text{ (number of divisions)} \\
 n_d &\geq 50 \\
 \rho_{\max} &= 0.999999 \text{ (in IEEE double precision format)}
 \end{aligned}
 \tag{4.16}$$

There is a good reason for specifying the minimum number of samples averaged, n_d . Remember that in Eqs. 3.29 we integrate the *product* of $g(x, y)$ and $p(x, y)$. Although the mound of $p(x, y)$ is symmetrical with an elliptical cross section, the shape formed by this product is neither elliptical nor symmetrical. Also recall that the variance of \hat{C} and \hat{Q} (when finding the cross spectrum variance) are inversely proportional to n_d . Small numbers of samples, n_d , result in an integration region that contains the origin. This causes trouble. The magnitude function, $g(x, y)$, is zero at the origin. Regardless of the value of $p(x, y)$ at the origin, the product of these two values is zero. Instead of having

a well behaved integration volume which probably resembles a lop-sided elliptical mound, we have a lop-sided elliptical mound with a zero height hole in it at the origin. If we are near the center of the PDF mound, this hole causes a volume high rates of change of surface derivatives in its vicinity. This region cannot be defined by a relatively few integration elements. In fact for small values of n_d even quadrupling the number of elements failed to give accurate results. The only tractable solution is to ensure that n_d is as given in Eq. 4.16. Under this condition the origin lies either on the edge or outside of the integration region and does not cause difficulty. Another reason for imposing this limitation on n_d is concerned not with the integration method, but the underlying assumptions which allow the integration method to be used. Normality for the cross spectral real and imaginary terms was justified by the Central Limit Theorem. It appears, from the simulation results in Chapter 6, that $n_d \geq 50$ is probably a minimum criteria for the CLT Normality effect to be valid.

A discussion on numerical precision is required. Although the measured values obtained from an FFT analysis are typically less than IEEE single precision, higher precision must be used in the numerical integration process. Because many of the volume elements are very small, their values may not show up accurately in a single precision computation. Therefore, all operations in the summations of Eq. 4.9 are carried out in double precision, though the final results are converted back to single precision format. With double precision format and a 15 X 15 integration grid, the expectations found by the summations of Eq. 4.9 are generally within one percent or less of the values found when using much finer grids, say 100 x 100.

The integration method used is not sophisticated. The volume above a rectangular element in the plane is based on the height above one point in the center of the element.

However this method was found to be the most efficient of several tried. A type of trapezoidal integration was used, where the volume was based on the heights at all four corners of the element. Surprisingly, this method needed a finer mesh (more elements) to converge than the simpler method used. A 5-point-Gaussian-quadrature was also used, but this did not have nearly the accuracy required for meaningful results (for a reasonably accurate variance result, we must have the expectation of the magnitude with an error of much less than 0.1 % !).

Chapter 5 - Experimental FRF Measurement

Simulations

Two types of simulations were done. Both simulated the experimental FRF measurement process model shown in Fig 1. A Gaussian (Normal) random number generator was used to generate random values directly in the frequency domain; therefore these simulations did not attempt to model the FFT problems of aliasing and leakage. The scope was limited to evaluating the performance and statistical characteristics of various FRF estimators whenever there is uncorrelated content present in the measurement system.

The first type of simulation used the Monte Carlo technique. Simulated FRF measurements were made repeatedly at a single spectral line. Each individual measurement was based on an average of n_s simulated FFT records. The results of these repeated simulated measurements were used to generate estimates of probability density functions and various statistical quantities.

The other type of simulation modeled a single FRF measurement over a number of spectral lines. This allowed comparison of the various FRF estimators simultaneously over a large range of the system response, $H(f)$. This simulation method was also used to evaluate the validity of the confidence bands generated by the variance calculations of Chapter 4 and the uncorrelated content estimates developed in Chapter 2. Both the single and multiple spectral line simulations used the same simulated FRF measurement technique, so that will be discussed first.

5.1 Simulating the FRF Measurement Process

Each spectral line was treated individually. Referring to Eqs. 2.9, the real and imaginary parts of $S(f)$, $K(f)$, $M(f)$, and $N(f)$ were treated as independent random variables of equal variance and generated using a zero-mean Gaussian random generator. The user entered the real and imaginary part standard deviations σ_S , σ_R , σ_M , and σ_N . The raw sample record auto spectra were found by Eq. 2.2. Because the random generation takes place in the frequency domain and is not related to any particular record time length T , this value may be chosen arbitrarily. To simplify computations a value of $T = 2$ was used in all simulations. Then, by Eqs. 2.2 and 2.24 we see that for say, $S(f)$

$$\begin{aligned}\tilde{G}_{ss} &= \frac{2}{2}[S_R^2 + S_I^2] = S_R^2 + S_I^2 \\ E[\tilde{G}_{ss}] &= 2\sigma_s^2\end{aligned}\tag{5.1}$$

The user was also required to enter the 'true' system FRF that was to be 'measured', $H(f)$. To simplify calculations and interpretation of results, the

amplifier/shaker/attachment-hardware system FRF, $\Gamma(f)$, was set to $\Gamma(f) = 1.0 - j0.0$ for all simulations. All other frequency-domain quantities were calculated by Eqs. 2.9.

An FRF measurement was simulated as follows: The real and imaginary parts of $\tilde{S}(f)$ were generated with the Gaussian random generator. A raw sample of \tilde{G}_n was calculated by Eq. 5.1 and stored for averaging with other raw samples. The random generator was called again for sample values of the real and imaginary parts of $\tilde{K}(f)$, which were added directly to $\tilde{S}(f)$ (since $\Gamma(f)$ is unity) to form $\tilde{U}(f)$. $\tilde{X}(f)$ was obtained by adding the random generated value $\tilde{M}(f)$ to $\tilde{U}(f)$. The 'true' structure response was found by $\tilde{V}(f) = \tilde{U}(f) H(f)$. The 'measurable' quantity $\tilde{Y}(f)$ was obtained by adding the generated value of $\tilde{N}(f)$ to the structure response. Raw sample values of \tilde{G}_{xx} , \tilde{G}_{yy} , \tilde{G}_{xz} , \tilde{G}_{yz} , and \tilde{G}_{yx} were calculated by Eqs. 5.1 and 2.3 and stored for averaging. This process was repeated n_d times to obtain simulated values of \hat{G}_n , \hat{G}_{xx} , \hat{G}_{yy} , \hat{G}_{xz} , \hat{G}_{yz} , and \hat{G}_{yx} . From this data estimates of the system FRF, $\hat{H}(f)$, could be found using the various FRF estimators.

5.2 Single Spectral Line Monte Carlo Simulations

The individual measurement simulations were repeated in order to obtain information about the statistical distributions of various quantities. The majority of Monte Carlo simulations were based on $p = 3000$ simulated measurements of $n_d = 50$ samples per measurement. The quantities which were evaluated in this manner were: \hat{G}_n , \hat{G}_{xx} , \hat{G}_{yy} , $|\hat{G}_{xz}|$, $|\hat{G}_{yz}|$, $|\hat{G}_{yx}|$, $|\hat{H}|$, $|\hat{H}|$, $|\hat{H}|$, \hat{y}_{xz}^2 , \hat{y}_{yz}^2 , and \hat{y}_{yx}^2 , as well as the real and imaginary parts of the complex quantities ${}^c\hat{H}$, ${}^1\hat{H}$, ${}^2\hat{H}$, \hat{G}_{xz} , \hat{G}_{yz} , and \hat{G}_{yx} .

We will denote the value of any one of these quantities in a single simulated FRF measurement by x . After each of the simulated FRF measurements single and squared values of x were summed to form the quantities $\sum x$ and $\sum x^2$. At the end of p repeated simulations, estimates of the expected values and variances were found by the standard statistical formulas

$$\bar{x} = \frac{\sum_{i=1}^p x_i}{p} \tag{5.2}$$

$$S_x = \sqrt{\frac{\sum x^2 - \frac{(\sum x)^2}{p}}{p-1}}$$

where \bar{x} and S_x are estimates of μ_x and σ_x , respectively. The full summation index notation was only used once in Eq. 5.2 for brevity.

On many of the of simulation runs, values of \hat{H}_R , \hat{H}_I , $|\hat{H}|$, \hat{G}_R , \hat{G}_I , and $|\hat{G}|$ were not only summed, but stored as separate values. These separate values were sorted into monotonic sequences for Normality testing and plotting approximate PDF plots in histogram form. Because there were typically $p = 3000$ real values to be stored for a single Normal test or PDF plot, only a limited number of quantities could be evaluated in this manner for any one simulation run.

5.3 Multiple Spectral Line FRF Measurement Simulations

Acceleration response equations were derived from the equations of motion for a two degree-of-freedom discrete mass system. Using 'unitless' mass and stiffness values of 1.0, and a viscous damping ratio (ζ) of 0.0005, the response equation for the acceleration of mass one to a force applied at mass one became

$$H_{11}(\omega) = \frac{-\omega^2(1 - \omega^2) - j0.0001\omega^3}{\omega^4 - 3.0001\omega^2 + 1 - j(0.03\omega^3 - 0.02\omega)}$$

where ω is the 'circular' frequency given by $\omega = 2\pi f$. An upper range of $\omega = 1.992$ was used. The 'true' FRF at the k^{th} spectral line was generated by calculating $H_k(\omega) = H(k \Delta\omega)$ where $\Delta\omega = \frac{1.992}{k}$. Thus, the actual discrete values of the 'true' FRF at any given region were dependent on the spacing of the spectral lines, $\Delta\omega$. That is, a small change in k could cause the spectral line FRF value calculated at $k \Delta\omega$ to move closer or farther to/from a resonance peak. Typically, though, this FRF model provided a dynamic range from resonance to anti-resonance of about 100 dB.

Once the 'true' $H_k(f)$ had been calculated for every spectral line, subsequent calculations treated each line as an independent quantity. The user entered quantities σ_S , σ_K , σ_M , and σ_N were taken as constants over all spectral lines. This is a more severe test than would normally be seen in an actual experimental FRF measurement, where only σ_S might be considered constant. In a real system G_{kk} , G_{mm} , and G_m are truly functions of frequency, with only one or two terms being dominant at any particular frequency. For example, G_m would dominate at antiresonance, where the 'true' system response output signal would be very small. At resonance, G_{kk} and G_{mm} would likely have the greatest

dominance. This could happen because the large structural response in this region might cause the shaker to be 'overdriven' resulting in loss of coherence between the source and the other two 'measurable' signals. Therefore, only one or two significant uncorrelated content terms would need to be estimated at any given spectral line, instead of all three as was done in these simulations.

Each run consisted of only one simulated FRF measurement, instead of the hundreds or thousands made in the Monte Carlo simulations. The results of the simulated measurement were in the form of plots of $|\hat{H}|$ generated by the various FRF estimators superimposed over the 'true' FRF. In this way the merits and biases of each of the estimators could be compared simultaneously. A benefit of using the simulated FRF measurements is that for a real life structure the 'true' FRF is never known exactly, so there is nothing with which to compare the measured estimates.

The single measurement simulations also allowed verification of the variance calculations for $|\hat{H}|$ shown in Chapter 4. Using the 'measured' values of the auto and cross spectra, the variance was estimated at each spectral line. The user entered the desired width of the confidence bands in terms of number of standard deviations. For example, if the confidence bands are placed at two standard deviations above and below the 'measured' value of $|\hat{H}|$, one would expect that the 'true' FRF would fall within these bands with about 95% certainty. With these bands plotted over a large number of spectral lines, one would expect to find the 'true' FRF within the confidence bands at about 95% of the lines. This expectation is of course based on the assumption that the variance estimator works equally well at each spectral line. This is not an assumption that can be made easily, and will be discussed further in Chapters 6 and 7.

Comparisons were also made between the true and estimated values of the uncorrelated content auto spectra, using the relations developed in Chapter 2 for the estimates.

Chapter 6 - Results of FRF Measurement

Simulations

This discussion will begin with a comparison of FRF estimates obtained with various estimators. Then Monte Carlo simulation results will be used to verify statistical calculations previously presented and show estimated probability density function (PDF) plots. Simulations showing estimates of confidence bands on the $|\hat{H}|$ estimator will be discussed. Results showing the strengths/weaknesses of the uncorrelated content estimators will be presented.

6.1 Comparison of FRF Estimators

Figure 8 shows a comparison of three $|H(f)|$ estimators: $|\hat{H}_1|$, $|\hat{H}_2|$, and $|\hat{H}_3|$. The estimates are based on $n_s = 200$ sample records. The 'source' auto spectrum was set to

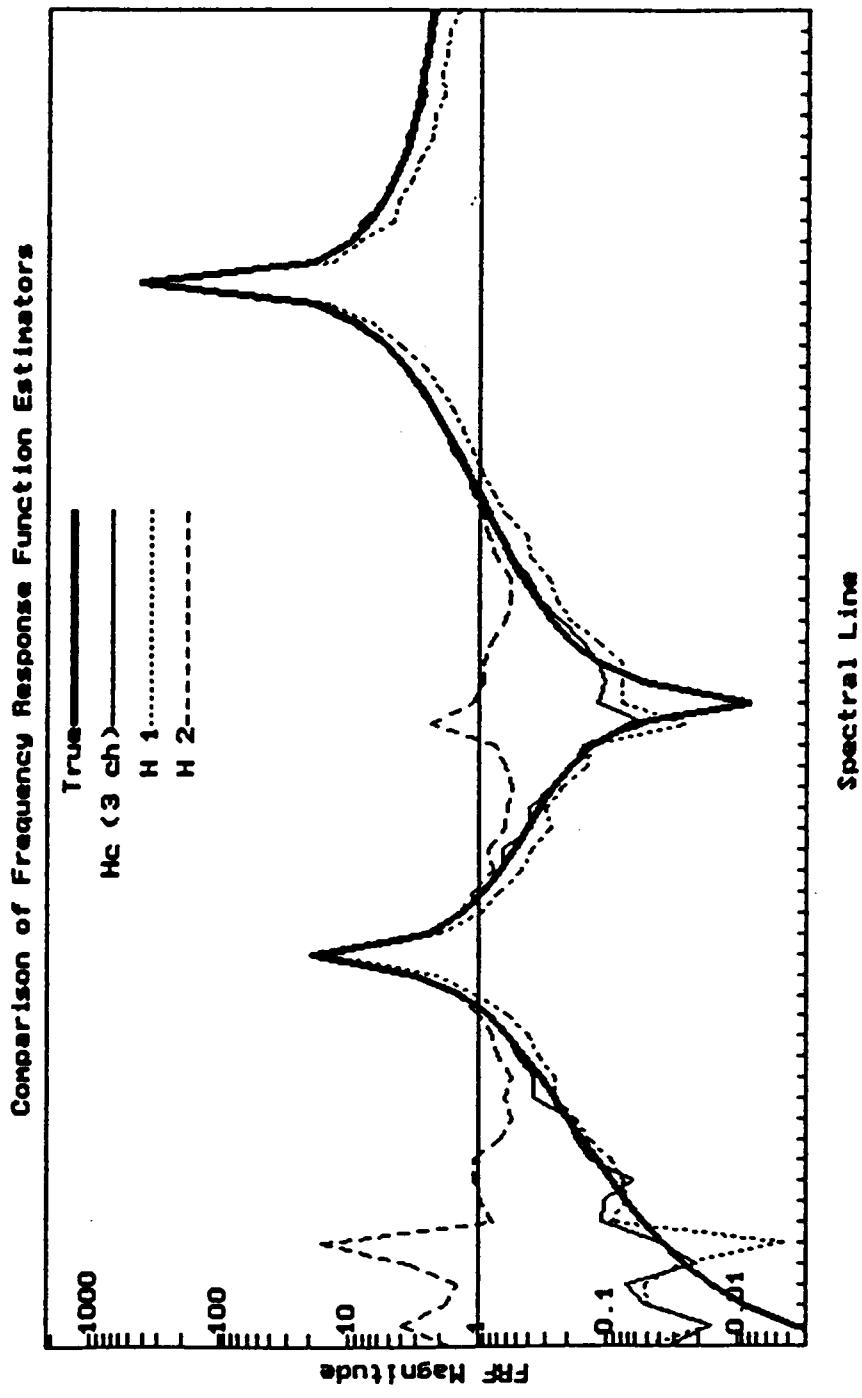


Figure 8. Comparison of Frequency Response Function Estimators

$G_{xx} = 18.0$ at all spectral lines. The uncorrelated content terms G_{kk} , G_{mm} , and G_{nn} were all assigned nominal auto spectra of 2.0 at each spectral line (See Eq. 5.1).

The uncorrelated content term G_{mm} causes the $|\hat{H}^1|$ estimator to find values that are consistently below the 'true' FRF magnitude, $|H(f)|$. Similarly, G_{nn} causes the $|\hat{H}^2|$ estimator to find consistently high values. Only $|\hat{H}^c|$ finds unbiased estimates of the system FRF at all frequencies with uncorrelated content present at all locations. The unbiased nature of $|\hat{H}^c|$ is valid only for the real and imaginary parts, as the magnitude bias effect will cause bias errors even with this estimator in anti-resonance regions. Recall that these simulations do not attempt to include the effects of FFT leakage. There is some speculation [7] that when leakage is present in an actual measurement, the nominal high bias of $|\hat{H}^2|$ tends to cancel leakage effects and give the most accurate estimates of the system FRF at resonance.

6.2 Monte Carlo Simulations

Six representative sets of Monte Carlo simulation results (data sets A - F) are shown in Tables 1 - 6. Below each simulation result there are one or two comparison values in parentheses. Whether these comparison are 'true' values or estimates depends on the quantity, and will be made clear in example calculations. Those comparison values marked with an asterik (*) were obtained by numerical integration of Gaussian probability density functions (PDFs), as discussed in Chapter 4. FRF and cross spectrum magnitudes marked with (##) are those which show a pronounced effect from the com-

Table 1. Simulation Data Set A

FRF = 0.0 + 0.0j				
3000 Single-Sample-Record Measurements				
Estimated Quantity	Mean	Variance	Std Dev	SD of Mean
	$G_{kk} = 2.0$	$G_{mm} = 2.0$	$G_{nn} = 2.0$	
	$G_{ss} = 18.0$			
G_{ss}	17.5659 (18)	318.7900 (308.5608)	17.8547 (17.5659)	0.3260 (+ 1.332)
G_{xx}	22.1703 (22)	488.8296 (491.5222)	22.1095 (22.1703)	0.4037 (-0.422)
G_{yy}	1.9413 (2)	3.6419 (3.7686)	1.9084 (1.9413)	0.0348 (+ 1.687)
C_{xs}	17.8437 (18)	356.5526 (353.9133)	18.8826 (18.8126)	0.3447 (+ 0.453)
Q_{xs}	-0.1110 (0)	34.0437 (35.5280)	5.8347 (5.9605)	0.1065 (+ 1.042)
$ \tilde{G}_{xs} $	18.8604 (17.8440)	353.2785 (389.4413)	18.7957 (19.7343)	0.3432 (-2.962)
C_{ys}	-8.768E-03 (0)	16.5876 (17.0469)	4.0728 (4.1288)	0.0744 (+ 0.118)
Q_{ys}	-0.0839 (0)	16.9272 (17.0538)	4.1143 (4.1296)	0.0751 (+ 1.117)
$ G_{ys} $ ##	4.5660 (0.0844)	12.6669 (34.1007)	3.5591 (5.8396)	0.0650 (-68.95)
C_{yx}	3.085E-03 (0)	20.8964 (21.5169)	4.5713 (4.6386)	0.0835 (-0.037)
Q_{yx}	-0.0729 (0)	21.4257 (21.5223)	4.6288 (4.6392)	0.0845 (+ 0.863)
$ G_{yx} $ ##	5.1555 (0.0730)	15.7394 (43.0392)	3.9673 (6.5604)	0.0724 (-70.20)
H_R	3.770E-03 (0)	0.4211	0.6489	0.0118 (-0.319)
H_I	1.242E-03 (0)	0.4933	0.7024	0.0128 (-0.097)
$ H $ ##	0.4643 (0.0040)	0.6988	0.8359	0.0153 (-30.08)
## - results showing a strong effect from the magnitude bias - All three FRF estimators are identical for single sample measurements - Coherences not shown since all are unity for a single sample measurement See example in text for explanation of comparison values in parentheses				

Table 2. Simulation Data Set B

FRF = 0.0 + 0.0j $G_{ss} = 18.0$ Estimated Quantity	3000 Measurements $G_{kk} = 2.0$ Mean	50 Samples per Measurement $G_{mm} = 2.0$ Variance	$G_{nn} = 2.0$ Std Dev	SD of Mean
G_{ss}	18.0763 (18)	6.7118 (6.5350)	2.5907 (2.5564)	0.0473 (-1.613)
G_{xx}	22.0684 (22)	9.7469 (9.7403)	3.1220 (3.1209)	0.0570 (-1.200)
G_{yy}	2.0032 (2)	0.0841 (0.0803)	0.2900 (0.2833)	5.295E-03 (-0.604)
C_{xs}	18.0714 (18)	7.3587 (7.2549)	2.7127 (2.6935)	0.0495 (-1.442)
Q_{xs}	-9.627E-04 (0)	0.6856 (0.7234)	0.8280 (0.8505)	0.0151 (+0.064)
$ G_{xs} $	18.0903 (18.0714) (18.0918)*	7.3598 (7.9783) (7.2386)*	2.7129 (2.8246) (2.6935)*	0.0495 (-0.382) (+0.030)*
r_{xs}^2	0.8192 (0.8182)	1.115E-03	0.0334	6.098E-04 (-1.640)
C_{ys}	-5.870E-03 (0)	0.3688 (0.3621)	0.6073 (0.6018)	0.0111 (+0.529)
Q_{ys}	-0.0121 (0)	0.3736 (0.3621)	0.6112 (0.6018)	0.0112 (+1.080)
$ G_{ys} $ ##	0.7604 (0.0134) (0.7394)*	0.1641 (0.7242) (0.1536)*	0.4051 (0.8510) (0.3920)*	7.396E-03 (-101.0) (-2.839)*
r_{ys}^2	0.0205 (0/0.02BIAS)	3.999E-04	0.0200	3.652E-04 (-56.1/-1.37BIAS)
C_{yx}	-4.577E-03 (0)	0.4495 (0.4421)	0.6704 (0.6649)	0.0122 (+0.375)
Q_{yx}	-0.0147 (0)	0.4519 (0.4421)	0.6722 (0.6649)	0.0123 (+1.195)
$ G_{yx} $ ##	0.8337 (0.0154) (0.8196)*	0.2063 (0.8841) (0.1876)*	0.4541 (0.9403) (0.4331)*	8.291E-03 (-98.70) (-1.701)*
r_{yx}^2	0.0203 (0/0.02BIAS)	4.151E-04	0.0204	3.725E-04 (-54.5/-0.805BIAS)
1H_R	-3.838E-04 (0)	9.406E-04	0.0307	5.605E-04 (+0.683)
1H_I	-7.434E-04 (0)	9.512E-04	0.0308	5.623E-04 (+1.322)
$ ^1H $ ##	0.0382 (0)	4.332E-04 (7.042E-04)	0.0208 (0.0265)	3.798E-04 (-100.6)
cH_R	-4.954E-04 (0)	1.158E-03	0.0340	6.207E-04 (+0.798)
cH_I	-7.586E-04 (0)	1.184E-03	0.0344	6.281E-04 (+1.208)
$ ^cH $ ##	0.0426 (0) (7E-4)*	5.255E-04 (5.062E-04)*	0.0229 (0.0225)*	4.181E-04 (-101.9) (-100.2)
2H_R	-0.0426 (0)	22.7097	4.7655	0.0870 (+0.499)
2H_I	0.0299 (0)	40.9880	6.4022	0.1169 (-0.256)
$ ^2H $ ##	3.8759 (0)	48.6731	6.9766	0.1274 (-30.42)

* - Quantities found by numerical integration method
- results showing a strong effect from the magnitude bias
See example in text for explanation of comparison values in parentheses

Table 3. Simulation Data Set C

FRF = 0.05 + 0.01j $G_{SS} = 18.0$ Estimated Quantity	3000 Measurements $G_{kk} = 2.0$ Mean	50 Samples per Measurement $G_{mm} = 2.0$ Variance	$G_{nn} = 2.0$ Std Dev	SD of Mean
G_{SS}	18.0216 (18)	6.7114 (6.4956)	2.5906 (2.5486)	0.0473 (-0.457)
G_{XX}	22.0141 (22)	9.6604 (9.6924)	3.1081 (3.1133)	0.0567 (-0.249)
G_{YY}	2.0545 (2.0520)	0.0830 (0.0844)	0.2881 (0.2906)	5.260E-03 (-0.475)
C_{XS}	18.0140 (18)	7.3153 (7.2123)	2.7047 (2.6856)	0.0494 (-0.283)
Q_{XS}	0.0148 (0)	0.7138 (0.7223)	0.8449 (0.8499)	0.0154 (-0.961)
$ G_{XS} $	18.0337 (18.0140) (18.0345)*	7.3196 (7.9346) (7.1960)*	2.7055 (2.8168) (2.6825)*	0.0494 (-0.399) (+0.016)*
γ_{XS}^2	0.8186 (0.8182)	1.122E-03	0.0335	6.116E-04 (-0.654)
C_{YS}	0.8803 (0.900)	0.3737 (0.3776)	0.6113 (0.6145)	0.0112 (+1.759)
Q_{YS}	0.1888 (0.180)	0.3834 (0.3629)	0.6192 (0.6024)	0.0113 (-0.779)
$ G_{YS} $ ##	1.1331 (0.9003) (1.1295)*	0.2837 (0.7405) (0.2752)*	0.5327 (0.8605) (0.5246)*	9.726E-03 (-23.94) (-0.370)*
γ_{YS}^2	0.0414 (0.023/0.042BIAS)	1.109E-03	0.0333	6.080E-04 (-30.6/+0.82BIAS)
C_{YX}	0.9801 (1.00)	0.4552 (0.4614)	0.6747 (0.6793)	0.0123 (+1.618)
Q_{YX}	0.2072 (0.20)	0.4553 (0.4431)	0.6748 (0.6657)	0.0123 (-0.585)
$ G_{YX} $ ##	1.2518 (1.0018) (1.2533)*	0.3467 (0.9045) (0.3375)*	0.5888 (0.9511) (0.5809)*	0.0107 (-23.36) (+0.140)*
γ_{YX}^2	0.0414 (0.023/0.043BIAS)	1.121E-03	0.0335	6.116E-04 (-30.1/+2.6BIAS)
1H_R	0.0445 (0.05)	9.222E-04	0.0304	5.550E-04 (+9.910)
1H_I	9.278E-03 (0.01)	9.582E-04	0.0310	5.660E-04 (+1.276)
$ {}^1H $ ##	0.057 (0.051)	6.895E-04 (7.549E-04)	0.0263 (0.0274)	4.802E-04 (-12.70)
cH_R	0.0489 (0.05)	1.128E-03	0.0336	6.135E-04 (+1.793)
cH_I	0.0102 (0.01)	1.202E-03	0.0347	6.335E-04 (-0.316)
$ {}^cH $ ##	0.0631 (0.051) (0.050)*	8.373E-04 (8.585E-04)*	0.0289 (0.0293)*	5.276E-04 (-22.93) (-24.83)*
2H_R	1.3847 (0.05)	7.6766	2.7707	0.0506 (-26.38)
2H_I	0.2560 (0.01)	10.3743	3.2209	0.0588 (-4.184)
$ {}^2H $ ##	2.3935 (0.051)	14.3039	3.7820	0.0690 (-33.95)

* - Quantities found by numerical integration method
- results showing a strong effect from the magnitude bias
See example in text for explanation of comparison values in parentheses

Table 4. Simulation Data Set D

Estimated Quantity	FRF = 0.05 + 0.01j $G_{SS} = 18.0$	3000 Measurements $G_{kk} = 2.0$	100 Samples per Measurement $G_{mm} = 2.0$	$G_{nn} = 2.0$	SD of Mean
		Mean	Variance	Std Dev	
G_{SS}		17.9812 (18)	3.1283 (3.2332)	1.7687 (1.7981)	0.0323 (+0.582)
G_{XX}		21.9927 (22)	4.7813 (4.8368)	2.1866 (2.1993)	0.0399 (+0.183)
G_{YY}		2.0536 (2.052)	0.0411 (0.0422)	0.2026 (0.2054)	3.699E-03 (-0.433)
C_{XS}		17.9884 (18)	3.4847 (3.5952)	1.8667 (1.8961)	0.0341 (+0.340)
Q_{XS}		0.0118 (0)	0.3524 (0.3594)	0.5937 (0.5995)	0.0108 (-1.093)
$ G_{XS} $		17.9982 (17.9884) (17.9985)*	3.4849 (3.9546) (3.5913)*	1.8668 (1.9886) (1.8951)*	0.0341 (-0.287) (+0.009)
γ_{XS}^2		0.8187 (0.8182)	5.226E-04	0.0229	4.181E-04 (-1.196)
C_{YS}		0.9052 (0.900)	0.1912 (0.1886)	0.4372 (0.4342)	7.982E-03 (-0.652)
Q_{YS}		0.1870 (0.180)	0.1871 (0.1807)	0.4325 (0.4251)	7.896E-03 (-0.887)
$ G_{YS} $ ##		1.0331 (0.9243) (1.0303)*	0.1653 (0.3693) (0.1620)*	0.4066 (0.6077) (0.4025)*	7.424E-03 (-14.66) (-0.377)
γ_{YS}^2		0.0329 (0.023/0.032BIAS)	5.148E-04	0.0227	4.144E-04 (-24.4/-1.21BIAS)
C_{YX}		1.0023 (1.00)	0.2296 (0.2306)	0.4792 (0.4802)	8.749E-03 (-0.263)
Q_{YX}		0.2010 (0.20)	0.2337 (0.2210)	0.4835 (0.4701)	8.828E-03 (-0.113)
$ G_{YX} $ ##		1.1438 (1.0223) (1.1395)*	0.1999 (0.4516) (0.1982)*	0.4471 (0.6720) (0.4452)*	8.163E-03 (-14.88) (-0.527)
γ_{YX}^2		0.0330 (0.023/0.033BIAS)	5.140E-04	0.0227	4.144E-04 (-24.1/-0.97BIAS)
1H_R		0.0456 (0.05)	4.554E-04	0.0213	3.889E-04 (+11.31)
1H_I		9.146E-03 (0.01)	4.881E-04	0.0221	4.035E-04 (+2.116)
$ {}^1H $ ##		0.0521 (0.0510)	3.944E-04 (3.977E-04)	0.0199 (0.0199)	3.633E-04 (-3.028)
cH_R		0.0503 (0.05)	5.637E-04	0.0237	4.327E-04 (-0.693)
cH_I		0.0103 (0.01)	5.853E-04	0.0242	4.418E-04 (-0.679)
$ {}^cH $ ##		0.0575 (0.0510) (0.0514)*	4.836E-04 (4.928E-04)*	0.0220 (0.0222)*	4.017E-04 (-16.18) (-15.18)
2H_R		1.7741 (0.05)	2.1004	1.4493	0.0265 (-65.06)
2H_I		0.3222 (0.01)	2.7366	1.6543	0.0302 (-10.34)
$ {}^2H $ ##		2.2579 (0.0510)	2.9896	1.7291	0.0316 (-69.84)

* - Quantities found by numerical integration method
- results showing a strong effect from the magnitude bias
See example in text for explanation of comparison values in parentheses

Table 5. Simulation Data Set E

FRF = 5.0 + 0.01j $G_{SS} = 18.0$ Estimated Quantity	3000 Measurements $G_{kk} = 2.0$ Mean	50 Samples per Measurement $G_{mm} = 2.0$ Variance	$G_{nn} = 2.0$ Std Dev	SD of Mean
G_{SS}	17.9767 (18)	6.5423 (6.4632)	2.5578 (2.5423)	0.0467 (+ 0.499)
G_{XX}	21.9746 (22)	9.7578 (9.6576)	3.1237 (3.1077)	0.0570 (+ 0.446)
G_{YY}	500.5980 (502.002)	5069.2090 (5011.967)	71.1984 (70.795)	1.2999 (+ 1.080)
C_{XS}	17.9732 (18)	7.2872 (7.1807)	2.6995 (2.6797)	0.0493 (+ 0.544)
Q_{XS}	-0.0147 (0)	0.7192 (0.7196)	0.8481 (0.8485)	0.0155 (+ 0.948)
$ G_{XS} $	17.9932 (17.973) (17.9937)*	7.2865 (7.9006) (7.1644)*	2.6994 (2.8108) (2.6766)*	0.0493 (-0.410) (+ 0.010)
r_{XS}^2	0.8184 (0.8181)	1.112E-03	0.0333	6.080E-04 (-0.493)
C_{YS}	89.8085 (90)	172.7023 (170.6463)	13.1416 (13.0632)	0.2399 (+ 0.798)
Q_{YS}	0.1784 (0.18)	9.4348 (9.3356)	3.0716 (3.0554)	0.0561 (+ 0.028)
$ G_{YS} $	89.8611 (89.8087) (89.8617)*	172.7219 (179.9820) (170.4419)*	13.1424 (13.4157) (13.0553)*	0.2399 (-0.218) (+ 0.003)
r_{YS}^2	0.8965 (0.8964)	3.989E-04	0.0200	3.652E-04 (-0.274)
C_{YX}	99.7951 (100)	211.4586 (209.5945)	14.5416 (14.4774)	0.2655 (+ 0.772)
Q_{YX}	0.2293 (0.20)	10.4633 (10.4143)	3.2347 (3.2271)	0.0591 (-0.496)
$ G_{YX} $	99.8476 (99.7954) (99.9005)*	211.4912 (220.0088) (209.3674)*	14.5427 (14.8326) (14.4695)*	0.2655 (-0.197) (+ 0.199)
r_{YX}^2	0.9056 (0.9055)	3.194E-04	0.0179	3.268E-04 (-0.306)
1H_R	4.5415 (5.0)	0.0218	0.1477	2.697E-03 (+ 170.6)
1H_I	0.0105 (0.010)	0.0220	0.1482	2.706E-03 (-0.185)
$ {}^1H $	4.5439 (5.00001)	0.0218 (0.0215)	0.1477 (0.1468)	2.697E-03 (+ 169.1)
cH_R	4.9969 (5.0)	0.0293	0.1711	3.124E-03 (+ 0.992)
cH_I	0.0140 (0.01)	0.0301	0.1734	3.166E-03 (-1.263)
$ {}^cH $	4.9999 (5.00001) (5.0025)*	0.0294 (0.0292)*	0.1713 (0.1710)*	3.128E-03 (+ 0.035) (+ 0.831)
2H_R	5.0160 (5.000)	0.0264	0.1625	2.967E-03 (-5.392)
2H_I	0.0117 (0.010)	0.0269	0.1640	2.994E-03 (-0.568)
$ {}^2H $	5.0187 (5.00001)	0.0264	0.1626	2.969E-03 (-6.298)

* - Quantities found by numerical integration method
See example in text for explanation of comparison values in parentheses

Table 6. Simulation Data Set F

Estimated Quantity	3000 Measurements		50 Samples per Measurement	
	Mean	Variance	Std Dev	SD of Mean
G_{rs}	17.9711 (18)	6.6228 (6.4592)	2.5735 (2.5415)	0.0470 (+0.615)
G_{xx}	21.9754 (22)	9.7522 (9.6584)	3.1229 (3.1078)	0.0570 (+0.432)
G_{yy}	324790.4 (325002.1)	2.121E+09 (2.110E+09)	46052.0 (45932.6)	840.79 (+0.252)
C_{xr}	17.9726 (18)	7.2516 (7.1794)	2.6929 (2.6794)	0.0492 (+0.557)
Q_{xr}	0.0102 (0)	0.6834 (0.7191)	0.8267 (0.8480)	0.0151 (-0.675)
$ G_{xr} $	17.9915 (17.9726) (17.9931)*	7.2546 (7.8984) (7.1631)*	2.6934 (2.8104) (2.6764)*	0.0492 (-0.384) (+0.033)
r_{xr}^2	0.8186 (0.8182)	1.067E-03	0.0327	5.970E-04 (-0.670)
C_{yr}	2246.45 (2250)	107759.9 (106784.1)	328.268 (326.778)	5.9933 (+0.592)
Q_{yr}	452.743 (450)	10458.9 (9952.7)	102.269 (99.763)	1.8672 (-1.469)
$ G_{yr} $	2292.90 (2291.62) (2292.93)*	112351.1 (116736.8) (110755.1)*	335.188 (341.668) (332.779)*	6.1197 (-0.209) (+0.005)
r_{yr}^2	0.9000 (0.9000)	3.552E-04	0.0188	3.432E-04 (0.0)
C_{yx}	2496.99 (2500)	131810.5 (131203.5)	363.057 (362.220)	6.6285 (+0.454)
Q_{yx}	501.990 (500)	11389.99 (11544.51)	106.724 (107.445)	1.9485 (-1.021)
$ G_{yx} $	2548.17 (2546.95) (2548.25)*	136973.8 (142748.0) (136101.0)*	370.099 (377.820) (368.919)*	6.7571 (-0.181) (+0.012)
r_{yx}^2	0.9090 (0.9091)	2.976E-04	0.0173	3.159E-04 (+0.317)
1H_R	113.630 (125)	13.3624	3.6555	0.0667 (+170.5)
1H_I	22.843 (25)	13.1787	3.6303	0.0663 (+32.54)
$ {}^1H $	115.960 (127.476)	13.4245 (13.4615)	3.6639 (3.6690)	0.0669 (+172.1)
cH_R	125.014 (125)	18.0410	4.2475	0.0775 (-0.181)
cH_I	25.1200 (25)	18.2014	4.2663	0.0779 (-1.540)
$ {}^cH $	127.583 (127.476) (127.652)*	18.1984 (18.2955)*	4.2660 (4.2773)*	0.0779 (-1.374) (+0.886)
2H_R	125.0248 (125)	16.2487	4.0310	0.0736 (-0.337)
2H_I	25.1332 (25)	15.9983	3.9998	0.0730 (-1.825)
$ {}^2H $	127.588 (127.476)	16.3437	4.0427	0.0738 (-1.518)

* - Quantities found by numerical integration method
See example in text for explanation of comparison values in parentheses

plex magnitude bias discussed in Chapter 3. Discussion of each set of calculations (auto spectra, cross spectra, etc) will be given along with the example calculations.

All six sets of data had the same input values

$$\begin{aligned}\sigma_S &= 3.0 \\ \sigma_K &= \sigma_M = \sigma_N = 1.0 \\ \Gamma(f) &= 1.0 - j0.0\end{aligned}$$

which, from Eq. 5.1, lead to the nominal input auto spectral values

$$\begin{aligned}G_{SS} &= 18.0 \\ G_{kk} &= G_{mm} = G_{nn} = 2.0\end{aligned}$$

All runs consisted of $p = 3000$ measurements, where each measurement was based on an average of $n_d = 50$ except for Table 4 (data set D), where $n_d = 100$. The variable parameter used in these runs was the 'true' FRF, $H(f)$. Values were chosen to represent measurements from anti-resonance to resonance, with varying phase angles.

The first column of the tables lists the simulated measured quantities. The second column shows the mean of 3000 measurements, while the third and fourth columns show the variance and standard deviation, respectively, of the 3000 measurements. The fifth column shows the standard deviation of the mean, which is found by

$$\text{standard deviation of mean} = \sqrt{\frac{\text{measurement variance}}{\# \text{ of measurements}}} \quad (6.1)$$

A note on statistical tests: A statistical test generally begins with the designation of a 'null hypothesis', H_0 , and includes an alternate hypothesis, H_a [27]. A 'test statistic' and 're-

jection region' are also decided upon. The most convincing results arise when we have strong evidence to reject the null hypothesis in favor of the alternate hypothesis. An example will clarify.

For our example test we wish to prove that a random sample x did not come from a Normal population of mean μ_0 and variance σ^2 . We begin with the null hypothesis that x did indeed come from this population, and then attempt to reject this hypothesis. Our test statistic in this case is the standardized Normal variable z given by

$$z = \frac{x - \mu_0}{\sigma} \quad (6.2)$$

From tables of the standard Normal variable, we find that 95.4 percent of values for our null hypothesis distribution will fall within the range of $\mu_0 - 2\sigma$ to $\mu_0 + 2\sigma$. If we reject the null hypothesis for values of x which are more than 2σ away from μ_0 (our 'rejection region') there is a probability of 0.046 that we will be wrong. This value is our 'level of significance', α . It is much more difficult to prove that a value *did* come from a given population. The only result that can be shown here is that the values are 'not significantly different'.

In the example above it was assumed that the value of σ was known. If σ is not known for a population of values, then the estimated value S_x (Eq. 5.2) must be used, and the appropriate test statistic is the 'Student t' distribution. The difference between the two distributions is large when the number of samples used to measure S_x is small, and the distributions converge as the number of samples becomes large. At 50 samples the errors of using the Normal distribution (instead of the 't' distribution) are small, and become nearly insignificant for over 100 samples.

We now state some approximations which will be used throughout the following evaluations.

1. The Normal distribution will be used. In the Monte Carlo simulations there are 3000 samples upon which to base S_x . We may assume approximate Normality for all of the means by the CLT, and with this many samples there is no discernible difference between the Normal and 't' distributions.

2. A level of significance of $\alpha = 0.05$ will be used in the tests. This corresponds to $|z| = 1.96$ (two-sided test). We will round this to 2.0 in the discussions that follow.

6.2.1 Auto Spectrum Calculations and Results

For each 'measurement', n_t raw values of the auto spectra, \tilde{G}_{xx} , \tilde{G}_{yy} , and \tilde{G}_{xy} were calculated using Eq 5.1 and averaged. The comparison values in parentheses below the simulation results in the second column are the expected values found by Eqs. 2.12 and 2.13. The comparison values in the fifth column is the difference in standard deviations between expected and measured' values. An example will illustrate.

Example 1: From Eq. 2.12

$$\begin{aligned} E[\hat{G}_{xx}] &= E[\tilde{G}_{xx}] = G_{xx}|\Gamma|^2 + G_{kk} + G_{mm} \\ &= (18)(1)^2 + 2 + 2 \\ &= 22 \end{aligned}$$

which is the same for all six sets of data and is shown in parentheses directly below the Monte Carlo 'measured' values. Using Table 3 data and Eq. 2.13

$$\begin{aligned}
E[\hat{G}_{yy}] &= E[\tilde{G}_{yy}] = |H|^2 \{G_{ss} |\Gamma|^2 + G_{kk}\} + G_{nn} \\
&= (0.05^2 + 0.01^2) \{(18)(1)^2 + 2\} + 2 \\
&= 2.052
\end{aligned}$$

Using Eqs. 2.32, 2.34, and 2.35 and the data from Table 3

$$\begin{aligned}
Var[\hat{G}_{xx}] &= \frac{G_{xx}^2}{n_d} \\
&= \frac{(22.0141)^2}{50} \\
&= 9.6924 = S_{\hat{G}_{xx}}^2 \\
S_{\hat{G}_{xx}} &= 3.1133
\end{aligned}$$

These values appear in parentheses below the Monte Carlo values in columns 3 and 4. Note that the 'measured' value of \hat{G}_{xx} was used in the variance calculation rather than the expected value calculated above, because this expected value would not normally be available when making variance estimates in a real life measurement situation.

The standard deviation in the fifth column indicates the spread of the estimate in the second column. For the data in Table 3

$$\begin{aligned}
\text{Std Dev of the Mean} &= \frac{\text{Std Dev of Measurements}}{\sqrt{\text{number of measurements}}} \\
&= \frac{3.1081}{\sqrt{3000}} = 0.0567
\end{aligned}$$

The comparison value in parentheses in the fifth column of each auto spectral data set shows the test statistic, z , found by taking the difference between the calculated expected value and the Monte Carlo value and normalized by dividing by the standard deviation of the mean

$$\begin{aligned}
z &= \frac{E[\hat{G}_{xx}] - \text{Mean of } \hat{G}_{xx}}{\text{Std Dev of Mean}} \\
&= \\
&= \frac{22.0000 - 22.0141}{0.0567} = -0.249
\end{aligned}$$

The magnitude of z is much less than the rejection criterion of 2.0, so we conclude that there are no significant statistical differences between the values. This concludes Example 1.

Auto Spectrum Simulation Summary: All of the predicted and simulated auto spectral values in the six data sets differ by less than two standard deviations. Therefore we may conclude that the simulation results 'do not disagree' with the expectations given by Eqs. 2.12 and 2.13.: Referring to the simulated and predicted variances in column 3 for all data sets, we see that these generally differ by 3 percent or less. This validates the auto spectral variance estimator of Eq 2.32 for raw samples (Table 1), and the variance reduction predicted by Eq. 2.34 (Tables 2 - 6).

6.2.2 Cross Spectrum Calculations and Results

Raw values of the cross spectra, \tilde{G}_{xy} , \tilde{G}_{yx} , and \tilde{G}_{xx} were calculated using Eq 2.3 and averaged to form estimates of \hat{C} , \hat{Q} , and $|\hat{G}|$ based on n_r raw samples. As before, 3000 of these estimates were averaged to obtain the values in column 2. The comparison values in parentheses below the *real and imaginary* parts are calculated using Eqs. 2.13. The cross spectral *magnitudes* have two rows of comparison values shown below them. The first row uses the assumptions and equations of [23,section 9.1.1] in calculating the expected value and variance of the magnitudes. The second row of comparison values

is calculated using the numerical integration method of Chapter 4. Those cross spectral magnitudes where these comparisons are significantly different (illustrating the magnitude bias effect) are marked with (###). Example calculations will illustrate.

Example 2: This example uses the calculations and results for G_{yr} of Table 3 (data set C). The expected values of the real and imaginary parts are found from Eqs. 2.13

$$\begin{aligned} E[\hat{C}_{ys}] &= E[\tilde{C}_{ys}] = G_{ss}\{Re(\Gamma H)\} \\ &= (18)\{Re[(1-j0)(0.05+j0.01)]\} = 0.900 \\ E[\hat{Q}_{ys}] &= E[\tilde{Q}_{ys}] = G_{ss}\{Im(\Gamma H)\} \\ &= (18)\{Im[(1-j0)(0.05+j0.01)]\} = 0.180 \end{aligned}$$

These expected values are shown in parentheses below the simulation results in the second column. Using the simulation values of C_{yr} , Q_{yr} and Eqs 2.31 we find estimates of the variance

$$\begin{aligned} Var[\hat{C}_{ys}] &= \frac{Var[\tilde{C}_{ys}]}{n_d} = \frac{G_{ss}G_{yy} + C_{ys}^2 - Q_{ys}^2}{2n_d} \\ &= \frac{(18.0216)(2.0545) + (0.8803)^2 - (0.1888)^2}{(2)(50)} = 0.3776 \\ Var[\hat{Q}_{ys}] &= \frac{Var[\tilde{Q}_{ys}]}{n_d} = \frac{G_{ss}G_{yy} + Q_{ys}^2 - C_{ys}^2}{2n_d} \\ &= \frac{(18.0216)(2.0545) + (0.1888)^2 - (0.8803)^2}{(2)(50)} = 0.3629 \end{aligned}$$

These values are shown in parentheses below the corresponding simulation result values in the third column, while the square roots of these are shown below the simulated values of standard deviation in the fourth column. The values in the fifth column are the simulation standard deviations of the fourth column divided by the square root of 3000.

The fifth column comparison values (in parentheses) for the real and imaginary parts of G_{yr} are the test statistic for comparing the simulation and expected values. This calculation is the same as that shown in Example 1.

The magnitude calculation of G_{yr} in Table 3 shows the magnitude bias effect. The first line of comparison values below the Monte Carlo results show the 'standard' method of calculating the magnitude and variance of the cross spectrum, given in Bendat [23, chapter 9]. Using the 'measured' estimates (mean values) of C_{yr} and Q_{yr} we would calculate the magnitude to be

$$\begin{aligned} |G_{ys}| &\cong \sqrt{\hat{\mu}_{C_{yr}}^2 + \hat{\mu}_{Q_{yr}}^2} \\ &\cong \sqrt{0.8803^2 + 0.1888^2} = 0.9003 \end{aligned}$$

From the fifth column, we see that the Monte Carlo result of 1.331 yields a test statistic of $z \cong -24$, indicating that the two values are clearly different. Using the method of Bendat [23, section 9.1.1] to calculate the variance

$$\begin{aligned} \text{Var}[|\hat{G}_{ys}|] &= \frac{G_{ss}G_{yy}}{n_d} \\ &= \frac{(18.0216)(2.0545)}{50} = 0.7405 \end{aligned}$$

Referring to either the comparison values in the table or the equations in Bendat we find that the variance of the magnitude is given as the sum of the variances of \hat{C}_{yr} and \hat{Q}_{yr} . Comparing the Monte Carlo variance, we see that it is *less than either* of these variances. As discussed in Chapter 3, the equations presented by Bendat are overestimates of variance.

The second line of comparison values, which are marked with an asterik (*), show the results of the numerical integration method discussed in Chapter 4. Referring to Eq. 3.30 we assign the values and variables

$$\begin{aligned}\mu_x &= \text{Mean of } \hat{C}_{ys} = 0.8803 \\ \mu_y &= \text{Mean of } \hat{Q}_{ys} = 0.1888 \\ \hat{C}_{ys} &\rightarrow x \\ \hat{Q}_{ys} &\rightarrow y \\ \text{Std Dev of } \hat{C}_{ys} &\rightarrow \sigma_x \text{ (Eqs. 2.31, 2.34 \& 2.35)} \\ \text{Std Dev of } \hat{Q}_{ys} &\rightarrow \sigma_y \text{ (Eqs. 2.31, 2.34 \& 2.35)} \\ \rho_{\hat{C}_{ys}\hat{Q}_{ys}} &\rightarrow \rho_{xy}\end{aligned}$$

The correlation coefficient is calculated from Eq. 2.39

$$\begin{aligned}\rho_{\hat{C}_{ys}\hat{Q}_{ys}} &= \frac{2\hat{C}_{ys}\hat{Q}_{ys}}{\sqrt{(\hat{G}_{ss}\hat{G}_{yy})^2 - (\hat{C}_{ys}^2 - \hat{Q}_{ys}^2)^2}} \\ &= \frac{2(0.8803)(0.1888)}{\sqrt{((18.0216)(2.0545))^2 - ((0.8803)^2 - (0.1888)^2)^2}} = 0.0090\end{aligned}$$

These values were used in the integration described in Section 4.2.1 to obtain the second row of comparison values. Comparing the expected magnitude from the numerical integration with the Monte Carlo result

$$\frac{1.1295 - 1.1331}{9.726E - 03} = -0.370$$

While the 'true' (based on system parameters) magnitude calculated above (0.9003) was nearly 24 standard deviations lower than the Monte Carlo result ($z \cong -24$), we see that the numerical integration magnitude prediction (which includes the magnitude bias ef-

fect) results in $z \cong -0.4$ when attempting to predict the Monte Carlo result. And comparing variances we see that the variance predicted by the numerical integration is within 3 percent of the Monte Carlo variance, while the method of Bendat predicts a variance that is 261 percent above. This concludes Example 2.

Cross Spectrum Simulation Summary: The Monte Carlo simulations verified the expectations for the real and imaginary parts of a cross spectrum given in Eqs. 2.13. In addition, the variance estimates given by Bendat [23] for the real and imaginary parts of the cross spectrum were confirmed. An example was discussed where the magnitude and variance of the cross spectrum differed significantly from the estimates used by Bendat, but were accurately predicted using the numerical integration method. It should be noted that the differences are not always as distinct as in Example 2. The magnitude bias tends to have more of an effect when the cross spectra tend to be relatively small, such as at anti-resonance, than they do with large signals. Referring to Tables 1 through 4 we find that the two estimates of the cross spectral magnitudes (for either $|\hat{G}_r|$ or $|\hat{G}_{xr}|$) show significant magnitude bias effects, while the estimates in Tables 5 and 6 are not significantly different. But most important, we find that the numerical integration method *always* does a better job of predicting the *variance* of the magnitude.

6.2.3 Coherence Calculations and Results

After each 'measurement', the ordinary coherences $\hat{\gamma}_{xx}^2$, $\hat{\gamma}_r^2$ and $\hat{\gamma}_{xr}^2$ were calculated by Eq. 2.14. The Monte Carlo results show the average, variance, and standard deviations of

these measurements. Only two comparison values are shown. One is the predicted value of the coherence calculated using one of Eqs. 2.15, and the other is the difference in standard deviations between the predicted value and the Monte Carlo result. Note that Table 1 does not show coherence values. Since this table consists of one sample record per measurement, all values of coherence are unity. Tables 2 through 4 show two comparison values for each Monte Carlo result, one of which includes a correction for a bias error inherent in coherence estimations.

This bias error is caused by having only a finite sample size in the estimation of the coherence via Eq. 2.14. Remember that the estimated coherence of a single measurement of even uncorrelated data is unity. This bias error also has a larger effect for small values of coherence. This bias error is derived by Carter [28] but may be found in Bendat [23,section 9.2.3] to be

$$b[\hat{\gamma}_{yx}^2] \cong \frac{1}{n_d}(1 - \hat{\gamma}_{yx}^2)^2 \quad (6.3)$$

These calculations are shown in an example.

Example 3: The estimate of $\hat{\gamma}_{ys}^2$ in Table 3 using Eq. 2.15b is computed as

$$\begin{aligned} \gamma_{ys}^2 &= \frac{G_{ss}|\Gamma H|^2}{\hat{G}_{ss}|\Gamma H|^2 + G_{kk}|H|^2 + G_{nn}} \\ &= \frac{(18)((0.05)^2 + (0.01)^2)}{(18)((0.05)^2 + (0.01)^2) + (2)((0.05)^2 + (0.01)^2) + (2)} = 0.023 \end{aligned}$$

which is the first comparison value shown beneath the Monte Carlo result in column two. From the first comparison value in column five we see that the Monte Carlo value

is over 30 standard deviations above the predicted value. However, let us now add the bias calculated by Eq. 6.3 (using the *predicted* value of the coherence)

$$0.023 + \text{bias} = 0.023 + \frac{1}{50}(1 - 0.023)^2 = 0.042$$

which is within a standard deviation of the Monte Carlo value. This ends Example 3.

Coherence Simulation Summary: Equations 2.15 accurately predict measured values of the coherence when the finite sample size bias error given by Eq. 6.3 has been added.

6.2.4 Frequency Response Function Calculations and Results

The Monte Carlo simulations gathered statistical data on three FRF estimators, \hat{H} , ${}^1\hat{H}$, and ${}^2\hat{H}$. Monte Carlo statistical estimates were gathered for the magnitudes and real and imaginary parts of each estimator. Below each value in parentheses is the true value of each quantity. When single sample measurements are made, all three FRF estimators find the same $|H(f)|$ values and have the same variance. All coherences are unity. This is consistent with the concept that the coherence function converges towards the true value from above. It is only through the process of averaging a number of sample records that the various FRF estimators converge to their respective values. Because Table 1 contains the results of simulated single sample measurements, only one set of estimated FRF values are shown.

The rest of this discussion will focus on the other five tables of data, which more realistically model a real measurement process. Comparison values of the complex *magnitude* variance are shown in the tables for $|\hat{H}|$ and $|\hat{H}|$. The magnitude variance of $|\hat{H}|$ was calculated using the numerical integration method of Chapter 4, while the magnitude variance of $|\hat{H}|$ was found using the relation given by [23, section 9.2.4]. No individual FRF real and imaginary component variance comparison calculations are shown, because none are known to exist. No variance comparison values are shown for the $|\hat{H}|$ estimator for the same reason.

6.2.4.1 Bias and Variance in the FRF Real and Imaginary Components

We begin with the real and imaginary parts of each of the FRF estimators. Except for Table 2 (Data set B) which simulates a zero $|H(f)|$ anti-resonance, we can see a definite low bias in the $|\hat{H}|$ estimator. Because the estimated value of $H(f)$ at anti-resonance cannot go below the 'true' value of zero, no $|\hat{H}|$ bias shows up in Table 2. Since all of the non-zero FRF data sets have $H(f)$ with a larger real than imaginary part, the $|\hat{H}(f)$ bias error shows more clearly on the real parts. From Tables 3 through 6 we see that this bias results in estimates of the real part which are from 10 to 170 standard deviations below the true value ($z \cong 10$ to 170) (Note that in column 5 these show as positive values, since the true value comparison is higher than the estimate). Remember that the simulations do not accurately model a real life measurement situation in all regions. For example, the bias error of $|\hat{H}(f)$ results from uncorrelated content in the measurement of the force, $X(f)$. While the uncorrelated content in the force measurement may be high at resonance, it is believed to be minimized at anti-resonance. These simulations only demonstrate that there is a bias error *if* there is uncorrelated content in the force measurement.

The ${}^2\hat{H}(f)$ estimator on the other hand shows a consistently high bias except near resonance. Although the response-measurement-uncorrelated-content auto spectrum is the same for all the simulations, its overall effect becomes smaller as the magnitude of the system FRF increases. The real and imaginary ${}^2\hat{H}$ estimates in Table 6 are slightly high, but this bias error is not statistically significant with z values of -0.4 and -1.8. As the size of the FRF goes down however, the bias increases to five standard deviations in Table 5 and 65 in Table 4. In Tables 2 and 3 there are *apparent decreases* in the bias error in the real and imaginary parts. Closer inspection reveals that the bias error is being 'lost' because the variance is becoming very large near anti-resonance. With the G_{yy} cross spectrum (which is approaching zero for small $|H(f)|$) in the denominator, ${}^2\hat{H}$ can become numerically unstable at anti-resonance. In Table 2 we see the variances of the real and imaginary parts of ${}^2\hat{H}$ are over 20, while the real and imaginary parts of ${}^1\hat{H}$ and ${}^0\hat{H}$ have variances on the order of 1×10^{-3} . It is this large variance which masks the bias error at anti-resonance.

Only ${}^0\hat{H}$ consistently finds unbiased estimates of the real and imaginary parts of $H(f)$. In Tables 2 through 6 every estimate is within two standard deviations of the true value ($|z| < 2.0$). This has come at the cost of a slight increase in variance however. In Tables 2 through 4 we find the component variance of ${}^0\hat{H}$ to be about 22 percent higher than for ${}^1\hat{H}$. In Tables 5 and 6 this increases to about 35 percent.

As we have already seen, the variance at anti-resonance is very large for the ${}^2\hat{H}$ estimator. The variance decreases however, as the FRF magnitude increases. In Tables 5 and 6 we see that for estimates of the real, imaginary, or magnitude of ${}^2\hat{H}$ the variance has fallen to between that of ${}^1\hat{H}$ and ${}^0\hat{H}$.

It was stated in Chapter 3 that the variance of the real and imaginary parts of the FRF estimators are equal. We can verify this by using a variance comparison test based on the F distribution. The test statistic is the ratio of the two sample variances being compared. For a two-sided test with $\alpha = 0.05$ and the 'degrees-of-freedom' for both the numerator and denominator being 2999, we find the acceptance region to be $0.9328 \leq \frac{S_{x_2}^2}{S_{x_1}^2} \leq 1.072$. Because the degrees-of-freedom are equal for both variances, we may choose to pick the larger of any two being compared for the numerator, thereby concerning ourselves with only the upper test value. The real and imaginary part variance ratios for ${}^c\hat{H}$ and ${}^1\hat{H}$ in Tables 2 through 6 range from 1.01 to 1.072. We conclude, therefore, that the variances of the real and imaginary parts of these estimators are not significantly different. The similarity of component variances also holds for ${}^2\hat{H}$ in regions away from anti-resonance, such as shown in Tables 5 and 6 where both test values are less than 1.02. (The similar variance test fails for ${}^2\hat{H}$ in the remaining tables).

The majority of F-statistic tabulations do not list values for large 'degrees-of-freedom' tests. The test values for the above test were found by an equation given in [29].

FRF real and imaginary part summary: The ${}^1\hat{H}$ calculation finds estimates of the real and imaginary parts of the system FRF which are biased low when there is uncorrelated content present in the force measurement. The ${}^2\hat{H}$ calculation results in high component estimates when there is uncorrelated content present in the response measurement. The ${}^c\hat{H}$ method finds unbiased component estimates with uncorrelated content present at either or both locations, but does so at the cost of slightly higher variance than ${}^1\hat{H}$. The variances of the real and imaginary parts of all of the FRF estimators may be considered equal, except for estimates made near anti-resonance with ${}^2\hat{H}$.

6.2.4.2 Bias and Variance in the FRF Magnitude Estimation

In Chapter 3 it was discussed that the degree of the magnitude bias error is partly a function of the variance of the real and imaginary components. If we could obtain zero variance component measurements, then we would have an exact and unbiased value for the magnitude. Reducing the variance of the component estimates not only reduces the variance of the magnitude estimate, but also reduces the bias error. With this in mind we return to Table 1. We see that although the single sample estimates of the real and imaginary parts are unbiased for the zero true value FRF, their variance is high and the estimated magnitude is 30 standard deviations high. The estimates of Table 2 are based on 50 sample records each. The variance and magnitude bias for all but ${}^1\hat{H}$ have been greatly reduced. When looking at the magnitude bias in these tables care should be taken to look at the numerical values of the magnitude and not the comparison value in standard deviations in the fifth column. The estimated magnitudes of the zero-true-value FRF from ${}^1\hat{H}$ and ${}^4\hat{H}$ have decreased by about ten-fold from Table 1 to Table 2. If we look at the bias in terms of standard deviations however, there appears to be an increase from a 30 standard deviation bias in Table 1 to a 100 standard deviation bias in Table 2. What has occurred is that the variance has decreased more rapidly than the bias error.

Tables 3 and 4 show simulated results of 50 and 100 sample measurements, respectively, of the same system FRF. From the CLT and Eq. 2.34 we would expect to the variance of the FRF estimates in Table 4 to be half that of the Table 3 variances. For the *real and imaginary parts* of ${}^1\hat{H}$ and ${}^4\hat{H}$ we find this confirmed to within a few percent. The variances of the *magnitude* do not appear to follow this trend, however, with reductions

of only about 40 percent for twice the number of samples. That is because the magnitude variance is a *function* of the component variances.

Because the 'special case' of Chapter 3 (equal variance but uncorrelated real and imaginary parts) applies to all of the FRF estimators (except \hat{H} near anti-resonance), we will pause and verify the bias and variance figures presented there.

Example 4: We will use the \hat{H} estimator data from Table 3 for finding the average variance for the real and imaginary parts

$$\text{average variance} = \frac{1.128E-03 + 1.202E-03}{2} = 1.165E-03$$

$$\sigma_{avg} = 0.0341$$

Using the 'true' magnitude of the FRF for $|Z|$ in Fig. 3

$$|Z| = |H| = \sqrt{0.05^2 + 0.01^2} = 0.0510$$

$$\frac{\sigma}{|Z|} = \frac{0.0341}{0.051} = 0.669$$

From Fig. 3 we find

$$\frac{\sigma_{|Z|}^2}{\sigma^2} \cong 0.73$$

Using the average component variance we can predict the magnitude variance as

$$(1.165E-03)(0.73) = 8.504E-04$$

which is within two percent of the Monte Carlo value of 8.373E-04. Figures 5 and 6 use the *expected biased* magnitude to find variance and bias. Using the Monte Carlo value as the expected magnitude we get

$$\frac{\sigma}{|\hat{Z}|_{\text{Exp}}} = \frac{0.0341}{0.0631} = 0.54$$

From Fig. 5 we find

$$\frac{\sigma_{|\hat{Z}|}}{\sigma} \cong 0.86$$

and from Fig. 6 we find

$$\frac{|Z|}{|\hat{Z}|_{\text{Exp}}} \cong 0.80$$

Using the average component standard deviation, σ_{avg} , we can predict the standard deviation of the magnitude

$$\sigma_{\text{magnitude}}(\text{predicted}) = (0.86)(0.0341) = 0.029$$

which is within one percent of the Monte Carlo value of 0.0289. We now predict the true magnitude from the Monte Carlo magnitude

$$|Z|(\text{predicted}) = (0.0631)(0.80) = 0.0505$$

where we find the predicted magnitude to be within one percent of the actual magnitude. Because in an FRF measurement we have currently only developed estimates for the magnitude variance, it is of little use to predict biases and variances using the component

variance. Figure 6 uses estimates of the magnitude standard deviation with the *expected biased* magnitude to correct for the magnitude bias.

$$\frac{\sigma_{|\hat{Z}|}}{|\hat{Z}|_{\text{Exp}}} = \frac{0.0289}{0.0631} = 0.46$$

which gives us, from Fig. 7

$$\frac{|Z|}{|\hat{Z}|_{\text{Exp}}} \cong 0.79$$

which is the same value which was just found from Fig. 6 This concludes Example 4.

Let us review. Besides the obvious verification of Figs. 3 through 7, we have seen that the variance reduction does not follow the relation shown in Eq. 2.34 (i.e., doubling the number of samples does not halve the variance of the magnitude). Now, Eq. 2.34 *does* apply to the real and imaginary parts of the FRF estimator, because the *expectations* of these estimates are the same whether we take one or many samples. Increasing the number of samples has no effect other than to reduce the variance of the estimate about the expectation. But when we consider the estimated *magnitude* of the FRF, we find that the *expectation of the magnitude changes with the number of samples averaged*. Since the variance is a function of expectation of the magnitude as well as the number of samples averaged, n_s , it becomes obvious that the change in variance cannot be described solely as a function of the number of averages.

Before continuing this discussion, a clarification on the application of the CLT is needed. According to the CLT, a sum of samples from *most* distributions tends toward a Normal distribution as the number of samples in the sum increases (an average is just a sum di-

vided by a constant). The variance of the sum is the variance of the samples divided by the number of samples in the sum. While the CLT cannot be used to justify Normality for averaged estimates of the magnitude, we find that for *most* cases the magnitudes follow a Normal distribution (we will see in the PDF discussion that this does not hold near anti-resonance). A difficulty arises in that the variance of the magnitude estimates (even with the assumption of Normality) do not follow the relation of Eq. 2.34. That is, if we know the variance of the magnitude for a given number of samples, and then double the number of samples, we do not necessarily find that the variance of the magnitude estimate has been halved.

We return to the discussion at hand. The situation we hope to achieve is that, given an FRF measurement and variance estimate based on n_s samples, we would be able to predict how many more samples would be needed to reduce the variance to a desired level. Because, as shown in Example 4, the magnitude variance reduction is not a readily defined function of the number of samples averaged (as it would be if the CLT variance assumption applied), we might expect some difficulty in this. However, for most ranges of interest it turns out not to be a problem. From Fig. 3 we find that when the true value of the FRF is greater than about five standard deviations of the component variance ($\frac{\sigma_{R,t}}{|Z|} \leq 0.2$), that the component and magnitude variances are nearly identical. Since the CLT does apply to the component variances when the FRF magnitude is larger than about 5 standard deviations (of either the magnitude or components), the components and magnitude have approximately the same variance, and the CLT variance reduction assumption does apply.

A general observation is that any time there is a magnitude bias effect (whether or not the 'special case' above applies), the magnitude variance may not follow the CLT as-

sumption. This effect can also be seen in the cross spectra G_{xx} and G_{yy} of Tables 3 and 4. The real and imaginary part variances are halved with double the averaged samples, while the magnitude variance reduction is substantially less.

We will now investigate the effect of the magnitude bias on the various FRF estimators. In Tables 1 - 4 we find that *all* of the estimated magnitudes are high, even the $|\hat{H}^1|$ estimate! This is, of course, contrary to the popular notion of $|\hat{H}^1|$ being a lower bound estimator. While the real and imaginary parts of \hat{H}^1 show a definite low bias in Tables 3 and 4, we see that the magnitude bias effect has produced magnitude estimates which are high. Because the other estimators produce magnitude estimates which are even higher, we find here that $|\hat{H}^1|$ is the best estimator near anti-resonance, even with uncorrelated content and magnitude bias affecting the estimate. This generalization may not hold for all cases. In this case the uncorrelated content causes the real and imaginary parts of $|\hat{H}^1|$ to be low, but this effect is opposed by the magnitude bias effect. Increasing the number of samples will decrease the magnitude bias effect, as will decreasing the uncorrelated content.

In Table 5 we find that the larger FRF has reduced the magnitude bias effect, and the inherent low bias of $|\hat{H}^1|$ shows in the magnitude as well as the real and the imaginary parts. $|\hat{H}^1|$ produces the best (and only unbiased) magnitude estimate, while $|\hat{H}^2|$ produces a high estimate. In the resonance simulation of Table 6 we find that $|\hat{H}^1|$ is decidedly low, while both $|\hat{H}^1|$ and $|\hat{H}^2|$ produce nearly identical estimates. Because the variance of $|\hat{H}^2|$ is slightly lower than that of $|\hat{H}^1|$, it might be considered the better estimator at resonance.

Summary of Bias and Variance in FRF Magnitude Estimation: The magnitude bias affect is largest near anti-resonance or anytime that the magnitude of an estimate is within about five standard deviations of that magnitude from zero. In this region the variance as a function of the number of samples averaged does not follow the CLT assumption. Figures 3 and 7 were compared with the Monte Carlo results for the FRF estimators and found to be in good agreement. The magnitude bias tended to cancel the low bias of $|\hat{H}^1|$ near anti-resonance and made this the preferred estimator in this region. $|\hat{H}^1|$ produces low-bias estimates any time that the magnitude bias is not strong (i.e., away from anti-resonance). $|\hat{H}^2|$ produces good estimates at resonance, and has a slightly lower variance than $|\hat{H}^1|$ in that region, but does very poorly at anti-resonance.

6.2.4.3 Estimates of FRF Variance

There is no current known estimator for the variance of $|\hat{H}^2|$, though Abom [22] makes some generalizations. $|\hat{H}^1|$ variance can be found using the methods of Chapter 4, as well as an estimate of the magnitude bias. An estimate of $|\hat{H}^1|$ variance can be found in [23, section 9.2] as

$$\text{Var}[|\hat{H}^1|] \cong \frac{(1 - \gamma_{yx}^2) |H|^2}{2\gamma_{yx}^2 n_d} \quad (6.4)$$

We begin with $|\hat{H}^1|$ variance, using the numerical integration method of Chapter 4. The variances for $|\hat{H}^1|$ are shown in Tables 2 through 6 below the Monte Carlo variances, and marked with (*). We find that the maximum difference between the Monte Carlo variances and the numerical integration estimate shown in Table 2 is less than 4 percent. We will find later in this chapter that the zero FRF of Table 2 causes $|G_r|$ not to be

Normally distributed. Although the numerical integration based variance estimation of $|\hat{H}|$ is based on the assumption of a Normal distribution for $|G_y|$, we find that it still gives good estimates of the variance *even when this assumption has been violated*. As the $|G_y|$ distribution becomes more Normal, we find the error to decrease even more. In Table 3 the numerical variance estimate is about 2.5 percent high, and less than 2 percent high in Table 4. In Tables 5 and 6 this error has dropped to less than 1 percent.

We will show some sample variance calculations with the $|\hat{H}|$ estimator of Eq. 6.4 to show an interesting effect.

Example 5: Using the data from Table 3, we will form two estimates of the variance using Eq. 6.4. The first estimate will use the 'true' (unbiased) values of $|\hat{H}|$ and γ_{yx}^2 . The second estimate will be made with the biased Monte Carlo results. For the first estimate

$$\begin{aligned} \text{Var}[|\hat{H}|] &\cong \frac{(1 - \gamma_{yx}^2)|H|^2}{2\gamma_{yx}^2 n_d} \\ &\cong \frac{(1 - 0.0230)(0.05^2 + 0.01^2)}{2(0.0230)(50)} = 1.104E - 03 \end{aligned}$$

which is 60 percent above the Monte Carlo value of 6.895E-04. Now we repeat this calculation with the *biased* estimates of the magnitude and coherence

$$\begin{aligned} \text{Var}[|\hat{H}|] &\cong \frac{(1 - 0.0414)(0.057)^2}{2(0.0414)(50)} \\ &\cong 7.523E - 04 \end{aligned}$$

which is less than 10 percent above the Monte Carlo variance. Because it was found that the 'biased' values of magnitude and coherence consistently gave better results in Eq.

6.4 than the 'true' values, the biased values were used to calculate the comparison $|\hat{H}|$ variances. This concludes Example 5.

Comparing variance estimates in the tables, we see that the $|\hat{H}|$ variance estimates have significant error in the anti-resonance region. In Table 2 (which models a zero FRF) we find the variance estimate to be over 60 percent above the Monte Carlo result. It is interesting to note that with a zero FRF the 'true' coherence is zero and Eq. 6.4 is indeterminate (0/0), leaving only the biased estimates that can produce a numerical solution. The variance estimate error drops rapidly away from anti-resonance, and is under 1.5 percent in Tables 4 - 6.

Some sample calculations using the variance estimate of Eq. 4.7 for the variance of $|\hat{H}|$ will now be made to illustrate the numerical difficulties with this method.

Example 6: Using the data of Table 5 we calculate the covariance using Eqs. 2.47 and 4.8

$$\begin{aligned} \text{Cov}(|G_{ys}|, |G_{xs}|) &\cong \frac{|G_{xs}| |G_{ys}| + G_{ss} |\hat{G}_{yx}|}{2n_d} \\ &\cong \frac{(17.9932)(89.8611) + (17.9767)(99.8476)}{2(50)} = 34.118 \end{aligned}$$

From Eq. 4.7

$$\begin{aligned} \text{Var}(|\hat{H}|) &\cong \frac{\text{Var}(|G_{ys}|) + |\hat{H}|^2 \text{Var}(|G_{xs}|) - 2|\hat{H}| \text{Cov}(|G_{ys}|, |G_{xs}|)}{|G_{xs}|^2} \\ &\cong \frac{172.7219 + (25)(7.2865) - 2(5)(34.118)}{(17.9932)^2} = 0.0423 \end{aligned}$$

which is over 40 percent above the Monte Carlo value of 0.0294. For illustration of computational sensitivity, we will arbitrarily increase the covariance estimate by 5 percent to 35.824

$$\text{Var}(|\hat{H}|) \cong \frac{172.7219 + (25)(7.2865) - 2(5)(35.824)}{(17.9932)^2} = -0.0104$$

where we see that this 5 percent change in covariance has taken us from a 40 percent high estimate to a *negative* estimate! Indeed, further calculations would show that only a 1.2 percent correction in the covariance would be needed to obtain the Monte Carlo result. Consider also that we used actual values of variance for the magnitudes of the cross spectra, and our 'measured' values of auto and cross spectra were based on $(n_d)(p) = 150,000$ samples. In an actual measurement we would not be able to get accurate estimates of the cross spectral variances without numerical integration. Moreover, the cross spectral magnitudes used in the covariance would have a lot higher variance than those estimates used in this example. This concludes Example 6.

Summary of FRF Variance Estimation: The numerical integration method of Chapter 4 gives very good estimates of the variance of $|\hat{H}|$, even at anti-resonance where some of the method assumptions are violated. The variance estimate given by [23] for $|\hat{H}|$ performs well away from anti-resonance regions, as long as biased estimates of the system FRF and coherence are used instead of the 'true' values. The computational instability of the closed-form $|\hat{H}|$ variance estimator of Eq. 4.7 was also shown.

Table 7. Uncorrelated Content Estimates

Nominal Values:		$G_{kk} = 2$	$G_{mm} = 2$	$G_m = 2$		
Quantity	B	C	Data Set		E	F
			D			
\hat{G}_{kk}	2.622	2.037	1.899	2.002	2.001	
\hat{G}_{mm}	1.380	1.970	2.098	2.003	2.003	
γ_{yx}^2	0.0203	0.0414	0.0330	0.9056	0.9090	
γ_{yz}^2	0.0205	0.0414	0.0329	0.8965	0.9000	
\hat{G}_m	2.003	2.004	2.001	1.940	38.76	
G_{yy}	2.003	2.055	2.054	500.6	324790	

6.2.5 Uncorrelated Content Estimates

The relations developed in Section 2.2.4 were used to find estimates of the uncorelated content. These are shown in Table 7. While the 'true' values of G_{kk} , G_{mm} , and G_m were not measured, we may use Eqs. 2.32 and 2.34 to find a probable range of values. Recalling that the mean values in Tables 2 through 6 are based on 3,000 sets of 50 or 100 samples, we use $n_d = (50)(3000) = 150,000$ in Eq. 2.34 for all but data set D where $n_d = (100)(3000) = 300,000$. We then find that 3σ confidence bands (99 percent probability) are within the range 1.98 to 2.02 for a nominal value of 2.

We find that the estimates \hat{G}_{kk} and \hat{G}_{mm} in Data Sets B through D fall outside of this range by varying degrees. Recall that the FRF's modeled by these Data Sets represent anti-resonance regions. From Eqs. 2.17 and 2.20 we see that these uncorrelated content estimates contain ratios of the coherences γ_{yx}^2 and γ_{yr}^2 . Reference to Tables 2 through 4 shows numerical values for these coherences in the range of 0.02 to 0.04. Because these values tend towards zero at anti-resonance, their ratio in the uncorrelated content estimates is approaching a (0/0) indeterminate form. This can cause large computational variations with small changes in either coherence estimate. We conclude, therefore, that the estimates of G_{kk} and G_{mm} do not do well at anti-resonance. On the other hand, these estimates are well within the 99 percent confidence range for Data Sets E and F where larger FRF's and, therefore, usually larger coherences are modeled.

The estimates of uncorrelated content in the response measurement (G_m) are found to be well within the range of expected values for Data Sets B through D, but are well outside of the range for Sets E and F. In fact, for Data Set F, we find an estimate of 38.76 for an anticipated value of 2! This apparently gross error becomes less so, de-

pending on the method of normalization. In terms of the 'true' value of G_m we are in error by nearly 2,000 percent. On the other hand, if we look at the error in terms of the size of the total response signal ($G_{yy} = 324,790$), we find that the error is on the order of 0.01 percent of the total signal. What we learn from this is that there is a limit as to how small a signal we may detect within 'computational noise'. Considering the large number of averages used in these estimates, it is probable that in a real-life measurement we will not be able to detect uncorrelated content accurately that is less than about one percent of the signal which contains it.

Each of the uncorrelated content estimators has computational problems in certain regions of an FRF. The G_{kk} and G_{mm} estimators do poorly at anti-resonance, while the G_m estimator has difficulty discriminating small signals at resonance. If, however, we consider the need for these estimates at various regions of the FRF, we find that these weaknesses are not severe limitations. At resonance we typically find the structure undergoing large amplitude oscillations. This can cause feedback into the force measurement and shaker amplification systems, causing the uncorrelated content terms at these locations to become large. But it is precisely in large response signal regions that these uncorrelated content estimators work well. Although the response measurement uncorrelated content estimator does not work well at resonance, we find that the large response signal tends to minimize the computational effects of uncorrelated content in the response signal. Its estimate is, therefore, not as important.

At anti-resonance we find the situation reversed. Because the response signal is very small, we find that output noise can dominate this signal. The structural undergoes only very small amplitude motion, minimizing the feedback effect in the force measurement and shaker amplification systems. This results in strong force measurement signals.

While the estimators of the uncorrelated content in the shaker system and force measurement are weak here, these noise values are typically low with respect to the force signal and of little concern. The dominant uncorrelated content term is that in the response measurement. We are able to obtain accurate estimates under these conditions.

We conclude, therefore, that although none of the uncorrelated content estimators works well at all regions of a FRF, they each work well in regions where that particular term dominates measurement errors.

6.3 Probability Density Function (PDF) Results From the Simulations

Certain quantities in the simulations were selected for investigation of the distribution functions. For the simulations of Tables 1 - 6 these quantities were the real parts, imaginary parts and magnitudes of \hat{G}_{yx} and \hat{H} . Each simulated measurement of these quantities was stored as a separate value. These values were then sorted into monotonic sequences for Normality testing and approximate PDF plots. Every test and plot discussed here based on $p = 3000$ individual measurements. The six tables already presented are labeled in terms of 'Data Sets A - F' and this designation will be used with the figures so that easy cross reference may be made.

The Kolmogorov ('D') and Kuiper ('V') empirical distribution function (EDF) statistics were used for Normalcy testing. Both are based on the same core calculations and are discussed by Stephens [30]. Because the results were the same with both statistics (ac-

cept or reject a given data set) only one will be used in the discussion. Some levels of significance for the 'D' statistic are: $\alpha_{0.15} = 0.775$; $\alpha_{0.10} = 0.819$; $\alpha_{0.05} = 0.895$; and $\alpha_{0.01} = 1.035$. As before, we will use $\alpha_{0.05}$. Then we accept as being Normal data sets whose 'D' values are less than 0.895 and reject Normality for those greater.

Before we investigate results, a check of the Gaussian random number generator is needed. Figure 9 shows the distribution of a set of 3000 generated values. The Normal distribution curve plotted over the histogram is based on the statistical estimates \bar{x} and S_x given by Eq. 5.2. The range of the abscissa for all plots is the range of values that are to be plotted. For this plot the generator was set to the standardized normal values of zero mean and unit variance. The sample mean for Fig. 9 is $-7.5E-03$ and the sample standard deviation is 1.0 (at 2 significant figures). The range of values of the 'D' statistic in nine separate tests of 3000 samples each was 0.44 to 0.71. These are all less than the critical value of 0.895, so we accept that the number generator is 'not significantly non-Normal'.

6.3.1 Cross Spectrum Probability Distributions

We begin with the \hat{G}_{yx} cross spectral distributions. The cross spectra used in the three-channel FRF estimation process are \hat{G}_{yx} and \hat{G}_{xy} , but the statistical behavior of all cross spectra is the same. The \hat{G}_{yx} cross spectrum is used in this discussion because it is the most familiar one in two-channel FRF estimations. The distributions of the real and imaginary cross spectrum parts for single sample measurements are shown in Figs. 10 and 11. We can see that the histogram distributions do not coincide with the Gaussian PDF. The 'D' statistics are 3.09 and 3.45, respectively, for the real and imaginary parts.

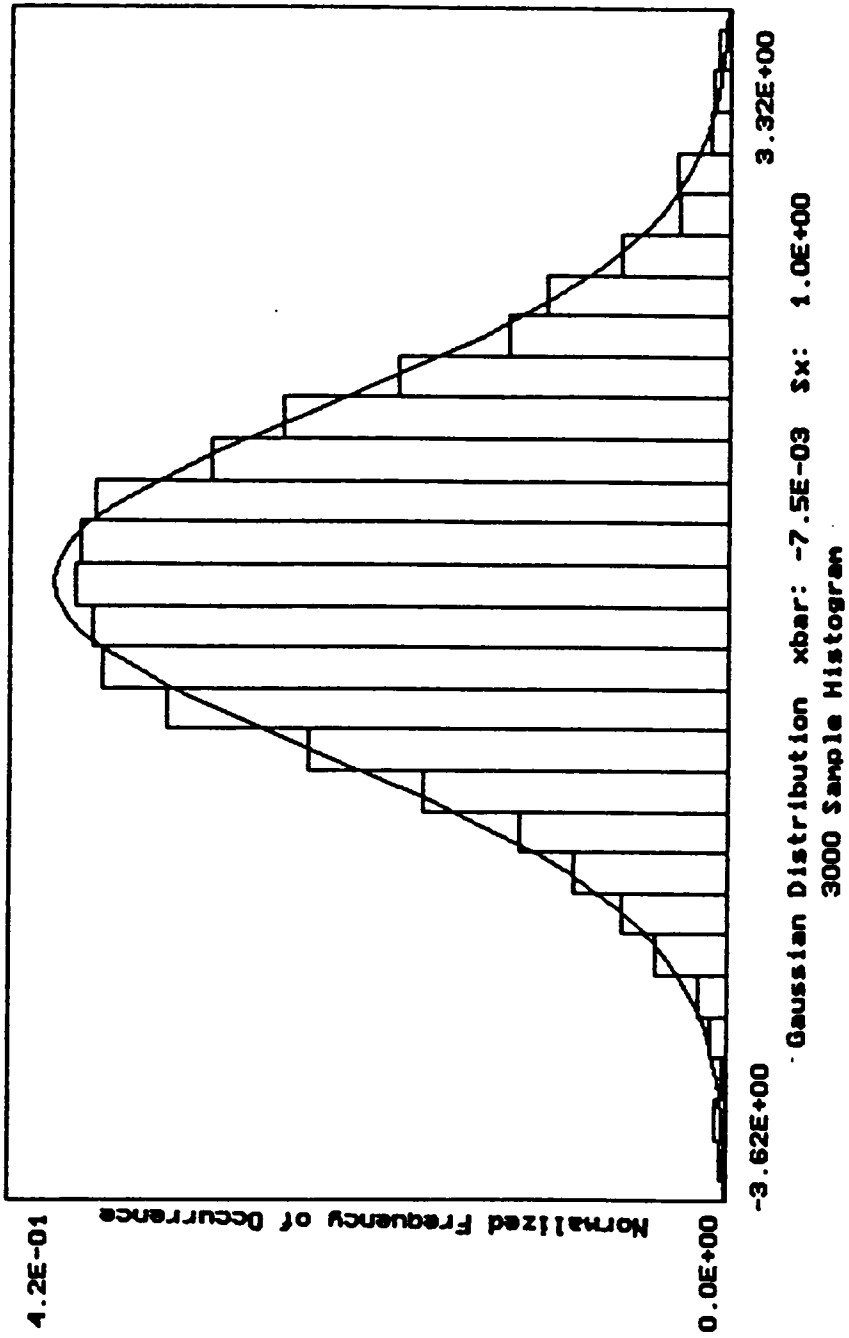


Figure 9. Gaussian Distribution Histogram

If the real and imaginary parts were Normal, the magnitude would follow the Rayleigh distribution, because the zero FRF of Data set A causes the real and imaginary parts to be zero mean. From Fig. 12 we see that no statistical test is needed to verify that the Rayleigh distribution does not describe the magnitude distribution.

Data set B is of particular interest because it models the example of the magnitude bias discussed in Section 3.1. We have the same zero value FRF of Data set A, but the measurements are each based on fifty raw samples. By the CLT we would expect that the real and imaginary part distributions are approaching Normality. We see in Figs. 13 and 14 that the histogram distributions follow the Gaussian function much more closely than was the case for Data set A. The 'D' statistic is 1.06 for the real part and 0.79 for the imaginary part. Thus we reject Normality for the real part and accept it for the imaginary part. This raises some questions. By the symmetry of an FRF with both real and imaginary parts being zero, we would expect both the distributions of the real and imaginary parts of the cross spectrum to be the same. And the CLT predicts (with large sample size) a Normal distribution. It appears, therefore, that $n_d = 50$ is a minimal criterion for the CLT Normality effect in a cross spectra.

Even though Normality has been rejected for the cross spectrum real part in this data set, the shape is close enough for purposes of illustrating the effect discussed in the Chapter 3 magnitude bias example. We take the average of the standard deviations of the real and imaginary parts (as discussed in Section 3.1, for this case they should be equal) for σ in Eq. 3.37 to plot the Rayleigh distribution function shown with the cross spectral magnitude data in Fig. 15. We see that even with the non-Normality of the real component the histogram PDF of the magnitude follows the general shape of the Rayleigh PDF function.

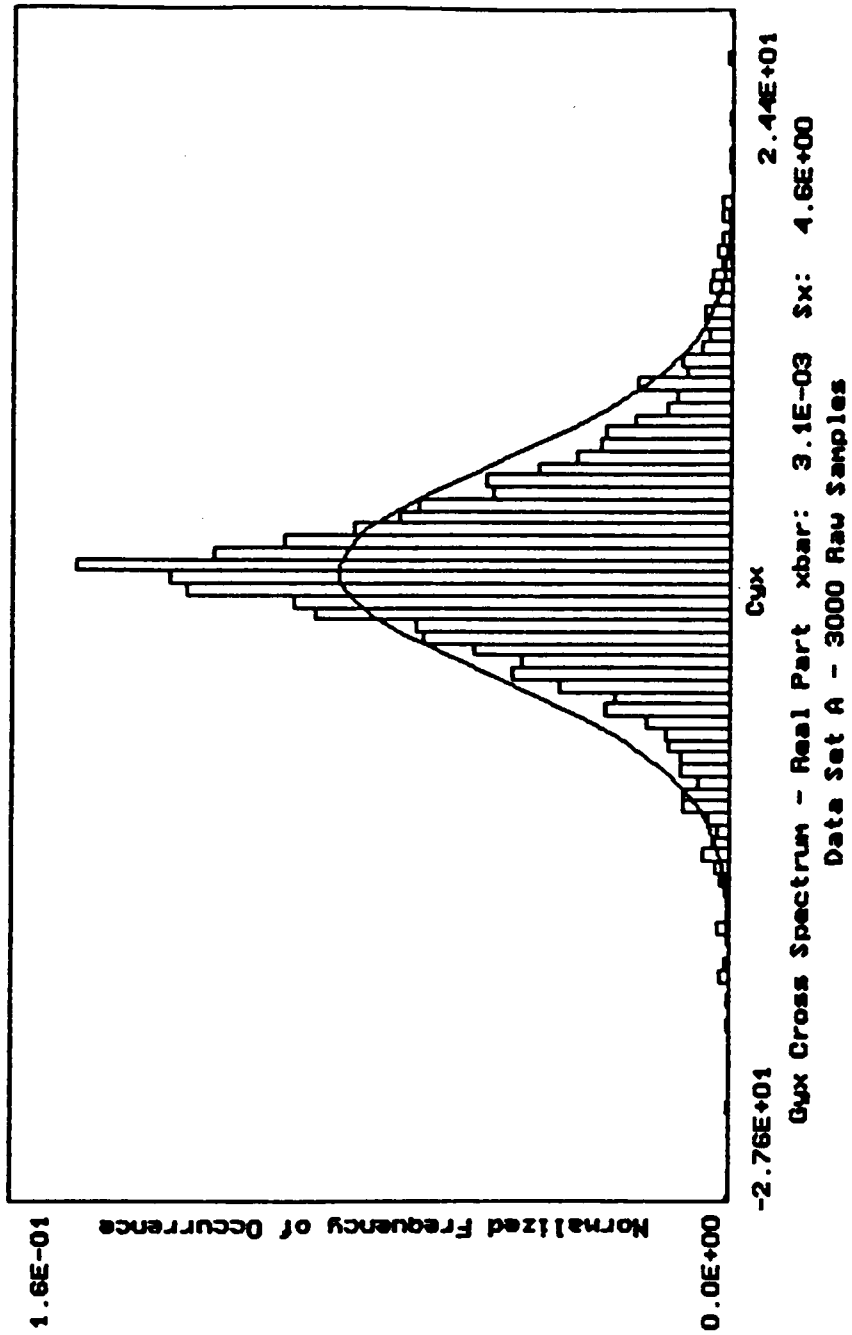


Figure 10. Histogram - Real Part of Data Set A Cross Spectrum

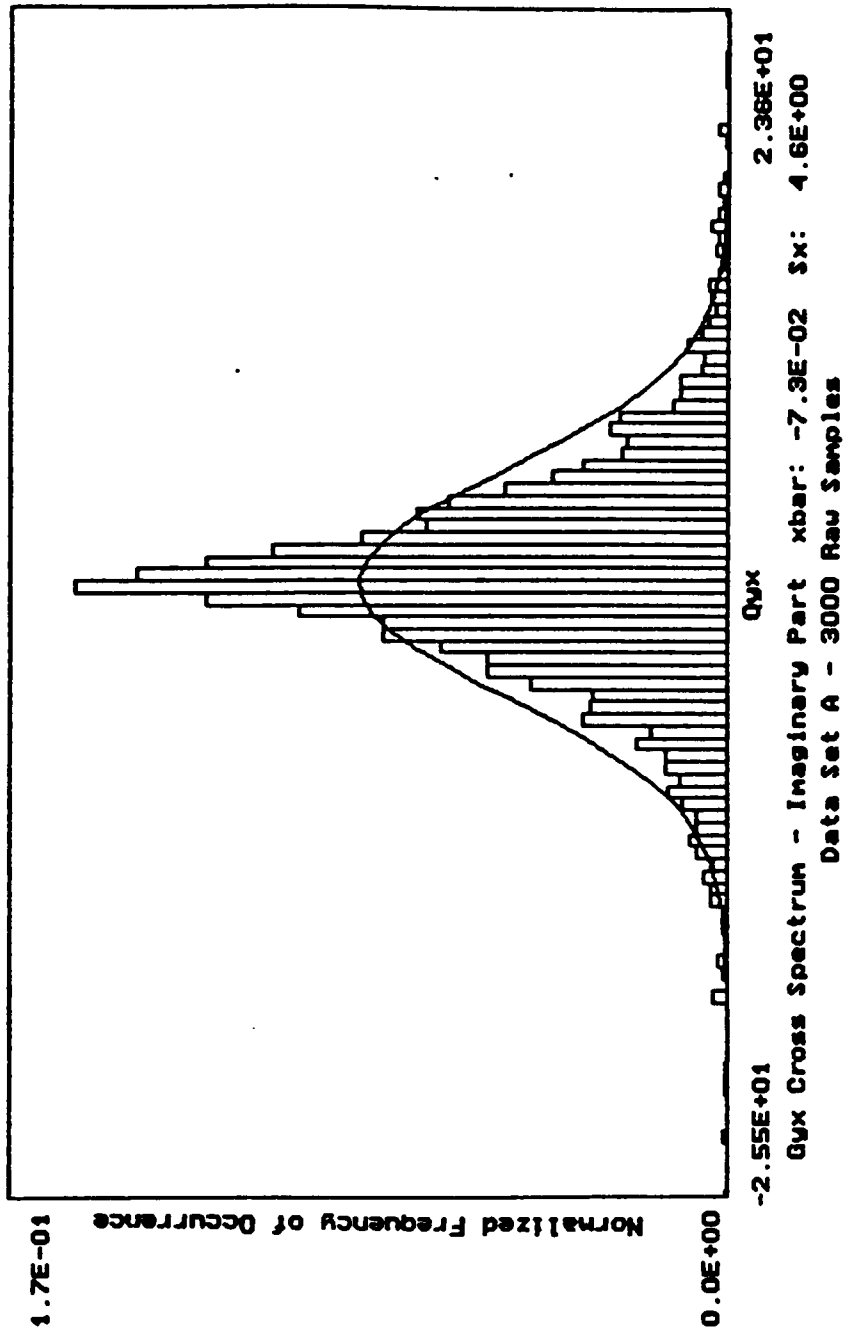


Figure 11. Histogram - Imaginary Part of Data Set A Cross Spectrum

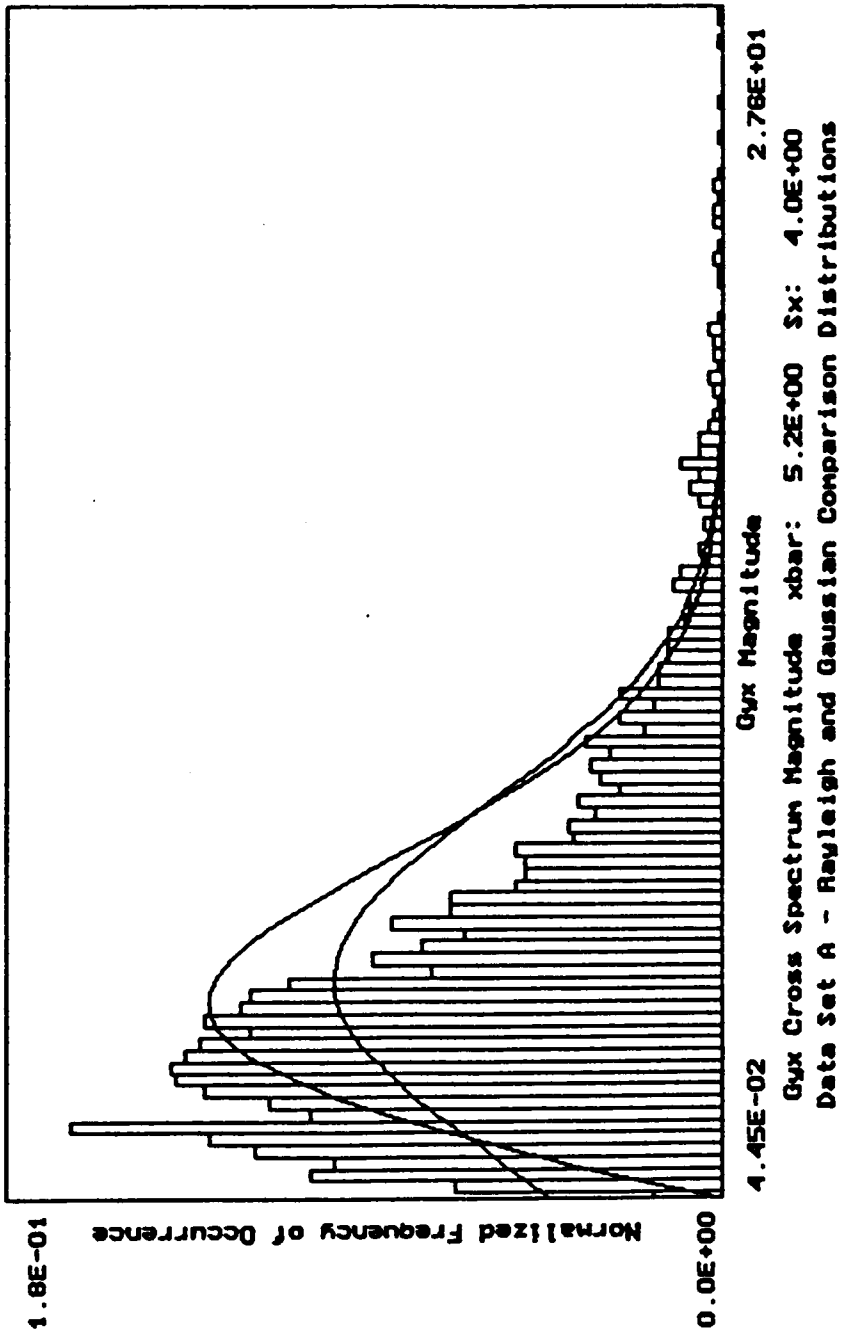


Figure 12. Histogram - Magnitude of Data Set A Cross Spectrum

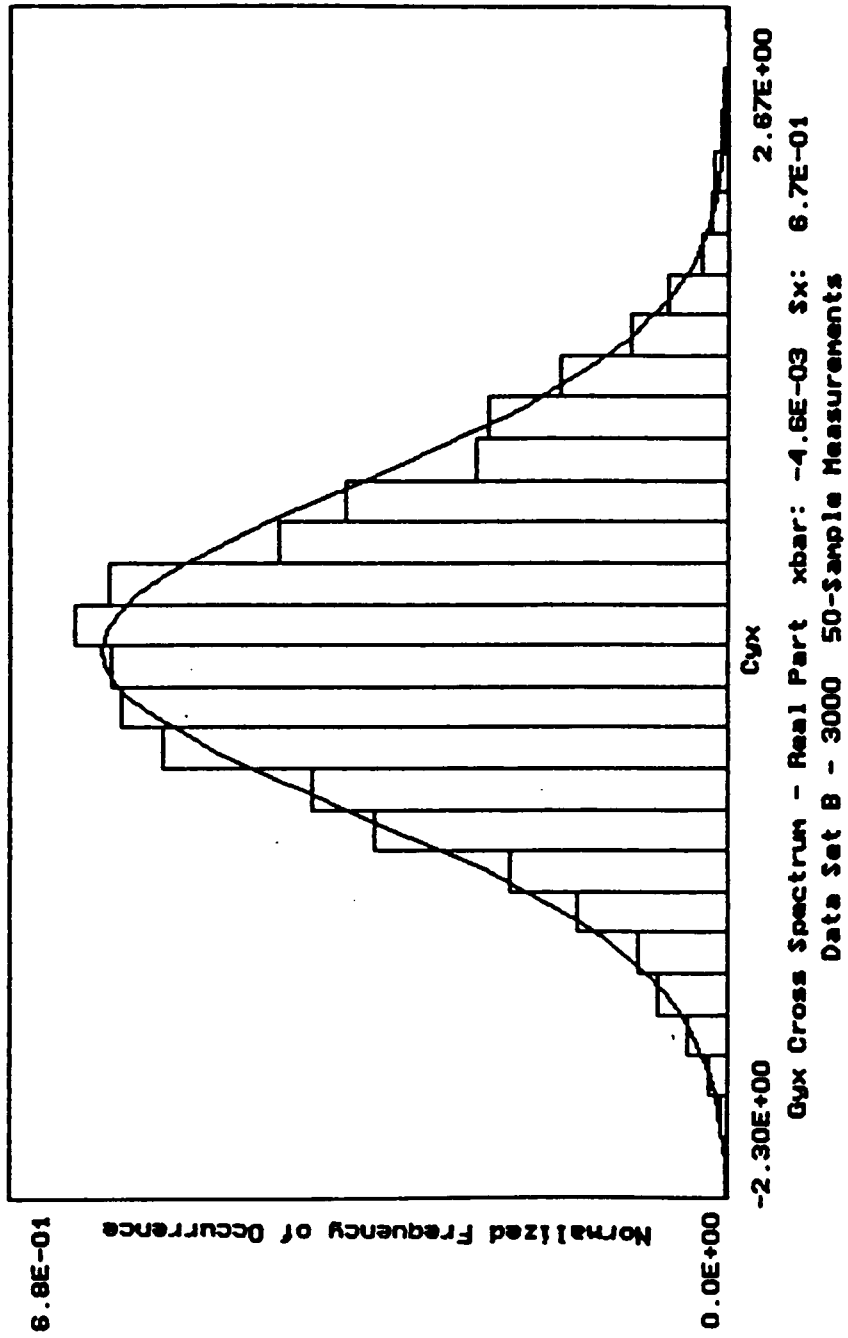


Figure 13. Histogram - Real Part of Data Set B Cross Spectrum

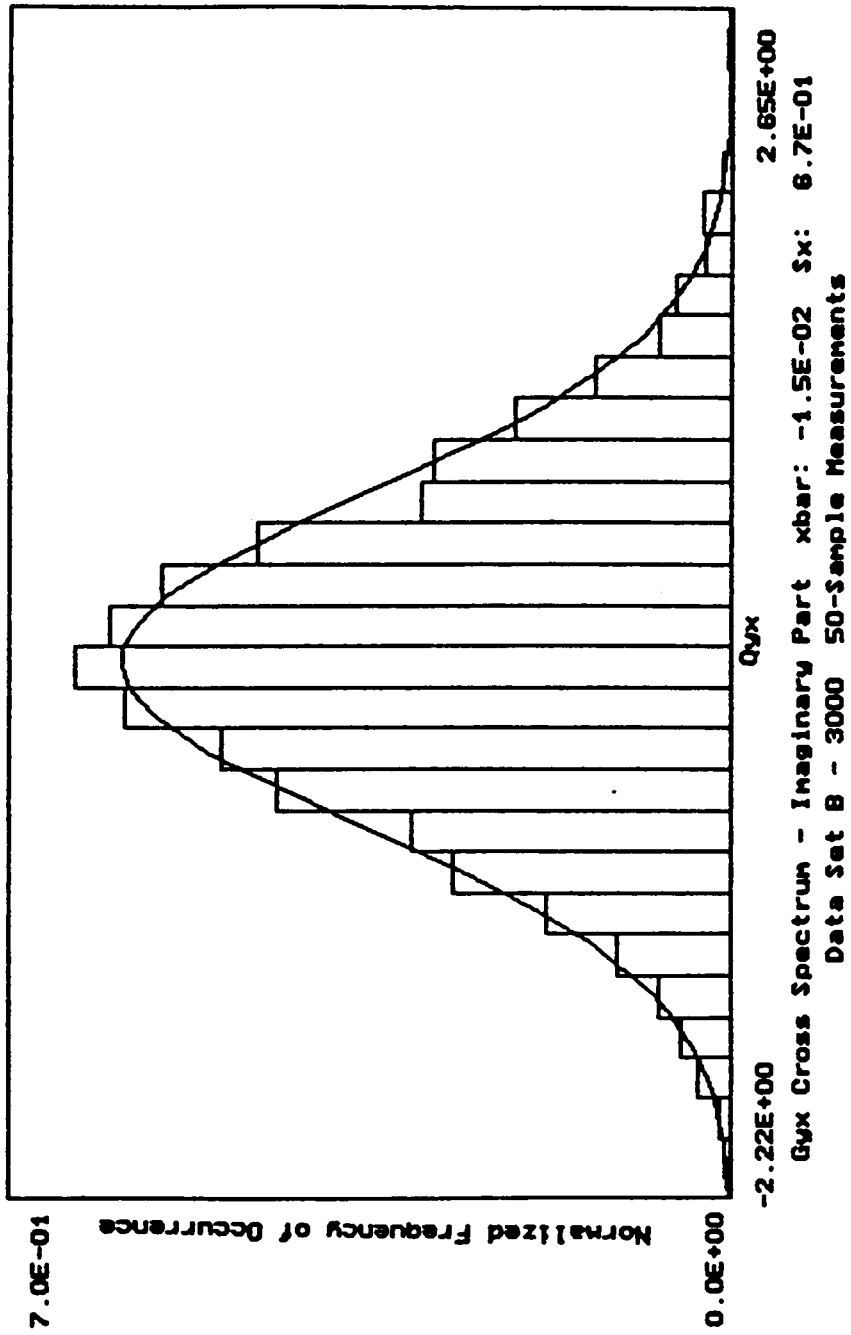


Figure 14. Histogram - Imaginary Part of Data Set B Cross Spectrum

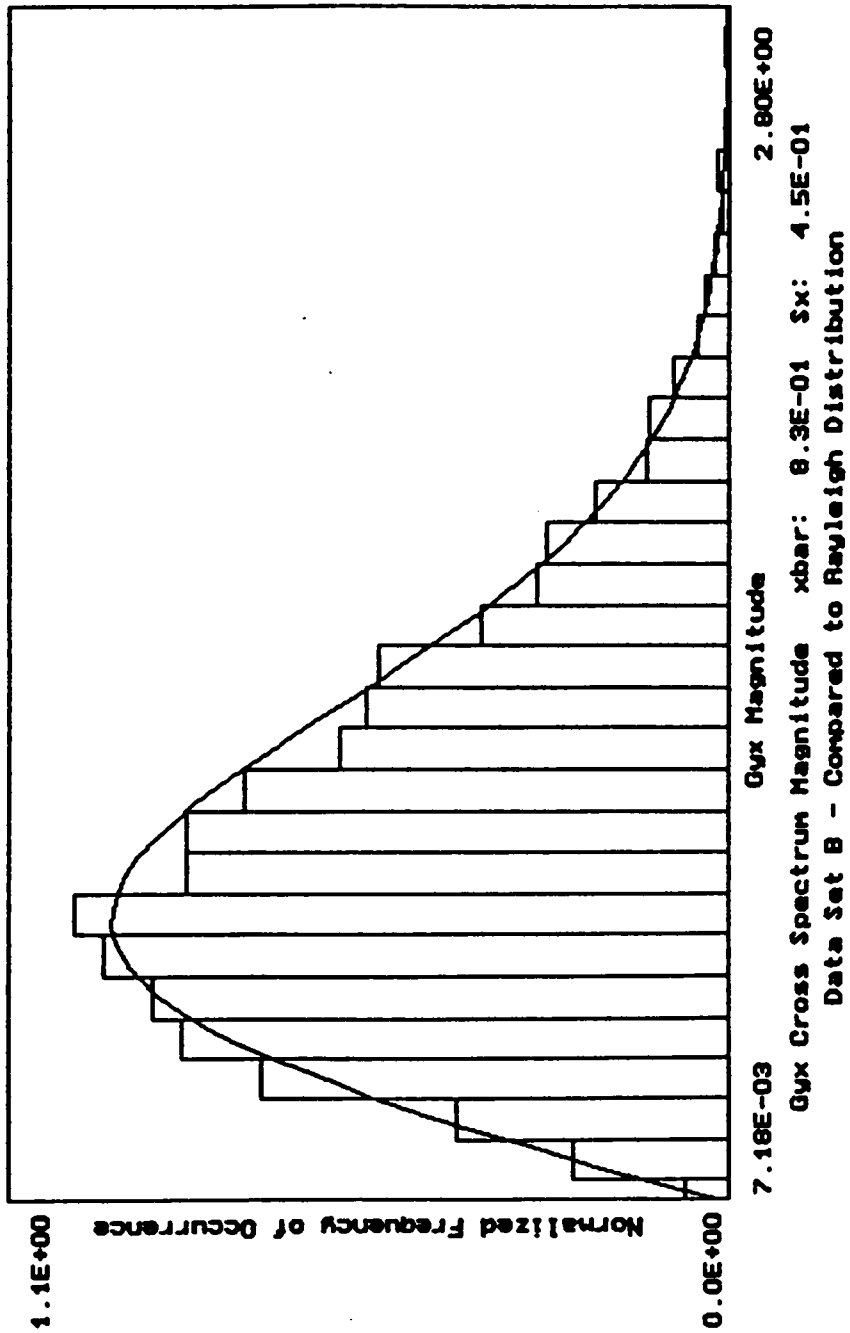


Figure 15. Histogram - Magnitude of Data Set B Cross Spectrum

The numerical variance estimation procedure uses the assumption of a Normal distribution for the cross spectral magnitudes. From Fig. 15 it is obvious that this particular magnitude distribution is not Normal ('D' = 3.45). Even though this is the distribution of $|G_{yx}|$ instead of $|G_{xy}|$, the trends should be the same. But if we compare variance results in Table 2, we find that the estimated and Monte Carlo variance differ by less than 4 percent. It appears that, *for variance estimates, Normality of the cross spectrum magnitude is not a strict requirement.*

In Data Sets C and D the 'D' statistic for the real and imaginary parts of the cross spectra ranged from 0.516 to 0.738, all within the acceptance range. For Data set E the real and imaginary 'D' values were 1.30 and 0.519, while for Data set F they were 1.45 and 1.47 respectively. All but one of these values is in the rejection region. To test for the CLT effect, another simulation run was made with the same parameters as Data set F, except that $n_d = 100$ was used instead of $n_d = 50$. The 'D' values dropped from 1.45 and 1.47 to 0.81 and 0.93 in this data set. Even though only one of these falls within the acceptance range, these 'D' values follow the CLT prediction that the distributions will become increasing Normal with large n_d . We therefore accept Normality for the real and imaginary parts for large sample sizes.

The distribution of the cross spectral magnitude is affected by the FRF. Starting with Data Set B parameters a small but finite value ($H(f) = 0.05 + j0.01$) is assigned to the FRF of Data set C. In Fig. 16 we see that the magnitude distribution has a more Normal appearance than in Fig. 15. The 'D' value has dropped from 3.45 to 1.93. For Data set D we increase n_d from 50 to 100 with no other changes. We see that the magnitude of the Data set D cross spectrum shown in Fig. 17 has become even more Normal. Our 'D' statistic has dropped to 0.79 and into the Normal acceptance region

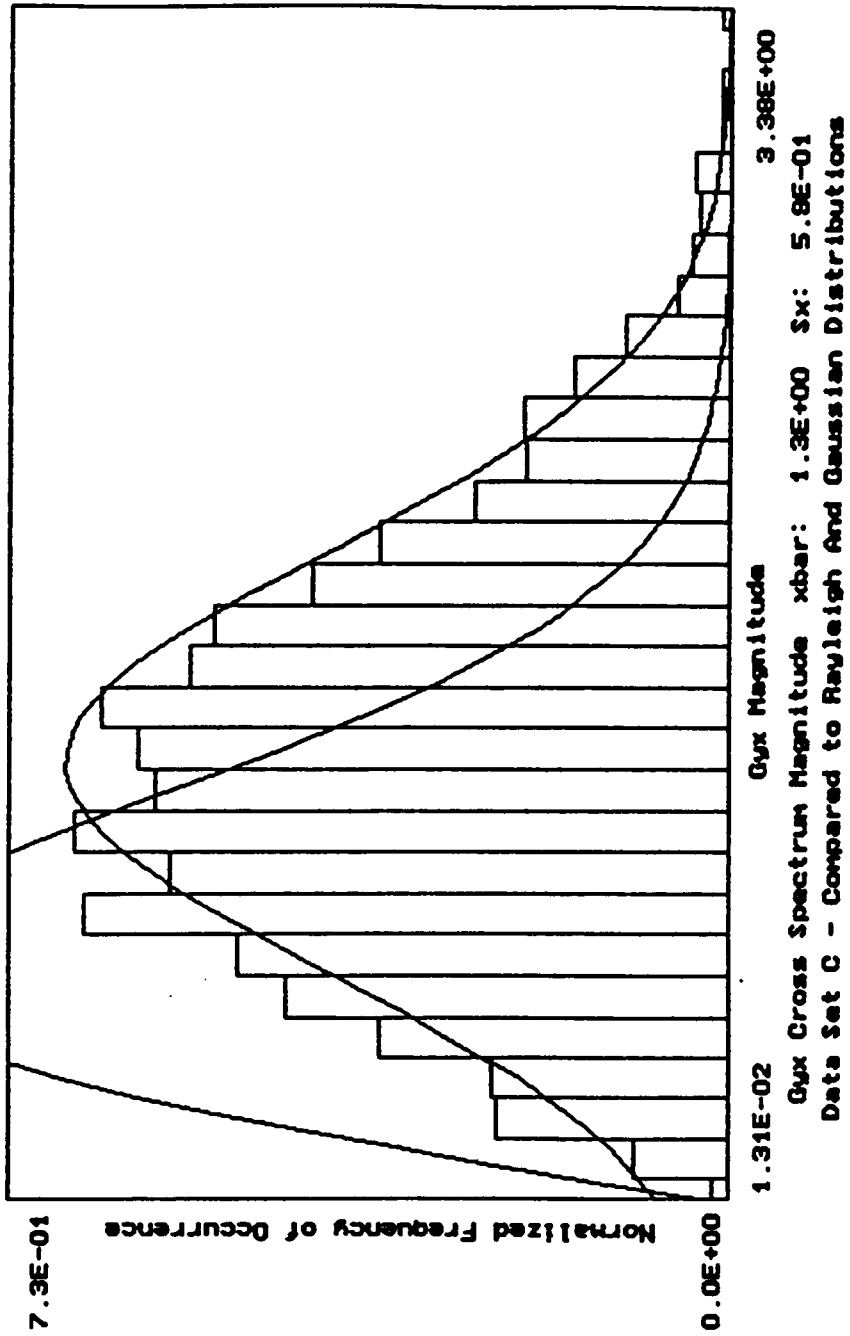


Figure 16. Histogram - Magnitude of Data Set C Cross Spectrum

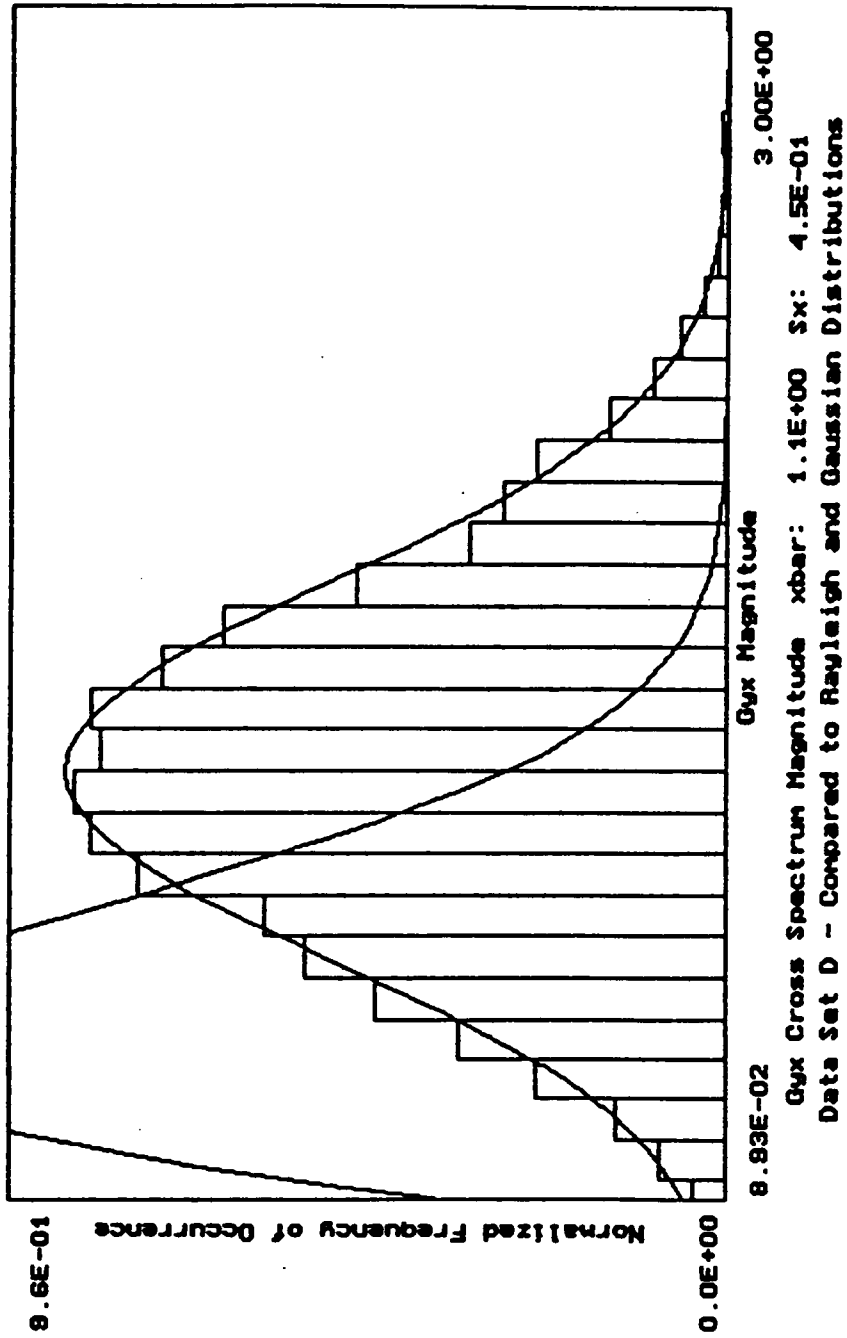


Figure 17. Histogram - Magnitude of Data Set D Cross Spectrum

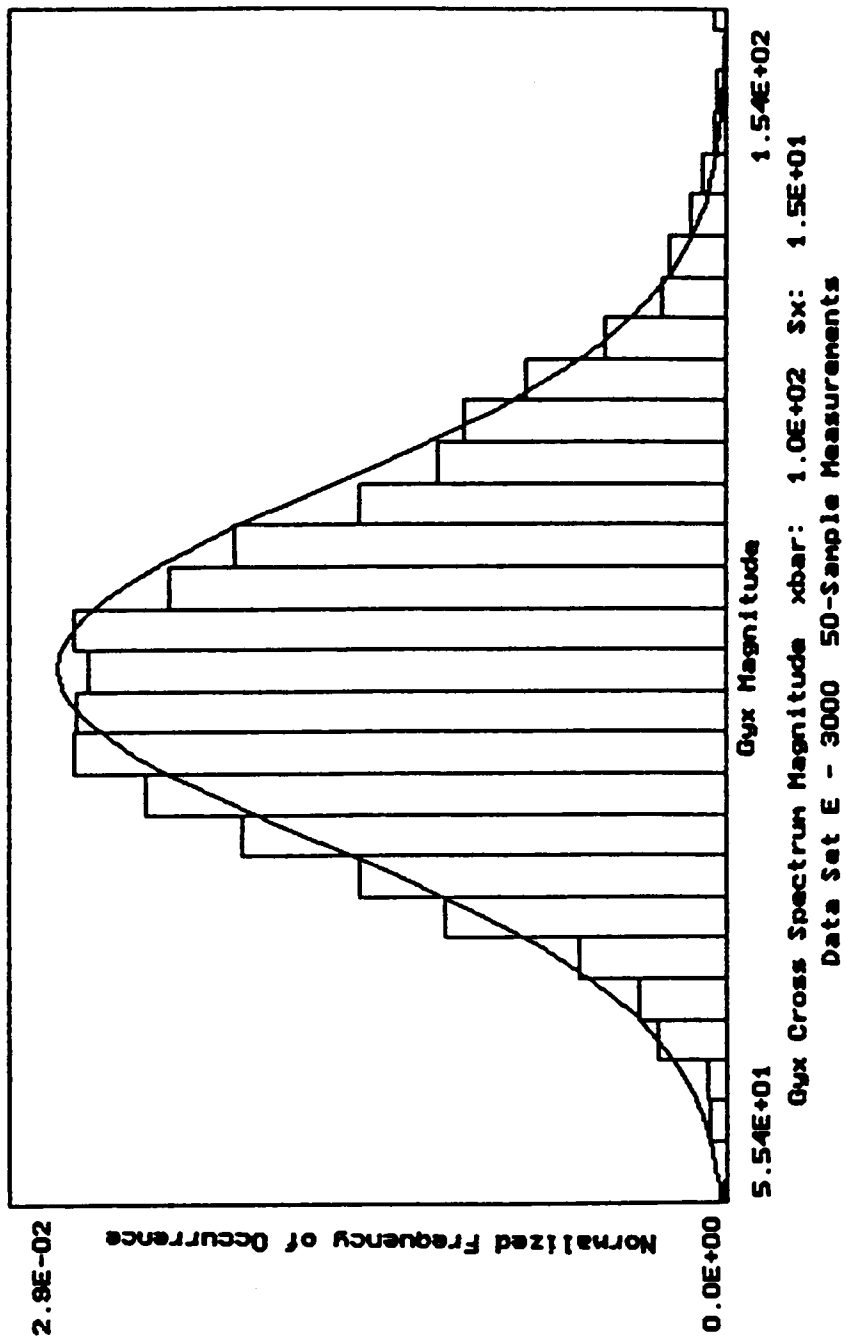


Figure 18. Histogram - Magnitude of Data Set E Cross Spectrum

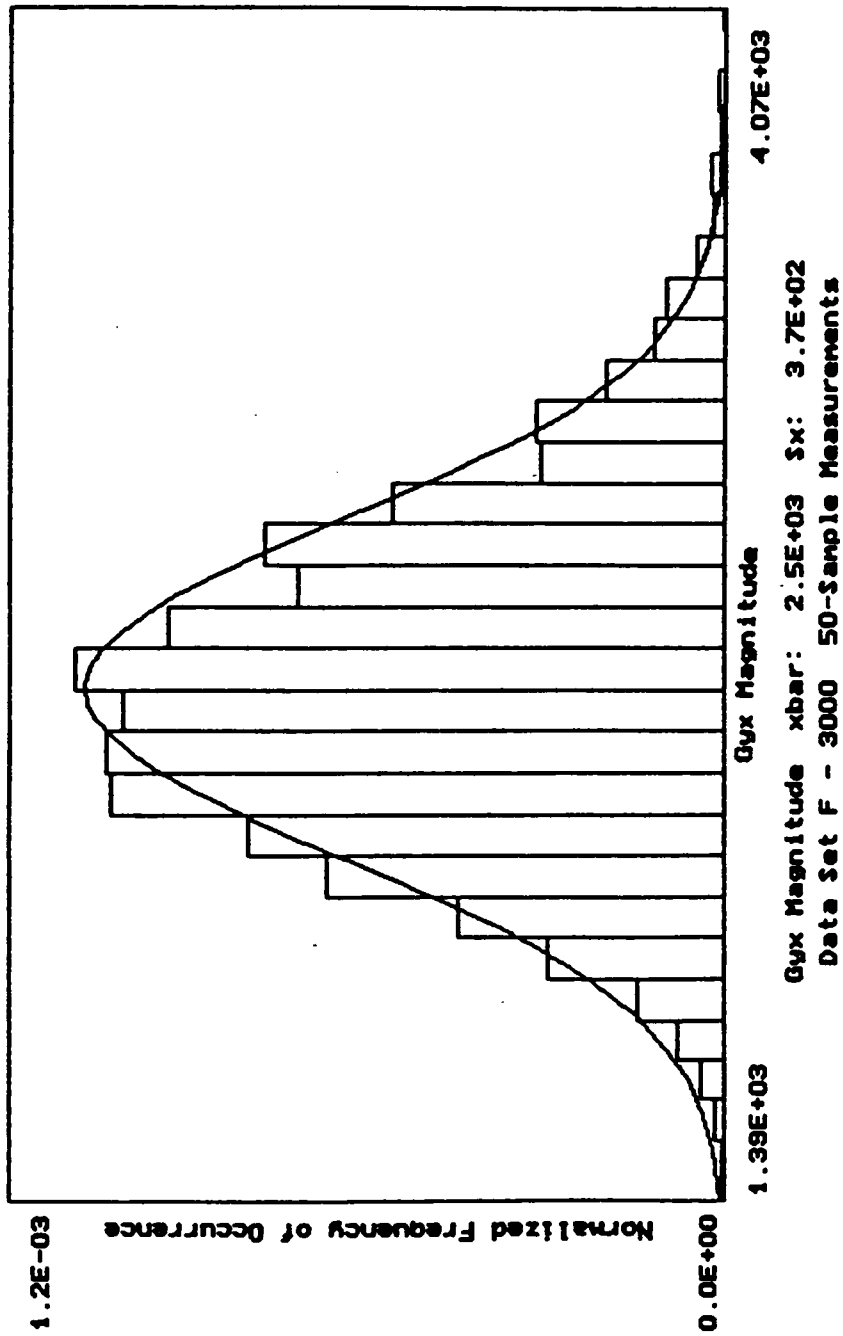


Figure 19. Histogram - Magnitude of Data Set F Cross Spectrum

(even though a small part of the left distribution 'tail' is clearly cut off). The decrease in variance with increase in the number of samples has the effect of moving the zero lower bound farther out along the 'tail' of the distribution. In Figs. 18 and 19 we find that the Normal distribution appears to be a reasonably good fit to the magnitude of the cross spectrum, though the 'D' statistics are 1.4 and 1.55, respectively. But with the second run of the F set data with $n_d = 100$, the 'D' value dropped to 0.72. We therefore accept Normality for the cross spectral magnitude under the condition of large n_d . It should be noted also, that even with Normality rejected for the cross spectral magnitudes of data sets E and F that the $|\hat{H}|$ variance predictions were within one percent of the Monte Carlo values.

We now make some generalizations about when we may assume Normality for the cross spectral magnitude. If we start with a large value of the FRF (as in Figs. 18 and 19), we find the distribution to be approximately Normal for large values of n_d (say, at least 100). If we then decrease the FRF magnitude with all else held constant, we see the distribution function slide along the abscissa towards the zero lower bound. The function remains approximately Normal until the zero lower bound is found to be within, say, 2 or 3 standard deviations from the distribution mean. Because no value of the magnitude can be below zero, the distribution becomes skewed. As the FRF approaches zero, the Normal distribution tends towards the Rayleigh distribution, which it becomes for a zero value FRF. No amount of averaging will change the distribution for a zero FRF. But in Figs. 16 and 17 we saw that increasing the number of samples averaged for a small FRF will tend to make the distribution more Normal. This happens because the reduced variance causes the tails of the distribution move closer together, and there is less skewing by the zero lower bound. Because the coherence function is a good relative measure of the magnitude of the cross spectrum (under the same restriction on n_d), it can

often indicate when the Normality assumption is appropriate. The coherences of Data sets C and D (Figs. 16 and 17) are around 0.03 - 0.04, and we saw that the distributions were starting to become approximately Normal, based on 50 to 100 samples per measurement. More samples would increase the Normality in this region, while fewer would decrease it. A conservative guideline might be that the cross spectrum magnitude could be considered to be approaching a Normal distribution whenever there is an ordinary coherence greater than 0.10 on a measurement of 100 or more samples.

Summary of Cross Spectrum Distributions: Raw samples of the real part, imaginary part, and magnitude of the cross spectrum are not Normally distributed. When measurements of the cross spectrum are based on an average of raw samples, the distributions of the real and imaginary parts will always tend towards Normality as the number of samples is increased. The cross spectrum magnitudes may be considered Normal for most regions of interest, with the number of samples averaged and the ordinary coherence being indicators. When the system FRF tends towards zero, the magnitude distribution function tends towards the Rayleigh distribution. Even for this limiting case, the assumption of Normality for the magnitude does not severely affect the numerical integration method of $|\hat{H}|$ variance estimation.

6.3.2 FRF Probability Distributions

Only the distributions for the \hat{H} estimator are shown and discussed here. It was found however, that the following discussion could be applied generally to the other FRF estimators with only one restriction. While the distribution functions for the $|\hat{H}|$ estimator

closely follow the trends discussed here for all values of $H(f)$, the distribution function of \hat{H} only follows these tendencies *so long as the system FRF is not close to zero*.

Figures 20 and 21 show the distribution of the real and imaginary parts of \hat{H} for single sample measurements with a zero system FRF. These are definitely not Normal. 'D' values are 9.6 and 10.6 respectively. The magnitude shown in Fig 22 is not modeled by either a Gaussian or Rayleigh distribution, with 'D' = 16.1. When the number of samples per measurement is increased to 50 as in Data set B, the real and imaginary part distributions tend towards Normality, with 'D' values of 0.89 and 0.76, respectively. An Example of this is seen in the distribution for the real part of the Data set B FRF shown in Fig. 23. Recall that these are only *functions* of variables to which the Central Limit Theorem applies. We cannot use the CLT to justify Normality of the real and imaginary parts of the FRF estimators. We see however, that Normality is a good approximation for Data set B. As with the cross spectrum of this data set, we would expect the Rayleigh distribution to apply to the magnitude, given that the real and imaginary parts are Normally distributed. While no test was made, we can see qualitatively from Fig. 24 that this is so.

The trends followed by the FRF estimators as the system FRF is increased are the same as for the cross spectrum. The real and imaginary parts tend towards Normality as the number of samples per measurement is increased, and the magnitude tends towards Normality so long as the tail of the Normal distribution does not meet the zero lower bound in a finite probability region. Figures 25 and 26 show the increase of Normality with increasing number of samples for a small magnitude FRF. The 'D' value for Fig. 25 data is 2.09 and drops to 0.79 for the distribution shown in Fig. 26. Figure 27 shows magnitude Normality for a larger magnitude FRF. The 'D' value for the distribution

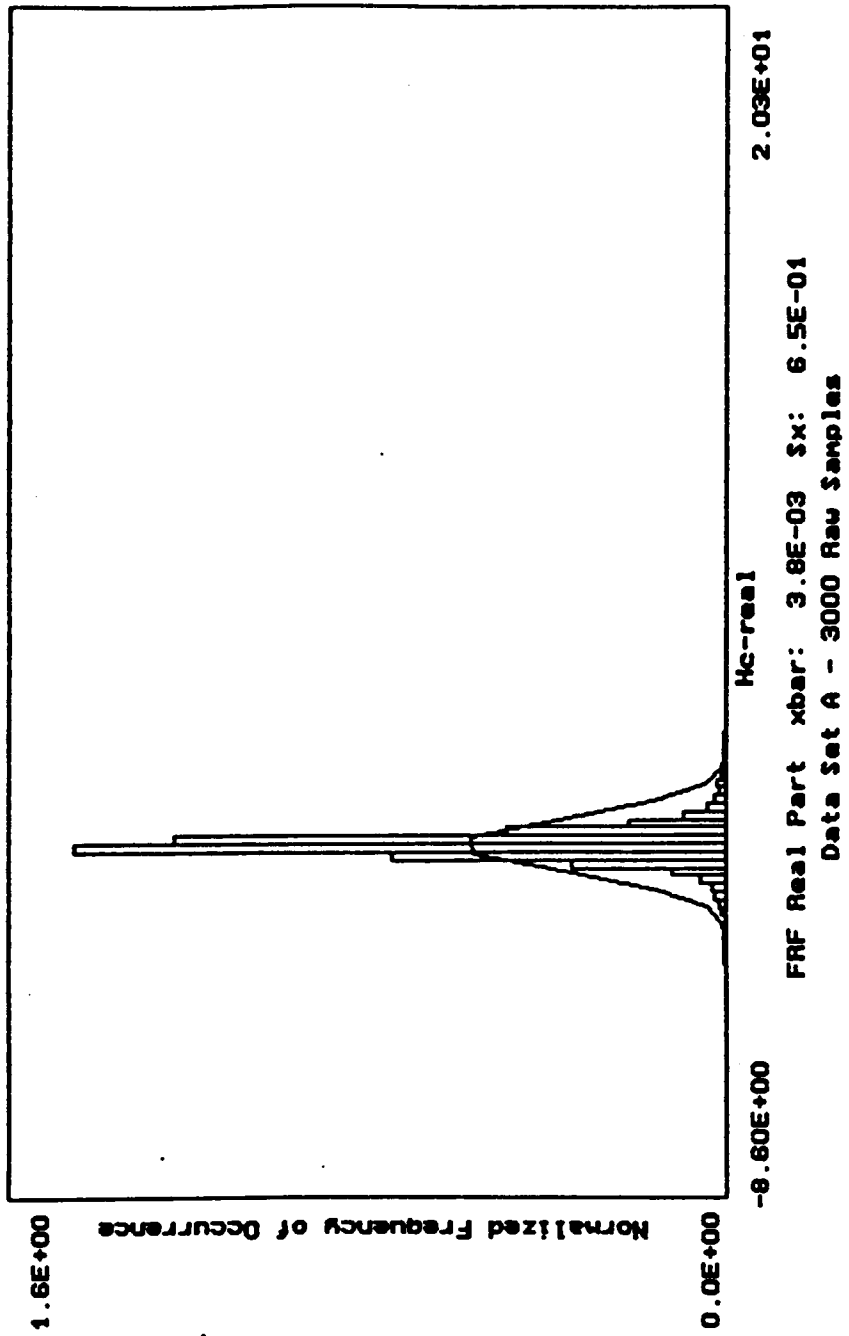


Figure 20. Histogram - Real Part of Data Set A FRF

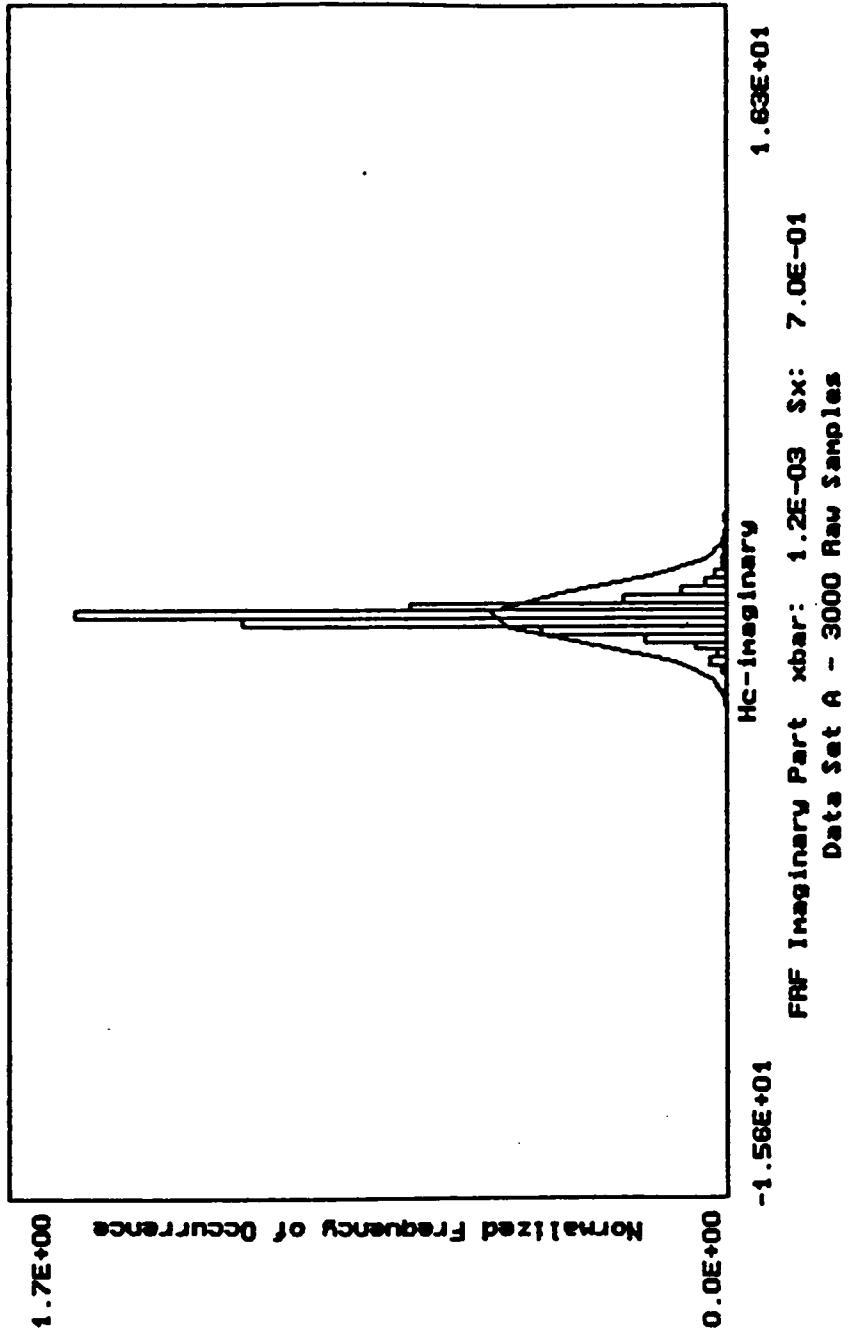


Figure 21. Histogram - Imaginary Part of Data Set A FRF

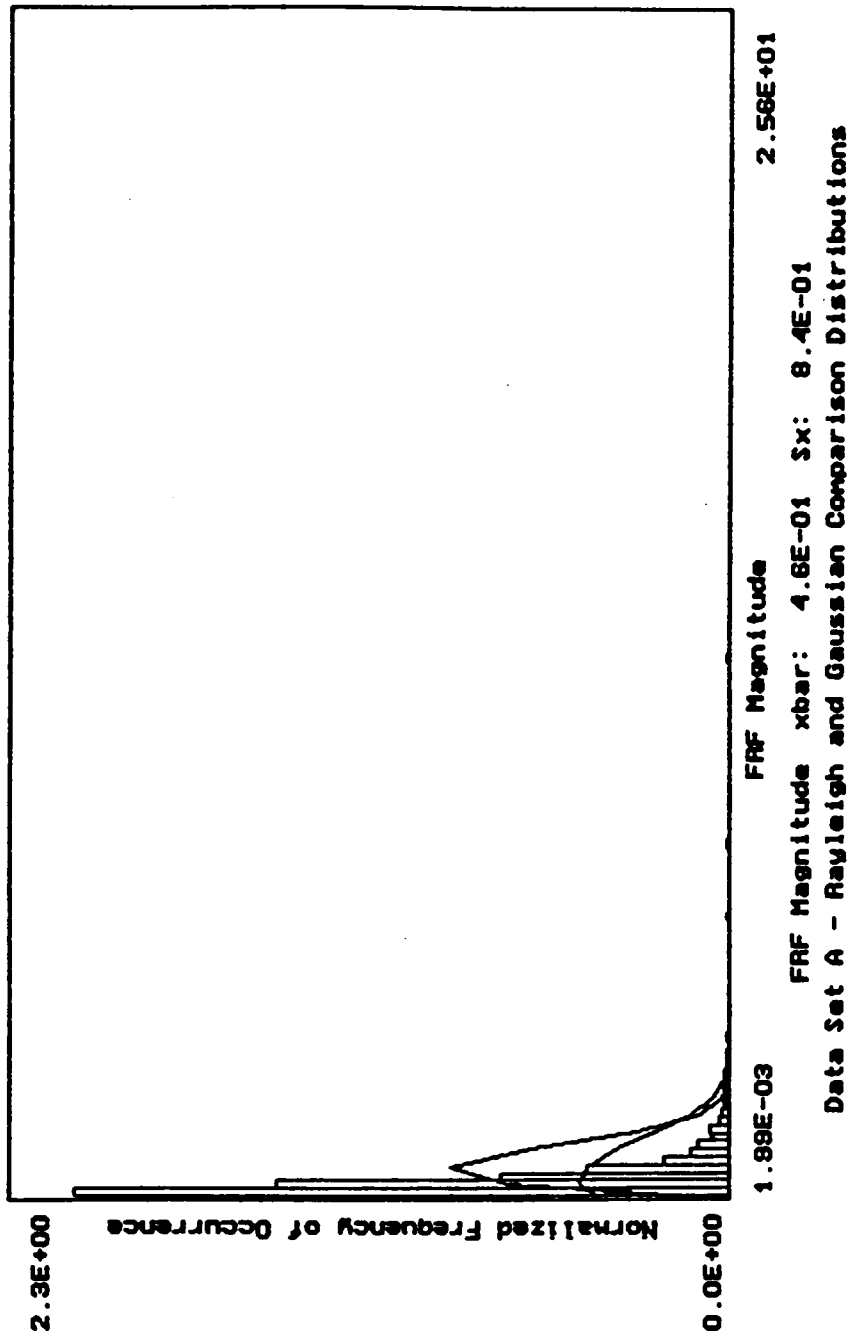


Figure 22. Histogram - Magnitude of Data Set A FRF

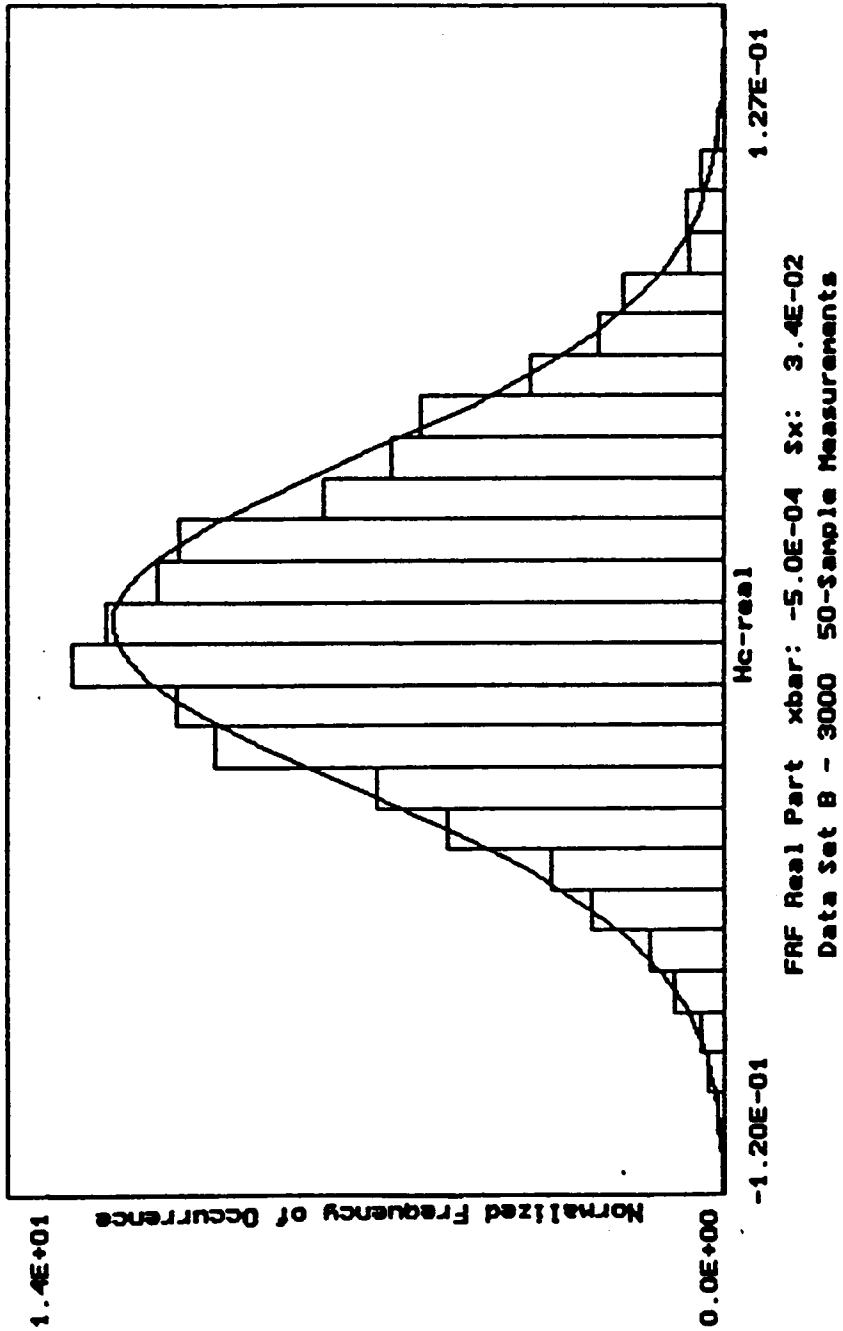


Figure 23. Histogram - Real Part of Data Set B FRF

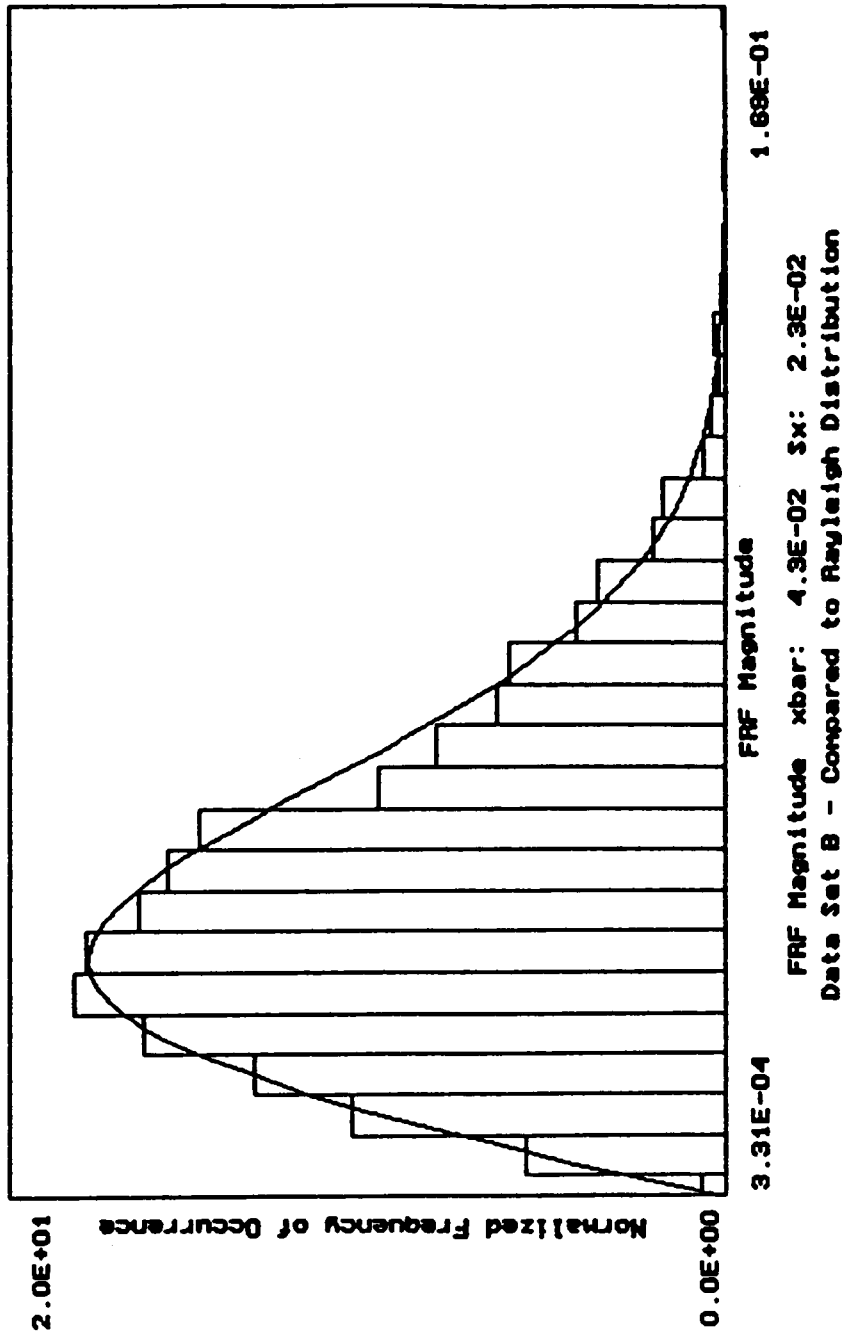


Figure 24. Histogram - Magnitude of Data Set B FRF

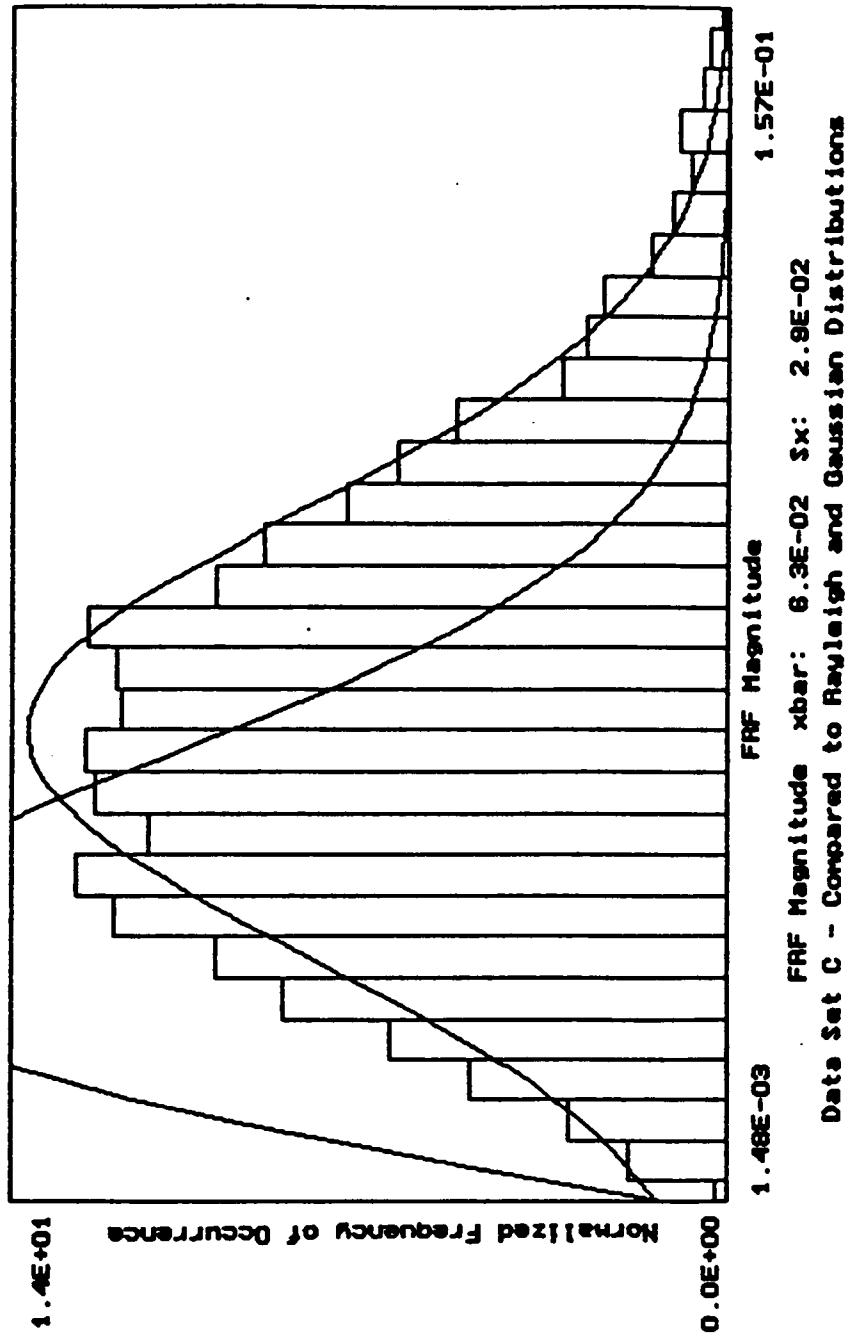


Figure 25. Histogram - Magnitude of Data Set C FRF

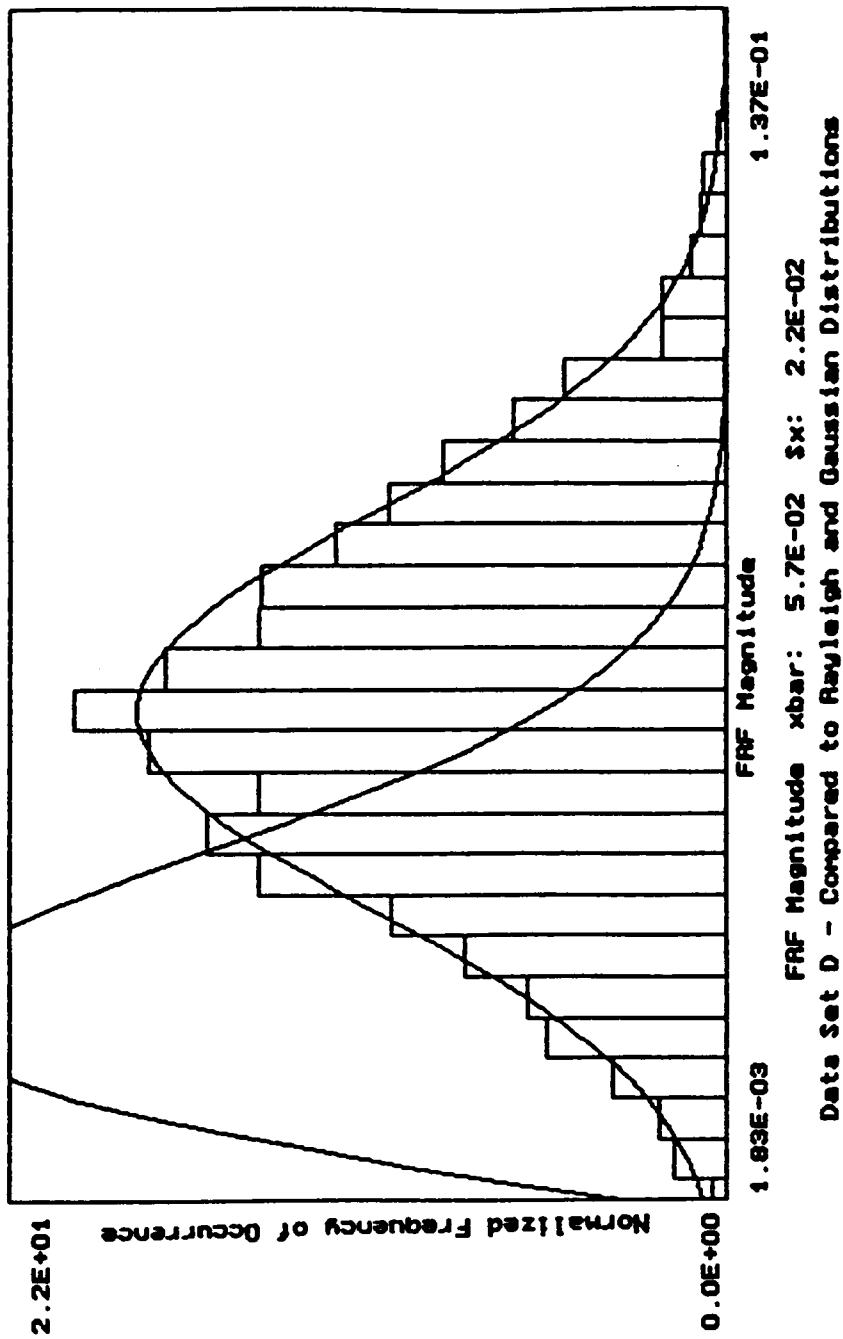


Figure 26. Histogram - Magnitude of Data Set D FRF

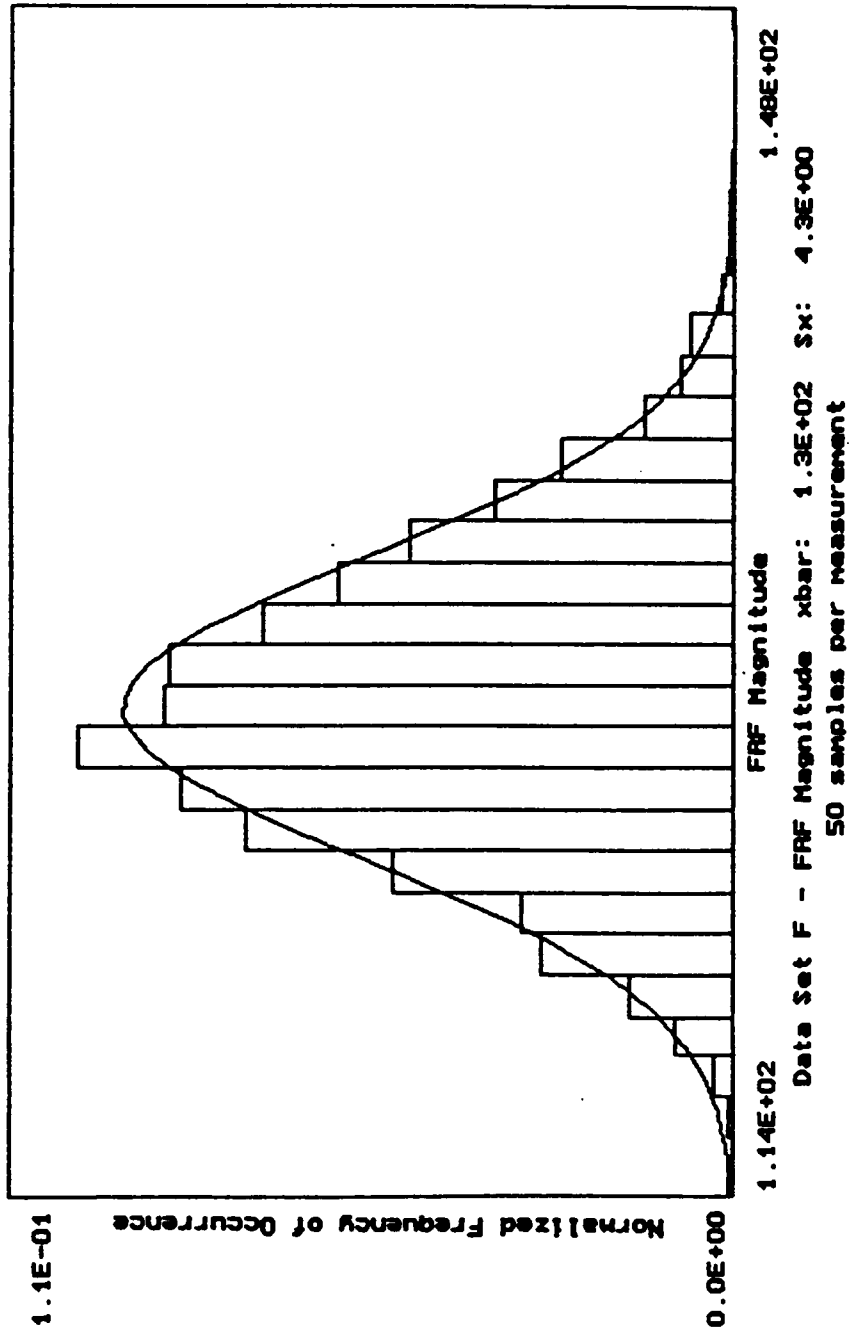


Figure 27. Histogram - Magnitude of Data Set F FRF

shown in the figure is 1.27, which dropped to 1.1 in the $n_d = 100$ run. This is still in the rejection region, but the decrease of 'D' with increase of n_d can be seen. It appears that, for large values of the FRF with relatively small sample size (say, $n_d = 50$ to 100) we can only justify *approximate* Normality.

6.4 Single Measurement Simulations

The Monte Carlo simulations repeated measurements at single spectral lines in order to gain information about the distributions of various quantities and verify the validity of relations previously derived. When computations were made using the Monte Carlo data, the values used were not those obtained from single measurement estimates, but rather the *mean of 3000* measurement estimates. Though the equations were found to be valid in most cases using these accurate values, the question remained as to how well the relations would work when single measurement estimates were used instead.

The simulations to be discussed in this section modeled an FRF measurement over a large number of spectral lines and a wide range of FRF magnitudes, similar to a real-life measurement. The uncorrelated content values, $\Gamma(f)$, and G_{rr} are the same as in the Monte Carlo simulations. The discussion will be divided into two parts: evaluation of the variance calculations and the uncorrelated content estimates.

6.4.1 Variance Estimates

After a simulated measurement had been made, the variance at each spectral line was calculated using the numerical integration method discussed in Chapter 4. 'Confidence bands' were then calculated and plotted together with the 'measured' FRF. As discussed in Section 6.2, the range of values for a given probability was based on the Normal distribution. For example, using approximate values, 95 percent probability bands were plus or minus two standard deviations from the measured value, while plus or minus one standard deviation gave about 68 percent probability.

A luxury afforded by the simulations that is not found in real-life measurements is that the 'right' answer is known. This can be used to evaluate the number of times that the 'right' answer falls within the confidence bands. A good verification would be to repeat the measurement process a large number of times. After each measurement a check would be made to see whether or not the 'true' value fell within the bands. If we used 95 percent confidence bands then we would expect, over a large number of measurements, to find the 'true' value at a given spectral line to fall within the confidence bands in about 95 percent of the measurements. But the question arises about how to obtain a verification without running hundreds of measurements.

If we can justify an admittedly large assumption about the nature of error in the variance estimates, we could use the hundreds of spectral lines in a single 'measurement' for verification. The assumption we must make is that the variance estimator works equally well at all regions of the FRF. If we can make this assumption, then we would expect that at 95 percent of the spectral lines in a single measurement the 'true' value would fall within the 2σ confidence bands. Without the condition of equal quality variance esti-

mates at each spectral line, such a result would be meaningless. For example, it would be very easy to develop 'confidence bands' that would contain the true values within the bounds at 95 percent of the spectral lines for every measurement. All that would be needed is to make very large estimates of the variance at 95 percent of the lines, and make exceedingly small estimates at the other five percent. One way of detecting this situation would be by changing the probability range of the confidence bounds. If the bounds were narrowed or widened, the percentage of 'in bounds' estimates should change accordingly.

In the following evaluations the assumption of equal quality variance estimates at all regions of an FRF is made. While this assumption is based on no rigorous statistical test, there is nevertheless good reason to believe it to be true:

1. In Tables 2 through 6 it was shown that the variance estimates obtained by the numerical integration method agreed with the Monte Carlo results within a few percent in every case. These data sets included a large range of FRF values and a number of instances where the assumed distribution functions had been violated.

2. In the results to be shown in this section, the percentage of spectral lines with 'in bounds' results closely followed the Normal distribution expectations as the width of the bands was varied.

3. In Chapter 7 a slightly different type of variance test was used, which involved plotting one measured FRF over the confidence bands from another measurement of the same FRF. Though the probabilities for this test change, the significant part here is that the probability be shown to be constant over the FRF. In the discussion of those results, it will be shown that approximately the same percentage of lines were 'in bounds' at the resonances and anti-resonances as there were over the entire FRF.

4. Comparison of the measured FRF's and confidence bands in the following discussions will reveal a further, but qualitative, verification. In regions where the FRF estimate is 'smooth' the confidence bands are very narrow, while regions where the FRF estimate is not smooth have much large bands. That the confidence bands 'track' the variability of the FRF can be clearly seen in many regions.

In Fig. 28 a simulated 300 spectral line, 50 sample FRF measurement is shown, along with the true value. In Fig. 29 the true value and the 95 percent (plus/minus 2 standard deviations) confidence bands are shown for this same measurement. The 'measured' FRF has not been shown in this figure for clarity. We see that the true FRF falls within the confidence bands at 94 percent of the 300 spectral lines. In Fig. 30 we see the confidence bands for a 300 sample measurement. Once again, only the confidence bands and true FRF are shown for clarity. The confidence bands are closer together, in accordance with the better estimate afforded by the additional samples. We see also that, coincidentally, 94 percent of the true values also fall within the bands (typically this value has ranged from about 92 to 97 percent in the simulations done). A further test is made by narrowing the confidence bands to plus/minus one standard deviation. By the Normal distribution we would expect the confidence bands at about 68 percent of the lines to contain the true FRF. In Fig. 31 we see that in this particular simulation the actual value was 63 percent, which was considered to be a satisfactory result. We conclude that the simulations predict that the variance calculation will work well using only single measurement estimates, and over a wide range of FRF magnitudes.

The next question is whether the variance reduction with increased samples noted above follows the Central Limit theorem prediction. The prediction by this theorem states that the variance of an average is inversely related to the number of samples in the average.

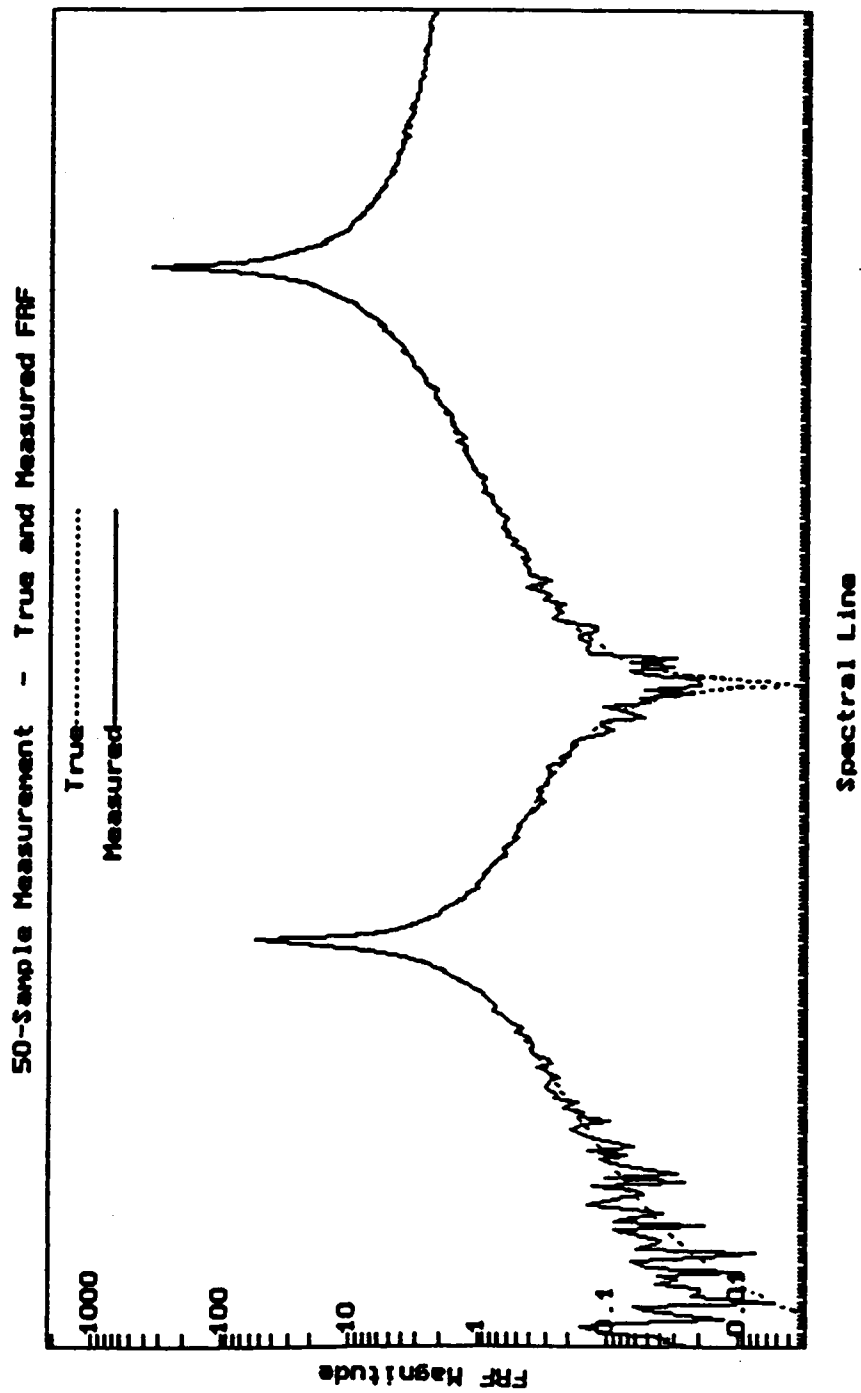


Figure 28. Simulated 50-Sample FRF Measurement

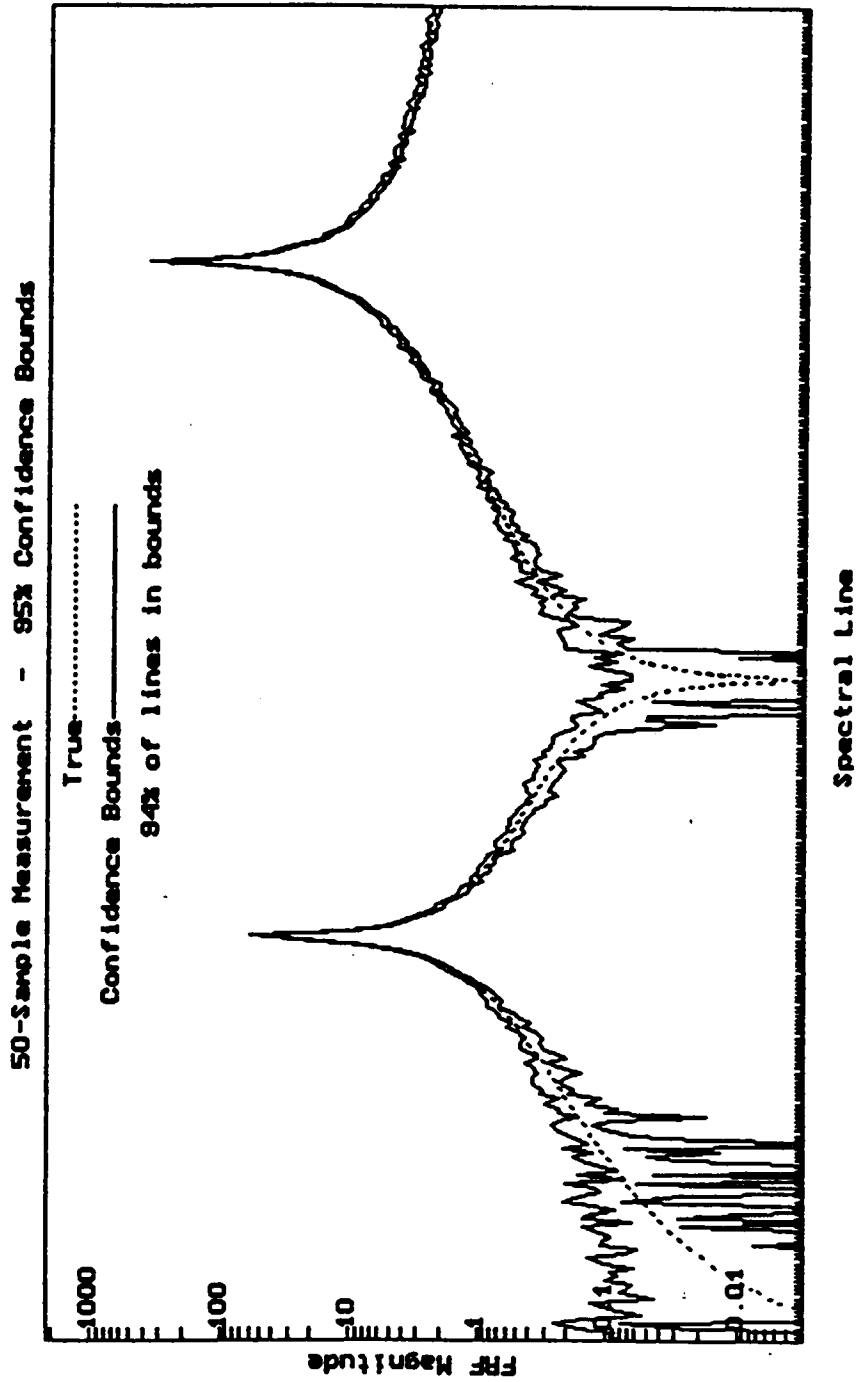


Figure 29. 95 Percent Confidence Bands - 50 Sample Measurement

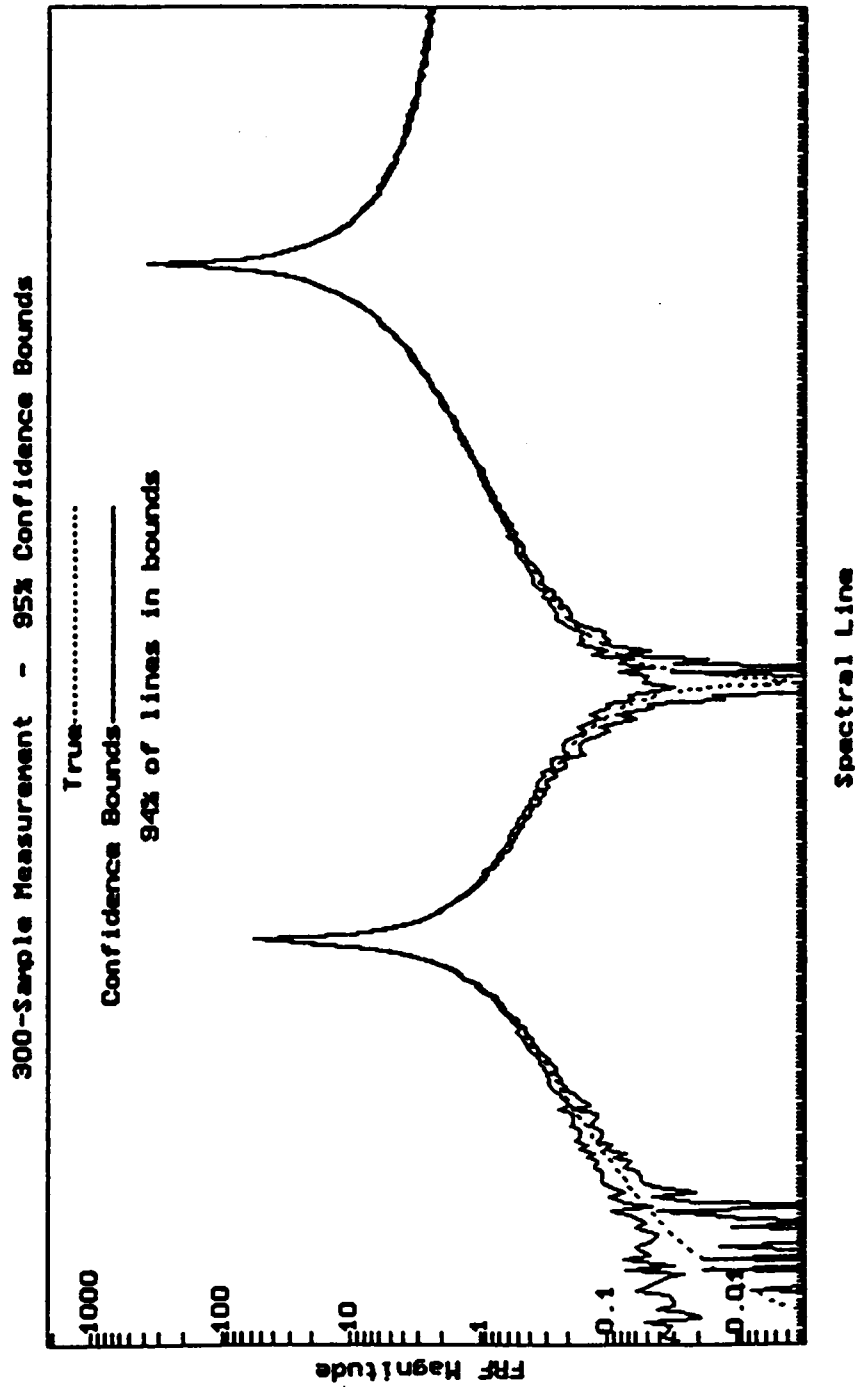


Figure 30. 95 Percent Confidence Bands - 300 Sample Measurement

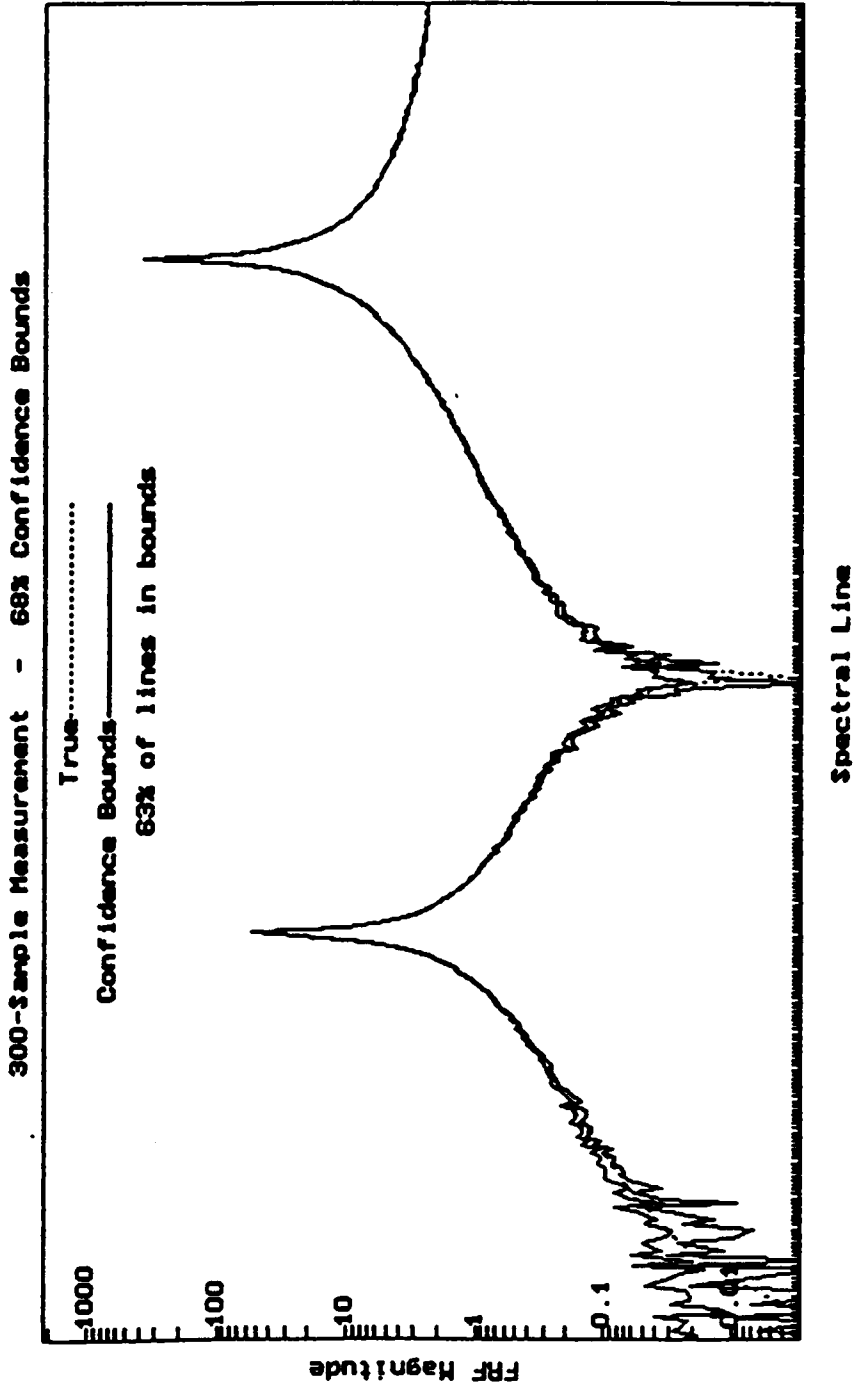


Figure 31. 68 Percent Confidence Bands - 300 Sample Measurement

Knowing how the variance is reduced as a function of the number of samples in the measurement would provide the experimenter with a guide as to how many more samples would be needed to reduce the variance by a given amount.

Example 7: This example will compare the variance difference in the simulations with the difference predicted by the CLT. For the two simulations discussed (50 and 300 sample measurements) the prediction is that

$$\frac{\text{variance of 50 sample measurement}}{\text{variance of 300 sample measurement}} = \frac{300}{50} = 6$$

In terms of standard deviations,

$$\frac{\sigma_{50}}{\sigma_{300}} = \sqrt{\frac{300}{50}} = 2.45$$

meaning that the predicted confidence bands for the 50 sample measurement are nearly 2.5 times larger than the bands for the 300 sample measurement. To find the corresponding ratio from the simulations, the standard deviations at each spectral line of the 50 sample measurement were divided by the corresponding 300 sample measurement spectral line standard deviations. Done over all 300 spectral lines, the average result was 2.44, in close agreement with the CLT prediction. While the distribution of this ratio is not known, the computed standard deviation of this ratio (S_r) was 0.36, providing some information about the variation of this ratio. This concludes Example 6.

A point to be made here is that accurate estimates of the variance are not necessarily found at each spectral line, since the quantities used to compute the estimates are random variables. The claim is that, on the *average*, the estimates of variance are accurate.

6.4.2 Uncorrelated Content Estimates

The uncorrelated content estimates shown here were made using the data from the 300-sample measurement discussed in the last section. The same nominal values for generation of the uncorrelated content were used (which also were used in the Monte Carlo simulations: $G_{kk} = G_{mm} = G_{rn} = 2$). For this simulation, the uncorrelated content values generated were stored, so that comparisons could be made between estimated and true values (not just nominal values). It should be noted that having uncorrelated content present at all three locations (shaker, force measurement, and response measurement) is a worst case scenario. It is unlikely in most real-life measurement situations that this would occur. It was found in the simulations that removing any one of the uncorrelated content terms from the model generally resulted in better estimates of the other two terms. Each of the uncorrelated content estimators worked well in certain regions of an FRF (i.e., resonance or anti-resonance), and poorly in others. In order to correlate the estimates with the region of the FRF, the true FRF is shown in compressed form at the bottom of each figure.

6.4.2.1 Estimates of Shaker and Force Measurement Noise

Figure 32 shows the auto spectrum estimate of 'shaker noise', \hat{G}_{kk} . Figure 33 shows the estimated force measurement noise auto spectrum, \hat{G}_{mm} . Both of these are contained in the measured force signal auto spectrum, \hat{G}_{xx} . This is shown in the figures as well for comparison. We see that both estimates do well in regions of the FRF away from anti-resonances, but very poorly at anti-resonances.

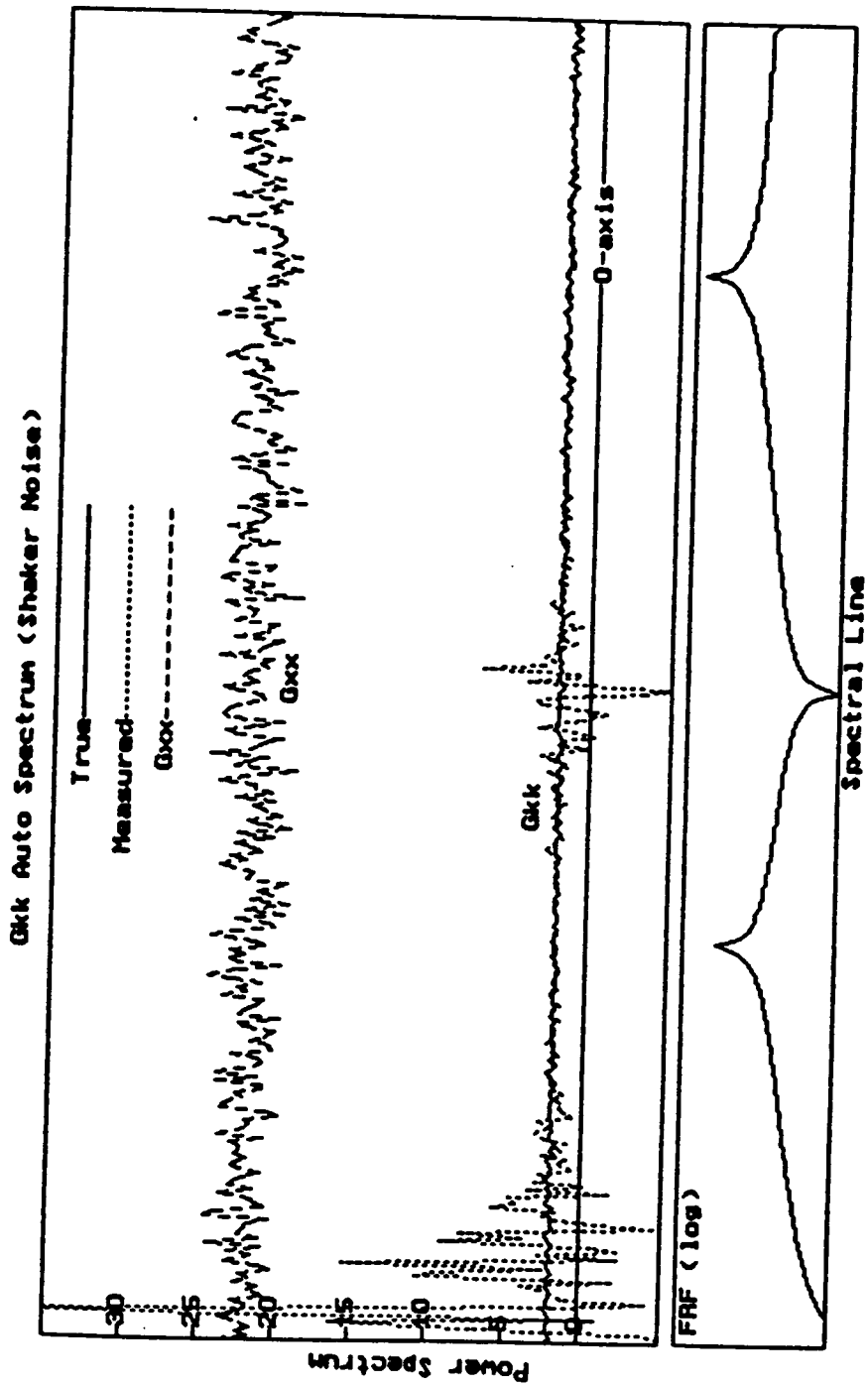


Figure 32. Estimate of Uncorrelated Content in Shaker System

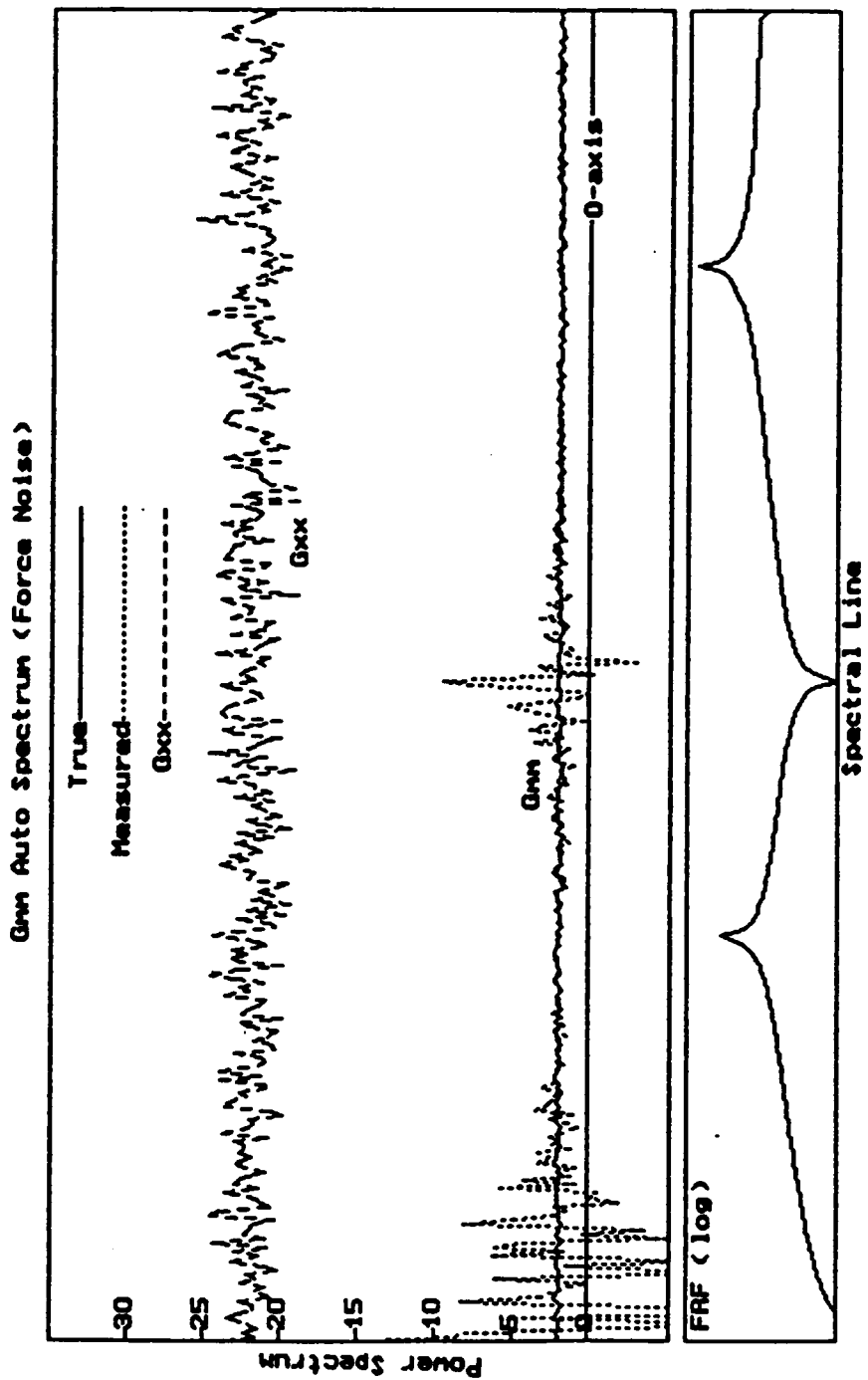


Figure 33. Estimate of Uncorrelated Content in Force Measurement

The reason for the poor performance at anti-resonance can be seen in Eqs. 2.19 and 2.22. Both expressions contain the term $\frac{|G_{xz}G_{yx}|}{|G_{yz}|}$. At anti-resonance both G_{yz} and G_{yx} tend towards zero, causing their ratio to approach a (0/0) indeterminate form. Small variations in the estimates of either of these cross spectra can result in large fluctuations of the overall estimate, including negative values (a physical impossibility for an auto spectrum). Further inspection of Eqs. 2.19 and 2.22 shows that where the troublesome cross spectrum ratio is positive in one equation it is negative in the other. When the two estimates are plotted together, as in Fig. 34, it can be seen that the errors are 'mirror images' of one another. That is, at a spectral line where one estimate is high, the other estimate will be low by a like amount. When the two estimates are summed and compared to the sum of the true values, as in Fig 35, we find the sums to be in close agreement.

The observations just noted suggest at least a partial error correction scheme. Since the sum of the two estimates agrees well with the sum of the true values, and because negative auto spectrum estimates are physically impossible, improvements can be made in the estimates by eliminating negative auto spectrum estimates. Every negative value of, say, \hat{G}_{kk} is added to \hat{G}_{mm} , and then the \hat{G}_{kk} estimate is clipped at zero. This process is repeated with negative values of \hat{G}_{mm} . We see that this does not alter the sum any, and results in improved estimates. Figure 36 shows the two estimates after correction.

Even after correction, the estimates at anti-resonance are poor. This does not seriously degrade the usefulness of these estimators, however. Consider that at anti-resonance frequencies there is very little response of the structure to the applied force. The shaker and force gage are applying and measuring a force on a relatively static structure. Under this condition uncorrelated content in the force gage or shaker system is likely to be low,

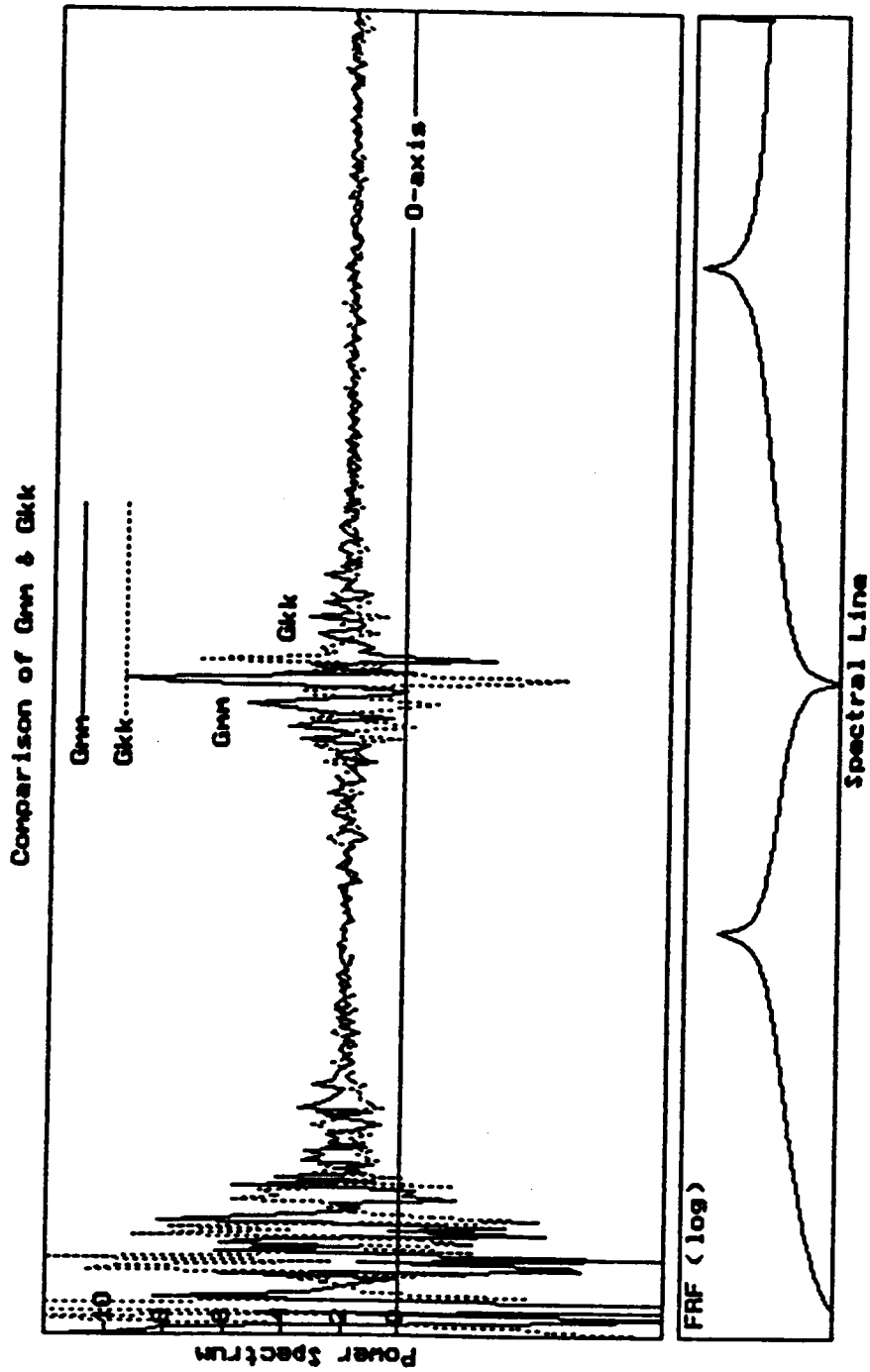


Figure 34. Comparison of Shaker and Measurement Noise Estimates

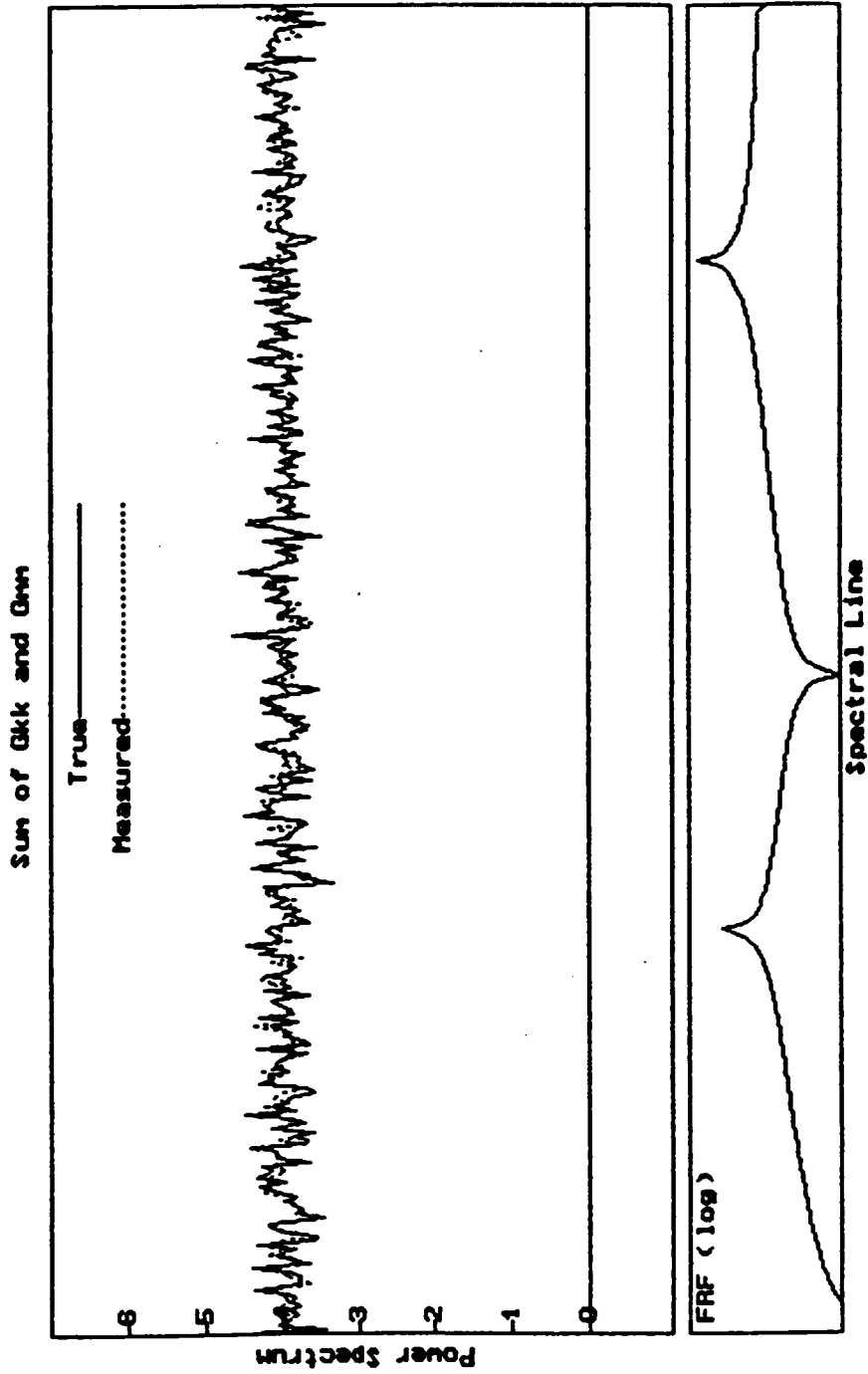


Figure 35. Sum of Shaker and Measurement Noise Estimates

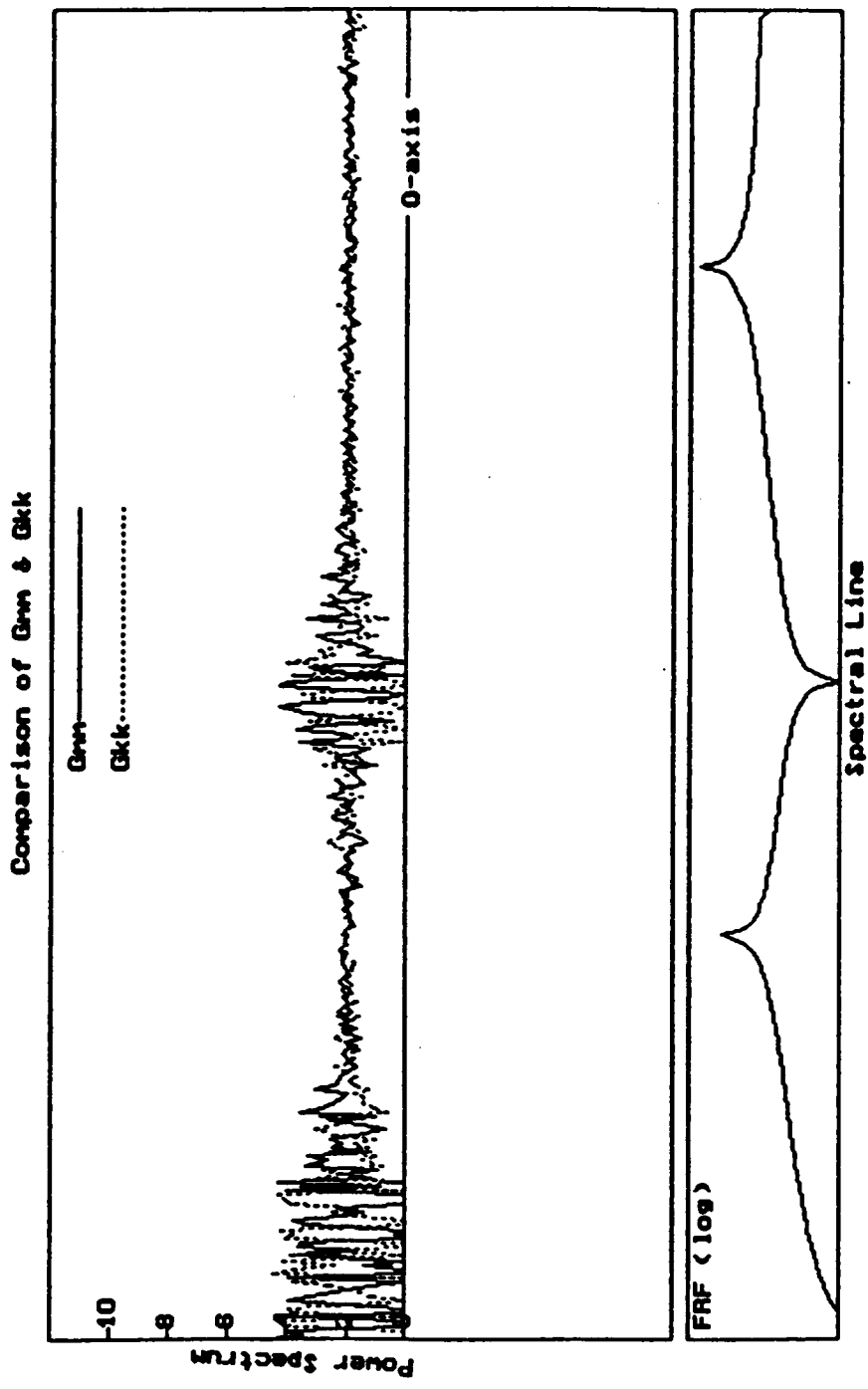


Figure 36. Corrected Shaker and Measurement Noise Estimates

so the need for an estimate of this uncorrelated content is also low. At resonance, on the other hand, the response of the structure causes feedback to the shaker and force gage, which increases the likelihood of uncorrelated content on the input measurement at resonance frequencies. Yet at these frequencies, where the uncorrelated content terms are likely to be high, the estimators work at their best.

6.4.2.2 Estimates of Response Measurement Noise

Figure 37 shows the estimate of the uncorrelated content in the response measurement, \hat{G}_m . The auto spectrum of the response measurement, \hat{G}_{rr} , is shown for comparison. Here we see the opposite problem to the other two uncorrelated estimators. This estimator works well at anti-resonance, while estimates at resonance are subject to large errors.

The only correction possible with this estimator is to clip the negative values to zero. Before one becomes too discouraged with the potential of this estimator, however, it is valuable to look at it from several different perspectives. First of all, at resonance the response signal is very high, making it unlikely that there will be a significant amount of uncorrelated content relative to the desired signal. Problems with uncorrelated content in the response measurement appear more readily at anti-resonance regions, where the response signal is small and any uncorrelated content in the signal is potentially large by comparison. Yet it is in these regions that the estimator performs well.

Another consideration is the manner in which one evaluates the size of errors. As seen in Fig. 37, estimates of \hat{G}_m are in error by several thousand percent when compared to the true value. Perhaps the error would be better evaluated in terms of the magnitude

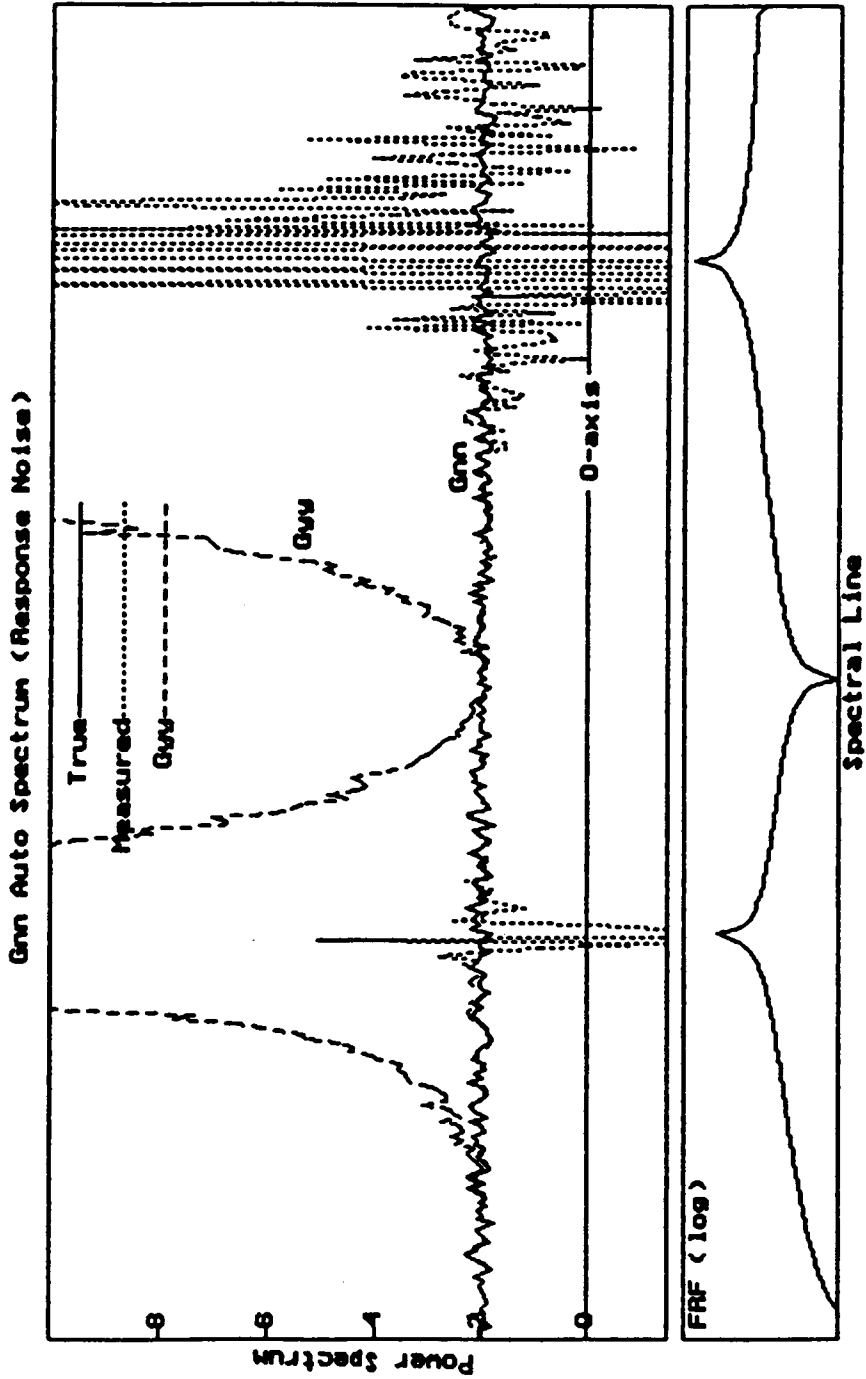


Figure 37. Response Measurement Noise Estimate

of the signal in which the uncorrelated content term is contained. If we increase the scale of the figure, as has been done in Figs. 38 and 39, we see that the difference in estimated and true values of G_m is but a very small fraction of the total response signal, \hat{G}_{yy} .

When normalized in the form

$$\text{percent error} = \frac{\hat{G}_{nn} - G_{nn}}{G_{yy}}$$

the percent error was found to be well under one percent at any spectral line. This estimator can provide good results at any frequency, so long as an accuracy of better than about one percent of the measured signal is not desired.

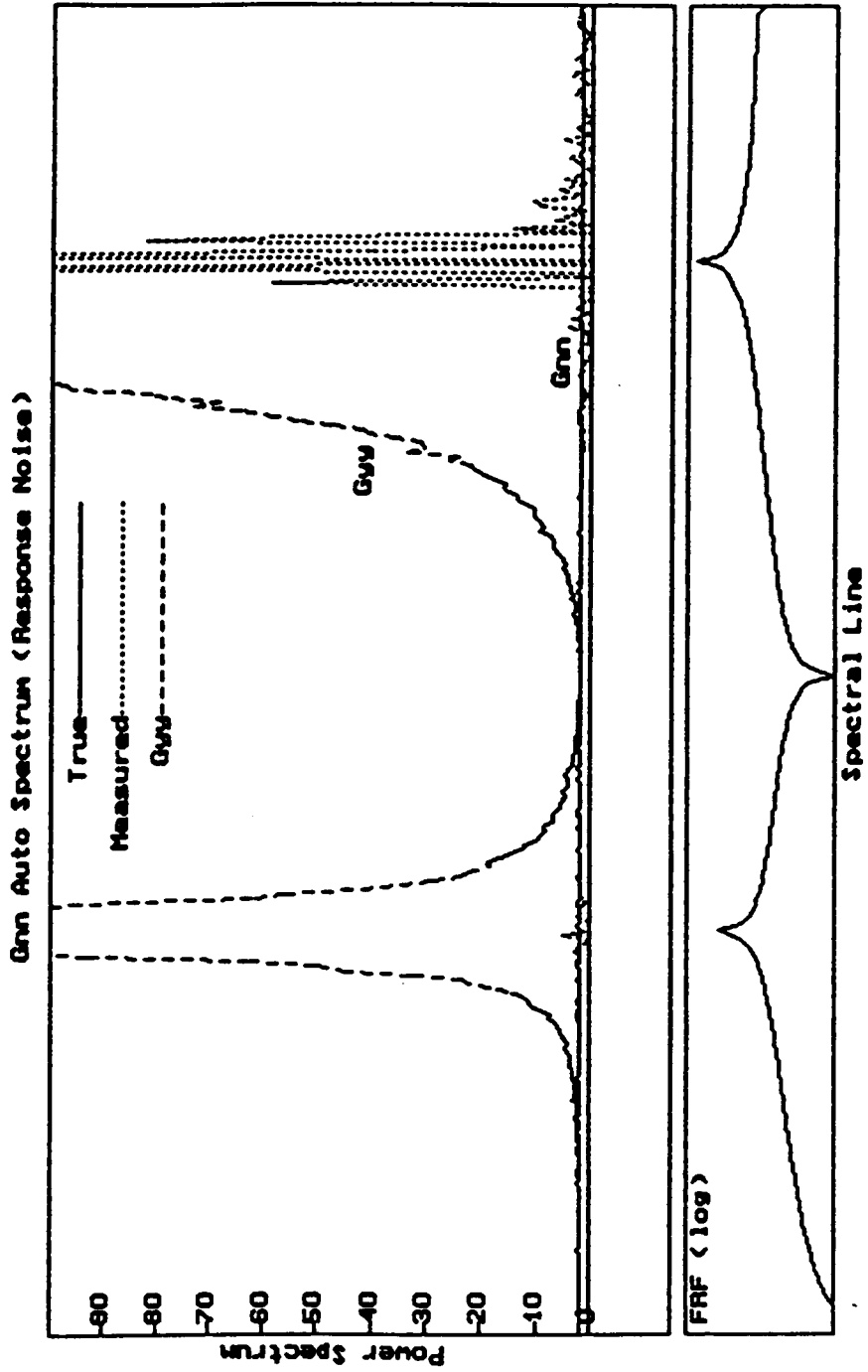


Figure 38. Response Measurement Noise Estimate - Increased Scale

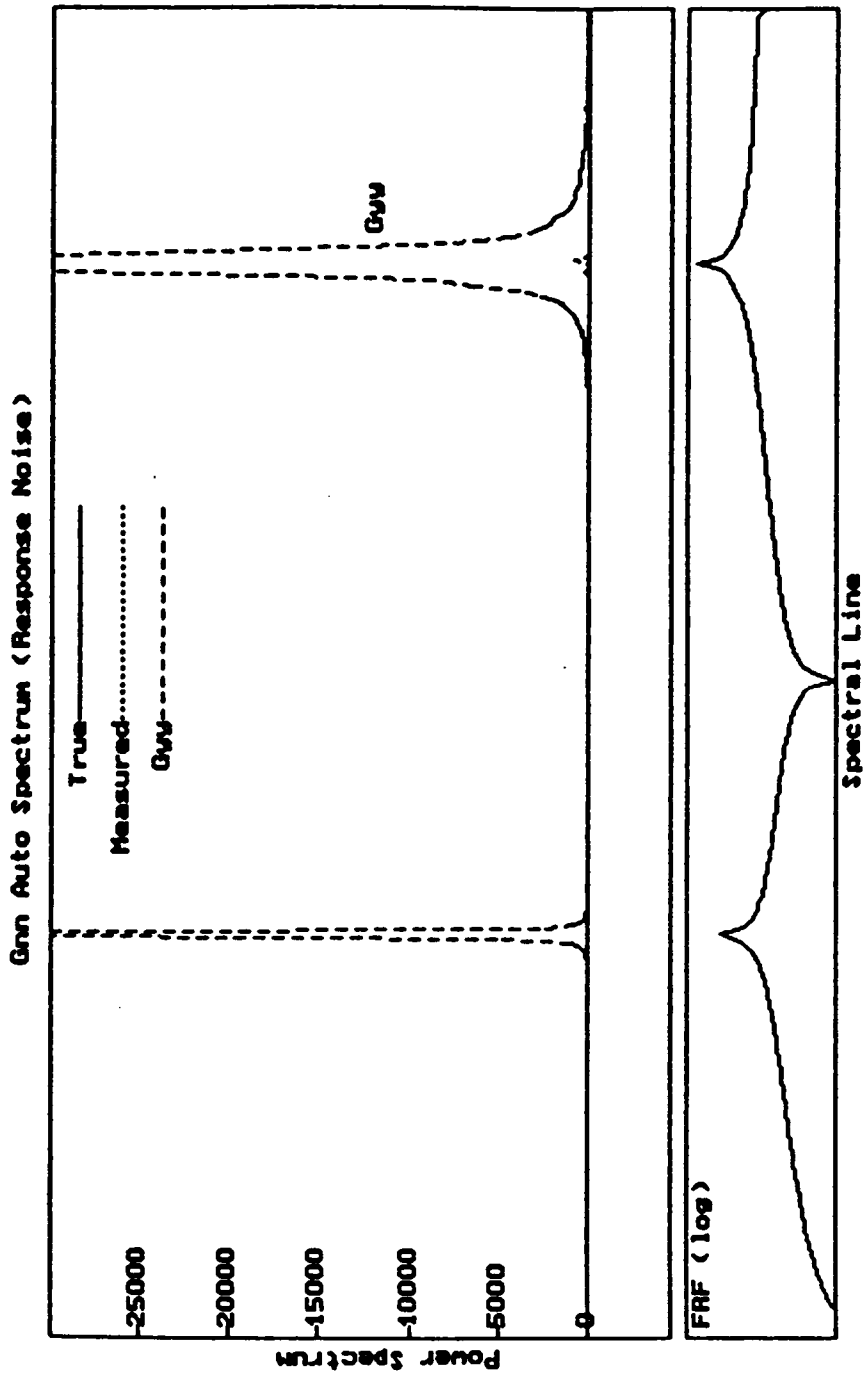


Figure 39. Response Measurement Noise Estimate - Large Scale

Chapter 7 - Results of Experimental Measurements

Experimental frequency response function measurements were made on a 50-pound calibration mass and a flat metal plate. Data was taken with a Zonic 6081 multi-channel FFT analyzer and ported to a DEC VaxStation 2000 for computation of variance and uncorrelated content estimates. The time necessary for uncorrelated content estimate computations is small (about a second), but the variance calculations are computationally intensive, requiring approximately two minutes (on the micro-Vax II) for each response channel.

Consider a typical measurement situation where a single force is applied to a structure and response measurements are made with a triaxial accelerometer. For the 'three-channel' estimator, a total of five channels are needed to measure: the source (signal generator), the force input, and three separate responses. Cross spectra are required between the force and each response, the source and each response, and between the force and source. This requires seven cross spectra (or 'channel pairs') in the measurement. From this data we obtain three frequency response function estimates, one cor-

responding to each response channel. To calculate the variance for all three FRF's requires approximately six minutes (clock time).

An interesting question arises when interpreting the uncorrelated content results. The derivations derived in Chapter 2 are based on the '3-channel' estimator (i.e., only one response channel is included in the model). When these equations are applied to a measurement with three response channels, we obtain for each response channel (Y_1 through Y_3) an uncorrelated content estimate ($\hat{G}_{n_1n_1}$ through $\hat{G}_{n_3n_3}$). However, for *each* response channel, we can also calculate an estimate of uncorrelated content in the source-signal-to-force generation process (which will be referred to as 'shaker noise'), and in the force measurement (or 'force noise'). Because these 'noise' terms (G_{kk} and G_{mm}) are independent of the response measurement, we obtain three separate estimates of both of these terms (using the triaxial accelerometer case). The question arises in how these three estimates might be used to obtain a single improved estimate.

The most obvious idea is to average the three estimates. The improvement obtained with this approach is questionable. Recall from the simulation results discussed in Chapter 6 that the estimators \hat{G}_{kk} and \hat{G}_{mm} do very poorly at anti-resonance regions of an FRF. Even with the corrections that can be made, large errors are still possible at these frequencies. If, at a given frequency, two of the response channel FRF's show an anti-resonance while a third does not, much better results will be obtained by using only the estimate based on the third channel, rather than averaging the three estimates. Consider also that in modal analysis the response is measured at multiple locations by moving the accelerometer. As long as the force gage and shaker system are undisturbed, numerous estimates of 'shaker noise' and 'force noise' may be made, even with a single axis accelerometer. If averaging of the estimates is desired for reduced variance, it is still

recommended that the experimenter first evaluate the data and select which estimates are to be used in the averaging process.

Two types of input signals were used in the experimental work: continuous random (used with the Hanning window), and 'burst' random (without a window). A 'windowing' procedure is required to taper the time record when using continuous random excitation, in order to reduce apparent (in the FFT process) 'leakage' of energy to adjacent spectral lines. The burst random technique applies a random signal only briefly to a structure at the beginning of each time record. Ideally, the response of the structure will decay to zero within the measured time record. Then the time records will begin and end with zero force and response values, without the need for an artificial time-domain windowing process. But for lightly damped structures the response seldom decays to zero within the measured time record. The first and most important consideration here is that the measurement of the next time record not begin while the structure is still responding to the last input or the new record will be contaminated. The second consideration is whether or not to window the response record so that, artificially at least, the measured response record decays to zero within the time record. The best window for burst random has an exponential decay shape [31], but even this effectively adds damping to the measurement. Although corrections can be made, if 'good' data (i.e., with high values of the coherence, $\hat{\gamma}_{xx}^2$) without windowing, then this is preferred.

7.1 Results of Measurements of the Calibration Mass FRF

A simple (but worthwhile!) verification of measurement system accuracy is to measure the FRF of a simple mass. If the mass is selected and mounted properly, the FRF is simply a straight line. That is

$$\frac{\textit{acceleration}}{\textit{force}} = \frac{1}{M}$$

at all measured frequencies, where the calibration mass is M . The cylindrical mass used in the measurements weighed 50 pounds (22.7 kg), and was suspended from elastic cords. The softness of the suspension together with the large mass resulted in a suspended natural frequency of 1 Hz or less, while the first continuum (axial) natural frequency of the cylinder was above 10 kHz. Over the calibration range of 2.5 Hz to 1 kHz used, neither of these natural frequencies could significantly affect the results.

The method of connecting the shaker to the force gage (and attaching the force gage to the structure) can significantly affect the excitation energy levels achieved [32]. Two different connectors were used to connect the shaker to the force gage. One was a wire, approximately 0.5 inch (13 mm) long and 0.030 inch (0.76 mm) in diameter, with threaded studs soldered on each end. The other connector type was a rod with the threaded studs attached via ball-end type swivel joints. The wire connector was very stiff in the axial direction, with no lost motion between the two ends. The ball-joints on the other connector were spring loaded. Significant displacement in the joints could be felt even under light loads.

The signal generator was set to generate a frequency-limited continuous random signal of uniform amplitude with an upper limit of 1 kHz. No burst random FRF calibration mass measurements were made. When the wire connector was used, the force applied to the structure was fairly uniform over the frequency range and highly correlated with the generated signal. We expect the lost motion in the ball-joint connectors, on the other hand, would have two effects: 1) the force applied to the structure would be attenuated at higher frequencies, and 2) the force signal would not be highly correlated with the generated signal, especially at higher frequencies. The nonlinear response resulting from lost motion in the joints would cause the second effect. The ball-joint connector was used so as to have an FRF with varying variance and to inject 'shaker noise' into the system. Because there would be little energy transmitted at higher frequencies, it was expected that the FRF estimate would be much more variable in that region. Also recall that 'shaker noise' results from any loss in correlation between the generated signal and the force applied to the structure. Nonlinear action will result in loss of correlation.

7.1.1 Variance Estimates for the Calibration Mass

Figure 40 shows the measured FRF using the ball-joint connector and the 3-channel measurement method. Superimposed on the FRF are the ordinary coherence between the force and response (γ_{xx}^2) and a straight line which is the average of the FRF over all frequencies. The coherence is plotted on a scale of zero to unity. Around 200 Hz the coherence is about 0.9, and a fairly uniform estimate of the FRF is found here. Because of the lost motion in the ball-joint connectors, force input is attenuated at all but very low frequencies. Approaching 1000 Hz, we see that the small force (and response) signal

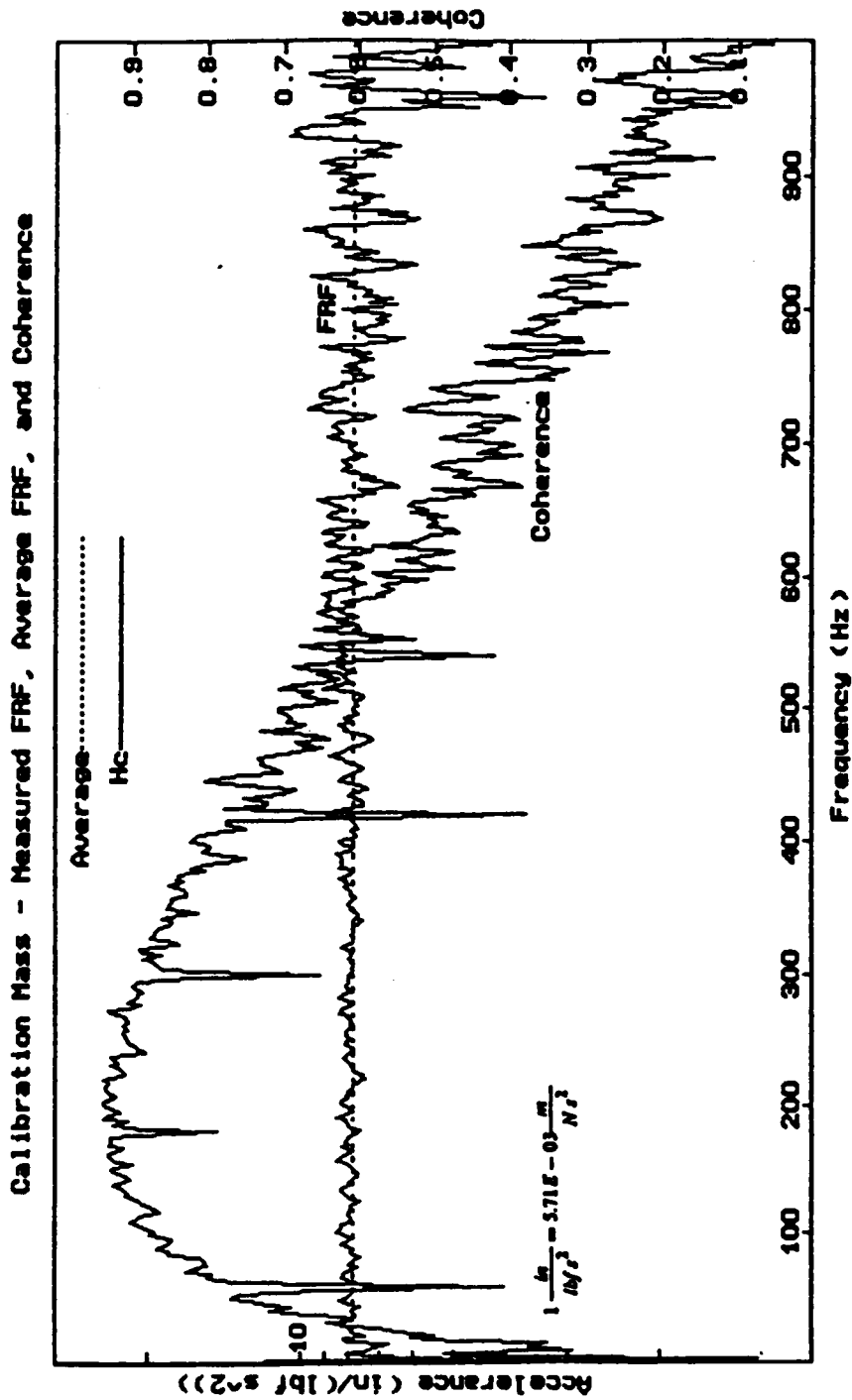


Figure 40. Measured Calibration Mass FRF and Average Value

levels allow system noise to dominate, driving the coherence down to 0.2 and below, resulting in large variations of the FRF estimate.

The weight of the mass, accelerometer, and 'mass-below-the-force-gage' was 50.01 lbs. The expected FRF value is then

$$\frac{1}{M} = \frac{(32.17 \frac{ft}{s^2})(12 \frac{in}{ft})}{50.01 \text{ lbf}} = 7.72 \frac{in}{\text{lbf} - s^2} = 0.4405 \frac{1}{kg}$$

The average measured value was $7.90 \text{ in/lbf} - s^2$ ($0.451 \frac{1}{kg}$), an overall system error of just over 2 percent. This error was not deemed large enough to require correction of the calibration factors. For purposes of evaluating the confidence bands, however, this average value was used rather than the calculated value.

Figure 41 shows the average FRF value line and the estimated 95 percent (plus/minus two standard deviations) confidence bounds. We find that at 94 percent of the spectral lines the average FRF value falls between these bounds.

Figure 42 shows the average FRF and 99 percent confidence bounds (plus/minus three standard deviations). At 99 percent of the spectral lines the average value falls within the bounds. As an additional verification of both the variance estimate and normality of the FRF magnitude, confidence bounds were placed at plus/minus one standard deviation, as shown in Fig. 43. For the Normal distribution this corresponds to 68 percent probability. In this example, the average value was found within the confidence bounds at 64 percent of the spectral lines.

Calibration Mass Confidence Band Summary: The constant FRF of a calibration mass allows verification of system operation and provides an FRF whose 'true' value is easily

Calibration Mass FRF - Average and 95% Confidence Bounds

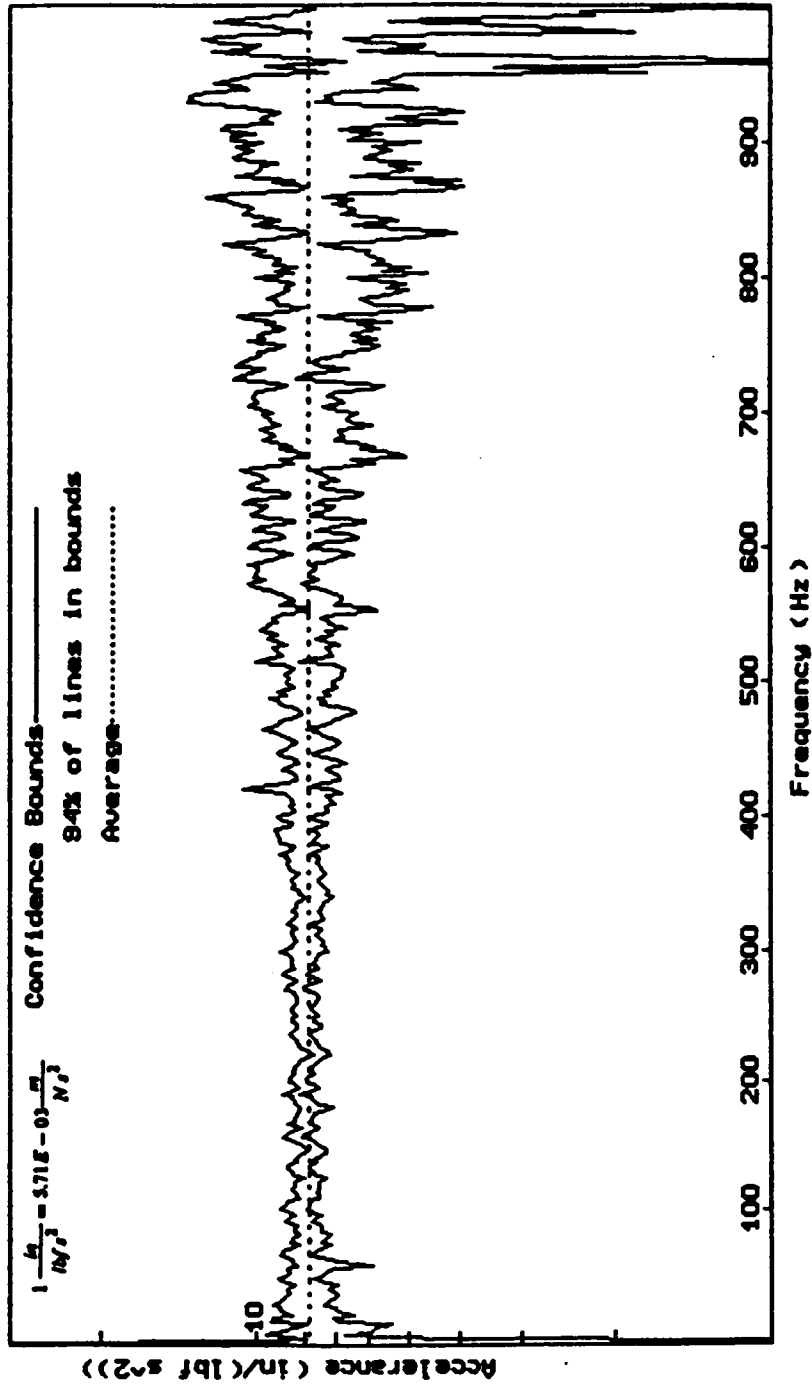


Figure 41. Calibration Mass - 95 Percent Confidence Bands

Calibration Mass FRF - Average and 99% Confidence Bounds

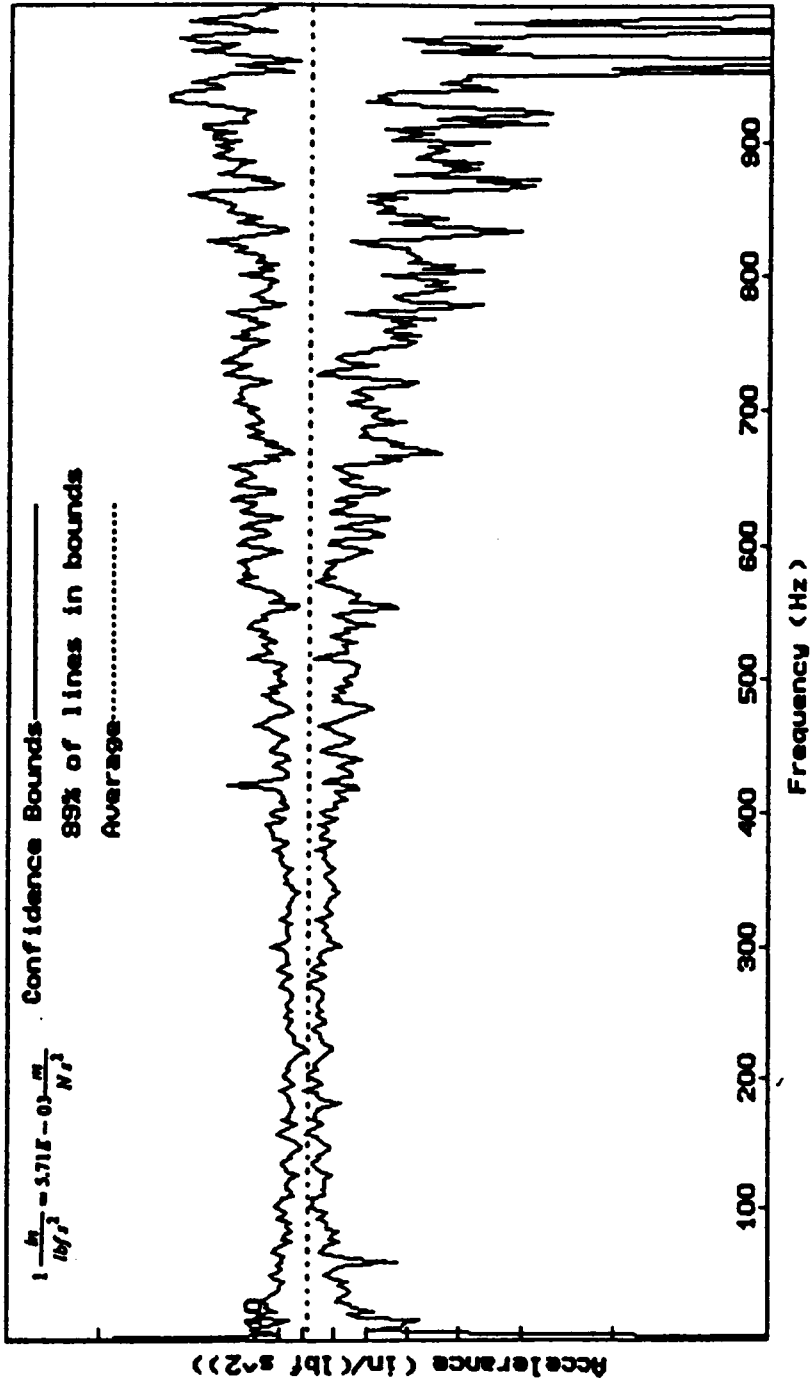


Figure 42. Calibration Mass - 99 Percent Confidence Bands

Calibration Mass - Average and 68% Confidence Bounds

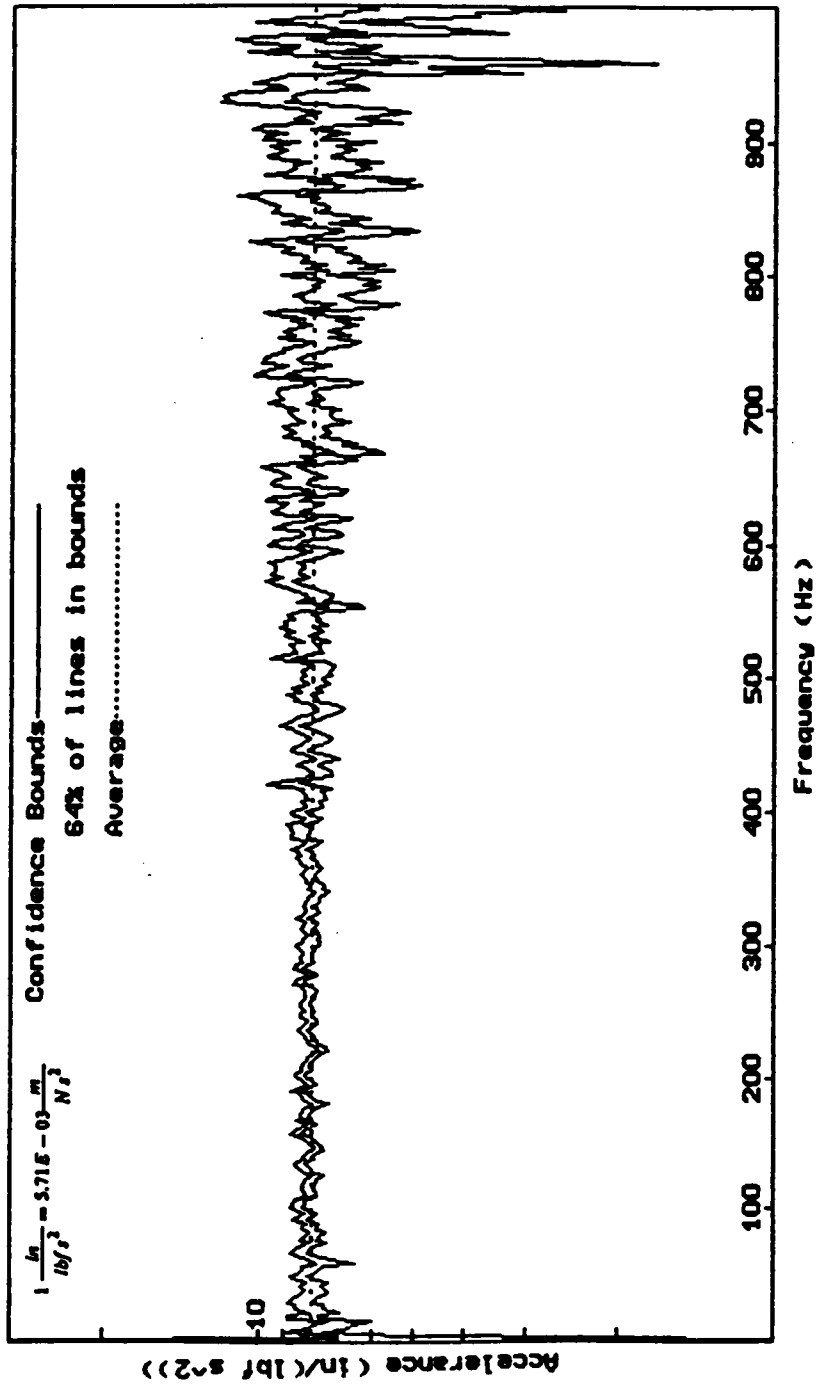


Figure 43. Calibration Mass - 68 Percent Confidence Bands

known. The numerical variance estimation method and Normal distribution were found to do a good job of predicting variability and probability over a range of values of input signal strength and ordinary coherence.

7.1.2 Uncorrelated Content Estimates for the Calibration Mass

All three uncorrelated content ('noise') estimates were calculated. Because the calibration mass did not contain any resonances (which can cause feedback into the shaker and result in force distortion [33]) in the analysis range, the uncorrelated content in the force measurement was expected to be small. The 'force noise' estimator did indeed calculate very small values of \hat{G}_{mm} over the entire range (up to 30 dB less than \hat{G}_{xx}), but that was the extent of verification possible for this estimator in this measurement. The two uncorrelated content estimates of most interest in the calibration mass FRF measurement are 'shaker noise' and 'response noise'.

Estimates of 'shaker noise' were made on data taken with both shaker attachment methods. Figure 44 shows the results of estimates made using the wire connector. The input force auto spectrum (\hat{G}_{xx}) is fairly flat, with little reduction of force at higher frequencies. Over most of the range the estimate of \hat{G}_{kk} ('shaker noise') is very small, averaging nearly 35 dB below \hat{G}_{xx} . Figure 45, on the other hand, shows \hat{G}_{xx} and \hat{G}_{kk} for the ball joint connector. Here we see the force auto spectrum fall off rapidly at higher frequencies, so that at 1 kHz it is approximately 25 dB below the maximum value obtained near zero Hz. The ball-joint connector is effectively acting as a vibration isolator. The uncorrelated content estimator shows low values of 'shaker noise' near zero frequency, which then increases relative to \hat{G}_{xx} until at the upper end of the range, where it is only

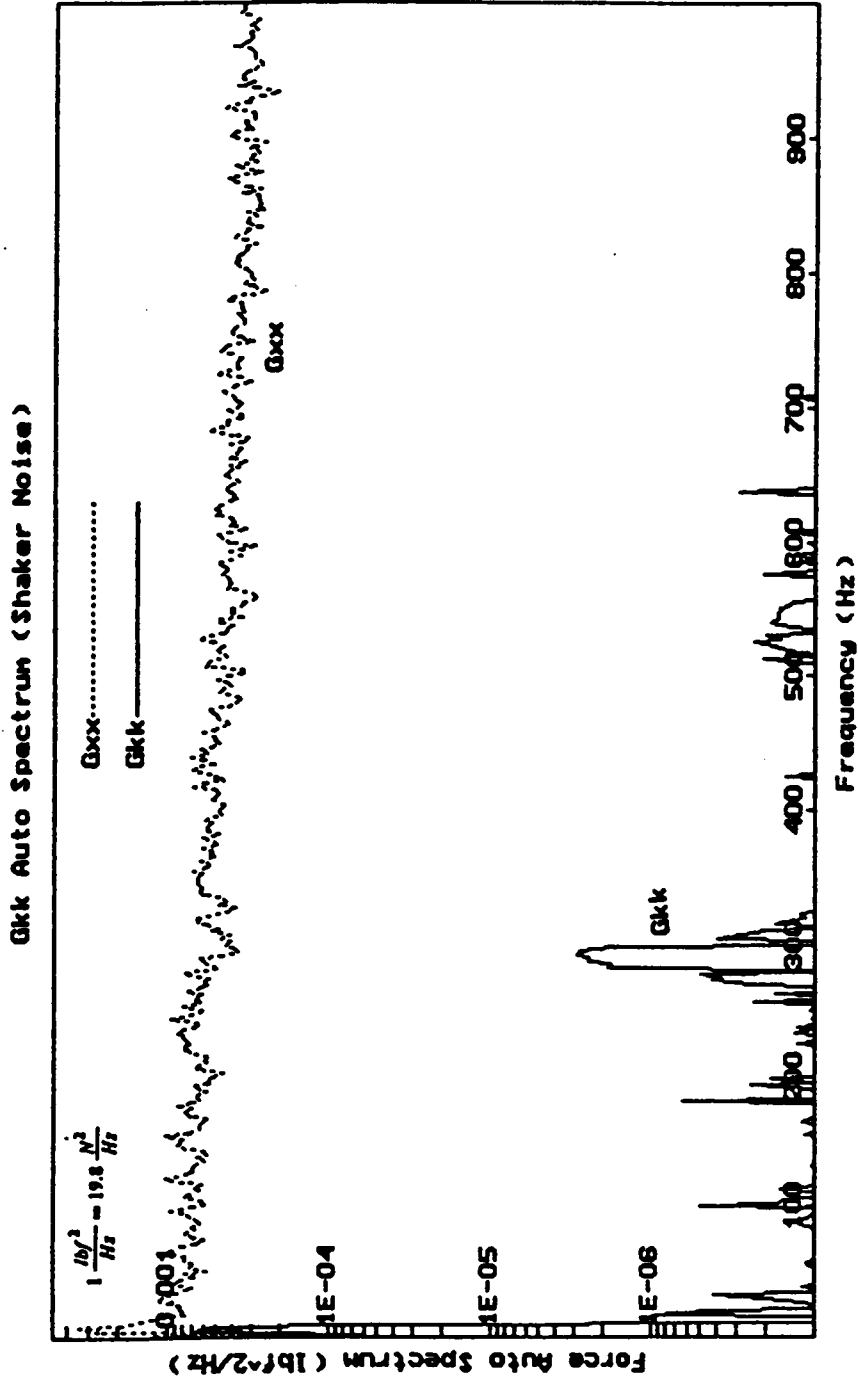


Figure 44. Auto Spectra of Force and Shaker Noise - Wire Connector

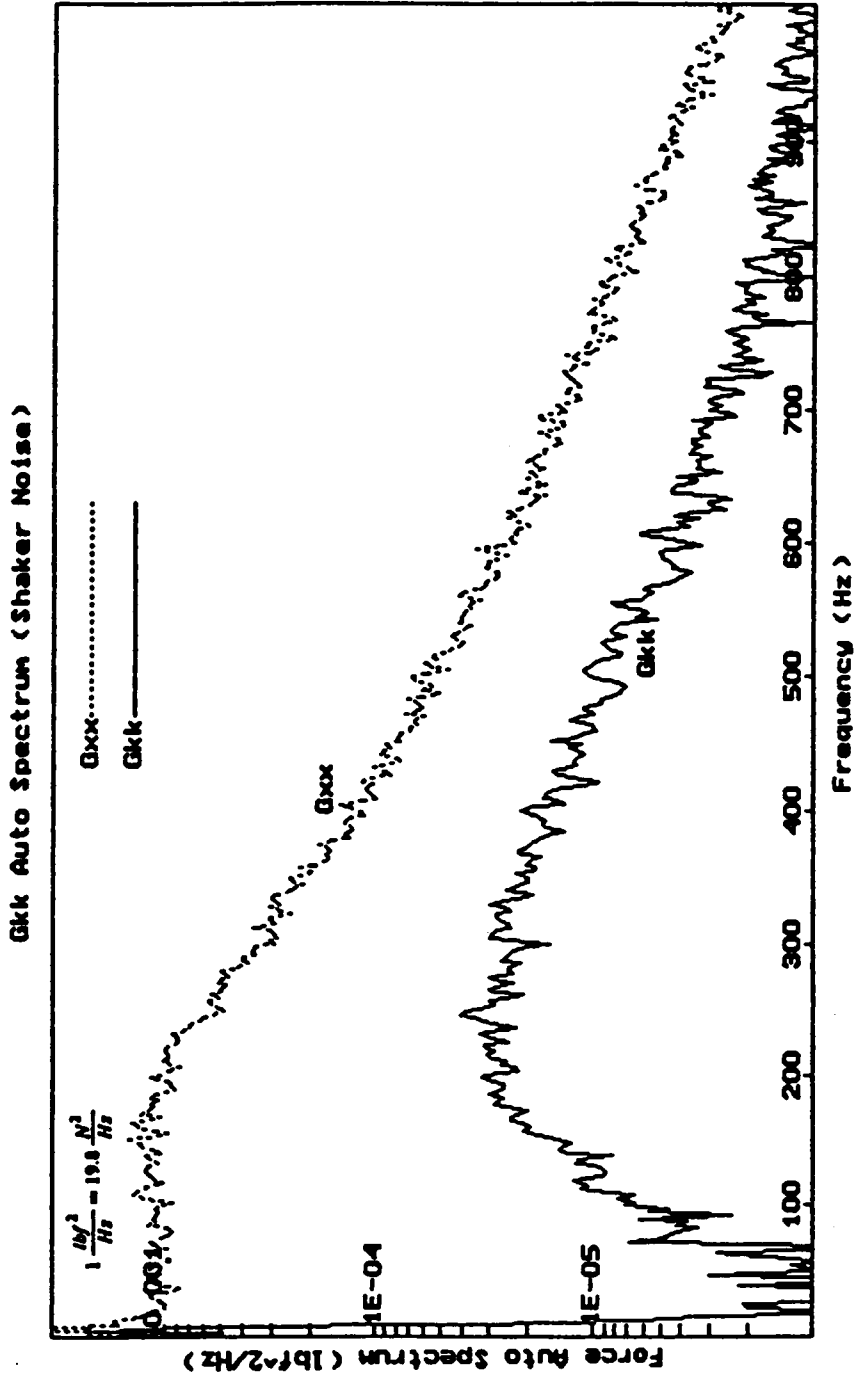


Figure 45. Auto Spectra of Force and Shaker Noise - Ball Joint Connector

5 dB below the force power spectrum. While there is no independent method available to quantitatively verify these estimates, it is worth noting that they follow the trends predicted for the two connectors, i.e., the input force auto spectrum decreases at higher frequencies, and is largely uncorrelated with the source signal.

A discussion of the implications of large values of 'shaker noise' is in order. This uncorrelated content term can arise from either electrical noise in the amplifier or nonlinearities in the amplifier, shaker, and attachment hardware. This discussion will assume the source to be the nonlinearities, which has the effect of changing probability distributions. A base assumption made in most measurement statistics calculations is that of Gaussian (Normal) random signals. Let us assume that the signal generator is indeed producing truly Normal signals. If the amplifier/shaker/hardware FRF, $\Gamma(f)$, is linear, then the force input is also Normal. But if $\Gamma(f)$ is non-linear (as with lost motion in connections), then the force signal is no longer necessarily Normal. A linear approximation of a nonlinear function may be made over a range of input values. For a given signal generator output level let us consider $\Gamma(f)$ to consist of the superposition of a linear approximation plus some nonlinear function. Normal signals (from the signal generator) pass through the linear part and result in a Normal force signal. The Normal signals which pass through the nonlinear part may result in non-Normal forces. Since the total force applied to the structure is a sum of Normal and non-Normal data, it is non-Normal. If a non-Normal force is applied to a structure, then even a completely linear structure will also have a non-Normal response with respect to the input signal generator.

The practical implications of these probability distribution changes are less clear. It can easily be argued that two-channel FRF estimates made with $|^1\hat{H}|$ and $|^2\hat{H}|$ are un-

changed with 'shaker noise'. These estimators do not require that the applied force have a particular distribution; FRF estimates are based solely on averaged levels of force and response. The only difficulty seen with the non-Normal force and response signals is in calculating various statistics (such as, say, the variance of an auto spectrum) which have the Normal assumption as a basis.

A more definite effect of 'shaker noise' is seen in the three-channel estimator. While the two-channel estimators use the entire force or response auto spectra to form their potentially biased estimates, $|\hat{H}|$ uses only those portions of the force and response signals that are linearly correlated with the signal generator. Recall that 'shaker noise' refers to that part of the input force which is not correlated with the signal generator. With large amounts of shaker noise, the cross spectra between the signal generator and force or response signals are relatively small compared to the total signal levels. While the FRF estimates they form are still unbiased, they have higher variability. When using $|\hat{H}|$ it is desirable to minimize the \hat{G}_{kk} ('shaker noise') term. This results in larger, more accurate, cross spectral estimates between the signal generator and other channels, and produces less variable FRF measurements.

The other uncorrelated content term of interest in this measurement is that of the 'response noise', \hat{G}_m . During much of the experimental work there appeared to be a problem with spurious signals in the accelerometer measurement circuitry. Spectral line 'spikes' of varying amplitudes would appear in the output autospectrum. These 'spikes' were at 60 Hz and higher odd harmonics (180, 300, 420, ...), suggesting a ground-loop problem. A multi-meter was used to check for shielding continuity and differences in ground potentials. Every attempt was made to isolate the system. A multiple-outlet connector was used so that all of the equipment was ultimately plugged into a single

110V outlet and the computer serial-port communications line was disconnected. The signal conditioners used on all transducers were battery operated. After several days of frustration, these signals suddenly (in the space of about a minute, with the system untouched) disappeared, and have not reappeared to a significant degree.

The calibration-mass FRF measurement discussed in this section was made while these spurious signals were present. These 'spikes' may be seen as notches in the coherence function of Fig. 40. This 'contaminated' measurement was used because it provided verification for the 'response noise' estimator. Figure 46 shows two output (\hat{G}_{yy}) auto spectra and the calculated estimate of G_m . One of the \hat{G}_{yy} plots and the \hat{G}_m plot are from the FRF measurement data. The second \hat{G}_{yy} plot (labeled 'Comparison' in Fig. 46) was made with no force applied to the system, and is a measurement of the electrical content present in the accelerometer circuit with the system at rest. The significance of this figure is that the estimate \hat{G}_m and the \hat{G}_{yy} measurement made with zero input overlay each other very closely (and are, in fact, difficult to discriminate). The 'response noise' estimator was able to accurately predict, from the FRF measurement data, the level of uncorrelated content in the accelerometer circuit, including the 'spikes' (which did not appear in either of the other two uncorrelated content estimators).

7.2 Results of the Flat-Plate FRF Measurements

FRF measurements were made on an 18 inch (0.457 m) square, 0.125 inch (3.2 mm) thick plate, using both burst and continuous random input signals. The analysis frequency range was 2.5 to 750 Hz and contained about a dozen large resonance peaks as

K1) Gnn Auto Spectrum (Response Noise)

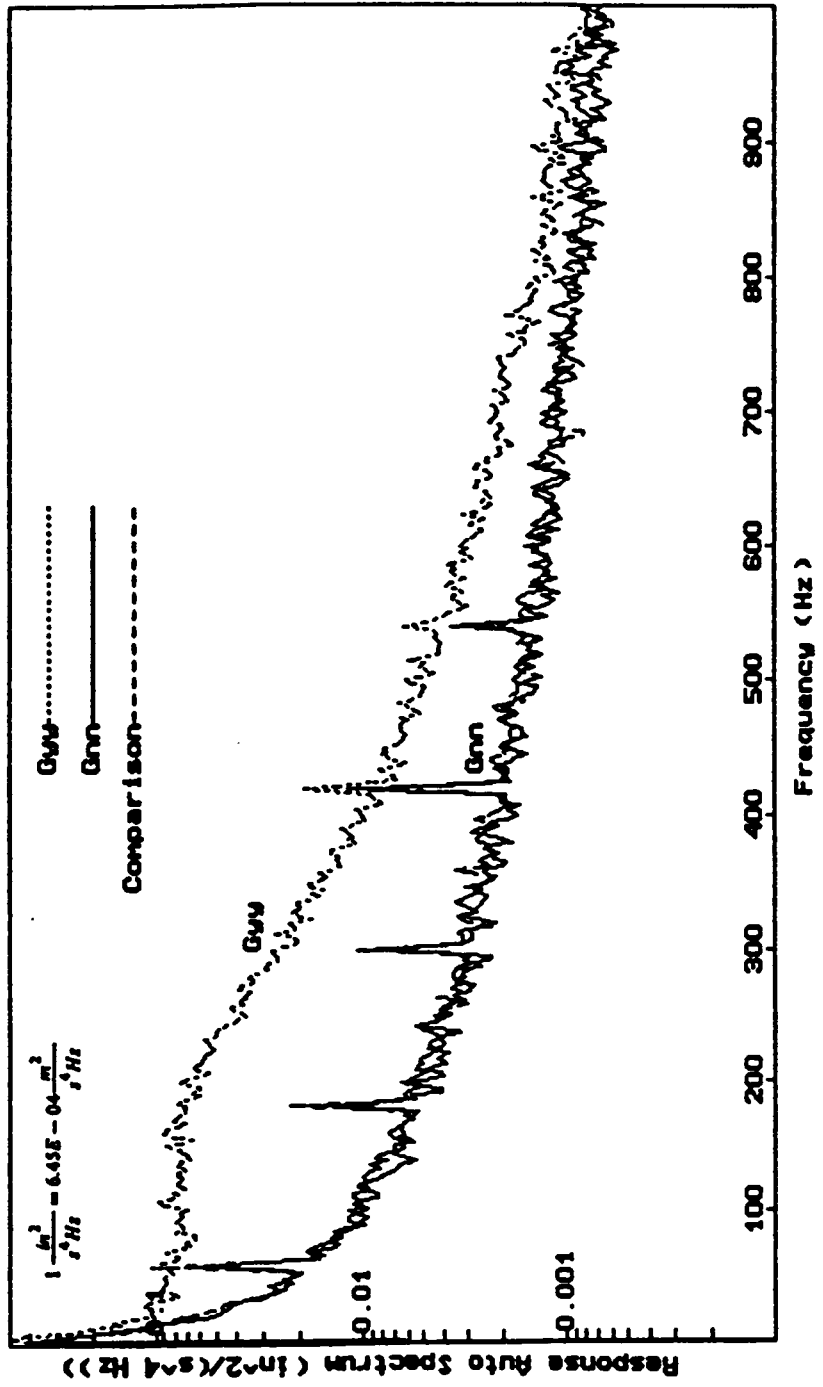


Figure 46. Response Auto Spectra and Uncorrelated Content Estimate

well as a number of smaller peaks. A hammer survey was done to find locations for force and response measurement that would include as many of these resonances as possible in a single FRF. All measurements were made using the one half inch wire connector between the shaker and force gage. Both the continuous and burst random signals had an upper frequency cutoff at about 800 Hz. The burst random signals were set for a duration of 0.1 second at intervals of 3 seconds to allow for response decay. The length of the time record for each measurement was 0.53 seconds.

Lightly damped, high resonance peak structures are difficult to measure accurately using a continuous random input force in the baseband mode. The leakage of energy at the resonance peaks (even with a Hanning window) causes large reductions in coherence. Typical continuous random input coherences at resonances were about 0.3 to 0.5, with a range from 0.1 to 0.9. Coherences at the resonance peaks for the burst random input, on the other hand, seldom fell below 0.95!

7.2.1 Flat-Plate FRF Variance Estimates

The original plan for this section of testing was to obtain accurate values for the 'true' FRF using the swept-sine FRF measurement technique and then evaluate how often this FRF fell within the confidence bounds of an FRF measured with FFT methods. This proved to be untenable for several reasons. The first reason is leakage in the FFT method. The variance estimator that has been developed is only capable estimating random variations in the three-channel FRF estimate. There is no claim that the three-channel estimator is unbiased in the presence of leakage. It is unbiased only in the presence of uncorrelated content in the measurement system. We would, therefore, ex-

pect the swept-sine-measured FRF (which is not susceptible to leakage) to differ significantly from the FFT measured FRF's at certain frequencies. Another, but less predictable, reason centered on apparent long-term variations in the FRF being measured. There are a number of possible reasons for this.

A measured FRF is actually a global measurement of a combination of systems, including transducers, signal conditioners, suspension systems, and the analyzer itself in addition to the structure under consideration. A change in any of these can affect the measurement. Figure 47 shows two FRF measurements made two days apart, using burst random excitation. A number of FRF measurements had been made during this two day period, using various excitation types and levels, but the system was undisturbed in any other manner. The most curious feature of this figure is that there is not an overall shift in the estimates, as one would expect with drift in a transducer calibration factor. We find rather that the estimates coincide closely at some frequencies and differ significantly at others. The most obvious differences occur in regions around 425, 525, and 650 Hz.

One hypothesized explanation for this variation is that the force is being applied to a nodal point of a particular mode. Excitation normal to the plate does not excite this mode, but a moment excitation could. A moment input could occur from slight changes in alignment of the shaker and force gage. This could account for some of the apparent variation in the FRF measurement.

At this point it became necessary to define exactly what the expectations are for the variance estimator. The derivation of the variance estimate was based on uncorrelated content in measured signals and, therefore, should correctly predict the variability of a particular FRF estimate at the time and under the conditions that the estimate was

Long Term Variation in FRF Measurements

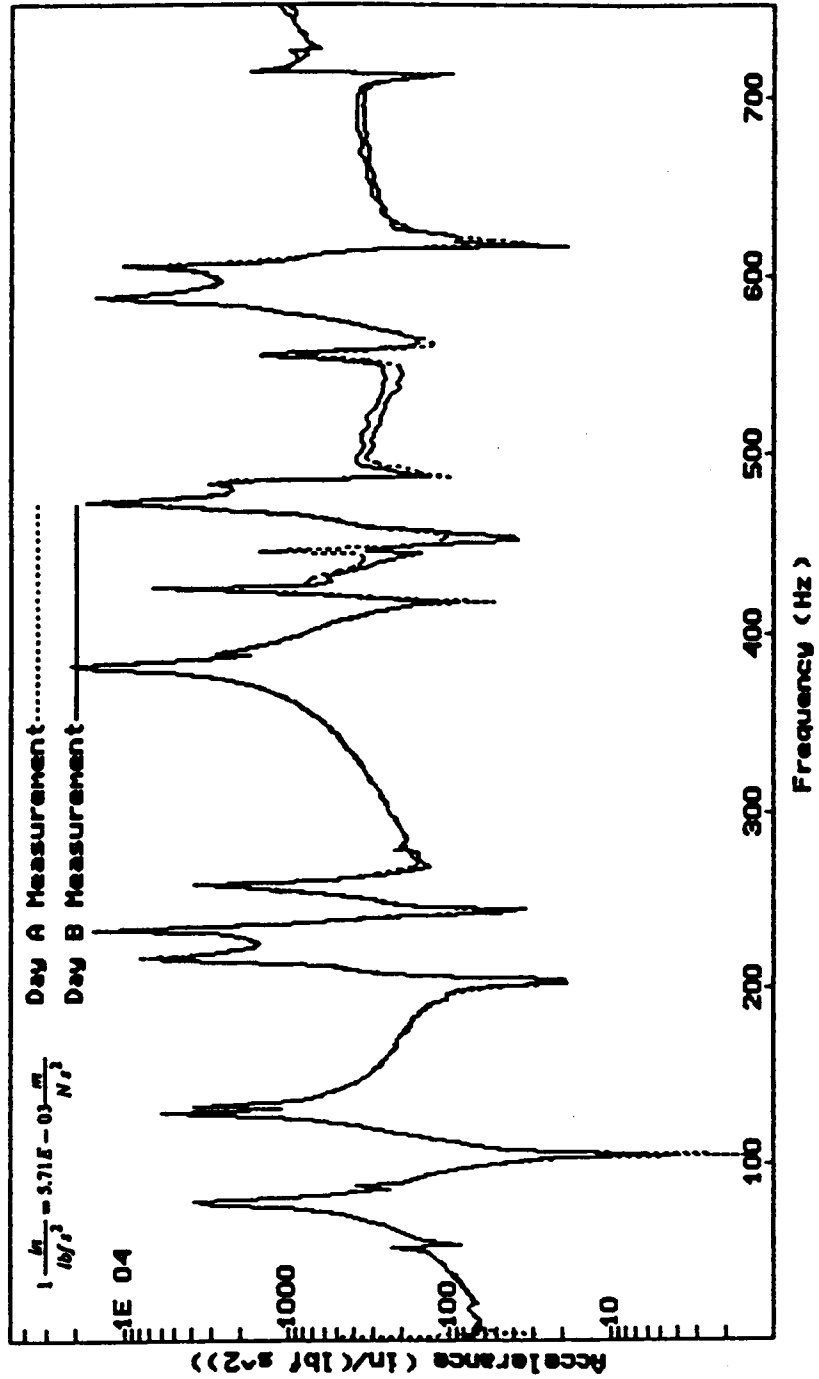


Figure 47. Long Term Variation in FRF Measurements

made. There is no reason to believe that the 'true' structure frequency response will necessarily fall within these bounds; nor for that matter that an FRF measurement made another day under seemingly similar conditions will fall within or close to these bounds. To do the job it was intended to do, it is only necessary to show that the variability of a given measurement is quantified.

The proposed test is as follows: several FRF measurements are made contiguously, variance estimates calculated, and results compared. The assumption here is that there will be little or no change in any system (structure or measurement) parameters over the span of several contiguous averaged measurements. We now need to develop a statistical test for comparison of the measurements.

This statistical test discussion will deal with a general Gaussian random variable x of mean μ and variance σ^2 , but also applies to an FRF magnitude estimate at a single spectral line. We take two random samples of x , x_1 and x_2 , and form the distribution of their difference, $y = x_1 - x_2$. The mean and variance of y are then zero and $\sigma_y^2 = 2\sigma^2$. Let us assume that we know the distribution of x and use our knowledge of σ to place a $+/- 2\sigma$ confidence band about x_1 . We know, by virtue of the Gaussian distribution, that there is about a 95 percent probability that the mean μ falls within this band. What we wish to know is the probability that x_2 will fall within the band placed about x_1 . The probability that x_2 will fall within a 2σ range of x_1 is the same as the probability that $|x_2 - x_1| \leq 2\sigma$. The distribution y is the distribution of the difference of x values, with a standard deviation $\sigma_y = \sqrt{2}\sigma$. This leads to the standardized Normal variable z :

$$z = \frac{y}{\sigma_y} = \frac{x_2 - x_1}{\sqrt{2}\sigma}$$

We are interested in the probability that $y \leq 2\sigma$, or

$$Prob\left[|z| \leq \frac{2\sigma}{\sqrt{2}\sigma}\right] = Prob[|z| \leq \sqrt{2}] = 0.84$$

where this value was found from a statistical table of the standardized Normal variable.

We now apply this result to the FRF magnitude estimates.

The Normality of the FRF magnitude under most conditions was verified in the PDF simulations. If we have an accurate estimate of the variance at a given spectral line, we would expect that 84 percent of the time an FRF estimate at this spectral line would fall within the 2σ bands placed about a previous estimate. *If we assume that the variance estimator works equally well at each spectral line (an assumption which was discussed in Section 6.4.1, with further discussion to follow in the next section), then we would expect the FRF magnitude estimates at 84 percent of the spectral lines in a single measurement to fall within the confidence bands placed about a previous estimate. How well this expectation was met was the test used to evaluate the FRF variance estimator in the flat-plate measurements.*

7.2.1.1 Variance Estimates Using Burst Random Excitation

Two sets of three contiguous FRF measurements each were made, with 100 averaged sample records per measurement. The data sets were taken with a two day separation between them. Figure 47 (previously discussed) compares one FRF from each set. Because of the differences in the measured FRF's from one set to another, only comparisons within a set could be made. The comparison method used was to plot the FRF from one measurement over the estimated $\pm i 2\sigma$ bounds from another estimate (in the

same set), and to determine the percentage of spectral lines at which the FRF estimate was within the bounds. This was done in a variety of combinations and permutations. The resulting percentages for comparisons within the 'Day A' set ranged from 62 to 70 percent, with an average of 67. Comparisons within the 'Day B' set resulted in percentages from 73 to 77, with an average of 75 percent. The differences in these figures imply that there were unspecified changes not only in the FRF measurement between the two days, but in the variability of the data as well. Further discussion will use the average result from the two sets, 71 percent.

We may use this average result to determine a correction factor for the standard deviation estimator, if we assume that this correction factor is the same at all frequencies. In the derivation for the 'target' probability of 84 percent, we used the form

$$Prob\left[z \leq \frac{2\sigma}{\sqrt{2}\sigma}\right] = Prob[z \leq \sqrt{2}] = 0.84$$

where the σ terms canceled because they were identical. Using the average probability result of 0.71 we rewrite this as

$$Prob\left[z \leq \frac{2\sigma_{estimated}}{\sqrt{2}\sigma_{true}}\right] = Prob\left[z \leq \frac{\sqrt{2}\sigma_{estimated}}{\sigma_{true}}\right] = 0.71$$

We find, from a statistical table, a value of $z \leq 1.06$ associated with the probability of 0.71. Then

$$\sqrt{2} \frac{\sigma_{estimated}}{\sigma_{true}} = 1.06$$

from which we find that the average estimate is 75 percent of the true value, or conversely

$$\sigma_{true} = 1.33\sigma_{estimated}$$

This factor was tested by application to a pair of contiguous FRF measurements from Day B. When the confidence bands were increased by 133 percent (from 2 to 2.66 standard deviations), the percentage of 'in bounds' lines rose from 73 to 82 percent.

There is no way of determining at this point whether this correction factor is a general result or specific to this data set. The error may result from the variance estimation method or from base assumptions about the signal generator distribution function. Recall that in the numerical integration variance estimation method we start with calculated estimates of the standard deviations of the cross spectral lines. These estimates are based on the assumption of a Normal source signal. If this signal were not truly Normal, then estimates of the cross spectral variance estimates would be in error. This error could magnify in the following estimates.

As discussed in Section 6.4.1 there has been an assumption made in these estimates that the FRF variance estimator performs equally at all regions of the FRF. A qualitative verification of this may be made by comparing the width of the confidence bounds with the apparent variability of the FRF estimate at various frequencies. For example, in the calibration mass figures (Figs. 40 through 43) we saw that the confidence bounds were narrow in the 2-300 Hz range, where the FRF estimate was nearly a straight line and the bands were wide where the FRF estimate became very variable. The calibration mass data show that for a constant value FRF the FRF variance estimate does a good job of predicting variance based on varying signal levels and varying uncorrelated content. The remaining question is how well the variance estimator performs over a wide dynamic range of FRF values.

Figure 48 shows the confidence bounds from one FRF measurement made on 'Day B', and a contiguous FRF plotted for comparison. In this figure we find the contiguous FRF to fall within the (uncorrected) confidence bounds at 73 percent of the spectral lines. Included at the top of this figure are vertical 'tic marks' which indicate the spectral lines at which the FRF *did not* fall within the confidence bounds. While there appear to be clusters of these marks at certain frequencies, they are not clearly related with any particular feature of the FRF, such as say resonance peaks or anti-resonance valleys.

A more quantitative verification would be preferred, however. To this end 12 prominent resonances and 8 anti-resonances were chosen. Then for each comparison of contiguous FRF's and confidence bounds, the percentage of FRF values at these resonances and anti-resonances that were within the bounds were counted. If the variance estimator is indeed uniform in accuracy, we would expect about the same percentage of values to be in bounds at the peaks and valleys as there are over the whole FRF. The average result at the resonances was 71 percent, while 78 percent of the anti-resonance values were within the bounds. The sample size is too small to draw any rigorous conclusions, but these values are certainly close to the overall 73 percent.

7.2.1.2 Variance Estimates Using Continuous Random Excitation

One set of three contiguous 100-average FRF measurements was made on each of two days, as with the burst random excitation FRF measurements. The percentages of FRF measurements within the confidence bands of contiguous measurements were consistent over the two days' data, unlike the burst random excitation data. The percentages ranged from 59 to 69 percent, with an average of nearly 64 percent. This is considerably lower than the burst random results, and well below the desired value of 84 percent. The

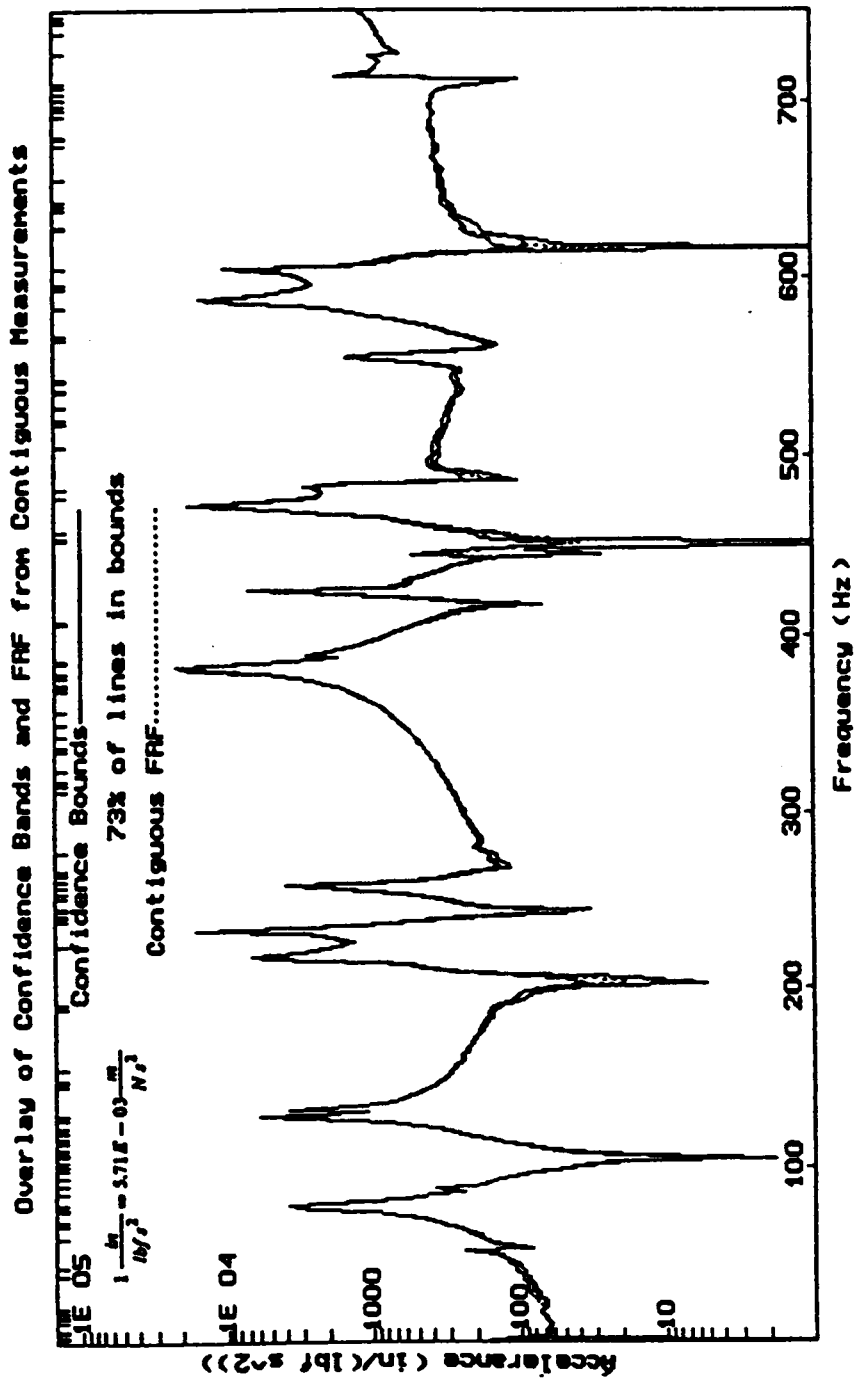


Figure 48. FRF and Two Standard Deviation Bounds for Contiguous Measurements

value of the Normalized variable, z , corresponding to a probability of 0.64 is approximately 0.915. Calculating a correction factor for the FRF variance as before results in an estimated correction of 1.55.

When the FRF variance correction factor was applied to the FRF estimates obtained using burst random excitation, the percentage of FRF estimates within bounds increased from 73 to 82 percent (with 84 percent predicted). This was not the case with the FRF estimates obtained from continuous random excitation. On the average, the confidence bounds had to be increased to about plus/minus five standard deviations (a correction of about 2.5) to obtain percentages in the vicinity of 84. The fact that the percentages did not follow the prediction using the Normal distribution assumption is a strong indication that the data obtained with the continuous random excitation is non-Normal. Whether this might be caused by leakage, the windowing procedure, or the nature of the excitation is unclear. Further insight into potential problems in the data may be gained by examining some typical values.

There is a large resonance peak at 382.5 Hz (spectral line 205). Using burst random excitation the coherence was found to be $\hat{\gamma}_{yx}^2 = 0.95$, and the FRF estimates $|\hat{H}^1|$, $|\hat{H}^2|$, and $|\hat{H}^3|$ ranged from 20,190 to $21,320 \frac{in}{lbf - s^2}$ (115.3 to $121.7 \frac{m}{N - s^2}$), with the estimated standard deviation of the three-channel FRF estimator being about 355 (2.03). For the continuous random case however, the coherence at the same spectral line was $\hat{\gamma}_{yx}^2 = 0.02(!)$, with the FRF magnitude estimates being: $|\hat{H}^1| = 2,156 \frac{in}{lbf - s^2}$ ($12.3 \frac{m}{N - s^2}$), $|\hat{H}^2| = 101,900$ (581.9), and $|\hat{H}^3| = 40,730$ (232.6). The estimated standard deviation of $|\hat{H}^3|$ was 12,090 (69.0). The low coherence and wide range of estimates is caused by severe 'leakage' in the FFT measurement. The effect of this leakage on the distribution of spectral estimates is unknown, but it is cer-

tainly possible that it causes the Normal assumption to be violated. While errors and variations of this size were not the case at every spectral line, they are also not atypical values.

Another difference between the burst and continuous random excitation data sets is the use of the Hanning window in the continuous random excitation data acquisition. Nuttall [34,35] discusses the effect of windowing on spectral estimates, including increases in the variance of estimates under certain conditions. It is unclear how these changes in variance estimates might be found or implemented in a given experimental test. Even if a variance 'correction' factor could be determined for the cross spectral magnitude real and imaginary part variance estimates (Eqs. 2.29 and 2.31) it would be difficult (because of nonlinear magnitude bias effects) to incorporate this correction in the covariance term of Eq. 2.47. An accurate estimate of this term is needed for calculating the correlation coefficient of Eq. 2.48. Recall also that the calibration mass tests were carried out using continuous random excitation with a Hanning window and no corrections were needed. Also, the probabilities associated with different width confidence bands tended to follow the expectations of a Normal distribution in that case. The only clear difference between the calibration mass and flat plate tests was the lightly damped nature of the plate. It may be that severe leakage can degrade the numerical integration variance estimates. Whatever other value is found in this experimental work, it has certainly impressed upon this experimenter the value of burst random excitation when measuring lightly damped structures!

7.2.2 Flat-Plate Uncorrelated Content Estimates

Estimates of 'shaker noise' (\hat{G}_{kk}), 'force noise' (\hat{G}_{mm}), and 'response noise' (\hat{G}_{nn}) were made from data obtained with both burst and continuous random excitation. Before these results are examined, a discussion of the dynamics of the measurement system (including the plate, shaker, attachment hardware, and suspension) is in order. The plate and shaker are suspended by long shock cords. The shaker is connected by a stinger to the force gage. This combination constitutes a dynamic system whose behavior is different from that of the plate alone. The system resonances will not generally occur at the same frequencies as the plate resonances. Since the force applied to the plate and the plate response are measured, a true representation of the plate FRF is still obtained. However, the combination-system dynamics do appear in the auto-spectra and amplifier/shaker FRF, $\Gamma(f)$.

In the calibration mass force auto spectrum (\hat{G}_{xx}) previously shown in Fig. 44 we saw a reasonably uniform input force level over the measurement frequency range. Yet in Fig. 49 we see that this is no longer the case. The force auto-spectrum shows strong resonance peaks and anti-resonance valleys. These are the result of interactions between the shaker and plate [36]. In addition to the force auto spectrum, Fig. 49 also shows the estimate of G_{kk} , with the structure FRF shown for comparison. Tomlinson [33] shows that there is effectively a feedback loop from the structure FRF to the shaker/amplifier FRF, $\Gamma(f)$. In a simplified two-degree-of-freedom model of the measurement system consisting of the shaker mass and structure modal mass Olsen [36] demonstrates that the shape of the force auto spectrum shown in Fig. 49 may be expected when measuring a lightly damped structure. One notable result was showing that the 'valleys' in the force auto spectrum coincide with structure resonances, and that the depth of these valleys

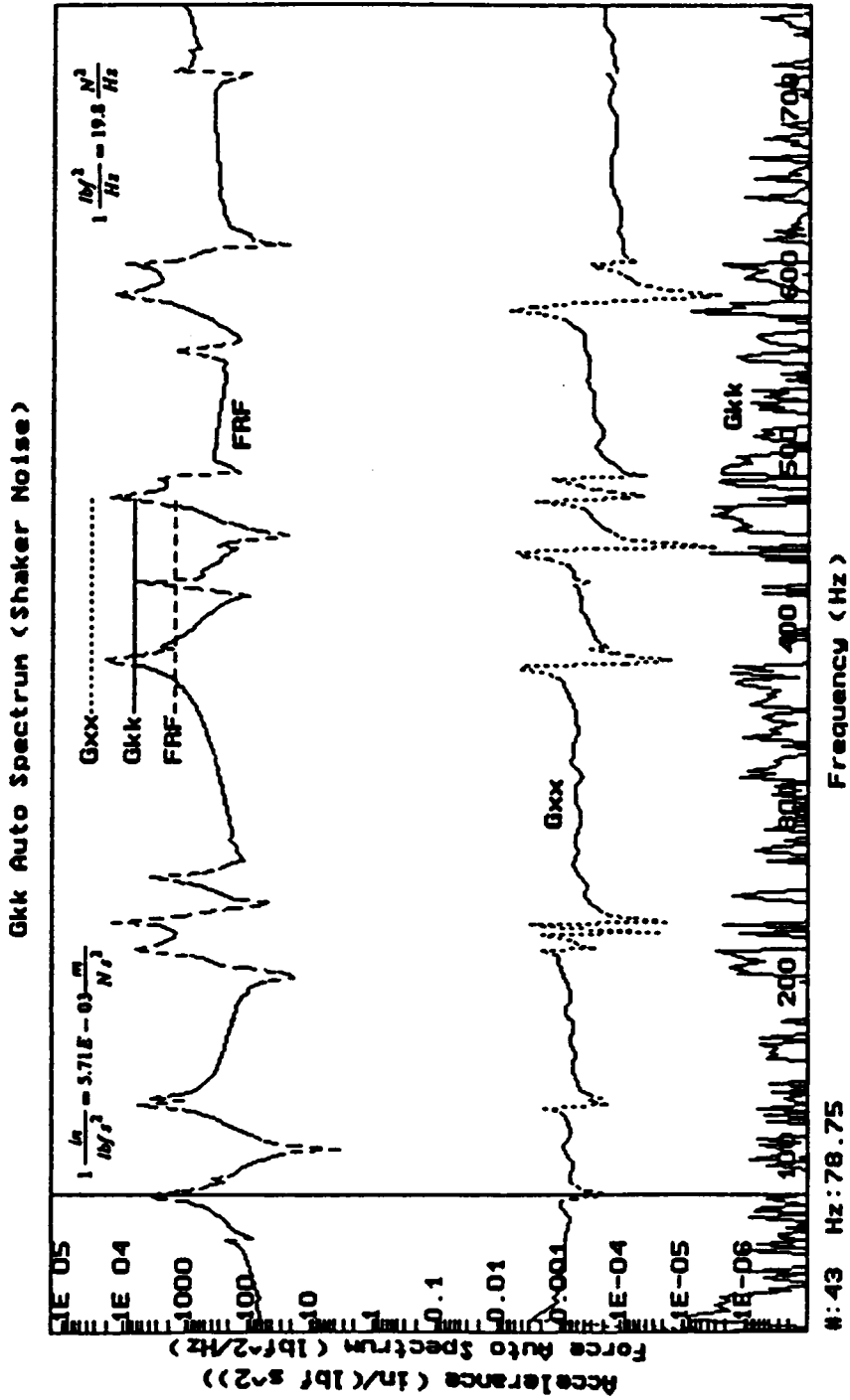


Figure 49. 'Shaker Noise' and Force Auto Spectra - Burst Random Excitation

may be reduced by decreasing the shaker armature mass. The alignment of the FRF peak and \hat{G}_{xx} valley is illustrated in Fig. 49 by a vertical line cursor just below 100 Hz. Another effect of the shaker/structure interaction is to cause the response auto spectrum to have peak values at frequencies other than those of the structure resonances.

Both the G_{kk} estimates in Fig. 49 and the G_{mm} estimates of Fig. 50 are about 50 dB below the measured force auto spectrum \hat{G}_{xx} . This data set was obtained with burst random excitation. This appears to be the limit of the ability of these estimators to discriminate uncorrelated content in an auto spectrum. We may only infer that the shaker and force uncorrelated content terms are too small to measure in this data set. Figures 51 and 52 show the same estimates on data obtained with continuous random excitation and a Hanning window. Nothing was changed between measurements except the excitation and window, yet we now see large estimates of shaker and force noise at peaks and valleys of the force auto spectrum. Uncorrelated content in the sense of true electrical or other 'noise' should be independent of the excitation signal.

The value of using burst random excitation to reduce leakage and increase coherence at resonance has been discussed. It is apparent that the uncorrelated content estimators are unable to discriminate between 'true noise' and the degradation of signals caused by leakage when continuous random excitation is used. We see that the uncorrelated content estimates are high in regions of the force auto spectrum where there are large differences in the measured values between adjacent spectral lines. These are prime areas for the 'leakage' of energy from one spectral line to another. Another term for this error is frequency resolution bias error. An interesting, though not conclusive, observation is that the peaks of the shaker noise estimates tend to lie at the same frequencies where the

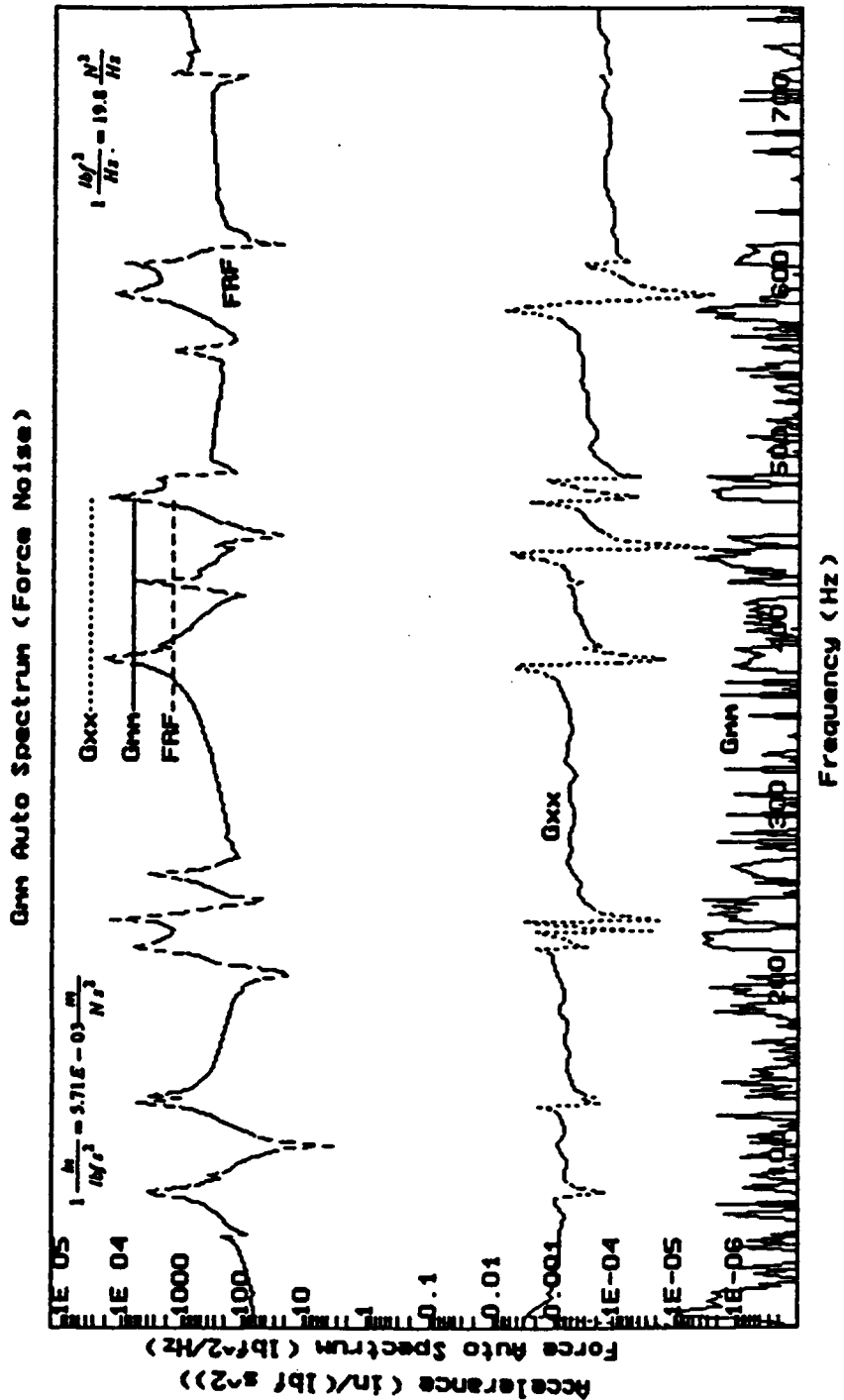


Figure 50. 'Force Noise' and Force Auto Spectra - Burst Random Excitation

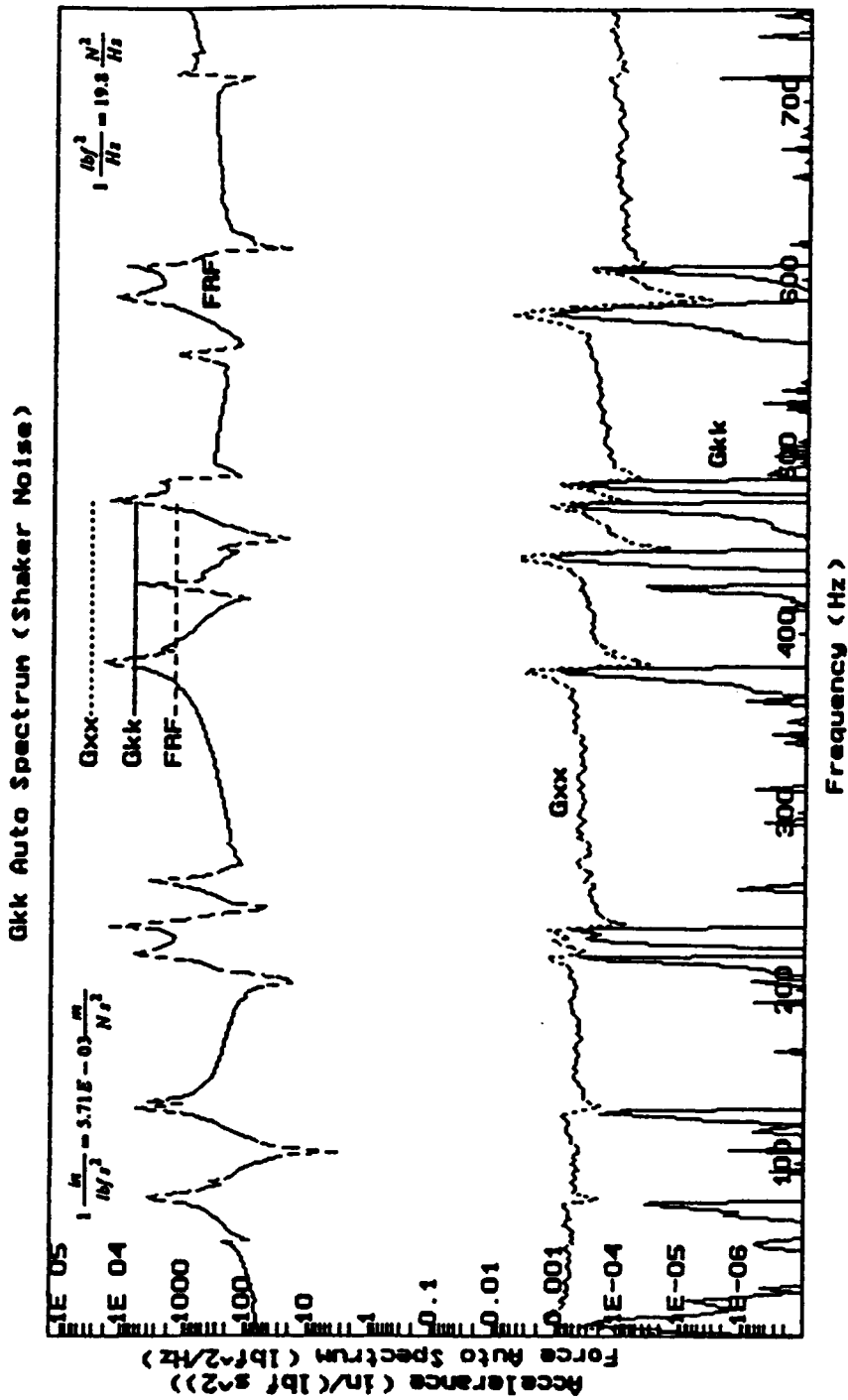


Figure 51. 'Shaker Noise' and Force Auto Spectra - Continuous Random Excitation

force auto spectrum peaks, while the force noise estimate peaks are closer to the valleys of the force auto spectrum.

The inability to distinguish between external noise and leakage is not a serious deficiency in the estimators. Either noise or leakage will negatively affect a measurement and should be eliminated or reduced. In addition, one would expect external noise to be continuous over a range of frequencies or exhibit peaks at frequencies that are not related with system behavior. Both of these behaviors were seen in the response noise of Fig. 46. If the uncorrelated content estimates peak at frequencies near resonances, then either leakage or nonlinear behavior should be suspected.

Figures 53 and 54 show overlays of the output power spectrum \hat{G}_y , the response noise \hat{G}_m , and the measured frequency response function, $|\hat{H}|$. Because the burst-random-measured FRF estimates appear to be the most precise, an average of three of these is plotted in both figures as the comparison FRF. We see the response noise peaks coincide with resonance regions of the FRF, although the noise estimates are much lower with the burst random excitation. At some of the frequencies of the continuous random data we see that \hat{G}_m is almost equal to \hat{G}_y , for example, at about 425 Hz in Fig. 54. Because the uncorrelated content estimates are related to FRF behavior, we would suspect that they are primarily estimates of nonlinearity or leakage, rather than system 'noise'.

In the simulations it was found that response uncorrelated content estimates were viable only to within one percent or so of the response auto spectrum (maximum signal-to-noise estimation capability of about 20 dB). In these figures we rarely see the response noise estimates fall further than 20 dB below the auto spectrum, confirming that as a practical limit of the response noise estimates.

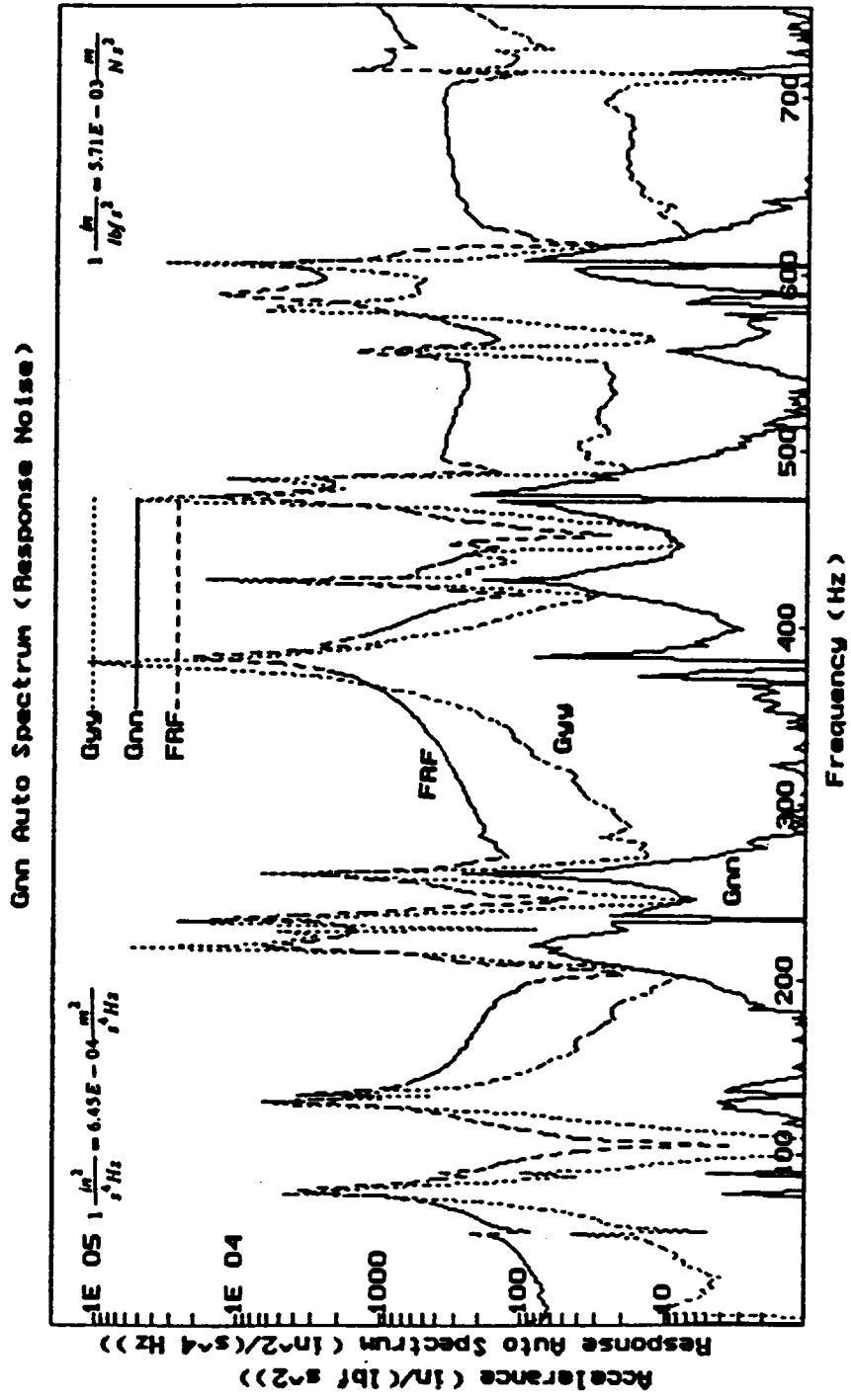


Figure 53. 'Response Noise' and Auto Spectra - Burst Random Excitation

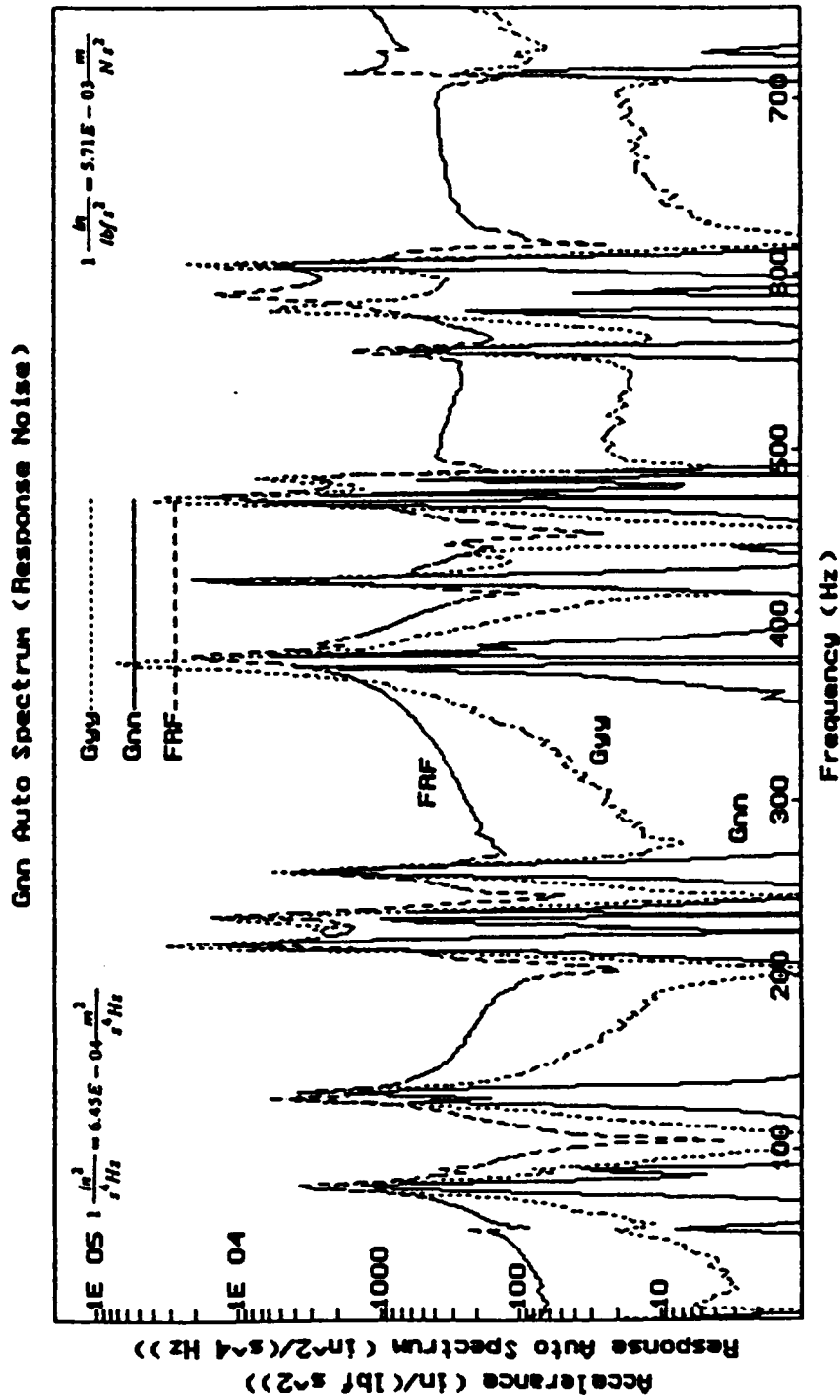


Figure 54. 'Response Noise' and Auto Spectra - Continuous Random Excitation

A singularity is seen in data obtained with either method of excitation, and occurs in regions where the peaks of \hat{G}_{yy} and the FRF do not coincide, but are separated by one or more spectral lines. At these regions we see very deep notches in \hat{G}_{xx} that extend below the scale of the graph. Clear examples of this can be seen in either figure at about 230 Hz, 380 Hz, and 475 Hz. Yet intuition of the behavior of physical systems would argue that the more or less continuous estimates of \hat{G}_{xx} on either side of these singularities are more reasonable expectations for system behavior than sudden drops at single spectral lines. Considering the apparent limit on the dynamic range of the estimator, these observations may possibly have no basis other than being some type of numerical singularity. From Eq. 2.21 we see that this estimate is based on a ratio of coherences, all of which are near unity at the singularity spectral lines. Even small errors in the estimates of these coherences could have large effects on the final result (since, at resonances, G_{yy} is very large). Yet the appearance of this 'glitch' was so consistent that it was considered at least worthy of mention.

Chapter 8 - The Three-Channel Estimator in Multiple Input/Output Estimates

The multiple-input measurement model shown in Fig. 55 is an extension of the single input three-channel model. While only a single output is shown in Fig. 55, this model is also valid for multiple-output measurements, where each output can be considered separately.

The source signal from each independent signal generator is amplified and applied to a shaker to produce a force. The force applied to the structure at any input location is the sum of the amplified and transduced source signal at that location, 'crosstalk' from other applied forces, and an uncorrelated force resulting from nonlinearities in amplification and signal-to-force transduction. This uncorrelated force is the 'shaker noise' discussed earlier, while the 'crosstalk' between input locations is caused by the frequency-dependent structural response.

This crosstalk may be seen by the following exercise. Consider a multiple shakers excited system driven by separate and uncorrelated random source signals. If the source

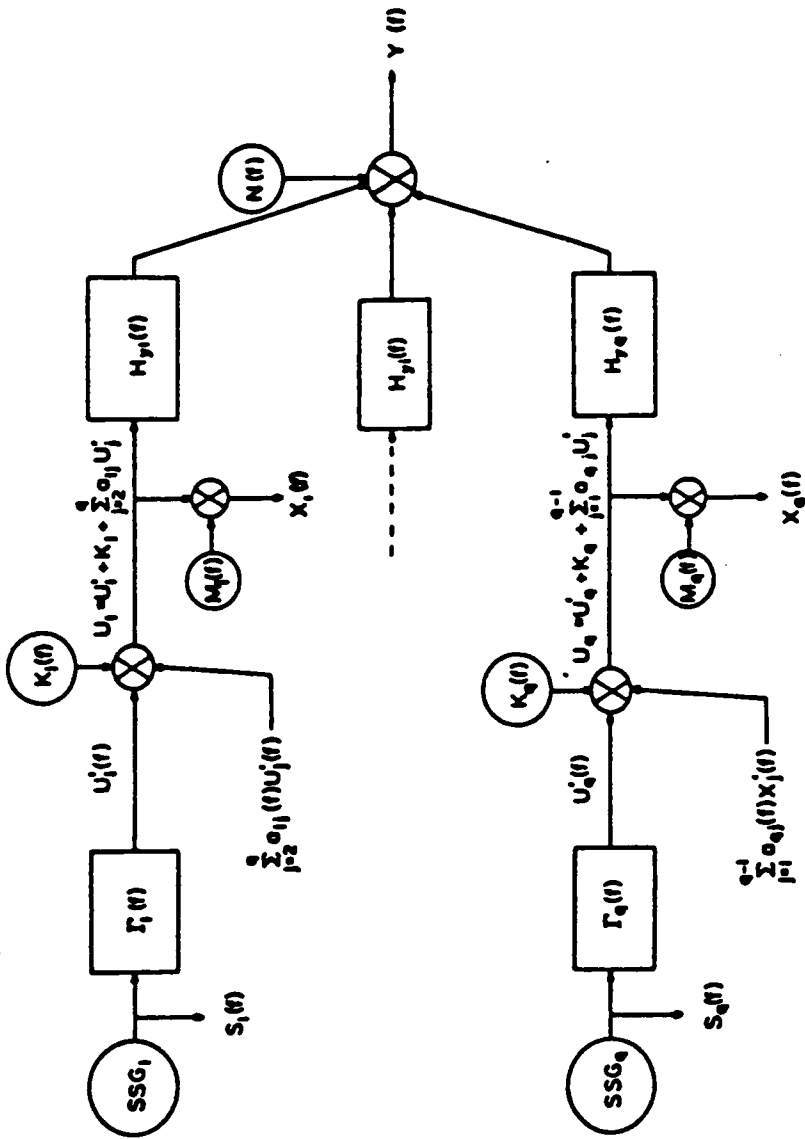


Figure 55. Multiple Input Measurement Model

signal is removed from one shaker (shut down the shaker), a force will nevertheless be measured at that shaker location. This force is directly correlated with the other input forces. This measured force is the result of acceleration at the measurement point caused by structural response to the forces applied at other locations. The force gage measures the inertia forces of the force transducer's mass above the force gage, of the stinger mass, and of the mass of the shaker armature. These inertia forces are correlated to the force signals at the active shaker locations. These correlated force signals represent a 'true' force input to the structure at the inactive shaker location.

Compounding the crosstalk described above is the possibility of noise in the measurement process which results in contaminated estimates of these forces. Possible noise in the structure response measurement also results in a contaminated output measurement.

8.1 Development of the Multiple Input/Output Estimator

The multiple input-multiple output FRF notation that will be used here was proposed by Cobb and Mitchell [18]. The general form of the notation is

$${}^a_n\hat{H}_{ij}(f)$$

where a is the estimator type, n is the number of averages in the measurement, and i and j are output / input locations, respectively. As an example, ${}_{150}^i\hat{H}_{32}(f)$ is an \hat{H} type estimate based on 150 averages of the response at location 3 caused by a force applied at location 2.

This derivation will begin by developing equations for the unbiased estimates of system FRF's in the presence of multiple inputs and a single output, Y . These equations will then be expanded in matrix form for the multiple input/multiple output case.

There are q uncorrelated random signal generators which drive q amplifiers, q shakers, and q force gages. Each input location has it's own frequency-dependent source-to-force FRF, $\Gamma_i(f)$, and 'shaker noise' term, $K_i(f)$. The portion of the 'true' force applied to the structure at location i , U'_i , that is directly related to the generated signal, $S_i(f)$ can be represented as

$$U'_i(f) = S_i(f)\Gamma_i(f) \quad (8.1)$$

From the discussion on the measurement model, there is a component of force at location i that is caused by input forces at all other locations, j . This 'crosstalk' is modeled by a frequency-dependent crosstalk term, $a_{ij}(f)$. This represents the *force* at location i caused by the *force* at location j . Including the 'shaker noise' term, the total 'true' force acting on the structure at location i is given by

$$U_i(f) = U'_i(f) + K_i(f) + \sum_{\substack{j=1 \\ j \neq i}}^q a_{ij}(f)U'_j(f) \quad (8.2)$$

If a_{ii} is defined as unity crosstalk gain, Eq. 8.2 becomes

$$U_i(f) = K_i(f) + \sum_{j=1}^q a_{ij}(f)U'_j(f) \quad (8.3)$$

$$a_{ii}(f) = 1.0$$

The measurement of the true force, $U_i(f)$, is contaminated by transduction noise, $M_i(f)$

$$X_i(f) = U_i(f) + M_i(f) \quad (8.4)$$

Considering the presence of noise in the output signal, $N(f)$, the measured output signal becomes

$$Y(f) = \sum_{i=1}^q H_{yi}(f) \left[\sum_{j=1}^q a_{ij}(f) U_j(f) + K_j(f) \right] + N(f) \quad (8.5)$$

The one-sided cross spectral density function between a given input force $X_i(f)$ and the response $Y(f)$, G_{yx_i} , is given by

$$G_{yx_i}(f) = \lim_{T \rightarrow \infty} \frac{2}{T} E[X_i^*(f) Y(f)] \quad (8.6)$$

where $E[\quad]$ indicates the expectation of the argument and T is the length of the measured time record. The one-sided cross spectral density function between source k and the output Y is given by

$$G_{ys_k}(f) = \lim_{T \rightarrow \infty} \frac{2}{T} E[S_k^*(f) Y(f)] \quad (8.7)$$

The expectation of the product of $S_k^*(f)$ and $Y(f)$ is given by

$$E[S_k^*(f) Y(f)] = \sum_{i=1}^q H_{yi}(f) \left\{ \sum_{j=1}^q a_{ij}(f) E[S_k^*(f) U_j(f)] + E[S_k^*(f) K_j(f)] \right\} + E[S_k^*(f) N(f)]; \quad a_{ii}(f) = 1.0 \quad (8.8)$$

Because the source generator is uncorrelated with the shaker noise and output noise, the terms containing $K_j(f)$ and $N(f)$ are zero. Applying the limit and scaling factor $\frac{2}{T}$ of Eq. 8.7 leads to

$$G_{y_s k}(f) = \sum_{i=1}^q H_{y_i}(f) \sum_{j=1}^q a_{ij}(f) G_{u'_{j s k}}(f) \quad (8.9)$$

Similarly, the expectation of the product of $S_k^*(f)$ and $X_i(f)$ is

$$\begin{aligned} E[S_k^*(f)X_i(f)] &= \sum_{j=1}^q a_{ij}(f) E[S_k^*(f)U'_j(f)] + E[S_k^*(f)K_i(f)] \\ &+ E[S_k^*(f)M_i(f)]; \\ a_{ij}(f) &= 1.0 \end{aligned} \quad (8.10)$$

For compactness the frequency function arguments in all frequency-domain terms are dropped. As before, the uncorrelated content terms become zero in the expectation operation. Applying the limit and scaling factor of Eq. 8.7 to Eq. 8.10 yields

$$G_{x_i s k} = \sum_{j=1}^q a_{ij} G_{u'_{j s k}} \quad (8.11)$$

But $G_{u'_{j s k}} = 0.0$ when $j \neq k$, so

$$G_{x_i s k} = a_{ik} G_{u'_{k s k}}; \quad a_{kk} = 1.0 \quad (8.12)$$

Equations 8.9 and 8.11 are now applied to a two input-single output system. Expanding Eq. 8.9 for source 1

$$G_{y_s 1} = H_{y_1} G_{u'_{1 s 1}} + H_{y_1} a_{12} G_{u'_{21}} + H_{y_2} a_{21} G_{u'_{1 s 1}} + H_{y_2} G_{u'_{2 s 1}} \quad (8.13)$$

The cross spectral density $G_{u'_{2s_1}}$ is zero because U'_2 is the uncrosstalked part of the input at point two. Therefore,

$$G_{ys_1} = H_{y1}G_{u'_{1s_1}} + H_{y2}a_{21}G_{u'_{1s_1}} \quad (8.14)$$

Following a similar development using Eq. 8.9 and source 2 yields

$$G_{ys_2} = H_{y2}G_{u'_{2s_2}} + H_{y1}a_{12}G_{u'_{2s_2}} \quad (8.15)$$

Assembling Eqs. 8.14 and 8.15 in a matrix formulation yields

$$\begin{bmatrix} G_{ys_1} & G_{ys_2} \end{bmatrix} = \begin{bmatrix} H_{y1} & H_{y2} \end{bmatrix} \begin{bmatrix} G_{u'_{1s_1}} & a_{12}G_{u'_{2s_2}} \\ a_{21}G_{u'_{1s_1}} & G_{u'_{2s_2}} \end{bmatrix} \quad (8.16)$$

Substituting Eqs. 8.12 in Eq. 8.16 yields

$$\begin{bmatrix} G_{ys_1} & G_{ys_2} \end{bmatrix} = \begin{bmatrix} H_{y1} & H_{y2} \end{bmatrix} \begin{bmatrix} G_{x_1s_1} & G_{x_1s_2} \\ G_{x_2s_1} & G_{x_2s_2} \end{bmatrix} \quad (8.17)$$

This matrix equation can be used to find the frequency response functions between the two inputs, X_1 and X_2 , and any output location Y . Inverting the cross spectral matrix in Eq. 8.17 and subscripting both the H and Y terms to reflect multiple output locations yields

$$\begin{bmatrix} H_{y,x_1} & H_{y,x_2} \end{bmatrix} = \begin{bmatrix} G_{y,s_1} & G_{y,s_2} \end{bmatrix} \frac{\begin{bmatrix} G_{x_2s_2} & -G_{x_1s_2} \\ -G_{x_2s_1} & G_{x_1s_1} \end{bmatrix}}{(G_{x_1s_1}G_{x_2s_2} - G_{x_1s_2}G_{x_2s_1})} \quad (8.18)$$

Once the matrix is inverted the FRFs may be found by matrix multiplication.

Equation 8.17 may be expanded to any general multiple degree-of-freedom system with q input forces and p output measurement locations. The only requirement is that there be q uncorrelated source signals driving the q shakers. For a 2 input ($q = 2$), 3 output ($p = 3$) system:

$$\begin{bmatrix} G_{y_1s_1} & G_{y_1s_2} \\ G_{y_2s_1} & G_{y_2s_2} \\ G_{y_3s_1} & G_{y_3s_2} \end{bmatrix} = \begin{bmatrix} H_{11} & H_{12} \\ H_{21} & H_{22} \\ H_{31} & H_{32} \end{bmatrix} \begin{bmatrix} G_{x_1s_1} & G_{x_1s_2} \\ G_{x_2s_1} & G_{x_2s_2} \end{bmatrix} \quad (8.19)$$

Using an abbreviated representation of these matrices:

$$[G_{ys}] = [H_{yx}][G_{xs}] \quad (8.20)$$

where any element of the H_{yx} matrix, $H_{y_i x_j}$ represents the response, Y_i , caused by a force, X_j . The G_{xx} matrix has dimensions of (qxq) , while the G_{yx} and H_{yx} matrices have dimensions of (pxq) . The estimate of Eq. 8.20 for a finite measurement of n sample records is given by

$$[{}_n^c \hat{H}_{yx}] = [{}_n^c \hat{G}_{ys}] [{}_n^c \hat{G}_{xs}]^{-1} \quad (8.21)$$

where the notation used for the FRF estimator is that proposed by Cobb and Mitchell [18].

Now a generalization can be made about the required number of measurement channels and the required number of cross spectral densities. Consider a system with q inputs and p outputs. $2q$ input signals (S_i and X_i) and p output signals (Y_j) must be measured. This means that $(2p + q)$ processing channels are needed. To form the G_{xx} matrix q^2 cross spectral density terms must be computed. An additional pxq cross

spectral density terms are needed for the G_{xx} matrix. Thus, the total number of cross spectral densities required for q inputs and p outputs is

$$\text{Number of cross spectral density terms} = (qxq) + (pxq) = q(q + p) \quad (8.22)$$

8.2 Other Multiple Input FRF Estimators

The most commonly used multiple input $H(f)$ estimation method is based on the ${}^1\hat{H}$ estimator. In terms of the notation used in Eq. 8.21:

$$[{}^1\hat{H}_{yx}] = [\hat{G}_{yx}][\hat{G}_{xx}]^{-1} \quad (8.23)$$

Because $[\hat{G}_{xx}]$ will always be a square matrix, the matrix inversion will always be possible so long as the matrix is not singular. A singular matrix would occur if 2 or more input forces were 100 percent correlated.

By analogy with the ${}^c\hat{H}$ and ${}^1\hat{H}$ estimators, a multiple input estimator based on ${}^2\hat{H}$ can be developed as

$$[{}^2\hat{H}_{yx}] = [\hat{G}_{yy}][\hat{G}_{xy}]^{-1} = [\hat{G}_{yy}][[\hat{G}_{yx}]^*]^T^{-1} \quad (8.24)$$

where the * indicates that each element in the matrix is replaced by its complex conjugate. A limitation of this method is that the $[\hat{G}_{xy}]$ matrix is not square unless the number of input force and response locations are equal. This is a severe limitation.

8.3 Multiple Input - Multiple Output Measurement

Simulations

A multiple input - multiple output computer simulation program was written, similar to the single input-output simulation program discussed earlier. A random number generator was used to generate the simulated source and uncorrelated content signals. Except that known values of system FRFs, shaker/amplifier gains, and crosstalk factors were substituted for their real-life counterparts, the simulated measurements were carried out using procedures identical to actual measurements. The simulation results shown here used a discrete three-mass model with three input force locations and three responses. This resulted in a square G_{xx} matrix which allowed comparison of the multiple input ${}^2\hat{H}$ estimator.

In Fig. 56 we find that the results for the multiple input-multiple output estimators are analogous to the results from their single degree-of-freedom counterparts. With 'cross-talk' and large amounts of uncorrelated content present, ${}^1\hat{H}$ was biased low, ${}^2\hat{H}$ was biased high, and ${}^3\hat{H}$ was unbiased. No experimental verifications have been carried out at this time.

Comparison of MDOF FRF Estimators

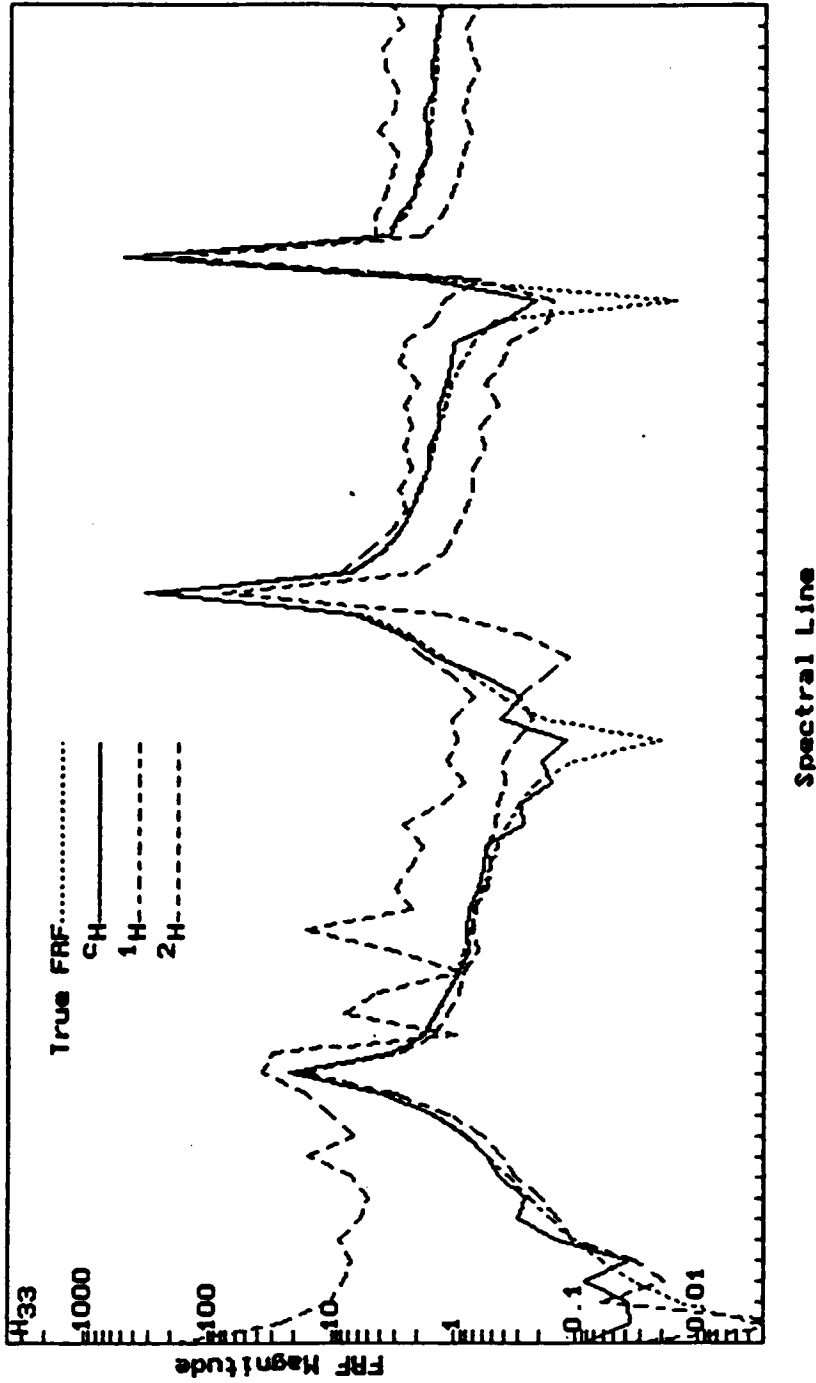


Figure 56. Simulated Multiple Input-Multiple Output FRF Measurement

Chapter 9 - Conclusions and Recommendations

9.1 Conclusions

Simulations and experimental results have shown the three-channel estimator performs well in obtaining unbiased FRF estimates, even in the presence of noise. Because it appears that leakage appears as uncorrelated content in the estimates, there is reason to believe that this estimator may also be unbiased in the presence of leakage. However, this claim cannot be made with certainty without further work. Advancements made in this work include:

1. Development of basic statistical estimates for the three-channel estimator in terms of both measured quantities and measurement system parameters.
2. Identification and characterization of the complex random variable magnitude bias error and its effect on statistical estimates.
3. A method for accurately estimating the variability of an FRF estimate obtained with the three-channel estimator. It is anticipated that this information will be of value in the estimation of system parameters from 'curve fits' of measured data. It will allow

weighting factors be applied to different estimates in the fitting process, depending on the relative variability.

4. The confidence bands allow the user to make a preliminary test to determine variance estimates. From these results an acceptable confidence band width can be decided on and the amount of averaging required to achieve that result estimated.

5. Development of uncorrelated content estimates using the three-channel measurement system. This finally allows quantitative estimates which could only be guessed at formerly. These estimators allow detection of leakage, nonlinear behavior, or extraneous noise, and provide information about the sources of these signal degraders.

6. The uncorrelated content estimators can be used as automatic detectors of system errors. They will also provide a tool for evaluating the merits of the various excitation methods.

7. Extension of the three-channel FRF measurement method to multiple-input/multiple-output estimates. The multiple-input version of the three-channel estimator has been shown in simulations to be unbiased in the presence of noise. It has promise for improving multiple-input FRF estimates and is useful for detecting such conditions as malfunctioning shakers or amplifiers.

9.2 Recommendations

While the variance estimator was found to give uniform estimates of variance, these were often low. A 'self-correcting' algorithm could be built in that would allow adjustments to be made. Its operation would be similar to the tests performed in Section 7.2.1. A possible implementation would be as follows: the experimenter makes two contiguous

FRF measurements. The variance is calculated for one set of data and the second FRF is plotted over the resulting 2σ confidence bounds. We saw in Section 7.2.1.1 that on the average 84 percent of the second FRF estimates should fall within these bounds. If the percentage was significantly different, an estimated correction could be calculated, and the test entire test repeated.

This test procedure would also allow verification of uniformity of variance estimates (i.e., that the probability of error predicted by the confidence bounds is the same at all regions of an FRF). This verification would be similar to the one done in Fig. 48. When plotting the confidence bounds and FRF from a contiguous measurement those spectral lines where the FRF estimates did not fall within the bounds could be flagged in some manner (as was done with the 'tic marks' in Fig. 48). Noting how uniformly these flags were distributed over the FRF would give an indication of areas where the variance was being over or under estimated. These two 'on site' tests would allow the experimenter to verify how well the variance estimates were working in his particular test situation, and eliminate the need to accept the results blindly.

The variance estimates appeared to be very low in the case of a lightly damped structure excited by continuous random input and using a Hanning window. From the work of Nuttall [34,35] the variance estimates could possibly be reformulated to account for the Hanning window effects. Initial investigations indicate that this would not be an 'add on' type correction, but would require new derivations (especially the covariance of G_{rr} and G_{rr} magnitudes).

The uncorrelated content estimators can be used to check system performance. Regularly checking these estimates would allow detection of leakage, poor connections (shaker, force gage, accelerometer), improper 'stinger' design, and other sources of un-

correlated content in the measurement system. Verification of the suitability of various excitation signals and windows could be made for the particular system under test.

The potential for the multiple input-multiple output \hat{H} estimator is high. It is capable of obtaining unbiased estimates in the presence of uncorrelated content. It can be used to detect such problems as inoperative shakers which can occur in multiple input tests. The 'crosstalk' between input locations can be quantified, which would be of use in optimizing input signal levels and force application locations.

References

1. Press, W. H., B. P. Flannery, S. A. Teukolsky, and W. T. Vetterling, *Numerical Recipes - The Art of Scientific Computing*, Cambridge University Press, New York, N.Y., 1986, pp. 390-391.
2. Cooley, J. W., and J. W. Tukey, "An Algorithm for the Machine Calculation of Complex Fourier Series", *Mathematics of Computation*, Vol. 19, 1965, pp. 297-301.
3. Mitchell, L. D., "An Improved Method for the Fast Fourier Transform (FFT) Calculation of the Frequency Response Function", *First European Signal Processing Conference*, Lausanne, Switzerland, September 16-19, 1980, p. 159-160.
4. Mitchell, L. D., "Improved Methods for the Fast Fourier Transform (FFT) Calculation of the Frequency Response Function", *Journal of Mechanical Design*, Vol. 104, April 1982, pp. 277-279.
5. Vold, H., J. Crowley, and G. T. Rocklin, "New Ways of Estimating Frequency Response Functions", *Sound and Vibration*, November 1984, pp. 34-38.
6. Elliott, K. B., and L. D. Mitchell, "The Improved Frequency Response Function and its Effect on Modal Circle Fits", *Journal of Applied Mechanics*, Vol. 51, September 1984, pp. 657-663.
7. Cawley, P., "The Accuracy of Frequency Response Function Measurements Using FFT-Based Analyzers With Transient Excitation", *Journal of Vibration, Acoustics, Stress, and Reliability in Design*, Vol. 108, January 1986, pp. 44-49.
8. Anon (YARD Ltd, Scotl.), "Note on the Calculation of Frequency Response Functions by the Inverse Method", *Journal of Sound and Vibration*, Vol. 93, (n3), April 1984, pp. 469-471.

9. Schmidt, H., "Resolution Bias Errors in Spectral Density, Frequency Response and Coherence Function Measurements, V: Comparison of Different Frequency Response Estimators", *Journal of Sound and Vibration*, Vol. 101 (n3), 1985, pp. 413-418.
10. Wicks, A. L., "Estimation of Frequency Response Functions in the Presence of Uncorrelated Content", Ph.D. Dissertation, Michigan Technological University, 1986.
11. Wicks, A. L., "Frequency Response Function Estimation and Quality Statistic", *Proceedings of the 1987 SEM Spring Conference on Experimental Mechanics*, Houston, Texas, June 14-19, 1987, pp. 517-525.
12. Wicks, A. L., and L. D. Mitchell, "A New Means of Estimation of Frequency Response Functions in the Presence of Uncorrelated Signals, Part I", *Proceedings of the 1987 SEM Spring Conference on Experimental Mechanics*, Houston, Texas, June 14-19, 1987, pp. 629-634.
13. Goyder, H. G. D., "Foolproof Methods for Frequency Response Measurements", *Proceedings of the Second International Conference on Recent Advances in Structural Dynamics*, Southampton, England, 1984.
14. Goyder, H. G. D., "Measurement of the Natural Frequencies and Damping of Loosely Supported Tubes in Heat Exchangers", *Proceedings of the Third International Conference on Vibration in Nuclear Plants*, London, England, May 11-14, 1982, pp. 258-272.
15. Ratcliffe, C. P., "Experimental Aspects of Nelson's Principle Applied to the Modal Analysis of Non-Linear Structures", *Proceedings of the International Modal Analysis Conference III*, Orlando, Florida, 1985, pp. 436-440.
16. Wicks, A. L., and Mitchell, L. D., "Methods for the Estimation of Frequency-Response Functions in the Presence of Uncorrelated Noise, A Review", *The International Journal of Analytical and Experimental Modal Analysis*, Vol. 2, (n3), July 1987, pp. 109-112.
17. Mitchell, L. D., R. E. Cobb, J. C. Deel, and Y. W. Luk, "An Unbiased Frequency Response Function Estimator", *Proceedings of the International Modal Analysis Conference V*, London, England, April 6-9, 1987, pp. 364-373.
18. Cobb, R. E., and L. D. Mitchell, "A Method for the Unbiased Estimate of System FRF's in the Presence of Multiple Correlated Inputs", *Proceedings of the International Modal Analysis Conference VI*, Orlando, Florida, February 1-4, 1988, pp. 1154-1160.
19. Cobb, R. E., and L. D. Mitchell, "Estimation of Uncorrelated Content in Experimentally Measured FRF's Using Three Measurement Channels", *Proceedings of the International Modal Analysis Conference VI*, Orlando, Florida, February 1-4, 1988, pp. 696-700.

20. Allemang, R. J., "Investigation of Some Multiple Input/Output FRF Experimental Modal Analysis Techniques", Dissertation, University of Cincinnati, 1980.
21. Bendat, J. S., "Statistical Errors in Measurement of Coherence Functions and Input/Output Quantities", *Journal of Sound and Vibration*, Vol. 59 (n3), 1978, pp. 405-421.
22. Acom, M., "A Note on Random Errors in Frequency Response Estimators", *Journal of Sound and Vibration*, Vol. 107 (n2), 1986, pp. 355-358.
23. Bendat, J. S., and A. G. Piersol, *Random Data - Analysis and Measurement Procedures*, 2d ed., John Wiley and Sons, New York, New York, 1986.
24. Papoulis, A., *Probability, Random Variables, and Stochastic Processes*, 2d ed., McGraw-Hill Book Company, New York, New York, 1984, pp. 112,139,142.
25. Hoel, P. G., *Introduction to Mathematical Statistics*, 3d ed., John Wiley and Sons, New York, New York, 1962, pp. 381-383.
26. Rao, C. Radhakrishna, *Linear Statistical Inference and its Applications*, 2d ed., John Wiley and Sons, New York, New York, 1973, p. 385.
27. Ott, L., *An Introduction to Statistical Methods and Data Analysis*, 2d ed., Prindle, Weber & Schmidt Publishers, Boston, Massachusetts, 1984, pp. 109-119.
28. Carter, G. C., Knapp, C. H., and Nuttall, A. H., "Estimation of the Magnitude-Squared Coherence via Overlapped Fast Fourier Transform Processing", *IEEE Transactions on Audio and Electroacoustics*, Vol. AU-21, August 1973, p.337.
29. Abramowitz, M., and Stegun, I. A., (eds), *Handbook of Mathematical Functions*, (National Bureau of Standards Applied Mathematics Series - # 55), John Wiley and Sons, New York, New York, 1964, p. 947, Eq. 26.6.13.
30. Stephens, M. A., "EDF Statistics for Goodness of Fit and Some Comparisons", *Journal of the American Statistical Association*, , September 1974, pp. 730-737.
31. Taber, R. C., Vold, H., Brown, D. L., and Rocklin, G. T., "Exponential Window for Burst Random Excitation", *Proceedings of the International Modal Analysis Conference III*, Schenectady, New York, January 1985, pp. 989-995.
32. Mitchell, L. D., and Elliott, K. B., "How to Design Stingers for Vibration Testing of Structures", *Sound and Vibration*, April 1984, pp. 14-18.
33. Tomlinson, G. R., "Force Distortion in Resonance Testing of Structures with Electro-Dynamic Vibration Exciters", *Journal of Sound and Vibration*, Vol. 63 (n3), 1979, pp. 337-350.

34. Nuttall, A. H., and Carter, G. C., "Spectral Estimation Using Combined Time and Lag Weighting", *Proceedings of the IEEE*, Vol. 70 (n9), September 1982, pp. 1115-1125.
35. Nuttall, A. H., "Analysis of a generalised framework for spectral estimation - Part 2: Reshaping and variance results", *Proceedings of the IEEE - Pt. F*, Vol. 130 (n3), April 1983, pp. 242-245.
36. Olsen, N. L., "Using and Understanding Electrodynamic Shakers in Modal Applications", *Proceedings of the International Modal Analysis Conference IV.*, Los Angeles, California, 1986, Vol. II, pp. 1160-67.

Appendix

Cross Spectrum Magnitude Covariance Derivation

The covariance of the cross spectrum magnitudes used in the three-channel FRF estimation method is needed for the correlation coefficient used in the numerical integration.

This derivation begins with Eq. 2.42 which is rewritten here as Eq. A.1

$$\text{Cov}(|\tilde{G}_{ys}|, |\tilde{G}_{xs}|) \cong \frac{1}{|G_{ys}| |G_{xs}|} [C_{ys}C_{xs}E[\Delta C_{ys}\Delta C_{xs}] + Q_{ys}Q_{xs}E[\Delta Q_{ys}\Delta Q_{xs}] + C_{ys}Q_{xs}E[\Delta C_{ys}\Delta Q_{xs}] + Q_{ys}C_{xs}E[\Delta Q_{ys}\Delta C_{xs}]] \quad (A.1)$$

The four expectation terms must be evaluated. We begin by simplifying the first expectation term in Eq. A.1

$$\begin{aligned} E[(\Delta C_{ys})(\Delta C_{xs})] &= E[(\tilde{C}_{ys} - C_{ys})(\tilde{C}_{xs} - C_{xs})] \\ &= E[\tilde{C}_{ys}\tilde{C}_{xs}] - E[\tilde{C}_{ys}C_{xs}] - E[C_{ys}\tilde{C}_{xs}] + C_{ys}C_{xs} \\ &= E[\tilde{C}_{ys}\tilde{C}_{xs}] - C_{ys}C_{xs} \end{aligned} \quad (A.2)$$

Similarly, the other three expectation terms may be reduced to

$$\begin{aligned}
E[(\Delta Q_{ys})(\Delta Q_{xs})] &= E[\tilde{Q}_{ys}\tilde{Q}_{xs}] - Q_{ys}Q_{xs} \\
E[(\Delta C_{ys})(\Delta Q_{xs})] &= E[\tilde{C}_{ys}\tilde{Q}_{xs}] - C_{ys}Q_{xs} \\
E[(\Delta Q_{ys})(\Delta C_{xs})] &= E[\tilde{Q}_{ys}\tilde{C}_{xs}] - Q_{ys}C_{xs}
\end{aligned} \tag{A.3}$$

Evaluation of each of the four expectations in Eqs. A.2 and A.3 follows a very similar development, so only the expectation $E[\tilde{C}_y\tilde{C}_x]$ will be carried out in detail. \tilde{C}_x is given by Eq. 2.26. From Eqs. 2.3 and 2.9 we find

$$\begin{aligned}
\tilde{C}_{ys} = \frac{2}{T} [&(S_R^2 + S_I^2)Re[\Gamma H] + S_R(K_R H_R - K_I H_I + N_R) + \\
&S_I(K_R H_I + K_I H_R + N_I)]
\end{aligned} \tag{A.4}$$

Multiplying these terms and taking the expectation

$$\begin{aligned}
E[\tilde{C}_{ys}\tilde{C}_{xs}] &= \frac{4}{T^2} E[(S_R^2 + S_I^2)^2 Re[\Gamma H] \Gamma_R + (S_R^3 + S_R S_I^2)(K_R H_R - K_I H_I + N_R) \Gamma_R + \\
&(S_R^2 S_I + S_I^3)(K_R H_I + K_I H_R + N_I) \Gamma_R + (S_R^3 + S_R S_I^2)(K_R + M_R) Re[\Gamma H] + \\
&S_R^2 (K_R + M_R)(K_R H_R - K_I H_I + N_R) + S_R S_I (K_R + M_R)(K_R H_I + K_I H_R + N_I) + \\
&(S_R^2 S_I + S_I^3)(K_I + M_I) Re[\Gamma H] + S_R S_I (K_I + M_I)(K_R H_R - K_I H_I + N_R) + \\
&S_I (K_I + M_I)(K_R H_I + K_I H_R + N_I)]
\end{aligned} \tag{A.5}$$

Expanding and collecting terms

$$\begin{aligned}
E[\tilde{C}_{ys}\tilde{C}_{xs}] = & \frac{4}{T^2}E[(S_R^4 + 2S_R^2S_I^2 + S_I^4)Re[\Gamma H]\Gamma_R + \\
& [S_R^3K_RH_R - S_R^3K_IH_I + S_R^3N_R + S_RK_RS_I^2H_R - S_RK_IS_I^2H_I + S_RN_RS_I^2 + \\
& S_R^2S_IK_RH_I + S_R^2S_IK_IH_R + S_R^2S_I N_I + S_I^3K_RH_I + S_I^3K_IH_R + S_I^3N_I]\Gamma_R + \\
& [S_R^3K_R + S_R^3M_R + S_RS_I^2K_R + S_RS_I^2M_R]Re[\Gamma H] + \\
& S_R^2K_R^2H_R - S_R^2K_RK_IH_I + S_R^2K_RN_R + S_R^2K_RM_RH_R - S_R^2M_RK_IH_I \quad (A.6) \\
& S_R^2M_RN_R + S_RS_IK_R^2H_I + S_RS_IK_RK_IH_R + S_RS_IK_RN_I + S_RS_I M_RK_RH_I + \\
& S_RS_I M_RK_IH_R + S_RS_I M_RN_I + S_RS_IK_IK_RH_R - S_RS_IK_I^2H_I + S_RS_IK_I N_R + \\
& [S_R^2S_IK_I + S_R^2S_I M_I + S_I^3K_I + S_I^3M_I]Re[\Gamma H] + \\
& S_RS_I M_IK_RH_R - S_RS_I M_IK_IH_I + S_RS_I M_I N_R + S_I^2K_IK_RH_I + S_I^2K_I^2H_R + \\
& + S_I^2K_I N_I + S_I^2M_IK_RH_I + S_I^2M_IK_IH_R + S_I^2M_I N_I]
\end{aligned}$$

Equations 2.4 - 2.6 may be used to reduce the great majority of the above terms to zero in the expectation operation. The remaining terms are then

$$E[\tilde{C}_{ys}\tilde{C}_{xs}] = \frac{4}{T^2}E[(S_R^4 + 2S_R^2S_I^2 + S_I^4)Re[\Gamma H]\Gamma_R + S_R^2K_R^2H_R + S_I^2K_I^2H_R] \quad (A.7)$$

These expectations may be found by using Eqs. 2.4 - 2.7 and remembering that Γ and H are system constants which may be factored out of the expectation operation. The result is

$$E[\tilde{C}_{ys}\tilde{C}_{xs}] = 2G_{ss}^2Re[\Gamma H]\Gamma_R + \frac{1}{2}G_{ss}G_{kk}H_R \quad (A.8)$$

For convenience, parts of Eq. 2.13 are repeated here in a rearranged form

$$\begin{aligned}
G_{ss}\Gamma_R &= E[\tilde{C}_{xs}] = C_{xs} \\
G_{ss}Re[\Gamma H] &= E[\tilde{C}_{ys}] = C_{ys}
\end{aligned} \quad (A.9)$$

When these substitutions are made in Eq. A.8 the result is

$$E[\tilde{C}_{ys}\tilde{C}_{xs}] = 2C_{xs}C_{ys} + \frac{1}{2}G_{ss}G_{kk}H_R \quad (A.10)$$

Inserting Eq. A.10 in Eq. A.2 yields

$$E[(\Delta C_{ys})(\Delta C_{xs})] = C_{ys}C_{xs} + \frac{1}{2}G_{ss}G_{kk}H_R \quad (A.11)$$

The expectations of the other three terms in Eq A.3 can be found in a similar manner:

$$\begin{aligned} E[(\Delta C_{ys})(\Delta Q_{xs})] &= C_{ys}Q_{xs} - \frac{1}{2}G_{ss}G_{kk}H_I \\ E[(\Delta Q_{ys})(\Delta Q_{xs})] &= Q_{ys}Q_{xs} + \frac{1}{2}G_{ss}G_{kk}H_R \\ E[(\Delta Q_{ys})(\Delta C_{xs})] &= Q_{ys}C_{xs} + \frac{1}{2}G_{ss}G_{kk}H_I \end{aligned} \quad (A.12)$$

where the one minus sign in Eq. A.12 is not a mistake. Inserting Eqs. A.11 and A.12 in Eq. A.1

$$\begin{aligned} \text{Cov}(|\tilde{G}_{ys}|, |\tilde{G}_{xs}|) &\cong \frac{1}{|G_{ys}| |G_{xs}|} [C_{ys}C_{xs}[C_{ys}C_{xs} + \frac{1}{2}G_{ss}G_{kk}H_R] + \\ &Q_{ys}Q_{xs}[Q_{ys}Q_{xs} + \frac{1}{2}G_{ss}G_{kk}H_R] + C_{ys}Q_{xs}[C_{ys}Q_{xs} - \frac{1}{2}G_{ss}G_{kk}H_I] + \\ &Q_{ys}C_{xs}[Q_{ys}C_{xs} + \frac{1}{2}G_{ss}G_{kk}H_I]] \end{aligned} \quad (A.13)$$

Expanding and collecting terms

$$\begin{aligned} \text{Cov}(|\tilde{G}_{ys}|, |\tilde{G}_{xs}|) &\cong \frac{1}{|G_{ys}| |G_{xs}|} [(C_{ys}C_{xs})^2 + (Q_{ys}Q_{xs})^2 + (C_{ys}Q_{xs})^2 + (Q_{ys}C_{xs})^2 \\ &\frac{1}{2}G_{ss}G_{kk}[H_R(C_{ys}C_{xs} + Q_{ys}Q_{xs}) + H_I(Q_{ys}C_{xs} - C_{ys}Q_{xs})]] \end{aligned} \quad (A.14)$$

The first four terms of Eq. A.14 may be rewritten in factored form from which we find

$$(C_{ys}^2 + Q_{ys}^2)(C_{xs}^2 + Q_{xs}^2) = |G_{ys}|^2 |G_{xs}|^2 \quad (A.15)$$

We also rewrite Eq. 2.51 as

$$\begin{aligned} H(f) &= \frac{G_{ys}}{G_{xs}} = \frac{C_{ys} - j Q_{ys}}{C_{xs} - j Q_{xs}} \\ &= \frac{(C_{ys} - j Q_{ys})(C_{xs} + j Q_{xs})}{C_{xs}^2 + Q_{xs}^2} \\ &= \frac{(C_{ys}C_{xs} + Q_{ys}Q_{xs}) - j(Q_{ys}C_{xs} - C_{ys}Q_{xs})}{|G_{xs}|^2} \end{aligned} \quad (A.16)$$

Substituting Eqs. A.15 and A.16 in Eq. A.14 we arrive at

$$\begin{aligned} \text{Cov}(|\tilde{G}_{ys}|, |\tilde{G}_{xs}|) &\cong \frac{1}{|G_{ys}| |G_{xs}|} \{ |G_{ys}|^2 |G_{xs}|^2 + \frac{1}{2} G_{ss} G_{kk} (H_R^2 + H_I^2) |G_{xs}|^2 \} \\ &\cong |G_{xs}| \left\{ |G_{ys}| + \frac{\frac{1}{2} G_{ss} G_{kk} |H|^2}{|G_{ys}|} \right\} \end{aligned} \quad (A.17)$$

which is Eq. 2.46.

**The vita has been removed from
the scanned document**